Driving Tissue Morphogenetic Cascades Using Tunable Nanolayered Surface Coatings

by

Nisarg Jaydeep Shah
B.S., Chemical and Biomolecular Engineering, Johns Hopkins University (2009)
S.M., Chemical Engineering Practice, Massachusetts Institute of Technology (2011)

SUBMITTED TO THE DEPARTMENT OF CHEMICAL ENGINEERING IN PARTIAL FULFILLMENT OF THE REQUIREMENTS FOR THE DEGREE OF

DOCTOR OF PHILOSOPHY IN CHEMICAL ENGINEERING
AT THE
MASSACHUSETTS INSTITUTE OF TECHNOLOGY

MAY 2014
[JUNE 2014]

Signature of Author. Signature redacted .....
Nisarg J. Shah
Department of Chemical Engineering
May 8, 2014

Certified by..... Signature redacted .....
Paula T. Hammond
David H. Koch (1962) Chair Professor in Engineering
Thesis Supervisor

Accepted by..... Signature redacted .....
Patrick S. Doyle
Singapore Research Chair Professor of Chemical Engineering
Chairman, Committee for Graduate Students

Driving Tissue Morphogenetic Cascades Using Tunable Nanolayered Surface Coatings

by

Nisarg Jaydeep Shah

Submitted to the Department of Chemical Engineering
on May 8, 2014, in partial fulfillment of the requirements for the degree of
Doctor of Philosophy in Chemical Engineering

Abstract

Harnessing the synergy between materials at the nanoscale can be a valuable tool in understanding and probing cellular phenomena and in driving specific processes that lead to tissue and organ regeneration and repair. Biomedical implants attempt to materially replace damaged tissues, restore function, improve mobility, and alleviate pain. However, these implants often fail to recapitulate the original tissue properties. In the context of orthopedic implants, the functional success of an implant critically depends on its stable interaction and bonding with the host tissue. Yet, aseptic implant loosening accounts for over half of all joint replacement failures. Non-biological implant materials such as metals and plastics are used for their mechanical strength, but these are typically not suitable for direct integration with the host tissue. Conversely, traumatic wounds and congenital defects that result in large bone tissue defects are often corrected with autograft bone, which results in the matching of native bone tissue properties. However, the limited availability of donor bone coupled with pain at the site renders autografting suboptimal therapy. Permanent implants require multiple rounds of surgery and are often unable to recapitulate complex tissue reconstruction with high fidelity and carry the risk of inducing a foreign body response. Orthogonally, therapies to alleviate diseases in the bone such as osteosarcoma and osteoporosis are of significant interest to improve clinical outcomes. However systemic delivery of these therapies leads to toxic side-effects that limit their clinical use. These significant challenges to improving human health can be overcome by designing and combining materials with complementary biological properties.

This body of work investigates the use of tunable, modular, nanoscale coatings that can prevent premature implant failure, induce targeted tissue repair by recapitulating aspects of the natural wound healing cascade and target therapy to the bone tissue. At the nanoscale, these coatings can impart multifunctionality to nanoparticles that can be used as a therapeutic agent. Central to the polymer-based multilayered coating, was a water-based layer-by-layer (LbL) deposition process, by which each component was introduced on the surface in nanoscale layers. On surrogate bone implants, coatings containing osteoconductive hydroxyapatite (HAP) and 5-10 μg of osteoinductive bone morphogenetic protein 2 (BMP-2) contained within the nanostructured coating acted synergistically to induce osteoblastic differentiation of endogenous progenitor cells in a rat. The tuned release of BMP-2 over 3-4 weeks, controlled by a hydrolytically degradable poly(β-amino ester), was essential for tissue regeneration and, in the presence of HAP, the modular coating encouraged the direct deposition of highly

cohesive trabecular bone on the implant surface with an interfacial tensile strength that was 2-3 fold higher than implants coated with bioactive bone cement. Importantly, the failure was as a result of bone fracture, rather than at the bone-implant interface. The coated implants demonstrated long-term stability and mechanical integrity.

To repair large bone defects, two strategies were employed that involved the use of adaptive growth factor delivery from LbL surface coatings. In the first instance, scaffolds made of polycaprolactone and β-tricalcium phosphate (β-TCP) were developed and used as osteoconductive scaffolds. The scaffolds were coated with multilayer films that sequestered BMP-2 and angiogenic vascular endothelial growth factor (VEGF). In vivo, at an intramuscular ectopic location, the mineral density of ectopic bone formed de novo by BMP-2/VEGF multilayer coated scaffolds resulted in bone formation that was approximately 33% higher than when only BMP-2 was delivered. Bone formed throughout the scaffold when both growth factors were released, which suggests more complete remodeling due to an increased local vascular network. Using another strategy for orthotopic, craniomaxillofacial bone repair, scaffolds made of a poly(lactic-co-glycolic acid) (50:50) copolymer were used with multilayer coatings containing tunable amounts of BMP-2 and mitogenic platelet derived growth factor (PDGF)-BB from 0.2-2μg. Complete release of the growth factors occurred over readily adapted time scales, which extended from 8-10 days and 22-25 days for PDGF-BB and BMP-2 respectively. Each component of the system was tested for its effect on tissue formation. The adaptive growth factor release and synergistic effect of BMP-2 and PDGF-BB promoted local bone formation that bridged a critical-size defect in the rat calvaria as early as 2 weeks after implantation. Dual growth factor delivery resulted in mechanically competent bone that restored the properties of the bone and regenerated the native calvaria form. This approach could be a customizable, off-the-shelf, cell-free option for bone tissue repair.

In addition to focusing on multilayer coatings for macroscale implants and scaffolds, an approach for generating polymer coated functional and targeted nanoscale drug carriers specifically for treating bone disease such as osteosarcoma and osteoporosis was developed. The approach utilized the modularity of LbL assembly to generate tissue-specific drug carriers for systemic administration. This was accomplished via surface modification of drug-loaded nanoparticles with an aqueous polyelectrolyte, poly(acrylic acid) (PAA), with 40% of side-chains functionalized with alendronate, a potent clinically used bisphosphonate. Encapsulation of doxorubicin at 5mg/kg in an LbL-targeted liposome demonstrated potent toxicity. Active targeting of 143B osteosarcoma xenografts in NCR nude mice prolonged tumor accumulation by over 7 days. Tumor burden reduced, and in some cases the entire tumor mass was eliminated within 40 days, with a 3 dose regimen.

Collectively, this work provides insight into probing and modifying cellular interactions to control morphogenetic processes at varying length and time scales, and in different disease states with a polymer-based multilayer coating approach. Towards the development of next-generation biomedical therapies this approach allows for driving cell morphogenetic phenomena and controlling local microenvironments to understand and engineer specific therapies with the ultimate goal to improve human health.

Thesis Supervisor: Paula T. Hammond
Title: David H. Koch (1962) Professor in Engineering

Thesis Supervisor

Paula T. Hammond, Ph.D.
David H. Koch (1962) Professor in Engineering
Department of Chemical Engineering
The David H. Koch Institute for Integrative Cancer Research
Massachusetts Institute of Technology

Thesis Committee

Sangeeta N. Bhatia, Ph.D.
John and Dorthy Wilson Professor
Harvard-MIT Division of Health Sciences and Technology
Department of Electrical Engineering and Computer Science
The David H. Koch Institute for Integrative Cancer Research
Massachusetts Institute of Technology

Robert S. Langer, Sc.D.
David H. Koch (1962) Institute Professor
Department of Chemical Engineering
Harvard-MIT Division of Health Sciences and Technology
The David H. Koch Institute for Integrative Cancer Research
Massachusetts Institute of Technology

Howard J. Seeherman, Ph.D., V.M.D.
Restituo LLC.

For my parents,
Jaydeep and Jaishri Shah

Acknowledgements

I have been fortunate to have worked with a set of phenomenally talented individuals who have contributed in a myriad of ways towards my graduate school experience. The work described in this thesis has been strongly influenced by my interactions with them.

My foremost appreciation is for my mentor and advisor, Prof. Paula Hammond. She has been an inspirational role-model for me and I have learned a tremendous amount from my interactions with her. She provided me with an opportunity to work on a fascinating, cutting-edge research project that challenged me and helped my professional development. She was open-minded about new research directions and enthusiastic about letting me pursue several independent projects that helped broaden my skills. Her enthusiasm and perpetual optimism was infectious and helped me overcome scientific challenges. She has all the qualities of an inspirational mentor, a leading scientist, and a truly wonderful person.

I would like to thank my thesis committee, Prof. Sangeeta Bhatia, Prof. Bob Langer and Dr. Howard Seeherman, for their participation. They brought a tremendous amount of experience and expertise between them and always offered reasoned and constructive feedback that helped overcome scientific challenges. Their support has been highly instrumental in shaping this body of work. I am also grateful to Profs. Myron Spector (VA Boston Healthcare System/Brigham and Women's Hospital), Robert Padera (Brigham and Women's Hospital) and Myron Nevins (Harvard School of Dental Medicine) who have been tremendously helpful collaborators and from whom I am learned a lot about biomedical research. I would like to acknowledge Prof. Justin Hanes (Johns Hopkins University), who welcomed me into his lab to pursue undergraduate research under the mentorship of Ben Tang. My experience in Justin's lab largely influenced my decision to pursue graduate school.

I am indebted to past and present Hammond Lab members who have been wonderful colleagues and friends and also helped make a positive work environment. Mara was a great mentor during my early days in the group, and helped me get started with my research. Ray was a truly gifted individual, full of ideas and an infectious enthusiasm, and helped me with animal studies in the early days. I am grateful to other members of

the LbL delivery subgroup for their input. In particular, Anita and Jessie, who provided valuable advice and Josh, whose advice and assistance has been invaluable. Zhiyong, Amanda and Abby could not have been better office-mates and I will always remember the breakfast club and the wonderful treats. I enjoyed discussing research and working with Nasim, who is a multitalented individual with tons of good advice. I would like to acknowledge Mohi, Stephen and Jason for their enthusiasm and assistance in lab. I am grateful to Christine and Liz, whose excellent organizational skills and constant willingness to help with the several important administrative aspects of graduate school so much easier. I have been fortunate to build strong friendships in this lab that will last a lifetime.

The support and administrative staff at MIT have been generous with their time, patient and generous with their advice. Suzanne, Katie and Joel at the student office have been extraordinarily supportive. Drs. Alison Hayward and Alton Swennes are extraordinary veterinarians and tremendously helpful. Catrina and Wayne were incredibly helpful surgery techs and their assistance made the animal studies more manageable.

I would like to dedicate this thesis to my family whose support has helped make this journey possible. To my parents, Jaydeep and Jaishri, who have always believed in me and provided me with boundless love and unconditional support to pursue opportunities to succeed. They have instilled in me a passion for education, a strong work ethic and a sense of perseverance to pursue my passions and bring them to fruition. I feel truly blessed to have the support of such wonderful parents. Being the only child, I can only imagine the decisions that they had to make so allow me to go far away from home to pursue higher education. To my uncles, aunts and cousins for their love, support and encouragement. To my grandparents, who have always been a supportive presence in my life. This is for all of you.

NISARG JAYDEEP SHAH
Massachusetts Institute of Technology
May 8, 2014

N.J. Shah is thankful for support from the MITSCEP 1936 Course Xa Fellowship, National Institutes of Health (NIH), the MIT Energy Initiative, the Henry C. & Frances Keany Rickard Health Science Fund at MIT, the MIT Portugal Program and the David H. Koch (1962) Professorship. This work was supported by the NIH (R01 AG029601, R01 EB010246) and in part by the David H. Koch Institute for Integrative Cancer Research (supported by the NCI through grant P30 CA014051), the Institute for Soldier Nanotechnologies (supported by the U.S. Army Research Office under contract W911NF-07-D-0004), the Center for Materials Science and Engineering MRSEC Shared Facilities (supported by the NSF through grant DMR-0213282) at MIT. The use of equipment in the laboratories of Prof. Sangeeta Bhatia and Prof. Robert Langer is gratefully acknowledged.

Contents

Figures

Figure 2.1. Design and fabrication of the osteophilic multilayer architecture. Components of the film (A) Chitosan (75%-85% deacetylated chitin), a polycation (B) Poly(acrylic acid) (PAA), (C) A hydrolytically degradable poly(β-amino ester) (Poly2), a polycation and (D) osteoinductive recombinant human bone morphogenetic protein 2 (rhBMP-2) (E) Schematic of the modular electrostatic assembly. Osteoconductive hydroxyapatite is complexed with chitosan and incorporated into nanoscale thick films along with poly(acrylic acid) in a bilayer architecture. A hydrolytically degradable poly(β-amino ester) based multilayer film incorporating osteoinductive rhBMP-2 lays atop the osteoconductive layer. (F) Scanning electron micrograph of a $[Chi(HAP)/PAA]_{20}$ bilayer film with the complexed hydroxyapatite nanoparticles. HAP particles complexed to chitosan strands are interwoven in the multilayer architecture (G) IR absorbance spectra of the different components of the osteoconductive layer (i) chitosan (ii) hydroxyapatite (iii) poly(acrylic acid) (iv) $[Chitosan/HAP]_1$ (v) $[Chitosan/PAA]_{20}$ and (vi) $[Chi(HAP)/PAA]_{20}$.

Figure 2.2. Characteristics of multilayer properties during assembly and degradation. (A) Multilayer film thickness increases linearly with incremental osteoconductive [Chi(HAP)/PAA] layers. Contributions of film thickness from the growth factor eluting layers (green) and hydroxyapatite containing layers (blue) are provided. (B) rhBMP-2 released from the films over 2 weeks. Surface and bulk morphologies of $[Chi(HAP)/PAA]_{20}$ + $[Poly2/PAA/rhBMP\text{-}2/PAA]_{20}$ multilayer films (C, F) HAP particles are distributed uniformly in the osteoconductive $[Chi(HAP)/PAA]_{20}$ multilayer surface, and the features are made rougher in (D, G) by the conformal coating of the $[Poly2/PAA/rhBMP\text{-}2/PAA]_{20}$ layers. (E, H, K) Once the growth factor is released by the degradation of the poly(β-amino ester) layers, there is an observable reduction in surface roughness. (F, G, H) Surface height profiles confirm that HAP particles are uniformly distributed with a lack of sequestration in a particular area. (I, J) Corresponding cross sectional scanning electron microscopy images confirm the presence of particles throughout the bulk of the film (I, J, K are at the same scale). C-H are atomic force microscopy images, where C-E are phase contrast images, F-H are height images. I-K are scanning electron microscopy images.

Figure 2.3. Mesenchymal stem cells differentiating into the osteoblast lineage. (A) Alkaline phosphatase (AP) quantification at 5 days after the differentiation cascade is initiated. (B) Alizarin red (AR) staining and quantification for calcium deposits 14 days after mesenchymal stem cells have been in culture under different conditions as indicated. Both AP and AR signals have been represented as fold increase or decrease of the Control +L-AA/β-GP case. A single factor ANOVA test allowed rejection of the null hypothesis for all assays; and a Tukey test between all groups was performed (s.d., n=9, ** $p < 0.01$; * $p < 0.05$; ns = not significant all others are $p < 0.001$). Temporal expression patterns of osteogenic markers in mesenchymal stem cells. Quantification of osteogenic markers (C) Osteocalcin, (D) visualized (green) from differentiating cells by fluorescence over the course of the study. (E) Osteoprotonegrin and (F) Osteopontin expression follows a similar trend to osteocalcin. In all the assays, the synergistic effect

of having an osteoconductive and an osteoinductive layer maximizes AP and AR signals. Expression of osteogenic markers may be accelerated and amplified by the introduction of the osteophilic multilayers leading to an environment conducive for bone formation. Peak and cumulative expression levels of the combination osteoconductive and an osteoinductive multilayers are statistically significant compared to other groups ($p<0.001$, Fig A4).

Figure 3.1. Structured coatings for bone regeneration are made up of two composite multilayers. (**A** to **C**) The base coating contains chitosan (Chi; 75-85% deacytelated chitin, $M_v \sim 100$ kDa) and hydroxyapatite [HAP; $Ca_{10}(PO_4)_6(OH)_2$] with poly(acrylic acid) (PAA; $M_v \sim 450$ kDa) in a bilayer repeat unit. (**D** and **E**) The osteogenic factor coating contains a hydrolytically degradable poly(β-amino ester) (Poly2, $M_v \sim 11$ kDa) and rhBMP-2 that are alternated with PAA on top of the osteoconductive base coating. **(F)** Schematic of the two sets of multilayers: osteoconductive and osteoinductive. (**G**) Cumulative release profile of rhBMP-2 from drilled implants. Data are means ± SEM (n = 9 per coating). (**H**) rhBMP-2 loading has a dose-dependent effect on calcium deposition, quantified by alizarin red at 14 days. Data are means ± SEM (n = 6-9). * $P <$ 0.05** $P < 0.01$, ANOVA with a Tukey post hoc test.

Figure 3.2. In vivo evaluation of rhBMP-2 release. rhBMP-2 was loaded into the multilayers that coated smooth and drilled PEEK rods and then implanted in the tibias of rats (n = 41-45 per group). (**A**) Controlled and burst release of fluorescently labeled rhBMP-2 was tracked in vivo over 30 and 3 days respectively. (**B**) Radiant efficiency at the implant site over time (n = 4-6 per group). (**C**) Bone marrow flushed out of excised tibiae was assayed for rhBMP-2 using ELISA for smooth and drilled implants. Data are means ± SEM (n = 5-6 per group).

Figure 3.3. Mesenchymal stem cells differentiate into osteoblasts. Five color flow cytometry was used to assess the percentage of osteoblasts in cells isolated from the tibia marrow around smooth and drilled implants. Each point represents individual implants. Means ± SEM (n = 5 per group). *$P < 0.05$, **$P < 0.01$, ANOVA with a Tukey post hoc test. FACS plots are provided in Appendix B; fig. B4.

Figure 3.4. Tensile force testing of implants from the rat tibia. Force data from individual implants are presented from smooth and drilled implants. Data are means ± SEM (n = 5 implants per group time point). *$p < 0.05$; **$p < 0.01$; ***$p < 0.001$, ANOVA with a Tukey post hoc test. Interfacial tensile strength data are provided (Appendix B; table B1 and B2).

Figure 3.5. Histology of implants with various coating formulations demonstrating bone tissue morphogenesis at the implant interface. (**A** to **F**) Implants coated with X_{20} + Y_{60} at 1, 2 and 4 weeks post-implantation demonstrating the process of implant integration with the parent bone tissue. Cement lines (broken black line) are observed on some sections. (**G**) The plane of fracture in implants with the X_{20} + Y_{60} coating is indicated by a broken black line at 4 weeks which depict an intact implant, partial separation from the host bone and complete separation from the host bone. The new bone-implant interface is intact. Sections were viewed under bright field microscopy. Scale bars: (A and C) are 200 μm; (B) and (D to G) are 50 μm. Arrows: black, bone/implant interface; red, active

osteoblasts; dark green, osteocytes; yellow, marrow cells. H&E: hematoxylin & eosin stain, TC: Masson's trichrome stain.

Figure 3.6. Bone deposition in the channels of drilled implants. Representative sections (n = 5-6 per group) of drilled implants after 4 weeks, which were coated with X_{20} + Y_{60}. (**A**) Granulation tissue (broken black line) penetrated the channel and supplied progenitor cells. (**B**) Newly deposited bone (blue) matures (red) and (**C**) gradually filled up the channel at 4 weeks. (**D**) Bone (blue and red) is present throughout the channel of a drilled implant. Sections were viewed under brightfield microscopy. Scale bars in (A, B and D) are 100μm and in (C) is 400 μm. Arrows: black, bone/implant interface; red, active osteoblasts; dark green, osteocytes; yellow, marrow cells. H&E: hematoxylin & eosin stain, TC: Masson's trichrome stain.

Figure 3.7. μCT imaging of bone formation on drilled PEEK implants. (**A**) Radiographs of bone formation around drilled implants with different coatings at 1, 2, and 4 weeks. Red arrows indicate location of the implant. (**B** and **C**) The images in (A) were used to quantify bone regeneration at 2 and at 4 weeks within (B) and outside the medullary canal (C) (using regions of interest marked by dotted red circles). Each point represents individual implants. Data are means ± SEM (n = 5-6 per group). *$p < 0.05$, **$p < 0.01$, ANOVA with Tukey post hoc test. Data for smooth implants are provided in Appendix B; fig. B11.

Fig. 4.1. Fabrication of polyelectrolyte multilayer films using the layer-by-layer method in a tetralayer architechture with [Poly2(+)/polyanion(-)/growth factor(+)/polyanion(-)] depicted below. Four different groups were fabricated. For single growth factor films (A) rhBMP-2 PEM films with architecture [Poly2/PAA/rhBMP-2/PAA]x, with x = 40, 80, 100, 120 and (B) $rhVEGF_{165}$ PEM films with architecture [Poly2/CS/$rhVEGF_{165}$/CS]y, where y = 20, 30, 40, 50. For dual growth factor films, (C) y = 40 was constant and x = 40, 80, 100, 120. (D) In another formulation, x = 80 was constant and y = 20, 30, 40, 50. The substrate was always a macroporous polycaprolactone/β-tricalcium phosphate (50wt% PCL/50wt% β-TCP) waffle cylinder scaffold, with diameter = 10mm and height = 2.5mm.

Fig. 4.2. Polyelectrolyte multilayer films were dipped in a Poly2/anion/growth factor/anion tetralayer repeat architecture on a macroporous polycaprolactone/β-tricalcium phosphate (50wt% PCL/50wt% β-TCP) waffle cylinder scaffold. Growth factor loading was controlled by varying the number of layers dipped on the scaffold. rhBMP-2 released over a period of about 2 weeks, whereas rhVEGF165 eluted completely within 8 days. 4 groups of films were fabricated and incubated in 1x PBS at pH 7.4 over 12 days to study growth factor release from the films. Growth factor release was quantified using ELISA and normalized per milligram of scaffold. Samples were in triplicate and the error bar is the standard deviation. Release from (A) Single growth factor $rhVEGF_{165}$ release and (inset) total $rhVEGF_{165}$ loading scales linearly with tetralayer number (R2 = 0.96). (B) Single growth factor rhBMP-2 release and (inset) total rhBMP-2

Fig. 4.3. Pre - osteoblast differentiation assay. Activity of rhBMP-2 released from the polyelectrolyte multilayer films is preserved. MC3T3-E1 cells were exposed to rhBMP-2 released from multilayer films, with the dose normalized per milligram of scaffold weight. Alkaline Phosphatase Assay demonstrates dose dependent early activation of bone

differentiation cascade at Day 5. After 21 days of culture, Alizarin Red Stain confirms the presence of calcium deposits laid down during the differentiation process. Visual inspection of cultures after Alizarin red staining confirms a dose dependent presence of calcium deposits. (A, B and C) Alkaline phosphatase assay at day 3 on cells differentiated with different release formulations as depicted. (D, E and F) Alizarin red assay at day 14 on cells differentiated with different release formulation as depicted. Representative images of the alizarin red stain are below the bar graph in (D, E, F). A single factor ANOVA test allowed rejection of the null hypothesis for both assays; and a Tukey test between different groups was performed (s.d., n=9, ** $p < 0.01$; * $p < 0.05$; ns = not significant; all others $p < 0.001$).

Fig. 4.4. Proliferation and Migration assays. Activity of rhVEGF165 released from the polyelectrolyte multilayer films is preserved. HUVEC cells exposed to $rhVEGF_{165}$ dose normalized per milligram of scaffold weight exhibited increased proliferation activity, as measured by BrdU. (A) 40, 80, 100 and 120 tetralayers of rhBMP-2 followed by 40 tetralayers of $rhVEGF_{165}$. (B) 40 tetralayers of rhBMP-2 followed by 20, 30, 40 and 50 tetralayers of $rhVEGF_{165}$ and (C) 20, 30, 40 and 50 tetralayers of $rhVEGF_{165}$. Closure of uniform "scratched" wound gap was monitored in HUVEC cell cultures over a period of 8 hours. Cells were fixed and imaged at 20x magnification (D) 40, 80, 100 and 120 tetralayers of rhBMP-2 followed by 40 tetralayers of $rhVEGF_{165}$. (E) 40 tetralayers of rhBMP-2 followed by 20, 30, 40 and 50 tetralayers of $rhVEGF_{165}$ and (F) 20, 30, 40 and 50 tetralayers of $rhVEGF_{165}$. A single factor ANOVA test allowed rejection of the null hypothesis for both assays; and a Tukey test between different groups was performed (s.d., n = 9, ** $p < 0.01$; * $p < 0.05$; ns = not significant; all others $p < 0.001$).

Fig. 4.5. Two dimensional microCT scans (2D) and matched three dimensional reconstructions (3D) of excised PCL-βTCP half disc scaffolds, which were implanted in the intramuscular region of rats. Implants were coated with (i) no growth factor, (ii) 6 μg of single growth factor rhBMP-2 and (iii) 6 μg of single growth factor rhBMP-2 followed by 4μg of $rhVEGF_{165}$. The amount of growth factor loaded was determined by fabricating triplicate companion copies along with the implanted scaffolds, releasing the growth factors in vitro and performing ELISA detection assays. (Top row) Control scaffolds without growth factors produce no detectable bone over the duration of the study. Low levels of backscatter is caused by the polymer. (Middle row) In single growth factor rhBMP-2 films lacking $rhVEGF_{165}$, bone formation is restricted to the periphery of the scaffold at 4 weeks and 9 weeks. (Bottom row) As a result of increased vascularity, scaffolds releasing $rhVEGF_{165}$ demonstrate a smooth, continuous profile in the ectopically formed bone which matures from 4 weeks to 9 weeks to fill the entire scaffold. In all the images, the bone formed takes the shape of the scaffold and grows inward when VEGF is present. Images are an isosurface rendering at 0.25 surface quality factor at a level threshold of 640, as defined by the proprietary Microview® software from GE Healthcare.

Fig. 4.6. (A) The bone mineral density (BMD) of ectopic bone formed by the rhBMP-2/$rhVEGF_{165}$ combination scaffolds is 28 ± 4.59% and 32 ± 2.73% higher than bone formed by rhBMP-2 scaffold at 4 and 9 weeks respectively at the periphery of the scaffolds. (B) In the interior, the BMD for the combination growth factor scaffolds is

higher than the single rhBMP-2 scaffolds indicating that more bone is present in the interior, which matures from 4 to 9 weeks as indicated by the increase in BMD. (C) The trabecular thickness of the bone formed is an important measure of bone maturation, and the trabecular thickness of the bone formed by the combination scaffolds is about 3 times and 4.5 times that of bone formed by rhBMP-2 scaffolds at 4 and 9 weeks. (s.d., n=9, ** $p < 0.01$; ns = not significant; all others $p < 0.001$)

Fig. 4.7. Histology sections from rat femur intramuscular implants. (A to D) Bone is absent in control scaffolds releasing no growth factors at 4 and 9 weeks verified by (A, C) H&E staining and (B, D) lack of brilliant blue collagen staining with Masson's trichrome stain. (A, B) Arrows indicate pockets where the (PCL/βTCP) polymer scaffold is present at 4 weeks which degrades over (C, D) 9 weeks, without any bone growth in the vacant space. (E to H) Bone present in scaffolds releasing single growth factor rhBMP-2. (E) Presence of trabecular bone with (inset) osteoblasts laying down new bone which is (F) restricted to the periphery of the scaffold at 4 weeks. Of particular interest is (G) the abundant presence of hematopoietic cells surrounding the bone in spaces identified as fatty marrow space (asterisk), where (H) most of the bone formation is restricted to the periphery at 9 weeks and (inset) as bone matures, it goes from an unorganized collagen matrix structure to a lamellar structure with aligned collagen fibrils that are birefringent under polarized light. (I to L) Bone present in scaffolds releasing rhBMP-2 and $rhVEGF_{165}$. (I) Spicules of trabecular bone which is present (J) throughout the scaffold as early as 4 weeks. (K) As osteoblasts lay down new bone, spicules mature into (L) bone that fills up the empty spaces throughout the scaffold as it degrades with (inset) a greater number of birefringent aligned collagen fibrils present than fibrils formed when single growth factor rhBMP-2 is released. Bone formed is always within the scaffold. A, C, E, G, I, K are hematoxylin and eosin (H&E) stains at 10x objective magnification. B, D, F, H, J, L are Masson's trichrome stains at 2x objective magnification. Images in inset are taken at 20x objective magnification.

Figure 5.1. Design of the multilayer polymer "skin". (a) Molecular structures of materials in the system. Hydrophobic PLGA is used to form the membrane. Poly2, PAA, BMP-2 and PDGF-BB are part of the bioactive interface that initiates the bone wound healing cascade. The bisphosphonate molecule alendronate is conjugated to PLGA. (b) Schematic of the phase-inversion membrane formation process. (1) A PLGA-DMF solution is poured on a glass plate. (2) A doctor blade is used to spread the polymer solution uniformly on the glass plate and is (3) immersed into a deionized water bath. (4) The resulting film detaches from the glass substrate. (c) Macroscopic image of the membrane structure that results in a uniform polymer support (scale bar, 8mm). (d) Scanning electron micrographs demonstrating a highly ordered cross section (scale bar, 10μm) (e) PLGA membrane coated with $[Poly2/PAA/rhBMP\text{-}2/PAA]_{40}$ + $[Poly2/PAA/rhPDGF\text{-}BB/PAA]_{40}$ (scale bar, 2μm)

Figure 5.2. In vivo and in vitro evaluation of growth factor release. PDGF-BB and BMP-2 were loaded into the multilayers that coated the membrane and then implanted in the critical size defect of a rat calvaria (n = 4-5 per group). (a) In vivo release of PDGF-BB and BMP-2 was tracked for 11 and 20 days respectively (b) In vitro Growth factor

release in single and combination films from PLGA membranes. Data represent the means±s.e.m.

Figure 5.3. μCT imaging of bone repair in live animals. (a) Representative radiographs of bone formation around drilled implants with different coatings at 1, 2, and 4 weeks. Red broken circle indicates the location of the defect in each radiograph and has an 8mm diameter. Defect closure was achieved in all animal groups with different treatment conditions within 4 weeks. n = 5 per group. (b) The images in (a) were used to quantify bone volume and bone mineral density at 2 and 4 weeks within the regions of interest marked by dotted red circles. Each point represents individual animal. Data are means±s.e.m. (n = 5-6 per group). *$p < 0.05$, **$p < 0.01$, ***$p < 0.001$, ns = not significant, ANOVA with Tukey post hoc test. All groups are compared with the mechanical properties of the M + $B_{0.2}$ +$P_{0.2}$ group.

Figure 5.4. Histology of new tissue formed with various coating formulations. (a) Each image is a cross section of the calvarial defect after 4 weeks, at which time different levels of bone tissue morphogenesis was observed at the defect site. The broken lines indicate the position of the defect site and are 8mm apart. Collagen is represented by blue and osteocytes (mature bone) is represented by red. Sections were stained with Masson's trichrome stain and viewed under bright field microscopy. (b) Granulation tissue layer at 1, 2 and 4 weeks during bone repair in the M + $B_{0.2}$ + $P_{0.2}$ treatment group. The tissue gradually reduces in thickness from 1 to 4 weeks as bone repair is completed. Pieces of the PLGA membrane were observed in some section (scale bar, 30μm). Arrows: red, PLGA membrane; yellow, granulation tissue layer.

Figure 5.5. Mechanical compression testing of calvaria bone (a) Stiffness and (b) Failure load from different groups are presented at 4 weeks after implantation. Data are means±s.e.m. (n = 5 implants per group). *$p < 0.05$; **$p < 0.01$; ***$p < 0.001$, ns = not significant, ANOVA with a Tukey post hoc test. All groups are compared with the mechanical properties of the M + $B_{0.2}$ +$P_{0.2}$ group.

Figure 6.1. Achieving bone tissue level specificity of LbL coated nanoparticles. (A) Aqueous anionic polyelectrolyte, poly(acrylic acid) [PAA, MW 450K], functionalized with the **(B)** bisphosphonate targeting moiety, alendronate [for high specificity to hydroxyapatite in bone], to yield **(C)** the aqueous, ligand-functionalized polymer at 40% side-chain functionalization (**Figure S1**), which is used for complementary, iterative adsorption to the polycationic component (poly-L-lysine, PLL) in the film on the NP substrate, schematically illustrated in **(D)**.

Figure 6.2. *in vitro* assessment of LbL-targeted QD NPs incubated with 143B osteosarcoma cells. (A) Confocal microscopy of 143B cells incubated with the LbL-targeted QD_{705} core NPs for 2 hours. Blue staining representative of a Hoescht nuclear stain, green representative of a phalloidin stain of the actin filamentous cell structure, and red representative of the nanoparticle fluorescence (QD_{705} fluorescence). Scale bar representative of 20μm. **(B)** Binding and relative cytotoxicity of 3 bilayer [PLL/PAA-Alendronate] LbL-targeted QD_{800} core NPs following incubation for 2 hours in 143B cells. Fluorescence emission data corresponds to that of the nanoparticle core (QD_{800}).

Figure 6.3. *in vivo* evaluation of LbL-targeted QD_{800} core NPs. (A) Representative live-animal imaging of LbL-targeted QD_{800} core NPs following systemic administration to 143B osteosarcoma xenograft-bearing NCR nude mice. Imaging conducted at λ_{ex} = 640 nm, λ_{em} = 800 nm for up to 8 days. Hind-flank xenografts identified in the pre-injection image; arrows at 5 minutes and 9 hours indicate binding to native bone tissue. **(B)** Quantification of fold tumor-specific accumulation normalized to tissue auto-fluorescence pre-injection for the systemically administered LbL-targeted QD_{800} core NPs, as visualized in **(A)**. n = 3 mice (6 tumors); data presented as mean +/- SEM. **(C)** Biodistribution data corresponding to endpoint of **(A)** (quantified as percent recovered fluorescence following harvest of relevant tissue after 8 days post-administration). n = 3 mice (6 tumors); data presented as mean +/- SEM. **(D)** Co-localization of QD_{800} NP core with LbL-film containing labeled PAA-$Alendronate_{700}$; top row [PAA-$Alendronate_{700}$ channel] – imaging conducted at λ_{ex} = 640 nm, λ_{em} = 700 nm, bottom row [QD_{800} channel] - imaging conducted at λ_{ex} = 640 nm, λ_{em} = 800 nm.

Figure 6.4. *in vitro* evaluation of LbL-targeted liposomal NPs in 143B cells. (A) Cryo-TEM of LbL-targeted doxorubicin-loaded liposomal NPs. Scale bar representative of 200 nm. **(B)** Binding (2 hour incubation) and relative cytotoxicity (48 hour incubation) of LbL-targeted empty liposomal NPs over a range of concentrations, based on fluorescence, in 143B cells (λ_{ex} = 675 nm, λ_{em} = 710 nm; tracked using PLL_{700} as cationic component in LbL film). **(C)** Confocal microscopy of 143B cells incubated with the LbL-targeted empty liposomal NPs [tracked via PLL_{700} polycationic component in LbL film] for 2 hours. Blue staining representative of a Hoescht nuclear stain, green representative of a phalloidin stain of the actin filamentous cell structure, and red representative of the nanoparticle fluorescence ($PLL_{Cy5.5}$ polymer shell fluorescence). Scale bar representative of 10 μm. **(D)** Representative cell-associated NP fluorescence following a 2 hour incubation of 143B cells with the LbL-targeted empty liposomal NPs. **(E)** *in vitro* cytotoxicity of LbL-targeted doxorubicin-loaded liposomal NPs and the corresponding **(F)** uncoated doxorubicin-loaded liposomal control following 48 hour (blue) and 72 hour (red) incubation periods over a range of doxorubicin concentrations.

Figure 6.5. Biological evaluation of LbL-targeted empty liposomal NPs. LbL-targeted empty liposomal NPs tracked via PLL_{700} polycationic component in surface coating. Circulation data in **(A)** normalized to % remaining particles recovered, on the basis of fluorescence [λ_{ex} = 640 nm, λ_{em} = 700 nm], immediately following systemic administration to immune proficient BALB/c mice; data presented as mean +/- SEM (n = 3). Two-compartment model fit to determine half-lives displayed. Data includes background subtraction of blood auto-fluorescence. **(B)** Quantification of fold tumor-specific accumulation normalized to tissue auto-fluorescence pre-injection for the systemically administered LbL-targeted blank liposomal core NPs to 143B xenograft-bearing NCR nude mice; data presented as mean +/- SEM (n = 3). **(C)** Biodistribution data corresponding to endpoint of **(B)** (quantified as percent recovered fluorescence [λ_{ex} = 640 nm, λ_{em} = 700 nm] following harvest of relevant tissue after 100 hours post-systemic administration); data presented as mean +/- SEM (n = 3).

Figure 6.6. 143B xenograft tumor remediation following treatment with doxorubicin-loaded liposomal formulations. (A) *in vivo* tumor remediation of 143B

xenografts in NCR nude mice for LbL-targeted doxorubicin-loaded liposomal NPs, against untreated and uncoated doxorubicin-liposomal NPs. Untreated control xenografts were sacrificed 19 days post-inoculation of xenograft due to tumor burden exceeding 1 cm. Untargeted and targeted Dox-liposomal formulations were sacked at 30 days post-inoculation following a dose-escalation study with the following treatment regimen: day 10 at 1 mg/kg, day 17 at 2 mg/kg, day 24 at 3 mg/kg. Terminal point shown with final tumor area displayed in **(B)**. Statistics are from an unpaired t-test, two-tailed to compare the untargeted and targeted formulations at each time point. Data presented as mean +/- SEM; n = 4. **(C)** Caliper measurements for *in vivo* tumor remediation with repeated dosing of 5 mg/kg for both targeted and untargeted formulations at 22 days, 28 days, and 35 days post-inoculation (displayed as day 0, day 6, and day 13 in **(C)**). Statistics are from an unpaired t-test, two-tailed to compare the untargeted and targeted formulations; $*p < 0.05$; $**p < 0.01$; $***p < 0.001$. Data presented as mean +/- SEM; n = 4. Resection of tumors from terminal point of **(C)**, n = 4 for each group, displayed from the final caliper measurement.

Figure 6.7. Representative histology of 143B tumors harvested at 18 days post-treatment corresponding to the terminal point in **Figure 6C**. **(left column)** tumors prior to treatment; **(right column)** tumors at the 18 day terminal point post treatment of 3 repeated injections at 5 mg/kg doxorubicin. **(top row)** tumors treated with PAA-Alendronate coated doxorubicin-loaded liposomes, **(middle row)** uncoated dox-loaded liposomes, and **(bottom row)** untreated animals. Masson's trichrome stain – red = 143B osteosarcoma cells, blue = connective tissue; scale bars representative of 100 μm.

Chapter 1

Introduction

This body of work explores the use of tunable nanoscale polymer coatings that can direct specific cellular processes to drive the repair of tissues and have the potential of revolutionizing the management of disease states. These coatings recapitulate aspects of the natural healing cascade and help integrate prosthetics with the existing body tissues. In addition, new approaches to treat large traumatic and congenital defects are explored, with a particular emphasis on restoring tissue form and function through the use of composite biodegradable implants using an approach which can also be extended to design targeted therapies for delivery of potent drugs to specific tissues within the body.

1.1. Biomedical implants designed for long-term functionality

Biomedical devices have received significant attention in recent years as the need to repair and replace worn-out or damaged tissues has increased as a result of an increase in the world population, as well as an aging population in developed economies. These devices, which may be permanent or biodegradable implants, can save and extend lives, replace damaged tissues, restore function, improve mobility, alleviate pain and significantly improve the quality of life of patients suffering from debilitating medical conditions. However, such medical devices also carry the risk of failure that manifests in different forms and can significantly impact the patient's health. There is a significant need to mitigate risks associated with implants which can be addressed in large part by an understanding of the interactions between the implant and the host environment in which it exists.

Orthopedic implants constitute a large percent of implanted biomedical devices, with over a million joint replacement surgeries occurring each year in North America alone[1]. Such implants typically last 15-20 years and allow for pain-free functional movement[2]. However, approximately 12% of hip and knee prosthesis fail prematurely, within ten years[3]. A major clinical issue that limits the success of such implants is failure owing to aseptic loosening and sub-optimal integration with the host tissue, which constitutes

more than half of all joint replacement failures[4]. Here, the original artificial joint must be removed and replaced with a new implant in a revision arthroplasty procedure. In elderly patients the danger of brittle fracture due to osteoporosis and slower rate of wound healing compounds the complexity of such a procedure. In order to prevent premature implant failure, there has been rising interest in the design and implementation of devices that can 'biologically' integrate with the host tissue for long term functionality.

1.2. Traumatic and congenital defects that result in large tissue loss

The primary treatment and closure of large-area bone defects continues to face major technical challenges. The gold standard for treatment of large bone defects is currently autograft transplantation, which involves transplanting bone from a donor site within the body. It is hampered by the limited supply of donor bone and the potential for considerable donor site morbidity associated with the tissue harvest[5]. CMF reconstruction is particularly challenging due to the complexity of reconstructing the three dimensional facial geometry with fidelity while protecting the underlying delicate organ systems[6]. Often multiple surgeries are needed that use complex permanent implant systems that can lead to permanent deformities, functional impairment and an alteration of physical appearance. There is a compelling need for an off-the-shelf device to manage many kinds of bony defects. Current challenges include the engineering of materials that can recapitulate bone healing and regenerate new bone tissue matrix that restores functional properties and is well-integrated with the native bone.

1.3. Tissue-specific delivery of drug in the body

The delivery of highly potent drugs to specific sites of disease within the body has the potential of reducing side-effects, while increasing the efficacy of the therapy. Bone tissue undergoes cell-mediated remodeling to sustain the structural integrity of the tissue. Disturbances in the physiological processes of osteoblast-mediated bone deposition and osteoclast-mediated bone resorption are observed in many bone-related disease states, such as osteosarcoma, cancer metastasis to bone, osteoporosis, and Paget's disease of the bone[7, 8]. The clinical outcomes for patients with these diseases continue to be very poor[9]. The arsenal of available agents to treat patients has not

made any substantial impact in improving their survival, and new methods for therapy are critical. Engineering a robust delivery platform with bone-tissue level specificity to treat these diseases can improve therapeutic efficacy, lower systemic toxicity, and improve disease management.

1.4. Controlled Drug Release

Traditional routes of administering medication are topically, orally, intravenously, intramuscularly, subcutaneously, or sublingually. These methods of systemic drug delivery often result in toxic side-effects and impact the efficacy of treatment. Controlled drug delivery, that is also localized, offers significant advantages over these methods. These include requiring lower drug doses, a greater control over drug toxicity and bioavailability, potential for extended release, potential for control over drug release profile directly at the site, and requiring lower number of drug administrations during treatment. There are numerous local drug delivery devices currently approved by the FDA that are routinely utilized[10]. Some of the prominent areas of use include drug-eluting stents, catheters, orthopedic devices, and wound dressings. In most of these devices, polymers are utilized to both load and control drug release behavior.

However, engineering challenges exist with respect to designing carriers and delivery systems for controlled drug release. This is particularly true for biological drugs, including nucleic acids and proteins, where there are additional challenges relating to preserving the activity of these molecules. The use of common biodegradable polymers, including the family of poly(lactic-glycolic acids) (PLGA), or polyanhydrides involve the need to process the polymers under harsh conditions of temperature and/or solvent, and acidic breakdown products of PLGA and similar polymers in confined spaces leads to acidic conditions that are deleterious to the proteins. Direct injection of growth factor to a site leads to the immediate breakdown and clearance before it can begin to exhibit desired results; the growth factor must be sustained at a minimal dose level over prolonged time periods of several weeks to be effective. When multiple growth factors must be delivered, it is desired to introduce appropriate amounts of growth factor at the right time for bone healing. This concept on the importance of timed delivery has also been illustrated with other growth factors examined for bone tissue growth[11, 12]. A lack of

adequate control over drug delivery timescales results in suboptimal response. Most of the current methods do not allow for complex delivery profiles, such as the sequential delivery of multiple therapeutics. In current devices, release is often a combination of drug diffusion and degradation or dissolution of polymer matrix, rather than a stimuli-responsive release.

Very few approaches exist for the highly controlled delivery of multiple drugs from the surfaces of standard medical implants and devices, although there is a true need for such systems, particularly in the form of conformal coatings that can be directly applied to implants such as prostheses without requiring the re-design of the entire implant. Complex, multicomponent or well-controlled release profiles can be obtained using microfabricated devices such as microelectronic chips or microfluidic channels in MEMS[13-16]; however such systems require elaborate processing and often utilize an external field for activation, making them unsuitable for simple, structural implant systems such as bone or hip prostheses. A major challenge in the area of passive implantable drug delivery involves the ability to incorporate complex delivery profiles on a range of nonplanar implant geometries. Because the goal of complex or multidrug delivery is more recently a recognized one for implant delivery and tissue engineering[17], attempts have been made recently to create tissue engineering scaffolds by incorporating drug nanoparticles in a polymer matrix as a secondary means of angiogenic drug release for vascularization[18, 19]; however, this approach lacks the ability to directly tune the release profile during construction of the film and does not provide the ease and flexibility to deliver multiple components in a controlled manner or to produce sequential or complex profiles. Furthermore, traditional polymer delivery systems require the handling of drugs with solvents and/or heat, which can greatly reduce activity of biologic drugs such as nucleic acids and growth factors.

1.5 Layer-by-Layer Assembly (LbL)

One method of drug delivery is via implant coatings, assembled in a very simple approach termed alternating electrostatic layer-by-layer (LBL) or polyelectrolyte multilayer assembly[20-22]. The process involves the formation of thin films through the alternating adsorption of positively and negatively charged polymer species at room

conditions. Each adsorbed layer in such films can range from 1 to 100 nm or more in thickness. Total therapeutic film thicknesses range from a few nm to as much as 10 microns. Film growth modulation is achieved by changing deposition solution pH or salt content, and the thickness of each layer can be varied by changing these adsorption conditions[23-25]. The electrostatic layer-by-layer (LbL) assembly technique is versatile, allowing the incorporation of a broad range of functional polymers and other charged species. Adsorption solution dip times can be as low as 1 minute, and new spray-LbL techniques have reduced process times down to seconds per process cycle, making this approach extremely competitive, highly controlled and in many cases superior to film casting using solvents or crosslink gel formation[26, 27]. For this reason, it is possible to create a multi-drug device with highly tailored release profiles in the form of this simple, conformal thin coating.

The use of polyelectrolyte multilayers as biomaterials for diverse applications has been well-examined by a number of research groups[28-38]. In the context of biomedical applications the LbL assembly method offers several key advantages:

1. *Layering active, unmodified drugs*: Drug can be directly incorporated into the multilayer thin films, without any modifications, as one of the electrostatically adsorbed layers, and the loading scales with the number of layers in a predictable manner. Biologic drugs such as growth factors, disease regulating peptides, enzymes, and biological signaling molecules can be introduced by interactions with the native charge and/or hydrogen bonding of such molecules with the other film components. Activity assays confirm that these drugs are active after release from the thin films and in some cases, even within the films itself.

2. *Combinatorial synergy between complementary materials:* Decoupling the mechanical and physical properties of a substrate from its drug release properties allows provides a broad parameter space to combine and apply materials of complementary functionality. Nano to micrometer size coatings can be applied conformally on a wide variety of complex surfaces with a broad size distribution and variation in geometric complexity. The two may have and continue to retain very different properties (e.x. hydrolytically degradable coatings on non-erodible scaffolds). This can be extended to materials within the coatings themselves that may have very

different physical properties. This makes the approach suitable for biomedical devices, implants, and tissue engineering scaffolds.

3. *Local drug release promotes targeted therapy:* Targeted and local delivery of therapeutics has emerged as a leading driver in nanomedicine. For releasing potent biologics, local delivery prevents systemic side effects and maintains therapeutically relevant concentrations. Delivering therapeutic protein from implanted medical devices has generally been difficult due to the challenges in processing them together. The ability to locally release therapeutics from several classes of therapeutic proteins, including growth factors from LbL nano to micrometer-scale coatings to mediate the host tissue response is a compelling application.

4. *Adaptive, time dependent release:* The ability to release different drugs over different, independent, time periods can be extremely powerful with a broad range of medical applications. Such an approach can serve both as a tool to understand cellular phenomena and one for therapeutic interventions. By spatially ordering these molecules in a LbL film, it is possible to obtain varying levels of control over the release profile of individual therapeutics. Such an approach can be used in the context of tissue engineering scaffolds and biomedical devices to modulate complex cell behavior for tissue remodeling or regeneration. At a smaller length scale, such an approach can be used to deliver multiple chemotherapeutic drugs to the same cell to overcome drug resistance and kill tumor cells. Prophylactic and therapeutic vaccination with an antigen and adjuvant may also benefit from this approach. This strategy using simple chemistry to control complex biological processes makes therapeutic materials simpler and more translatable.

LbL has been applied to the area of tissue regeneration, and in particular bone, has in recent years. Applications range from coating implants, scaffolds, capsules, calcium phosphate and polymer scaffolds with materials that facilitate osteogenesis in different settings. Active LbL coated capsules, composed of polypeptides and growth factors were demonstrated to induce bone formation when incubated with embryonic stem cells in vitro and in vivo[39]. LbL coated TCP/HAP granules were demonstrated to sequester significant amounts of growth factor, in which the degree of LbL film cross-linking influenced the quantity of growth factor trapped within the films[40]. These granules

induced calcification in vitro and bone formation at an ectopic site in vivo. The manner of growth factor presentation also appears to influence bone formation[41]. Recent work demonstrated that when LbL coated implants with growth factor are sterilized using gamma radiation, significant loss in growth factor activity was observed in vitro, but the activity in vivo appeared to be preserved[42]. These studies represent important advancements in the area of regenerative medicine and implant technology. Approaches to improve upon this technology towards clinical translation would complement this body of work.

1.6. Thesis Overview

This thesis focuses on the development of improved bone implants through the use of ultrathin, multilayered implant coatings that can induce bone tissue formation. Orthopedic implant surfaces are a compelling application because the polyelectrolyte multilayer approach can have direct and immediate benefit in this area due to the need for sequential and controlled delivery of several therapeutic systems. In the proposed work, we will further this approach for the development of coated orthopedic implants for revision arthroplasty and bone reconstruction, using modeling and new experimental approaches as a guide to gaining desired release, and engineering these systems to enable true bone integration at implant surfaces.

In Chapter 2 an osteophilic modular coating for substrates is described, that can accelerate the regeneration of stable bone tissue. Introduction of hydroxyapatite and rhBMP-2 upregulated osteogenic markers at earlier times in MSCs which resulted in greater calcium deposition in culture, with an upregulation of osteogenic markers[43].

In Chapter 3, we demonstrate that a two-part osteophilic coating can promote stable mechanical fixation of an implant in a surrogate rodent model. Osteoconductive hydroxyapatite (HAP) and osteoinductive bone morphogenetic protein 2 (BMP-2) contained within the nanostructured coating acted synergistically to induce osteoblastic differentiation of endogenous progenitor cells within the bone marrow, without indications of a foreign body response[44].

Towards recapitulating the natural healing cascade, the delivery of multiple growth factors may lead to accelerated tissue development. In Chapter 4, the use of multiple

growth factors from a scaffold surface coating for bone growth is described. PEM films that sequestered BMP-2 and angiogenic VEGF (vascular endothelial growth factor) in different ratios were explored. In vivo, the mineral density of ectopic bone formed de novo by dual growth factor delivery was approximately 33% higher than when only BMP-2 was introduced, with a higher trabecular thickness. Bone formed throughout the scaffold when both growth factors were released, which suggests more complete remodeling due to an increased local vascular network[45].

In Chapter 5, the use of multiple growth factors on a flexible, biodegradable implant surface is described to repair critical size bone defects in a rat calvaria. The polymer "skin" promoted local bone formation that bridged a critical-size defect in the rat calvaria as early as 2 weeks after implantation. Mature, mechanically competent bone regenerated the native calvaria form, indicating the potential of this approach as an off-the-shelf, cell-free option for bone tissue repair and restoration[46].

Lastly, in Chapter 6, a new method to target potent chemotherapeutic drugs to the bone tissue is described. This work investigated an approach for generating functional and targeted drug carriers specifically for treating primary osteosarcoma. This was accomplished via surface modification of drug-loaded nanoparticles with an aqueous polyelectrolyte, poly(acrylic acid) (PAA), side-chain functionalized with alendronate, a potent clinically-used bisphosphonate. Active targeting of 143B xenografts in NCR nude mice with the LbL-targeted doxorubicin liposomes promotes enhanced, prolonged tumor accumulation and significantly improved efficacy[47].

Finally, Chapter 7 concludes with a discussion of the primary conclusions from Chapters 2 through 6. Additionally, Chapter 7 provides suggestions for future work that may advance the current findings of this thesis.

1.7 References

1. Bernard, L.; Hoffmeyer, P.; Assal, M.; Vaudaux, P.; Schrenzel, J.; Lew, D., Trends in the treatment of orthopaedic prosthetic infections. *J. Antimicrob. Chemother.* 2004, 53, 127-129.

2. Neumann, L.; Freund, K.; Sorenson, K., Long-term results of Charnley total hip replacement. Review of 92 patients at 15 to 20 years. *Journal of Bone & Joint Surgery, British Volume* 1994, 76, 245-251.

3. Labek, G.; Thaler, M.; Janda, W.; Agreiter, M.; Stöckl, B., Revision rates after total joint replacement CUMULATIVE RESULTS FROM WORLDWIDE JOINT REGISTER DATASETS. *Journal of Bone & Joint Surgery, British Volume* 2011, 93, 293-297.

4. Ulrich, S. D.; Seyler, T. M.; Bennett, D.; Delanois, R. E.; Saleh, K. J.; Thongtrangan, I.; Kuskowski, M.; Cheng, E. Y.; Sharkey, P. F.; Parvizi, J., Total hip arthroplasties: What are the reasons for revision? *International orthopaedics* 2008, 32, 597-604.

5. Woodruff, M. A.; Lange, C.; Reichert, J.; Berner, A.; Chen, F.; Fratzl, P.; Schantz, J.-T.; Hutmacher, D. W., Bone tissue engineering: from bench to bedside. *Materials Today* 2012, 15, 430-435.

6. Alsberg, E.; Hill, E. E.; Mooney, D. J., Craniofacial tissue engineering. *Critical reviews in oral biology and medicine : an official publication of the American Association of Oral Biologists* 2001, 12, 64-75.

7. Rodan, G.; Martin, T., Therapeutic approaches to bone diseases. *Science (New York, N.Y.)* 2000, 289, 1508-1514.

8. Mundy, G., Metastasis to bone: causes, consequences and therapeutic opportunities. *Nature reviews. Cancer* 2002, 2, 584-593.

9. Wang, D.; Miller, S.; Kopecková, P.; Kopecek, J., Bone-targeting macromolecular therapeutics. *Advanced Drug Delivery Reviews* 2005, 57, 1049-1076.

10. Middleton, J. C.; Tipton, A. J., Synthetic biodegradable polymers as orthopedic devices. *Biomaterials* 2000, 21, 2335-2346.

11. Ginebra, M.; Traykova, T.; Planell, J., Calcium phosphate cements as bone drug delivery systems: a review. *Journal of Controlled Release* 2006, 113, 102-110.

12. Seeherman, H.; Wozney, J. M., Delivery of bone morphogenetic proteins for orthopedic tissue regeneration. *Cytokine Growth Factor Rev* 2005, 16, 329-45.

13. Santini, J. T.; Richards, A. C.; Scheidt, R.; Cima, M. J.; Langer, R., Microchips as controlled drug-delivery devices. *Angewandte Chemie-International Edition* 2000, 39, 2397-2407.

14. LaVan, D. A.; McGuire, T.; Langer, R., Small Scale Systems for in vivo drug delivery. *Nature Biotechnology* 2003, 21, 1184-1191.

15. Razzacki, S. Z.; Thwar, P. K.; Yang, M.; Ugaz, V. M.; Burns, M. A., Integrated microsystems for controlled drug delivery. *Advanced Drug Delivery Reviews* 2004, 56, 185-198.

16. Richards Grayson, A. C.; Scheidt Shawgo, R.; Li, Y.; Cima, M. J., Electronic MEMS for triggered delivery. *Advanced Drug Delivery Reviews* 2004, 56, 173-184.

17. Leach, J. K.; Mooney, D. J., Bone engineering by controlled delivery of osteoinductive molecules and cells. *Expert Opinion On Biological Therapy* 2004, 4, 1015-1027.

18. Simmons, C. A.; Alsberg, E.; Hsiong, S.; Kim, W. J.; Mooney, D. J., Dual growth factor delivery and controlled scaffold degradation enhance in vivo bone formation by transplanted bone marrow stromal cells. *Bone* 2004, 35, 562-569.

19. Richardson, T. P.; Peters, M. C.; Ennett, A. B.; Mooney, D. J., Polymeric system for dual growth factor delivery. *Nature Biotechnology* 2001, 19, 1029-1034.

20. Decher, G., Fuzzy Nanoassemblies: Toward Layered Polymeric Multicomposites. *Science* 1997, 277, 1232.

21. Hammond, P. T., Form and function in multilayer assembly: New applications at the nanoscale. *Advanced Materials* 2004, 16, 1271-1293.

22. Dubas, S. T.; Schlenoff, J. B., Factors Controlling the Growth of Polyelectrolyte Multilayers. *Macromolecules* 1999, 32, 8153-8160.

23. Zacharia, N. S.; Modestino, M.; Hammond, P. T., Factors Influencing the Interdiffusion of Weak Polycations in Multilayers. *Macromolecules* 2007, 40, 9523-9528.

24. Porcel, C.; Lavalle, P.; Decher, G.; Senger, B.; Voegel, J. C.; Schaaf, P., Influence of the Polyelectrolyte Molecular Weight on Exponentially Growing Multilayer Films in the Linear Regime. *Langmuir* 2007, 23, 1898-1904.

25. Shukla, A.; Fleming, K. E.; Chuang, H. F.; Chau, T. M.; Loose, C. R.; Stephanopoulos, G. N.; Hammond, P. T., Controlling the release of peptide antimicrobial agents from surfaces. *Biomaterials* 2010, 31, 2348-2357.

26. Krogman, K.; Cohen, R.; Hammond, P.; Rubner, M.; Wang, B., Industrial-scale spray layer-by-layer assembly for production of biomimetic photonic systems. *Bioinspiration & biomimetics* 2013, 8, 045005.

27. Krogman, K. C.; Lowery, J. L.; Zacharia, N. S.; Rutledge, G. C.; Hammond, P. T., Spraying asymmetry into functional membranes Layer-by-Layer. *Nature Materials* 2009, 8, 512-518.

28. Hyder, M. N.; Shah, N. J.; Hammond, P. T., Design and Translation of Nanolayer Assembly Processes: Electrochemical Energy to Programmable Pharmacies. In *Multilayer Thin Films*, Wiley-VCH Verlag GmbH & Co. KGaA: 2012; pp 393-435.

29. Koktysh, D. S.; Liang, X. R.; Yun, B. G.; Pastoriza-Santos, I.; Matts, R. L.; Giersig, M.; Serra-Rodriguez, C.; Liz-Marzan, L. M.; Kotov, N. A., Biomaterials by design: Layer-by-layer assembled ion-selective and biocompatible films of TiO2 nanoshells for neurochemical monitoring. *Advanced Functional Materials* 2002, 12, 255-265.

30. Constantine, C. A.; Gattas-Asfura, K. M.; Mello, S. V.; Crespo, G.; Rastogi, V.; Cheng, T. C.; DeFrank, J. J.; Leblanc, R. M., Layer-by-layer biosensor assembly incorporating functionalized quantum dots. *Langmuir* 2003, 19, 9863-9867.

31. Benkirane-Jessel, N.; Schwinte, P.; Falvey, P.; Darcy, R.; Haikel, Y.; Schaaf, P.; Voegel, J. C.; Ogier, J., Build-up of polypeptide multilayer coatings with anti-inflammatory properties based on the embedding of piroxicam-cyclodextrin complexes. *Advanced Functional Materials* 2004, 14, 174-182.

32. Ge, L. Q.; Mohwald, H.; Li, J. B., Biointerfacing polyelectrolyte microcapsules. *Chemphyschem* 2003, 4, 1351-1355.

33. Kumar, G.; Wang, Y. C.; Co, C.; Ho, C. C., Spatially controlled cell engineering on biomaterials using polyelectrolytes. *Langmuir* 2003, 19, 10550-10556.

34. Zhu, Y. H.; Yang, X. L.; Li, P. L.; Ying, H., From layer-by-layer assembled core-shell particles to medical/biochemical diagnostics and drug delivery. *Progress in Chemistry* 2003, 15, 512-517.

35. Ai, H.; Meng, H. D.; Ichinose, I.; Jones, S. A.; Mills, D. K.; Lvov, Y. M.; Qiao, X. X., Biocompatibility of layer-by-layer self-assembled nanofilm on silicone rubber for neurons. *Journal of Neuroscience Methods* 2003, 128, 1-8.

36. Tan, Q. G.; Ji, J.; Barbosa, M. A.; Fonseca, C.; Shen, J. C., Constructing thromboresistant surface on biomedical stainless steel via layer-by-layer deposition anticoagulant. *Biomaterials* 2003, 24, 4699-4705.

37. Jewell, C. M.; Zhang, J.; Fredin, N. J.; Lynn, D. M., Multilayered polyelectrolyte films promote the direct and localized delivery of DNA to cells. 2005.

38. Jewell, C. M.; Lynn, D. M., Multilayered polyelectrolyte assemblies as platforms for the delivery of DNA and other nucleic acid-based therapeutics. *Advanced Drug Delivery Reviews* 2008, 60, 979-999.

39. Facca S, et al. (2010) Active multilayered capsules for in vivo bone formation. Proc Natl Acad Sci U S A 107(8):3406-3411.

40. Crouzier T, et al. (2011) The performance of BMP-2 loaded TCP/HAP porous ceramics with a polyelectrolyte multilayer film coating. Biomaterials 32(30):7543-7554.

41. Crouzier T, Fourel L, Boudou T, Albiges-Rizo C, & Picart C (2011) Presentation of BMP-2 from a soft biopolymeric film unveils its activity on cell adhesion and migration. Adv Mater 23(12):H111-118.

42. Guillot R, et al. (2013) The stability of BMP loaded polyelectrolyte multilayer coatings on titanium. Biomaterials 34(23):5737-5746.

43. Shah, N. J., Hong, J., Hyder, M., & Hammond, P. T. (2012). Osteophilic multilayer coatings for accelerated bone tissue growth. Advanced Materials, 24(11), 1445-1450.

44. Shah, N. J., Hyder, M. N., Moskowitz, J. S., Quadir, M. A., Morton, S. W., Seeherman, H. J., Padera, R.F., Spector, M., & Hammond, P. T. (2013). Surface-Mediated Bone Tissue Morphogenesis from Tunable Nanolayered Implant Coatings. Science translational medicine, 5(191), 191ra83-191ra83.

45. Shah, N. J., Macdonald, M. L., Beben, Y. M., Padera, R. F., Samuel, R. E., & Hammond, P. T. (2011). Tunable dual growth factor delivery from polyelectrolyte multilayer films. Biomaterials, 32(26), 6183-6193.

46. Shah, N.J., Hyder, M.N., Quadir, M.A., Dorval Courchesne, N.M., Seeherman, H.J., Nevins, M.L., Spector, M., Hammond, P.T. (2014) A multilayer regenerative polymer "skin" for synergistic bone tissue repair and reconstruction (in review).

47. Morton, S.W.*, **Shah, N.J.***, Quadir, M.A., Deng, Z.J., Poon, Z., Hammond, P.T. (2013) Osteotropic therapeutic delivery via layer-by-layer nanoparticles, Advanced Healthcare Materials (DOI: 10.1002/adhm.201300465).

Chapter 2

Osteophilic Multilayer Coatings for Accelerated Bone Tissue Growth

2.1 Introduction

About 10% of total hip prostheses need revision within a decade after surgery due to mechanical aseptic loosening of the implant, and the number of revisions is expected to rise due to the increasing number of arthroplasties.[1, 2] To address the issue of implant failure, there has been an increased interest in moving to a fixation model that does not involve poly (methyl methacrylate) based bone cement and instead promotes direct integration of the implant with the host tissue by bone in-growth into the porous implant.[3]

Hydroxyapatite (HAP, $Ca_{10}(PO_4)_6(OH)_2$), the principal inorganic component of human hard tissues such as cortical bone and teeth to which it has a high binding affinity[4], has been investigated as a coating of orthopedic and dental implants[5], and as a component of biopolymer composite films.[6] Various physical coating processes, such as plasma spray coating, sputtering, and pulsed laser deposition on implant surfaces, have been used for the deposition of HAP films on artificial materials.[7] Although the deposition rates of these physical and reactive chemical processes are relatively high, it is often difficult to tune the composition and structure of the products and to obtain a uniform and stable HAP coating because of the thermally unstable character of HAP.[8] Plasma deposited hydroxyapatite coating, which can be up to several hundred microns thick, has a decreased resistance to mechanical shear and a lack of bonding with inefficient stress relief between the layers has been suggested as a possible cause.[9] Additionally, high temperature processes are unfavorable for the incorporation of biologics such as bone morphogenetic protein (BMP) which are potent mediators of bone tissue formation.[10-12]

2.2 Materials and Methods

2.2.1. Materials.

Poly (β-aminoester) (Poly2) was synthesized as previously described.[34] All other materials were purchased from Sigma Aldrich (St. Louis, MO) or Invitrogen (Carlsbad, CA) unless otherwise noted.

2.2.2 Preparation of electrostatic films.

Hydroxyapatite nanoparticle suspension (10 wt%) was diluted 5 fold in sodium acetate buffer (0.1 M), sterile filtered through a 0.45 μm cellulose acetate membrane (VWR Scientific, Edison, NJ) and added 1:1 (v/v) to chitosan solution in sodium acetate buffer (2 mg/ml). Poly(acrylic acid) and Poly2 dipping solutions were prepared in sodium acetate buffer (1 mg/ml). rhBMP-2 solution, a gift from Pfizer Inc. (Cambridge, MA), was diluted to 250 μg/ml in sodium acetate buffer from a 10mg/ml stock solution. Plasma treated glass or silicon substrates were alternatively dipped into these solutions with an intermediate washing step in water, first to fabricate the osteoconductive [Chi(HAP)/PAA] base layers followed by the degradable [Poly2/PAA/rhBMP-2/PAA] layers. Film thickness was measured using a Dektak 150 Profilometer and surface characterization was performed using a Nanoscope IV atomic force microscope. Scanning electron microscope (SEM) images and energy dispersive X-Ray spectroscopy (EDX) line-scans were performed in a JEOL JSM 6700 scanning electron microscope. All films were fabricated and characterized at least in triplicate.

2.3.3 In vitro cellular assays.

Adult mesenchymal stem cells (Lonza, Hopkinton, MA) were cultured in α-MEM supplemented with 20% FBS, 1% penicillin-streptomycin solution and plated on glass cover slips coated with the electrostatic films as described. Alkaline phosphatase and alizarin red assays were routinely performed using a previously described protocol.[40, 45]

Media was changed and aliquots from culture were frozen down every 48 hours and assayed for specific bone marker proteins using human bone panel assay 1B (Millipore, Billerica, MA) according to the manufacturer's protocol. In parallel, cells were fixed and stained for morphology and osteocalcin production for visualization at pre-determined time points. All assays were performed at least three times in triplicate.

2.3 Results and Discussion

Electrostatic multilayer assemblies fabricated using the layer-by-layer (LbL) technique[13] offer a unique platform for creating a biomimetic environment by incorporating materials of superior biological and mechanical properties to create a system that supports the growth and proliferation of target cells and allows them to assemble into a functional tissue unit.[14, 15] Precursor stem cells residing in the bone marrow, commonly known as mesenchymal stem cells (MSCs) can differentiate into osteoblasts which are responsible for laying down new bone. In the context of bone tissue engineering, it is crucial to have a substrate with appropriate signals that can support the attachment and direct the growth, proliferation and differentiation of these osteoprogenitor cells into osteoblasts.[16, 17] Incorporation of hydroxyapatite into LbL architectures can make them highly osteoconductive; i.e., capable of specifically supporting the attachment and proliferation of new osteoblasts and osteoprogenitor cells, providing an interconnected structure through which new cells can migrate and new vessels can form.[18] *In vivo*, the dissolution of HAP releases calcium and phosphate ions from the coating to the surrounding fibrous tissue and leads to the formation of a crystalline carbonated calcium phosphate layer, with the conversion and incorporation into the bone collagenous matrix.[3, 19] Additionally, these hybrid electrostatic films allow the localized introduction of bone morphogenetic protein-2 (BMP-2) which has the ability to differentiate MSCs into osteoblasts, a property referred to as osteoinduction, and has been demonstrated to greatly enhance bone tissue regeneration.[10] The benefits of release of growth factors such as rhBMP-2 include rapid healing of tissue around the implant and greater bone remodeling over shorter time periods[20]; hence there is a therapeutic advantage to the controlled introducing growth factors from the surface of implants during the healing process.[21-23]

Towards developing a versatile implant coating which would confer osteophilic properties, we incorporated hydroxyapatite nanoparticles complexed with chitosan into nanoscale non-degradable electrostatic multilayers which were capped with a degradable poly(β-amino ester) based film incorporating physiological amounts of rhBMP-2. By incorporating elements that mimicked native wound healing processes, we demonstrated an upregulation of osteogenic markers which increased the rate of MSC differentiation and resulted in greater calcium deposition over shorter time periods when compared to a control substrate with no multilayer coating and multilayer films containing only hydroxyapatite or rhBMP-2.

The multicomponent film consisted of a set of osteoconductive base layers under a poly(β-amino ester) based hydrolytically degradable multilayer film for promoting differentiation by introducing controlled amounts of osteoinductive rhBMP-2 (Fig. 3.1.). Hydroxyapatite nanoparticles were complexed with chitosan, a linear polysaccharide; in these complexes, it is reported that the calcium ion in HAP interacts with the primary amine group of chitosan.[24] Chitosan is known to be a highly osteoconductive[25, 26], hemostatic material that speeds up wound healing and bone reformation.[27, 28] At acidic and physiological conditions, the amine group in the chitosan structure is protonated (pKa ~ 6.5)[29] conferring a net positive charge to the macromolecule which is necessary for electrostatic film assembly. We anticipated that using poly(acrylic acid) (PAA), a weak polyanion (pKa ~ 4.5), as the complimentary polyanion for this system would yield an ionically crosslinked film which would further assist in stabilizing the HAP complex.[30] ATR IR absorbance spectroscopy indicated the prevalence of a peak at wavenumber 1000cm^{-1} corresponds to a phosphate group[31] and is present only when hydroxyapatite is a component of the film (Fig. 3.1G). The carbonyl peak present in the spectra can be explained by the use of sodium acetate salt which is present in the polyelectrolyte solutions for partial charge shielding. Substrates coated with HAP particles less than 100 nm in size have been demonstrated to have a greater bone bonding strength compared to the control.[32] Hence, particle aggregation was another consideration, since a uniform surface coating is necessary for creating an optimal osteoconductive surface.[33] A hydrolytically degradable poly(β-amino ester), (Poly2)[34] based multilayer was fabricated atop the osteoconductive $[Chi(HAP)/PAA]_{20}$ base layers. Under neutral

to acidic pH conditions of film fabrication, Poly2 is stable and the amines present along the backbone of Poly2 are protonated, yielding a positive charge necessary for electrostatic LbL assembly. Similarly, rhBMP-2 (Fig. 3.1D; structure extracted using NCBI's Cn3D MMDB program[35]) is positively charged and stable under acidic conditions (pI ~8.5).[36] The presence of an osteoinductive agent is necessary for bone regeneration.[10] During bone tissue formation and repair processes, rhBMP-2 induces osteoblast differentiation which results in the laying down of new bone that progressively expands to replace damaged tissue.

These coatings contain osteoconductive and osteoinductive elements, both of which are necessary for bone formation, and are conformal to the complex geometry of the implant for complete biological fixation. We envisioned the controlled degradation of the Poly2 containing layers and the release of rhBMP-2 into the surrounding media and the differentiation of MSCs into osteoblasts which subsequently preferentially adhere to the underlying osteoconductive module consisting of $[Chi(HAP)/PAA]_{20}$, abutting the substrate, which is not degradable over the time scale of the growth factor release from the $[Poly2/PAA/rhBMP\text{-}2/PAA]_{20}$ multilayers and remains adhered to the substrate, as demonstrated (Fig. 3.2.). The growth factor release would not be tunable if chitosan was the only polycation used in the system because it would not be readily degradable; on the other hand, using Poly2 as the only polycation would result in the degradation of the entire multilayer structure, eliminating the ability to enhance bone growth with the permanent osteoconductive base layer. This is also true if a composite [Chi(HAP)/PAA/Poly2/PAA/rhBMP-2/PAA] system had been employed. Rigid hydroxyapatite nanocomposites[37, 38] are used as bone fillers and not suitable as coatings to form new bone tissue independently and hence fix implants to the host tissue.

In these osteophilic multilayers, the electrostatic assembly grows linearly with the number of [Chi(HAP)/PAA] baselayers, increasing at 8.98 nm ± 0.13 nm per bilayer (Fig. 3.2A). Consistent surface charge reversal observed after periodic streaming ξ-potential measurements indicated uniform surface charge density consistent with linear film growth (Appendix A; Fig. A1). Surface roughness was proportional to film thickness, which increases as particle density within the film increases. We observed that under

the conditions of film assembly, HAP particles dispersed uniformly throughout the base film at [Chi(HAP)/PAA]$_{20}$ without aggregating, as confirmed by EDX and calcium mapping (Figure S4-S8). The nanofilm thickness for [Chi(HAP)/PAA]$_{20}$ was 163.6 ± 27.3 nm with a roughness of 36.7 ± 4.5 nm (Figure 3.2A, S3). Simultaneously controlling the quantity of growth factor release from the film is critical, as a large excess can lead to incidences of elevated bone resorption and hematoma.[39] Constant localized extended release of rhBMP-2 represents a more physiological dosing and a top layer of [Poly2/PAA/rhBMP-2/PAA]$_{20}$ coated on silicon, contained approximately 250 ng/cm^3 of growth factor which eluted from the films and thus this architecture was suitable for eluting active growth factor over 2 weeks (Fig. 3.2E). The release of active growth factor from the degradable multilayer films had two phases, as observed previously.[40] The rhBMP-2 released at a relatively constant rate of approximately 30 ng cm^{-3} day^{-1} for the first 7 days of release, which was then reduced to 5 ng cm^{-3} day^{-1} until complete elution. Comparable amount of growth factor was incorporated and released over the same time scale from films independent of the number of osteoconductive base layers. Surface profiles of the films in different states of assembly and degradation indicate a uniform distribution of HAP particles (Fig. 3.2F, 3.2I) within and on the osteoconductive base layers. The degradable growth factor releasing multilayers coat over the osteoconductive base layers; generally, these films have a consistent roughness of about 200 nm regardless of the size of the features in the underlying base film (Fig. 3.2D, 3.2G, 3.2J). After the release of the growth factors, the osteoconductive layer persists and there is a reduction in the surface roughness (Fig. 3.2H, 3.2K, A3) from the original base layer, suggesting the release of calcium and phosphate ions from the hydroxyapatite into the surrounding media, and thus a reorganization of HAP particles after an exchange of calcium and phosphate ions with the surrounding media which decreases the size and number of particles in the base film. This release is beneficial to the recruitment of MSCs in an *in vivo* environment.[3] Interestingly, after the release of growth factors, the osteoconductive base layer persists at the same thickness in the dry state.

Pluripotent adult mesenchymal stem cells have the ability to differentiate into a variety of different cell types such as osteocytes, chondrocytes, cardiac muscle and

endothelial cells. However, the repair of damaged bone tissue requires migration of MSCs into the damaged area via chemoattractive signals followed by proliferation and differentiation of MSCs to osteoblasts.[41] Such a favorable biological environment is created by the presence of HAP particles which stimulate osteoconduction and rhBMP-2 which provides the primary signal for non-committed MSCs to differentiate into mineral depositing osteoblasts. MSCs were seeded on glass cover slips coated with the osteophilic films. Cells attached to the coated substrate and subsequently responded to substrate signals by appropriate proliferation and differentiation behavior. Alkaline phosphatase (ALP) is a membrane bound glycoprotein which hydrolyzes various monophosphate esters and is expressed at relatively high levels in osteoblasts; it serves as a standard early marker of induction of new bone differentiation from progenitor cells. Alizarin red (AR) stains the calcium deposits and allows quantification of the total deposition *in vitro*. While the presence of either HAP or rhBMP-2 upregulates ALP and AR production, a maximum in the ALP/AR signal is observed when both HAP and rhBMP-2 are present in the LbL film architecture, indicating a synergistic response by the osteogenic materials after 5 days of culture (Fig. 3.3A, 3.3B). This is especially pertinent in light of the observation that the AP/AR signals were statistically insignificant for the $[Chi(HAP)/PAA]_{20}$ and $[Poly2/PAA/rhBMP\text{-}2/PAA]_{20}$.

In order to determine the ability this system to mimic a favorable bone forming environment, we examined the expression of 3 specific protein markers expressed by osteoprogenitor cells during differentiation. Osteocalcin is a small calcium binding protein that tightly adsorbs to hydroxyapatite mineral surfaces, comprising about 10% of the total non-collagen proteins in bone.[42] Similarly, osteopontin is a cell and HAP binding protein synthesized by osteoblasts implicated in bone resorption.[43] Osteoprotonegrin is an osteoblast-secreted receptor, which acts as an antagonist to osteopontin.[44] Together, these form the major group of proteins controlling the bone deposition and remodeling processes. In this study, aliquots of conditioned media, in which the cells were cultured, were collected every two days and assayed for the 3 markers. In all cases there was a peak in the expression levels of the different markers. When $[Chi(HAP)/PAA]_{20}$ and $[Poly2/PAA/rhBMP\text{-}2/PAA]_{20}$ were presented together, there was a 2 fold upregulation in the peak and cumulative secretion levels of all 3

osteoblast differentiation markers, compared to the control cells in differentiation media and a 20-50% upregulation compared to the individual $[Chi(HAP)/PAA]_{20}$ and $[Poly2/PAA/rhBMP\text{-}2/PAA]_{20}$ controls indicating that simultaneous presentation of an osteoconductive and an osteoinductive agent may be most beneficial to active bone deposition and remodeling (Fig. 3.3C – 3.3F and Appendix A; fig. A4). Additionally, the peak expression of these markers was up to 48 hours earlier when both HAP and rhBMP-2 were present, compared to all the other groups, indicating that the differentiation cascade may be accelerated. This observation is consistent with greater alkaline phosphatase production and calcium deposition for this multilayer combination. Control cells proliferating on plain coverslips do not express any of the markers. In all cases, cell morphology as observed by nuclear (hoechst) and actin (phalloidin) staining indicates that the cells adhere well to the films and are able to grow and proliferate in layers over the course of the study.

2.4 Conclusions

In conclusion, we have demonstrated the ability to create a biomimetic modular coating for substrates that simultaneously present hydroxyapatite, an inorganic component of the bone complexed with biocompatible polymers, and rhBMP-2, a bone growth factor to accelerate the regeneration of stable bone tissue. Our findings highlight the characteristics of this alternative uniform coating method for hydroxyapatite, which can be performed at ambient conditions, without the need for high temperature processes. This osteoconductive base layer persists and offers an osteophilic platform on which MSCs can proliferate and differentiate, while the utility of rhBMP-2 has been well documented in mediating interactions between host tissue and implant. This electrostatic multilayer coating delivers physiological nanogram amounts of active rhBMP-2 over two weeks and induces a differentiation response on physiologically responsive MSCs. Introduction of hydroxyapatite and rhBMP-2 upregulated osteogenic markers at earlier times in MSCs which resulted in greater calcium deposition in culture. We have presented an alternative method for the fabrication of hybrid multilayer films consisting of organic and inorganic components for bone tissue healing. The ease of fabrication and the scalability of this platform approach make it easily translatable to a

variety of orthopedic implants and devices, with the goal of offering successful and lasting joint replacement, wound healing and repair.

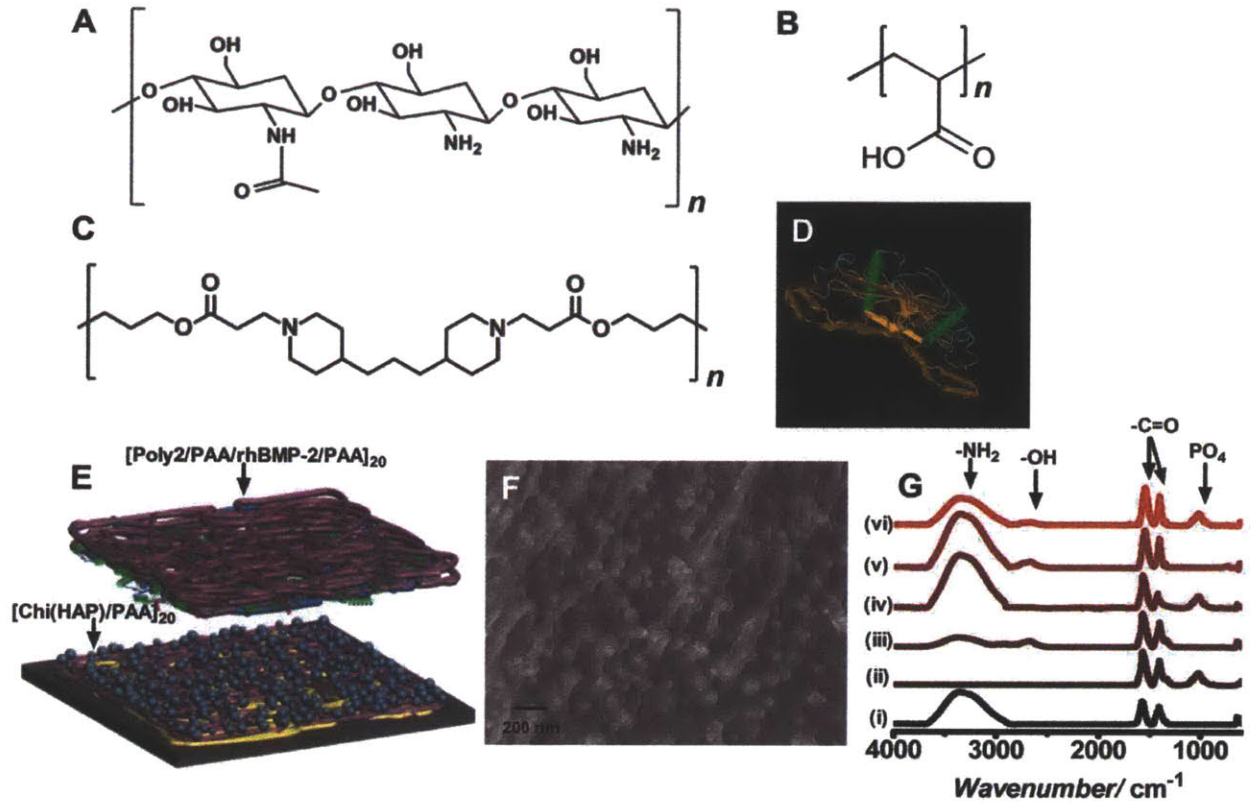

Figure 2.1. Design and fabrication of the osteophilic multilayer architecture. Components of the film (A) Chitosan (75%-85% deacetylated chitin), a polycation (B) Poly(acrylic acid) (PAA), (C) A hydrolytically degradable poly(β-amino ester) (Poly2), a polycation and (D) osteoinductive recombinant human bone morphogenetic protein 2 (rhBMP-2) (E) Schematic of the modular electrostatic assembly. Osteoconductive hydroxyapatite is complexed with chitosan and incorporated into nanoscale thick films along with poly(acrylic acid) in a bilayer architecture. A hydrolytically degradable poly(β-amino ester) based multilayer film incorporating osteoinductive rhBMP-2 lays atop the osteoconductive layer. (F) Scanning electron micrograph of a $[Chi(HAP)/PAA]_{20}$ bilayer film with the complexed hydroxyapatite nanoparticles. HAP particles complexed to chitosan strands are interwoven in the multilayer architecture (G) IR absorbance spectra of the different components of the osteoconductive layer (i) chitosan (ii) hydroxyapatite (iii) poly(acrylic acid) (iv) $[Chitosan/HAP]_1$ (v) $[Chitosan/PAA]_{20}$ and (vi) $[Chi(HAP)/PAA]_{20}$.

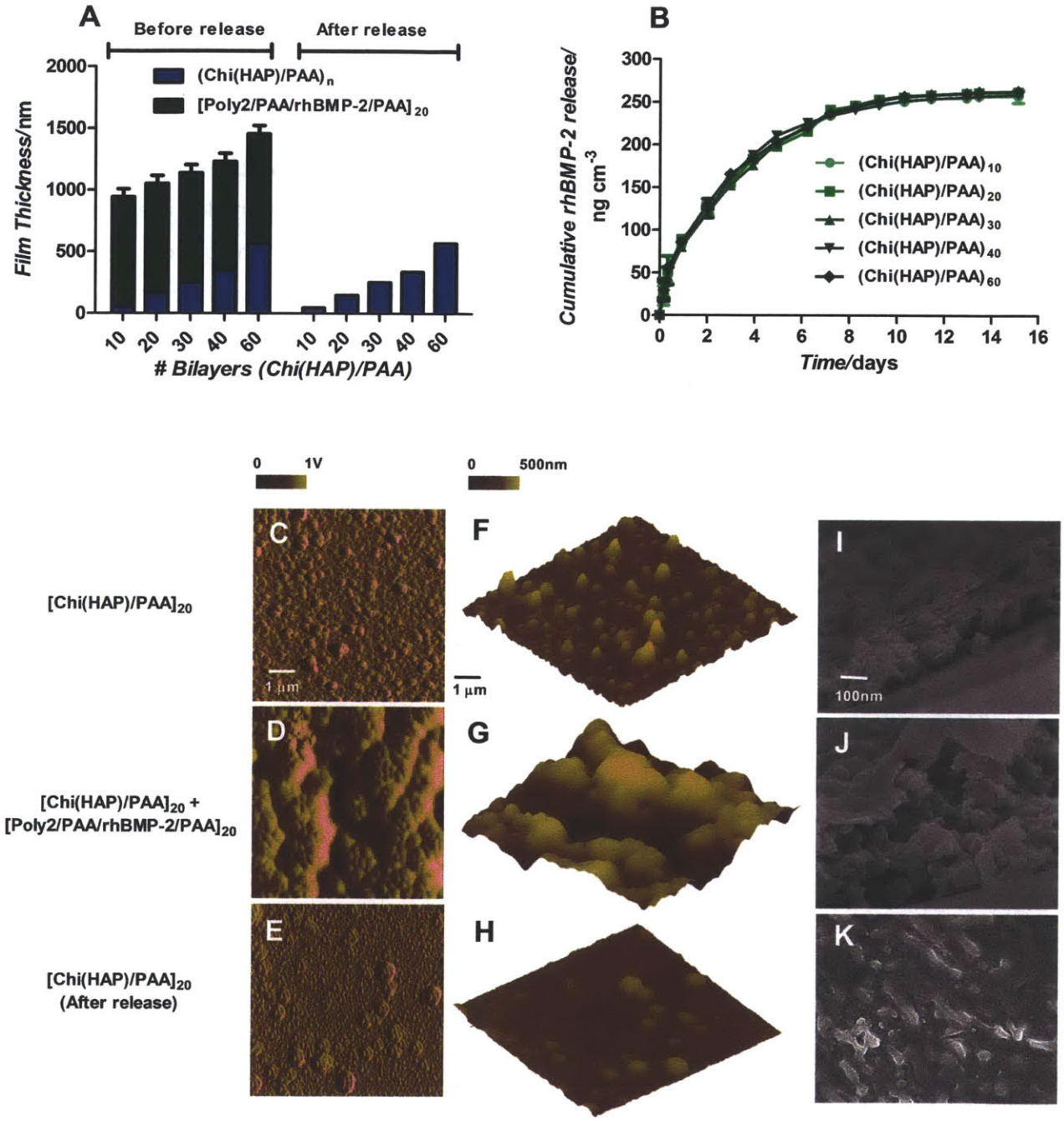

Figure 2.2. Characteristics of multilayer properties during assembly and degradation. (A) Multilayer film thickness increases linearly with incremental osteoconductive [Chi(HAP)/PAA] layers. Contributions of film thickness from the growth factor eluting layers (green) and

hydroxyapatite containing layers (blue) are provided. (B) rhBMP-2 released from the films over 2 weeks. Surface and bulk morphologies of $[Chi(HAP)/PAA]_{20}$ + $[Poly2/PAA/rhBMP\text{-}2/PAA]_{20}$ multilayer films (C, F) HAP particles are distributed uniformly in the osteoconductive $[Chi(HAP)/PAA]_{20}$ multilayer surface, and the features are made rougher in (D, G) by the conformal coating of the $[Poly2/PAA/rhBMP\text{-}2/PAA]_{20}$ layers. (E, H, K) Once the growth factor is released by the degradation of the poly(β-amino ester) layers, there is an observable reduction in surface roughness. (F, G, H) Surface height profiles confirm that HAP particles are uniformly distributed with a lack of sequestration in a particular area. (I, J) Corresponding cross sectional scanning electron microscopy images confirm the presence of particles throughout the bulk of the film (I, J, K are at the same scale). C-H are atomic force microscopy images, where C-E are phase contrast images, F-H are height images. I-K are scanning electron microscopy images.

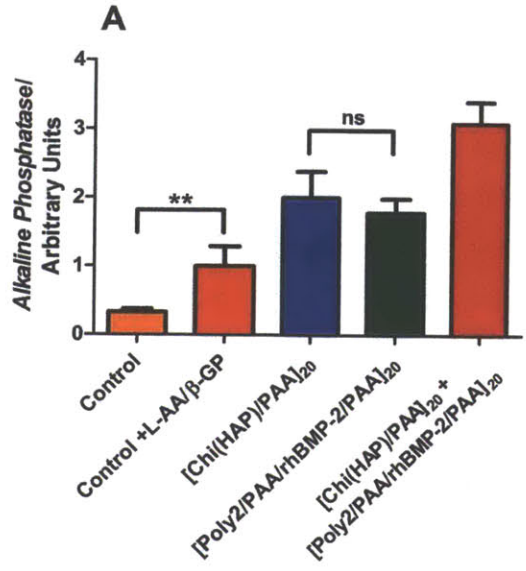
A
Alkaline Phosphatase/ Arbitrary Units
**
ns
Control
Control +L-AA/β-GP
[Chi(HAP)/PAA]20
[Poly2/PAA/rhBMP-2/PAA]20
[Chi(HAP)/PAA]20 + [Poly2/PAA/rhBMP-2/PAA]20

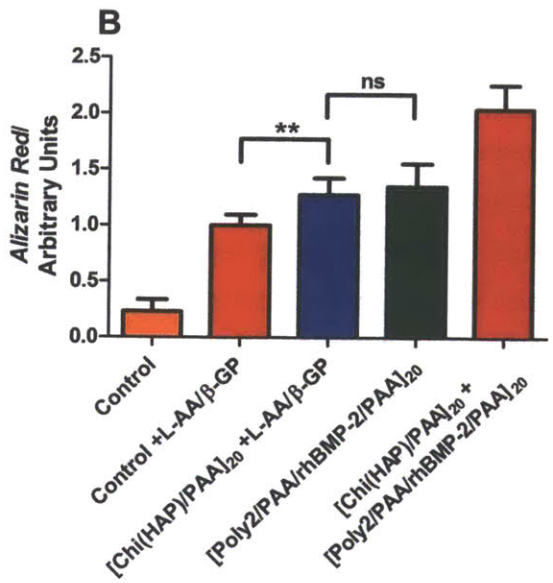
B
Alizarin Red/ Arbitrary Units
**
ns
Control
Control +L-AA/β-GP
[Chi(HAP)/PAA]20 +L-AA/β-GP
[Poly2/PAA/rhBMP-2/PAA]20
[Chi(HAP)/PAA]20 + [Poly2/PAA/rhBMP-2/PAA]20

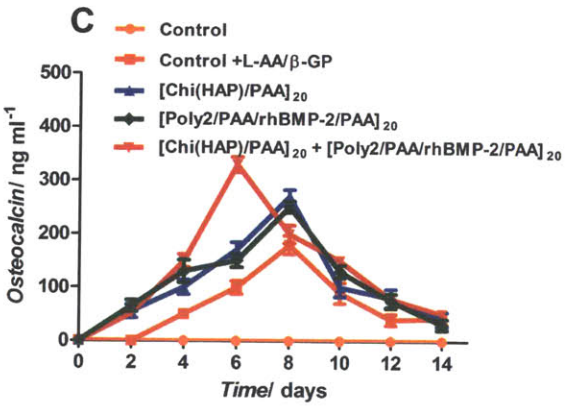
C
Control
Control +L-AA/β-GP
[Chi(HAP)/PAA]20
[Poly2/PAA/rhBMP-2/PAA]20
[Chi(HAP)/PAA]20 + [Poly2/PAA/rhBMP-2/PAA]20
Osteocalcin/ ng ml-1
Time/ days

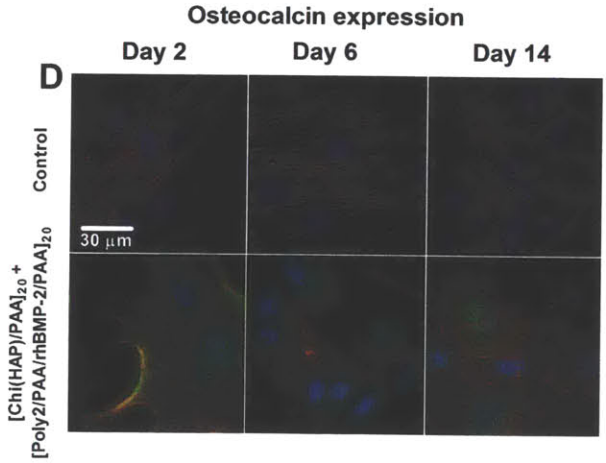
Osteocalcin expression
Day 2
Day 6
Day 14
D
Control
[Chi(HAP)/PAA]20 + [Poly2/PAA/rhBMP-2/PAA]20
30 μm

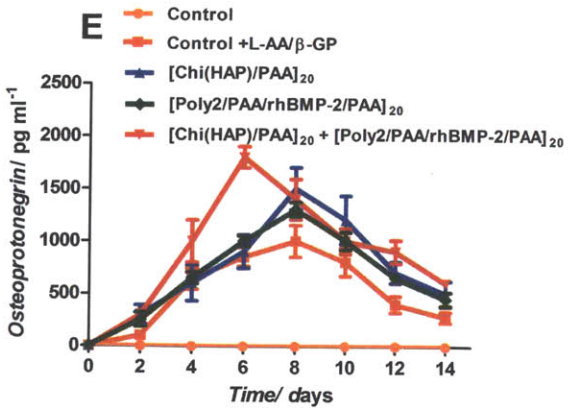
E
Control
Control +L-AA/β-GP
[Chi(HAP)/PAA]20
[Poly2/PAA/rhBMP-2/PAA]20
[Chi(HAP)/PAA]20 + [Poly2/PAA/rhBMP-2/PAA]20
Osteoprotonegrin/ pg ml-1
Time/ days

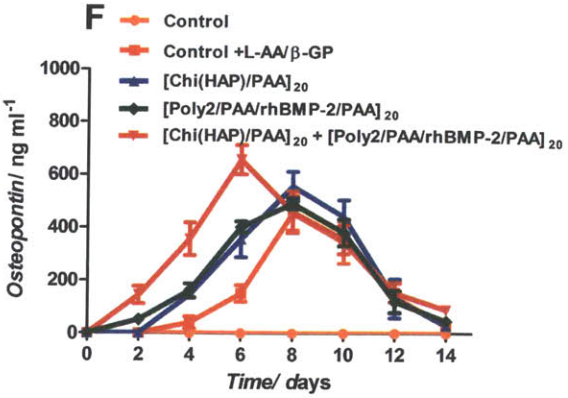
F
Control
Control +L-AA/β-GP
[Chi(HAP)/PAA]20
[Poly2/PAA/rhBMP-2/PAA]20
[Chi(HAP)/PAA]20 + [Poly2/PAA/rhBMP-2/PAA]20
Osteopontin/ ng ml-1
Time/ days

Figure 2.3. Mesenchymal stem cells differentiating into the osteoblast lineage. (A) Alkaline phosphatase (AP) quantification at 5 days after the differentiation cascade is initiated. (B) Alizarin red (AR) staining and quantification for calcium deposits 14 days after mesenchymal stem cells have been in culture under different conditions as indicated. Both AP and AR signals have been represented as fold increase or decrease of the Control +L-AA/β-GP case. A single factor ANOVA test allowed rejection of the null hypothesis for all assays; and a Tukey test between all groups was performed (s.d., n=9, ** $p < 0.01$; * $p < 0.05$; ns = not significant all others are $p < 0.001$). Temporal expression patterns of osteogenic markers in mesenchymal stem cells. Quantification of osteogenic markers (C) Osteocalcin, (D) visualized (green) from differentiating cells by fluorescence over the course of the study. (E) Osteoprotonegrin and (F) Osteopontin expression follows a similar trend to osteocalcin. In all the assays, the synergistic effect of having an osteoconductive and an osteoinductive layer maximizes AP and AR signals. Expression of osteogenic markers may be accelerated and amplified by the introduction of the osteophilic multilayers leading to an environment conducive for bone formation. Peak and cumulative expression levels of the combination osteoconductive and an osteoinductive multilayers are statistically significant compared to other groups ($p<0.001$, Appendix A; fig A4).

2.5. References

[1] A. Ince, J. Rupp, L. Frommelt, A. Katzer, J. Gille, J. F. Lohr, *Clin. Infect. Dis.* **2004**, *39*, 1599.

[2] W. H. Harris, C. B. Sledge, *N. Engl. J. Med.,* **1990**, *323*, 725.

[3] K. Soballe, S. Overgaard, *J. Bone Joint Surg. Br.,* **1996**, *78*, 689.

[4] B. H. Lee, A. Oyane, H. Tsurushima, Y. Shimizu, T. Sasaki, N. Koshizaki, *ACS Appl. Mater. Interfaces,* **2009**, *1*, 1520.

[5] C. Knabe, F. Klar, R. Fitzner, R. J. Radlanski, U. Gross, *Biomaterials,* **2002**, *23*, 3235.

[6] M. Uchida, A. Oyane, H. M. Kim, T. Kokubo, A. Ito, *Adv. Mater.,* **2004**, *16*, 1071.

[7] F. J. Garcia-Sanz, M. B. Mayor, J. L. Arias, J. Pou, B. Leon, M. Perez-Amor, *J. Mater. Sci. Mater. Med.,* **1997**, *8*, 861.

[8] S. Raynaud, E. Champion, D. Bernache-Assollant, P. Thomas, *Biomaterials,* **2002**, *23*, 1065.

[9] A. K. Lynn, D. L. DuQuesnay, *Biomaterials,* **2002**, *23*, 1937.

[10] J. M. Wozney, V. Rosen, A. J. Celeste, L. M. Mitsock, M. J. Whitters, R. W. Kriz, R. M. Hewick, E. A. Wang, *Science,* **1988**, *242*, 1528.

[11] H. Ai, S. A. Jones, Y. M. Lvov, *Cell Biochem. Biophys.*, **2003**, *39*, 23.

[12] S. Facca, C. Cortez, C. Mendoza-Palomares, N. Messadeq, A. Dierich, A. P. R. Johnston, D. Mainard, J.-C. Voegel, F. Caruso, N. Benkirane-Jessel, *Proc. Natl. Acad. Sci. U. S. A.*, **2010**, *107*, 3406.

[13] G. Decher, *Science*, **1997**, *277*, 1232.

[14] N. A. Kotov, Z. Y. Tang, Y. Wang, P. Podsiadlo, *Adv. Mater.*, **2006**, *18*, 3203.

[15] P. T. Hammond, *Adv. Mater.*, **2004**, *16*, 1271.

[16] A. J. Engler, S. Sen, H. L. Sweeney, D. E. Discher, *Cell*, **2006**, *126*, 677.

[17] W. L. Murphy, S. Hsiong, T. P. Richardson, C. A. Simmons, D. J. Mooney, *Biomaterials*, **2005**, *26*, 303.

[18] A. S. Greenwald, S. D. Boden, V. M. Goldberg, Y. Khan, C. T. Laurencin, R. N. Rosier, C. B. Implants, *J. Bone Joint Surg. Am.*, **2001**, *83A*, 98.

[19] K. Soballe, E. S. Hansen, H. Brockstedt-Rasmussen, C. Bunger, *J. Bone Joint Surg. Br.*, **1993**, *75*, 270.

[20] H. P. Jennissen, *Ann. N. Y. Acad. Sci.*, **2002**, *961*, 139.

[21] T. A. Linkhart, S. Mohan, D. J. Baylink, *Bone*, **1996**, *19*, 1S.

[22] V. Luginbuehl, L. Meinel, H. P. Merkle, B. Gander, *Eur. J. Pharm. Biopharm.*, **2004**, *58*, 197.

[23] T. Boudou, T. Crouzier, K. Ren, G. Blin, C. Picart, *Adv. Mater.*, **2010**, *22*, 441.

[24] C. Chai, K. W. Leong, *Mol. Ther.*, **2007**, *15*, 467.

[25] R. A. Muzzarelli, G. Biagini, M. Bellardini, L. Simonelli, C. Castaldini, G. Fratto, *Biomaterials*, **1993**, *14*, 39.

[26] A. Di Martino, M. Sittinger, M. V. Risbud, *Biomaterials*, **2005**, *26*, 5983.

[27] E. M. Bueno, J. Glowacki, *Nat. Rev. Rheumatol.*, **2009**, *5*, 685.

[28] I. Wedmore, J. G. McManus, A. E. Pusateri, J. B. Holcomb, *J. Trauma*, **2006**, *60*, 655.

[29] W. Liu, S. Sun, Z. Cao, X. Zhang, K. Yao, W. W. Lu, K. D. Luk, *Biomaterials*, **2005**, *26*, 2705.

[30] G. S. Sailaja, P. Ramesh, H. K. Varma, *J. Appl. Polym. Sci.*, **2006**, *100*, 4716.

[31] I. Yamaguchi, K. Tokuchi, H. Fukuzaki, Y. Koyama, K. Takakuda, H. Monma, T. Tanaka, *J. Biomed Mater. Res. A*, **2001**, *55*, 20.

[32] T. T. Li, J. H. Lee, T. Kobayashi, H. Aoki, *J. Mater. Sci. Mater. Med.*, **1996**, *7*, 355.

[33] P. Habibovic, F. Barrere, C. A. van Blitterswijk, K. de Groot, P. Layrolle, *J. Am. Ceram. Soc.*, **2002**, *85*, 517.

[34] D. M. Lynn, R. Langer, *J. Am. Chem. Soc.*, **2000**, *122*, 10761.

[35] Y. L. Wang, K. J. Addess, J. Chen, L. Y. Geer, J. He, S. Q. He, S. N. Lu, T. Madej, A. Marchler-Bauer, P. A. Thiessen, N. G. Zhang, S. H. Bryant, *Nucleic Acids Res.*, **2007**, *35*, D298.

[36] C. Scheufler, W. Sebald, M. Hulsmeyer, *J. Mol. Biol.*, **1999**, *287*, 103.

[37] Q. L. Hu, B. Q. Li, M. Wang, J. C. Shen, *Biomaterials*, **2004**, *25*, 779

[38] X. Wang, J. Zhuang, Q. Peng, Y. D. Li, *Adv. Mater.*, **2006**, *18*, 2031.

[39] J. Zara, R. K. Siu, X. Zhang, J. Shen, R. Ngo, M. Lee, W. Li, M. Chiang, J. U. Chung, J. Kwak, B. Wu, K. Ting, C. Soo, *Tissue Eng. Part A*, **2011**, *17*, 1389.

[40] N. J. Shah, M. L. Macdonald, Y. M. Beben, R. F. Padera, R. E. Samuel, P. T. Hammond, *Biomaterials*, **2011**, *32*, 6183.

[41] S. P. Bruder, A. A. Kurth, M. Shea, W. C. Hayes, N. Jaiswal, S. Kadiyala, *J. Orthop. Res.*, **1998**, *16*, 155.

[42] J. B. Lian, C. M. Gundberg, *Clin. Orthop. Relat. Res.*, **1988**, *226*, 267.

[43] F. P. Reinholt, K. Hultenby, A. Oldberg, D. Heinegard, *Proc. Natl. Acad. Sci. U. S. A.*, **1990**, *87*, 4473.

[44] M. Wan, X. Shi, X. Feng, X. Cao, *J. Biol. Chem.*, **2001**, *276*, 10119.

[45] C. A. Gregory, W. G. Gunn, A. Peister, D. J. Prockop, *Anal. Biochem.*, **2004**, *329*, 77.

Chapter 3

Surface-mediated bone tissue morphogenesis from tunable nanolayered implant coatings

3.1 Introduction

Implantable devices and scaffolds can replace damaged tissues, restore function, improve mobility, and alleviate pain. A major clinical issue that limits the success of orthopedic implants is failure owing to aseptic loosening and sub-optimal integration with the host tissue, which constitutes more than half of all joint replacement failures[1, 2]. Implant loosening prolongs patient recovery times and increases post-operative complications and morbidity. The principal determinants of implant success are the nature and integrity of the bond between the implant and the bone, the rate at which the bond forms, and the amount of bone surrounding the implant that participates in stabilizing the device. Rapid, early stabilization of an implant by bone, without the formation of an avascular, loose fibrous tissue capsule are key determinants of long term implant function and integrity. Creating a mechanically competent, stable, permanent bond between implant and host bone through direct bone/implant contact is crucial for the success of dental implants and whole-joint replacement prosthesis.

Although widely accepted as the technique of choice for cemented hip and knee replacement implants, self-curing poly(methyl methacrylate) (PMMA)–based bone cements do not facilitate the formation of a reliable and mechanically coupled implant–bone bond owing to a substantial elastic modulus mismatch at the bone interface. PMMA has low compressive strength (70 – 120 MPa), is not bioresorbable, and is prone to fragmentation[3]. Furthermore, the in situ formation of PMMA is a highly exothermic process that causes local tissue necrosis and makes it unfavorable for the incorporation and release of biologics that mediate the interaction between the host and implant. Other strategies to bond uncemented implants with the native bone have involved porous metallic coatings that have been clinically proven to induce bone ingrowth. However, this approach has been largely abandoned in knee implants owing to

inadequate bone ingrowth and mechanical fixation[4].

Coatings that incorporate osteoconductive bioceramics, such as hydroxyapatite (HAP), have been used in the clinic for osseointegration of dental and orthopedic implants. However, plasma-deposited HAP coatings are several microns thick, have low tensile (45 – 65 MPa) and shear (25 – 40 MPa) strengths, are typically monolithic with invariant structural or mechanical properties, and have inadequate stress relief, which often results in cracks, rapid wear, and long-term instability within the body[5, 6]. Consequently, failures associated with current HAP-based coatings occur at the implant-bone interface. High temperatures and grit blasting with high mechanical force have been used for the deposition of nanoscale HAP[7]. However, this process is unfavorable for the incorporation of biologics. Modification of implant surfaces with cell adhesion molecules is inherently challenging owing to low selectivity across a variety of cell types, which can result in nonspecific attachment. These systems also lack tunable control over how long they are able to actively provide biochemical cues[8].

One of the proven bone differentiation factors currently employed in the clinic is bone morphogenetic protein 2 (BMP-2). The promise of this growth factor for bone tissue engineering depends critically on its delivery strategy[9, 10]. Bolus release of BMP-2 from injectable or implantable carriers or depots results in a rapid clearance of the protein from the target site by serum proteins. Large quantities of recombinant human BMP-2 (rhBMP-2)—sometimes several orders of magnitude higher than needed—have been used in the clinic to compensate for suboptimal BMP-2 release characteristics of the carrier[11]. The result was a lowered impact on tissue regeneration and undesired side effects[12]. Hydrogel-based delivery systems can control the rate of release, but these systems deform easily and are unsuitable for imparting strong adhesion and mediating surface interactions on a permanent prosthesis.

We addressed these issues by coating implants using a layer-by-layer (LbL) technique[13-15]. The polymer coatings (< 2 μm thick) consisted of osteoconductive base layers with HAP and osteoinductive BMP-2-releasing layers[16]. The layered approach enabled tunable release of therapeutic levels of BMP-2 while providing an osteoconductive matrix for direct adhesion of osteoblasts. This thin multilayer coating conformed to implant geometries and recruited endogenous progenitor cells to form

bone directly on the implant surface that integrated with the host cortical bone. The cohesive bone–implant interface resulted in the bonding and long-term stable fixation of the implant in vivo with rodent host tissue.

3.2 Materials and Methods

3.2.1. Rationale and study design

HAP and rhBMP-2 have been shown to benefit bone formation. We focused on evaluating tunable bone implant coatings containing these materials. The experiments compared the effect of their serial incorporation in multilayer implant coatings on bone integration. For animal studies, power analysis was conducted using GPower Analysis, using ANOVA repeated measures, between factors test. We assumed an effect size (f) of 0.5, an α error probability of 0.05, power of 0.95 and a correlation of 0.2. There were a total of 8 experimental groups with a at least 41 test animals per group. Each animal one implant in each leg (considered independent). Within each group, at least 5 implants were used for each measurement (IVIS, FACS, pull-out tensile testing and μCT) per time point. Some samples were used for representative histology. End-points were pre-determined to study the temporal effect of coatings of bone formation and implant integration. All experiments were randomized and non-blinded.

3.2.2. Preparation of electrostatic films

Poly2 (M_n = 11,910) was synthesized as described[25] and confirmed by NMR (Appendix B; fig. B12). Materials were purchased from Sigma unless otherwise noted. Sodium acetate buffer (0.1M, pH 4.0) was used for preparing polyelectrolyte solutions. Multilayer coatings were made using the LbL method[13-15]. HAP nanoparticle suspension in buffer (0.1% w/v) was sterile-filtered and added 1:1 (v/v) to chitosan solution in buffer (2 mg/ml). Polyelectrolyte solutions were prepared at 1 mg/ml (PAA, Poly2). Dipping solutions were prepared at 250 μg/ml rhBMP-2 (Pfizer). Detailed LbL film fabrication and characterization is described in Appendix B.

PEEK (McMaster-Carr) and titanium dowels (Titanium Industries) were machined into implants. These were plasma treated with air for 10 and 2 minutes, respectively, and alternatively dipped for 5 minutes each, into the prepared solutions with an intermediate

washing step in water. The osteoconductive base layers (X) were deposited first followed by the osteoinductive layers (Y). X_{20}, or 60 bilayers of Poly2/PAA were incubated in a 250 µg/ml solution of rhBMP-2 at 4°C overnight.

3.2.3. Animal studies

All animal procedures were approved by the IACUC at MIT. Implants were inserted below the patella ligament in both the tibiae of adult male Sprague-Dawley rats. The implant (diameter 1.3 mm) was inserted in a drilled hole (diameter 1.4 mm). Details in Appendix B.

3.2.4. Pull-out tensile testing

After euthanasia, tibiae were explanted and stored in PBS for immediate mechanical tensile testing (Instron 5943). The exposed head of the implant was connected to a load cell and was then subjected to a constant pull rate of 0.1 N/s. The pull-out force, parallel to the long axis of implant, was the maximum load achieved before implant detachment due to failure. Interfacial shear strength was calculated by dividing the pull-out force by the total surface area of the implant.

3.2.5. Histology

After euthanasia, tibiae were explanted and were fixed in 4% paraformaldehyde (PFA). PFA-fixed tibiae with implants were partially decalcified for about 4 hours using a rapid decalcifying formic acid/hydrochloric acid mixture (Decalcifying Solution, VWR) and embedded in paraffin wax. Sections (5 µm) of the bone/implant interface were stained with routine hematoxylin and eosin (H&E) and Masson's trichrome stain. Implants were embedded in glycol methacrylate (JB-4 Plus, Polysciences) following the manufacturer's protocol and sectioned.

3.2.6. µCT analysis

Anesthetized live animals were imaged with a µCT (eXplore CT120, GE Medical Systems). Scanning protocol: Shutter speed (325 s), 2×2 binning, 70 kV, 50 mA, 220 images, 0.877° increments, gain: 100 and offset: 20. Images were reconstructed and

analyzed with MicroView (GE Healthcare). A threshold value and ROI was chosen by visual inspection of images (constant for all groups) and BC/BV was measured.

3.2.7. Statistical analysis

Prism 5 (GraphPad) was used for all analyses. Results are presented as means ± SEM. Time points are after implanting. Data were analyzed by ANOVA and comparisons were performed with a Tukey post hoc test (multiple groups) or a Student's *t* test (two groups). ANCOVA was used to analyze trends in temporal measurements. $P < 0.05$ was considered significant.

3.3 Results

3.3.1 A two-part multilayer osteogenic coating

The base coating of the multicomponent film consisted of a set of permanent osteoconductive layers composed of a positively charged complex of cationic chitosan (Chi) (Fig. 1A) and HAP (Fig. 1B), alternated with anionic poly(acrylic acid) (PAA) (Fig. 1C) to form bilayers, indicated as $[Chi(HAP)/PAA]_X$ (where X is the number of bilayers). The mechanical properties of the film were examined using nanoindentation and revealed an elastic modulus of 11.39 ± 0.3 GPa (SEM) (Appendix B; fig. B1A). The elastic modulus dropped to 5.98 ± 0.32 GPa (SEM) in Chi/PAA polymer films without HAP.

The second component of the multilayer coating consisted of a polycationic degradable poly(β-amino ester), Poly2 (Fig. 1D). Poly2 was alternated with anionic PAA and positively charged rhBMP-2 (Fig. 1E) to generate a set of hydrolytically degradable layers atop the osteoconductive base (Fig. 1F) in the form of tetralayers, written as $[Poly2/PAA/rhBMP\text{-}2/PAA]_Y$ (where Y is the number of tetralayers). Under the acidic pH conditions of film fabrication, Poly2 was stable and the amines along its backbone were protonated, yielding a positive charge for electrostatic LbL assembly. The repeat unit for the osteoconductive base layers $[Chi(HAP)/PAA]_X$ and that of the growth factor–releasing layer $[Poly2/PAA/rhBMP\text{-}2/PAA]_Y$ are referred to as X and Y, respectively, and subscripted by the number of iterations.

Growth factor loading increased linearly with the number of layers, as observed in

vitro for degradable LbL-coated PEEK and titanium implants with three different amounts of rhBMP-2 (Appendix B; fig. B1B). The total rhBMP-2 dose varied from 104.4 ± 16.8 (SEM) ng/mm^2 for the X_{20} + Y_{20} coating (or Y_{20} alone) to 301.3 ± 17.2 (SEM) ng/mm^2 for the X_{20} + Y_{60} (or Y_{60} alone) growth factor–loaded films (Fig. 1G). At pH 7.4, hydrolysis of the ester bonds in the exposed Poly2 chains resulted in the first-order in vitro release of rhBMP-2 from the LbL coating which lasted up to 15 days in cell culture media. All loaded rhBMP-2 eluted from the film, and none remained bound to the osteoconductive base layer. LbL coatings with extended incubation in rhBMP-2 solution had a higher total loading (than ng/mm^2 values seen for the rhBMP-2 deposited coatings): 1.8 μg/mm^2 for the X_{20} base layer and 2.9 μg/mm^2 with the 60 bilayer repeat [Poly2/PAA] coating. The osteoconductive base layer was designed to be permanent and maintained the same thickness on the substrate even after the release of growth factors (Appendix B; fig. B1C).

In all of the controlled-release layer formulations, 90 ± 1.1% (SEM) of rhBMP-2 eluted by 1 week. The average rate of release per day was 12.7 ± 0.1% (SEM) of total load with no burst release. rhBMP-2 retained bioactivity in vitro after release (Appendix B; fig. B2). Release profiles in vitro did not depend on implant geometry (Fig. 1G). By comparison, >90% of the therapeutic eluted within 24 hours of bolus release when the LbL films were loaded by extended incubation in rhBMP-2 solution.

To determine the physiological effect of these films, human mesenchymal stem cells (hMSCs) were cultured on the coated substrates and assayed for osteogenic differentiation via alizarin red. No calcium deposits were observed on uncoated substrates in growth media (Fig. 1H). Cells on uncoated substrates in differentiation media exhibited osteogenic differentiation and this average absorbance value (OD_{600}) was used to normalize all the experimental groups. The amount of calcium deposition did not improve beyond X_{20} in growth medium and was selected for further in vivo evaluation. The differentiation assay with X_{20} and varying numbers of rhBMP-2–releasing layers (Y) revealed a dose-dependent effect on calcium production. The results from X_{20} with extended incubation in rhBMP-2 solution were not significant compared to the X_{20} alone (P = 0.19, n = 9, Student's t test) and the effect of the biologic was not observed. The degradable $[Poly2/PAA]_{60}$ incubated for an extended

time in rhBMP-2 was not significant from the uncoated control in growth media (P = 0.17, n = 9, Student's t test). This observation is consistent with rapid elution of growth factor and clearance after periodic changes of cell culture media.

3.3.2 Surface-mediated rhBMP-2 delivery

Implant integration and improvement of the rate and quality of tissue repair are the ultimate goals for biomaterial-based therapeutic strategies. To this end, we examined the effects of different combinations of the coating on poly(ether ether ketone) (PEEK) implants and medical-grade titanium implants that were either smooth or had 150-μm diameter channels drilled into the surface (Appendix B; table B1). Radiolucent PEEK permitted the use of radiography to monitor bone regeneration in real-time. The titanium implant model is a surrogate for dental and orthopedic clinical procedures in which the mechanical and biological integration of the implant with the surrounding bone is critical to its stability. In the clinic, porous implants are designed to enable adhesion interlock with bone and to increase the surface area for bone integration. In this study, each implant was press-fit into a circular unicortical defect drilled into the proximal tibia of a rat.

A near-IR fluorescent reporter was used to label rhBMP-2 and track its presence at the implant site over time in rodents (Fig. 2A). When rhBMP-2 release was controlled, the fluorescent signal at the implant site decreased over the course of 30 days. The gradual decline suggests that protein was retained within the peri-implant space, rather than being rapidly cleared by the local vascular transport systems. A pseudo–zero order regime was observed in vivocompared to the first-order release observed in vitro (Fig. 1G). Although in vivo rhBMP-2 release is primarily driven by hydrolytic degradation of the multilayers and would therefore be first-order, diffusion may play a role and the confined space at the implant site is a smaller sink than the highly dilute buffer solution used for *in vitro* measurements. LbL coatings on the implant subject to extended incubation in rhBMP-2 solution exhibited a burst release in vivo that was 3 orders of magnitude higher than the controlled release system and the profile was independent of the coating composition (Fig. 2B). The released rhBMP-2 was rapidly cleared in vivo, as measured by fluorescence, and was not detectable at the implant site 4 days after

implantation.

These observations correlated with rhBMP-2 detected in homogenized bone marrow isolated from the tibia. rhBMP-2 was detected in the bone marrow aspirates of animals with both drilled and smooth implants in a dose-dependent manner (Fig. 2B). A peak in the dosage profile was detected several days after implantation of smooth PEEK implants followed by a subsequent monotonic reduction in rhBMP-2 that lasted for up to 4 weeks after implantation. Growth factor release from PEEK implants with drilled holes persisted over the same time scale as the smooth implants; however, instead of a defined peak, we observed a consistently high concentration over an extended multi-day period. This suggests that higher cumulative exposure to rhBMP-2 may be available at the drilled implant site for a prolonged period of times, owing to the sequestration of additional protein-loaded film within the channels.

In vitro release studies and a mass balance of total drug load in vivo revealed that the drilled implants had a higher drug load that correlated to the increase in total surface area of the drilled (20.26 mm^2) over the smooth (17.60 mm^2) implants (table S2). The effect of geometry on dosing in vivo was also observed with LbL coatings on implants incubated for an extended time in rhBMP-2 (Fig. 2B; Appendix B; fig. B3). Decreases in fluorescent signal correlated with a drop in detectable levels of rhBMP-2 by ELISA, which suggested clearance of the growth factor from the implant site rather than degradation of the fluorophore.

Fluorescence-activated cell sorting (FACS) analysis on mesenchymal stem cells from the marrow revealed an increase in the osteoblast cell population ($CD29^+CD44^+CD45^-CD90^+BMPR1/2^+$) at 1 week, which was 3-fold greater in the $X_{20} + Y_{60}$ coating compared to X_{20} and Y_{60} alone, and 1.5-fold greater than $X_{20} + Y_{20}$ and $X_{20} + Y_{40}$ (Fig. 3; Appendix B; fig. B4). The percentage of osteoblast cells in the total cell population plateaued between week 4 and week 6 (Fig. 3), suggesting that a higher dose is beneficial primarily for the initial upregulation of the osteoblast population. This plateauing marks the end of the bone deposition process and the beginning of homeostasis. The pattern of cell activation on drilled implants was indistinguishable from smooth implant coatings at the same time point (Fig. 3) ($P > 0.2$, $n = 5$, Student's t test).

3.3.3 Integration of the implant with the bone tissue

Mechanical pull-out testing of the bone–implant interface was used to quantify the anchoring of the implant with bone. In this model of implant integration, the interfacial tensile strength was derived from bone adhesion to the implant surface and the connections that were made with the native bone tissue. The pull-out force increased over time in all groups with the LbL coatings for all types of implants (Fig. 4; Appendix B; fig. B5). The pull-out force was significantly higher in all implants coated with a combination of X and Y, compared to uncoated and to X_{20} or Y_{60} alone implants, including those incubated for an extended time in rhBMP-2 up to 4 weeks after surgery ($P < 0.05$, n = 5 implants per group time point, ANOVA with a Tukey post hoc test).

We investigated bone ingrowth into coated PEEK implants with smooth surfaces versus drilled holes (150 μm diameter). This size has been reported to encourage osteoid formation, and the ingrowth of mineralized bone (*17*). We observed a maximum pull-out force of 65.5 ± 1.3 N (SEM) following 4 weeks with the X_{20} + Y_{60} coating on drilled implants and 39.7 ± 1.6 N (SEM) on smooth implants (Fig. 4). At 4 weeks, the pull-out force was found to be at least 2-fold higher when implants were coated with a combination of both X and Y coatings than implants with either the X_{20} or Y_{60} coating alone, and 32-fold higher than uncoated systems for both implant geometries. The pull-out force at 4 weeks was independent of rhBMP-2 dose. The same trends in pull-out force were observed with coated medical-grade titanium implants as with the PEEK implants. We observed a maximum pull-out force of 64.7 ± 2.2 N (SEM) following 4 weeks with the X_{20} + Y_{60} coating on drilled implants and 41.1 ± 2.2 N (SEM) on smooth implants (Appendix B; fig. B6). The pull-out force at 4 weeks appeared to be independent of the implant material.

The pull-out force remained unchanged from 4 weeks to 18 months in groups with uncoated or Y_{60} coated PEEK implants. (Fig. 4). At this time point, the pull-out force of implants coated with the osteoconductive coating X_{20} was the same as the synergistic coating X_{20} + Y_{60} ($P = 0.96$, n = 5, Student's *t* test), but the pull-out force of implants coated with just Y_{60} did not increase to match the other coatings thus confirming that HAP has a role in mediating formation of a mechanically competent interface. These data suggest that early bonding between bioactive materials and parent bone through

the HAP layer is important to bone tissue apposition and ingrowth. The interfacial tensile strength of coated implants, calculated by dividing the pull-out force by the implant surface area (table S3; table S4), with a combination of both X and Y was found to be 2- to 3-fold higher than HAP coatings on smooth implants using other methods of deposition (0.72-1.5 MPa)[18] and at least 3-fold higher than bioactive bone cements (0.07-0.9 MPa) in animals[19]. While the LbL coatings maintain long-term strength over 18 months, a decrease in strength is observed other HAP coating methods over the same period[18]. Burst-release rhBMP-2 does not have an effect on implant integration when it is introduced in LbL $[Poly2/PAA]_{60}$ films via a single post-coating extended incubation step in both drilled and smooth implants (Fig. 4; table S3; table S4).

3.3.4 Host-implant interactions at the cellular level

Histological sections of excised tibiae with intact PEEK implants with the dual X_{20} + Y_{60} coating (Fig. 5) showed active bone formation and remodeling in time with activated, migrating osteoblasts forming cement lines (Fig. 5A). The new bone was laid down directly on the implants containing HAP in the coating, without a cartilaginous intermediate. We observed that the new bone progressively expanded outward to integrate with the surrounding parent bone. Consistent with stable bone adhesion, bone tissue was observed on the surface of implants that were pulled out of the tibiae, as the tensile tests resulted in cohesive fracture of bone rather than adhesive failure at the bone/implant interface (Fig. 5B). By comparison, for the osteoconductive base layer X_{20} alone, bone deposited on the surface of the PEEK implant with limited contact area, but connected with the host bone (Appendix B; fig. B7). When rhBMP-2 alone (Y_{60}) was introduced, the newly synthesized bone did not directly deposit on the implant surface (Appendix B; fig. B8).

In all coated implants, osteocytes were observed in the newly synthesized bone, indicating bone maturation (Fig. 5; Appendix B; fig. B7B; fig. B8B). Newly synthesized bone formation was restricted to the peri-implant space (Fig. 5A). The collagen fibrils in maturing new bone exhibited birefringence and were oriented along the implant surface (Appendix B; fig. B9A) and extended outward from the implant surface (Appendix B; fig. B9B). Hematopoietic cells were observed around areas of new trabecular bone (Fig.

3.5A), suggesting vascularization.

In implants containing drilled holes, mature bone formed within the implant pores coated with X_{20} + Y_{60}. Granulation tissue penetrated the channel and supplied progenitor cells that progressively filled in tissue from the periphery (Fig. 6, A and B). After 4 weeks, the entire channel filled with new bone (Fig. 6, C and D).

Fibrous tissue growth that is characteristic of a foreign body response was observed around implants without a coating (Appendix B; fig. B10, A and B), and did not convert into bone tissue after 4 weeks. This observation confirmed the lack of osseointegration with uncoated implants. There were no indications of adverse foreign body reactions in the animal in coated implants as evidenced by the lack of foreign body giant cells long-term inflammation or infection (Fig. 5).

3.3.5 Quantifying bone deposition

Micro-computed tomography (μCT) was used to image and quantify temporal bone volume and bone coverage in the peri-implant space (Fig. 7). Because the implant spanned the width of the medullary canal and protruded outside, bone was quantified at these regions of interest (ROIs). Within the medullary canal the ingrowth of bony tissue was observed and increased in volume and coverage over the course of 18 months for drilled and smooth implants coated with X_{20} + Y_{60} (Fig. 7A). Interdigitation of the trabecular shell around the implant occurred at the cortical interface with the endosteal tissue. The volume and coverage of trabecular bone generally increased over time around coated implants (Fig. 7B). Limited calcification of the tissue was observed on implants coated with X_{20} layers alone. Greater calcification was observed with the Y_{60} coating alone.

The presence of rhBMP-2 by itself (Y_{60}) was not sufficient to induce bone apposition to the implant. In fact, the bone coverage/bone volume (BC/BV) around implants with the X_{20} coating was higher at 2 weeks than the Y60 coating alone. The BC/BV of new bone was significantly greater around implants coated with X_{20} + Y_{20} or X_{20} + Y_{60} than those coated with X_{20} or Y_{60} only over the course of 4 weeks. After 18 months, however, implants with the X_{20} coating had the same BC/BV as the combination X_{20} + Y_{60}. Nevertheless, bone coverage of the combination coatings reached > 90% in 2 weeks.

Bone volume for the X_{20} + Y_{60} surface coating increased from 113.5 ± 6.4 mm^3 (SEM) to 183.1± 9.0 mm^3 (SEM) between 2 and 4 weeks. Implants with surfaces coated with only X_{20} were slower to reach similar BC/BV, with < 50% coverage and only 75.1 ± 3.9 mm^3 (SEM) bone volume at 4 weeks.

On the periosteal side, no BV was observed around implants with the osteoinductive coating alone (Fig. 7C). Notably, the BC plateaued at 2 weeks post implantation, but the BV increased from 2 to 4 weeks for both X_{20} coated implants and implants coated with a combination of X and Y. This is consistent with the participation of progenitor cells from the periosteum in bone formation, on implants with the X_{20} layers. In all groups, no bone was observed to form a 'cap' around the implant on the periosteal side and resistance to tensile forces was entirely due to shear resistance of the new bone (Fig. 7A).

Similar observations were made for the smooth implants as for the drilled implants (Appendix B; fig. B11). However, the volume of bone formed in the medullary canal was lower in smooth versus drilled across different coating groups, probably owing to the reduced total surface area from a lack of drilled channels. The difference was 12.3 ± 2.1% (SEM), corresponding to the 13.1% lower surface area in smooth implants.

3.4 Discussion

Worldwide revision rates for hip and knee prosthesis are about 12% after ten years and over half of all failures are due to aseptic loosening[1]. Revision surgeries are burdensome on the patient, increase recovery times and often permanently restrict mobility. For knee revisions alone, the projected hospital costs may exceed $2 billion by 2030[20]. Revision surgeries stretch healthcare resources and result in significant financial losses in the system. This burden, coupled with a projected increase in demand for hip, knee and dental implants is a significant driving force for the attenuation of premature implant failures.

In this study we have used a rational materials approach to rapidly induce implant

fixation via a coating, using a programmable layer-by-layer technique. Chitosan (deacetylated chitin) is a linear cationic polysaccharide which is a hemostatic, antibacterial material, induces minimal foreign body reaction when used in composite scaffolds for bone regeneration, and contributes to the mechanical properties of the osteoconductive base layers[21]. It is hydrolytically stable, and films made of chitosan have been demonstrated to be stable over several months[22]. PAA is a well-characterized weak polyanion with a high charge density with a non-erodible backbone that has been listed as an approved excipient in the FDA's Inactive Ingredient Guide and is used in the clinic. LbL coatings span a wide range of elastic moduli (100 MPa – 20 GPa)[23]. In this study, the elastic modulus of the osteoconductive base layer mimicked that of trabecular bone (~11 GPa)[24]. This allowed for creating a graded transition between an implant and the host bone, thus eliminating mechanical mismatch.

The success of the LbL growth factor delivery strategy requires a polyion with a suitably low degradation rate. In this application, the use of a hydrolytically degradable polyion within the release films was key, as it enabled degradation independent of the presence of specific enzymes or cell types; furthermore, the release rate, critical for optimal tissue response, was readily tuned by the selection of the polymer. Poly2 is a synthetic polymer that belongs to the poly(β-amino ester) family of polymers, which have been used in gene delivery applications and deliver therapeutic payloads without cytotoxicity[25-27].

In prior LbL work, the substrate was coated with the polymer layers alone and then incubated in a concentrated solution of rhBMP-2 for an extended time[28, 29]. In vivo, these systems induce bone formation. Typically, such systems exhibit a burst release

profile, in which much of the therapeutic is ejected from the LbL coatings very quickly (>80% in less than 24 hours). We also observed this behavior in the implants incubated for an extended time in rhBMP-2, where more than 90% of the biologic was eluted after 24 hours. This behavior is akin to known clinical bulk collagen carriers and depots in which 40 – 60% of the encapsulated protein is immediately released in the first three hours with low therapeutic effect[11, 30]. The consequence of such release behavior in this study was none to suboptimal integration, in which the effect of rhBMP-2 is not observed. In addition, the LbL films described in this study are inherently osteoconductive due to the presence of HAP and can be deposited on virtually any bone implant material which may not be osteogenic.

HAP has been known to directly bind BMP-2 primarily via electrostatic interactions along with a number of other secondary interactions[31]. However, HAP coatings that directly adsorb BMP-2 on hydroxyapatite lack the ability to load and release predictable amounts of growth factor[32]. The release is purely diffusive and consequently dependent on loading concentration and environment conditions. The in vivo release kinetics of these systems is unclear, which has direct bearing on bone formation.

When the delivery is controlled, rhBMP-2 acting synergistically with HAP was more effective at mediating implant integration. The released rhBMP-2 bound to the bone matrix after gradual release was detectable with ELISA and in combination with a slow clearance rate from the implant site, an overall accumulation of BMP-2 was achieved. The observation of growth factor retention is consistent with similar observations of delivered therapeutic molecules in other systems[33]. Additional factors that may have contributed to rhBMP-2 accumulation include lower hydrolysis rate due to the adsorption

of proteins and shifts in pH in the wound healing environment at the implant site.

The dose of rhBMP-2 is essential successful osseointegration of implants, but current carriers lack dose tunability[34, 35]. The coatings described here combine the advantages of synthetic materials with key biologics that regulate bone tissue development. Each component of the system can be reproducibly synthesized by chemical means with no risk of disease transmission, which compares favorably to the current clinical standard of bovine-derived absorbable collagen sponge. The coating architecture can be tailored by altering the total number of layers or by tuning the physical properties of the structural components. The mild, water-based coating scheme is adaptable and versatile. This system can be easily extended to incorporate and deliver several physiologically relevant growth factors together or in sequence.

It is important to note the limitations of the study as well as the remaining questions that warrant further investigation. First, the animal model, while standard for implant integration studies, is a surrogate for a joint or dental implant that would experience different dynamic loading conditions. Further evidence from pre-clinical investigations in large animals would be needed using joint and dental implants, as complex implant geometry and surface modification are both important for integration. Long-term superiority of the LbL system over more conventional rhBMP-2 loading strategies remains to be proven and has direct consequence to regulatory approval. The LbL coating may be best suited where there is a major clinical need, such as revision arthroplasty, where the implant has already failed, and primary joint replacements in osteoporotic patients, where there is a need to augment the lack of local bone. Second, although the LbL technique can coat a broad range of substrates—as we have

demonstrated for both PEEK (plastic) and medical-grade titanium—and is extremely versatile, clinical manufacturing of dip- or spray-coated implants will require assembly in a sterile clean-room. The shelf-life of these implants would need to be determined. It is noted that some implant manufacturing companies have explored cyclic drop casting of rhBMP-2 on dental implants in a sterile environment[35]. Orthogonally, methods for rapid high-throughput LbL coatings for non-medical applications are available[36]. For a commercial implant LbL coating process, it may be necessary to harness the synergy of these processes as the ability to automate an efficient coating process in a sterile environment will be critical for feasible scale-up. Initially it may be advantageous to setup this process as stand-alone and subject to separate regulatory validation. Sufficient market demand could warrant integration with an existing implant manufacturing process and re-validation.

In summary, our study demonstrates that a tunable, programmed tissue engineering biointerface can integrate bone implants with the host tissue. Using osteoconductive hydroxyapatite and osteoinductive rhBMP-2 incorporated into a single thin polymer implant coating, we demonstrated a serial effect of implant integration in a relevant rodent model. The results of this study suggest that a synthetic materials approach can be harnessed to access the osteogenic differentation potential of endogenous precursor bone marrow stem cells and mediate specific, long-term host-tissue interactions. This approach provides a path to developing next-generation biologically integrated bone implants with superior stability, fewer incidences of failure and lower rates of patient morbidities.

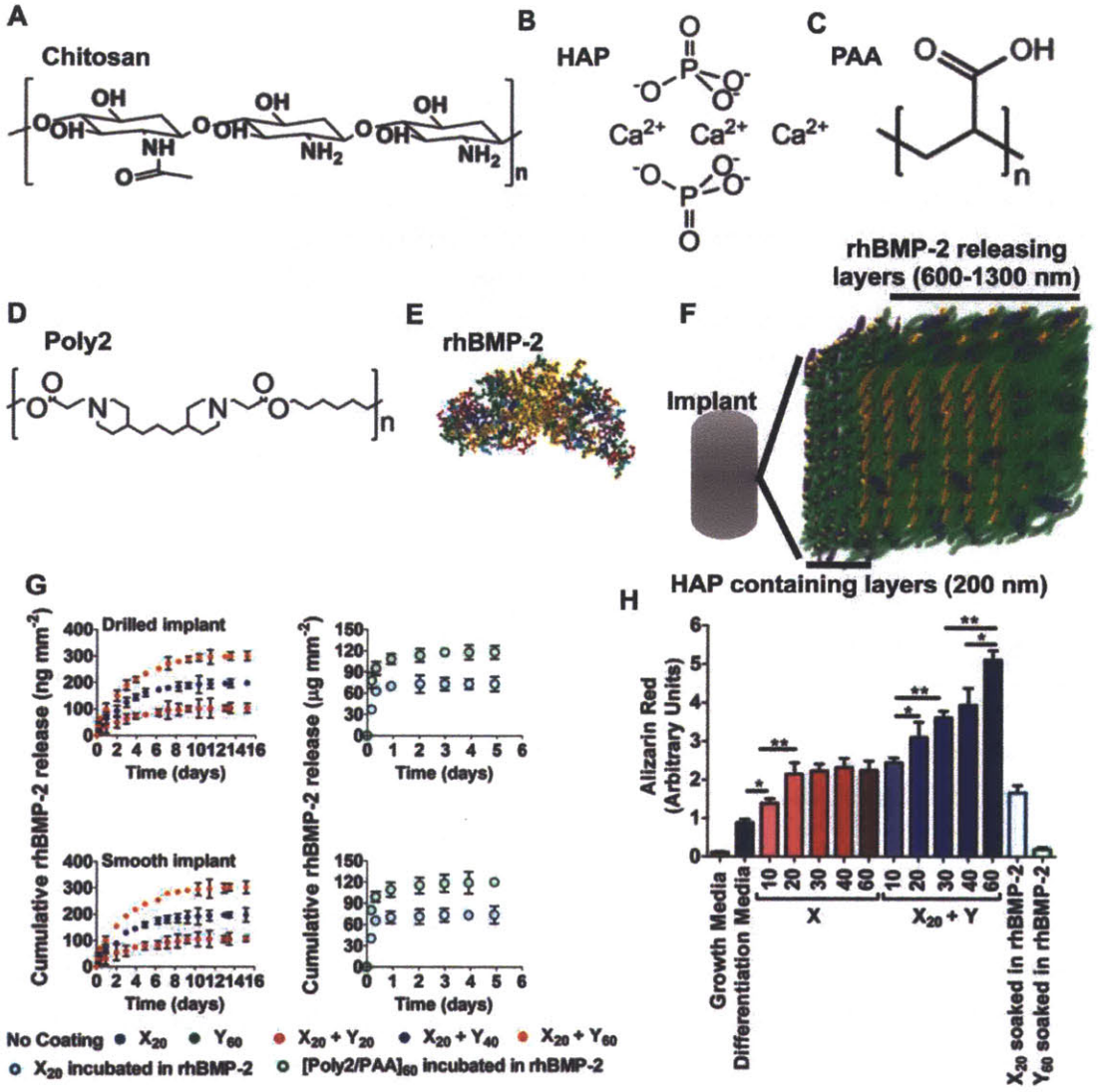

Figure 3.1. Structured coatings for bone regeneration are made up of two composite multilayers. (**A** to **C**) The base coating contains chitosan (Chi; 75-85% deacytelated chitin, M_v ~ 100 kDa) and hydroxyapatite [HAP; $Ca_{10}(PO_4)_6(OH)_2$] with poly(acrylic acid) (PAA; M_v ~450 kDa) in a bilayer repeat unit. (**D** and **E**) The osteogenic factor coating contains a hydrolytically degradable poly(β-amino ester) (Poly2, M_v ~ 11 kDa) and rhBMP-2 that are alternated with PAA on top of the osteoconductive base coating. **(F)** Schematic of the two sets of multilayers: osteoconductive and osteoinductive. (**G**) Cumulative release profile of rhBMP-2 from drilled implants. Data are means ± SEM (n = 9 per coating). (**H**) rhBMP-2 loading has a dose-dependent effect on calcium deposition, quantified by alizarin red at 14 days. Data are means ± SEM (n = 6-9). * $P < 0.05$** $P < 0.01$, ANOVA with a Tukey post hoc test.

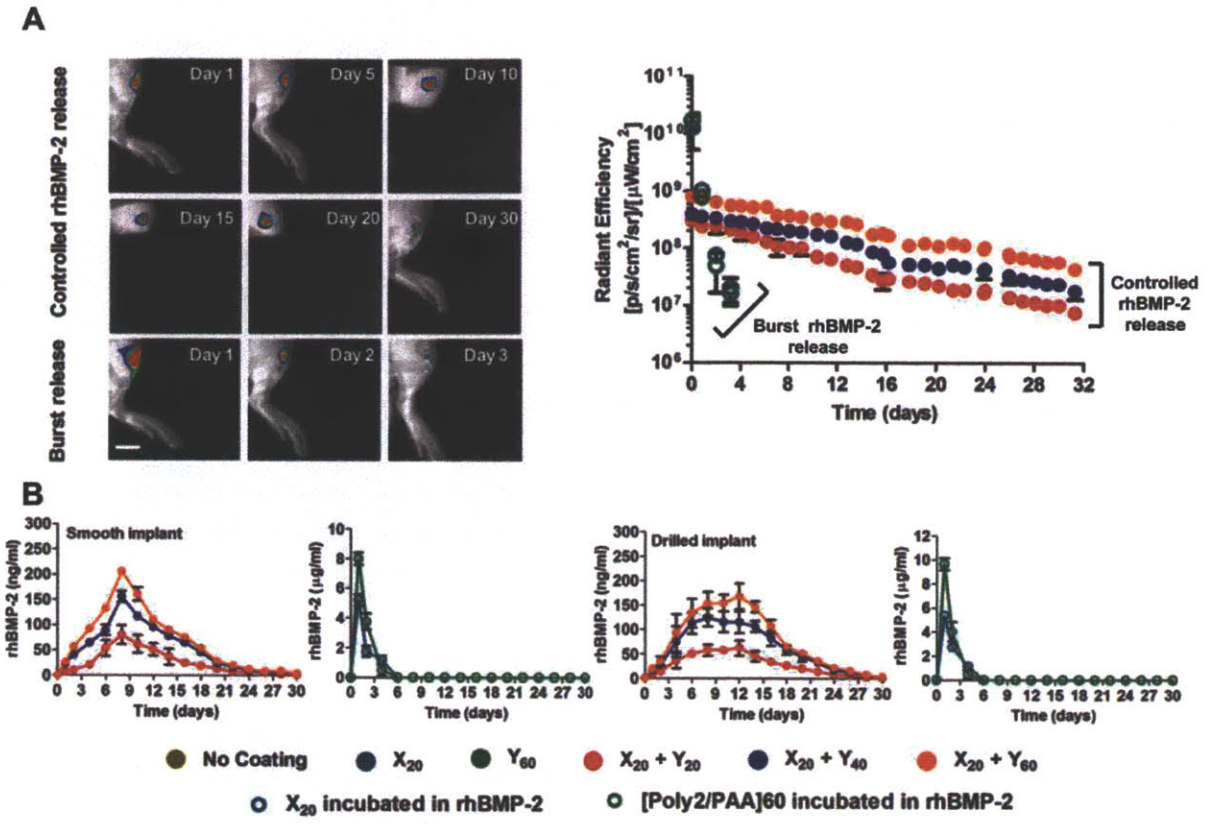

Figure 3.2. In vivo evaluation of rhBMP-2 release. rhBMP-2 was loaded into the multilayers that coated smooth and drilled PEEK rods and then implanted in the tibias of rats (n = 41-45 per group). (**A**) Controlled and burst release of fluorescently labeled rhBMP-2 was tracked in vivo over 30 and 3 days respectively. (**B**) Radiant efficiency at the implant site over time (n = 4-6 per group). (**C**) Bone marrow flushed out of excised tibiae was assayed for rhBMP-2 using ELISA for smooth and drilled implants. Data are means ± SEM (n = 5-6 per group).

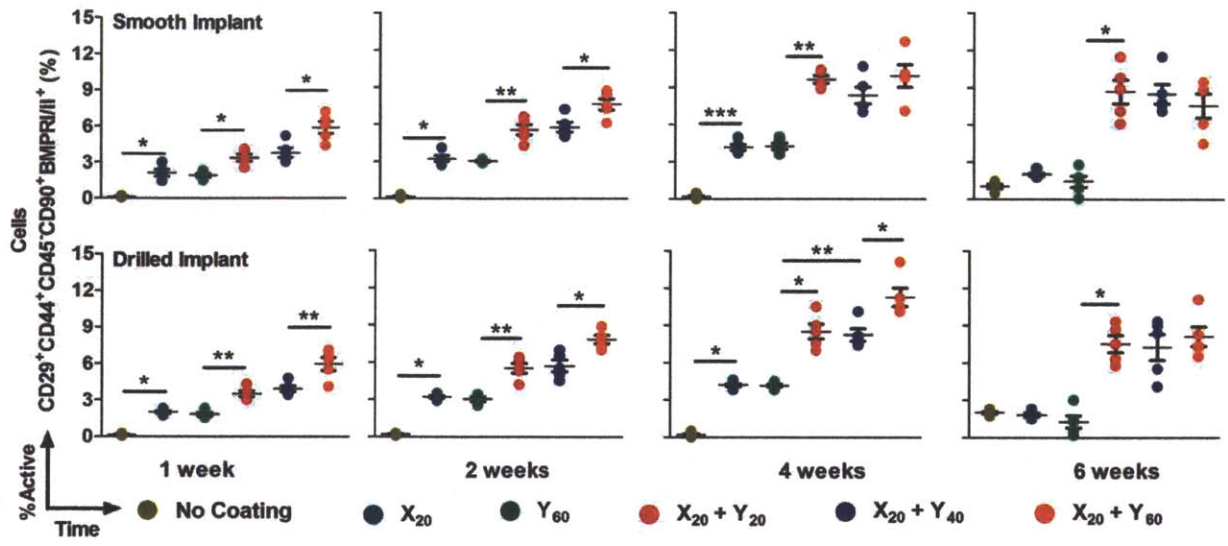

Figure 3.3. Mesenchymal stem cells differentiate into osteoblasts. Five color flow cytometry was used to assess the percentage of osteoblasts in cells isolated from the tibia marrow around smooth and drilled implants. Each point represents individual implants. Means ± SEM (n = 5 per group). *P < 0.05, **P < 0.01, ANOVA with a Tukey post hoc test. FACS plots are provided in appendix B; fig. B4.

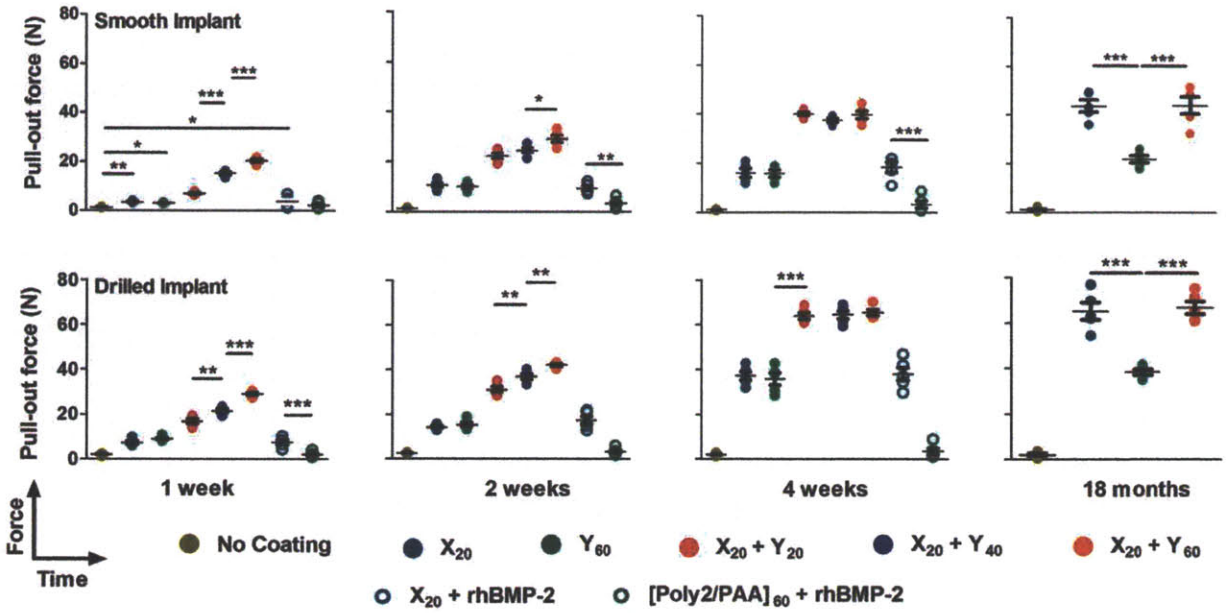

Figure 3.4. Tensile force testing of implants from the rat tibia. Force data from individual implants are presented from smooth and drilled implants. Data are means ± SEM (n = 5 implants per group time point). *p < 0.05; **p < 0.01; ***p < 0.001, ANOVA with a Tukey post hoc test. Interfacial tensile strength data are provided (Appendix B; table B1 and B2).

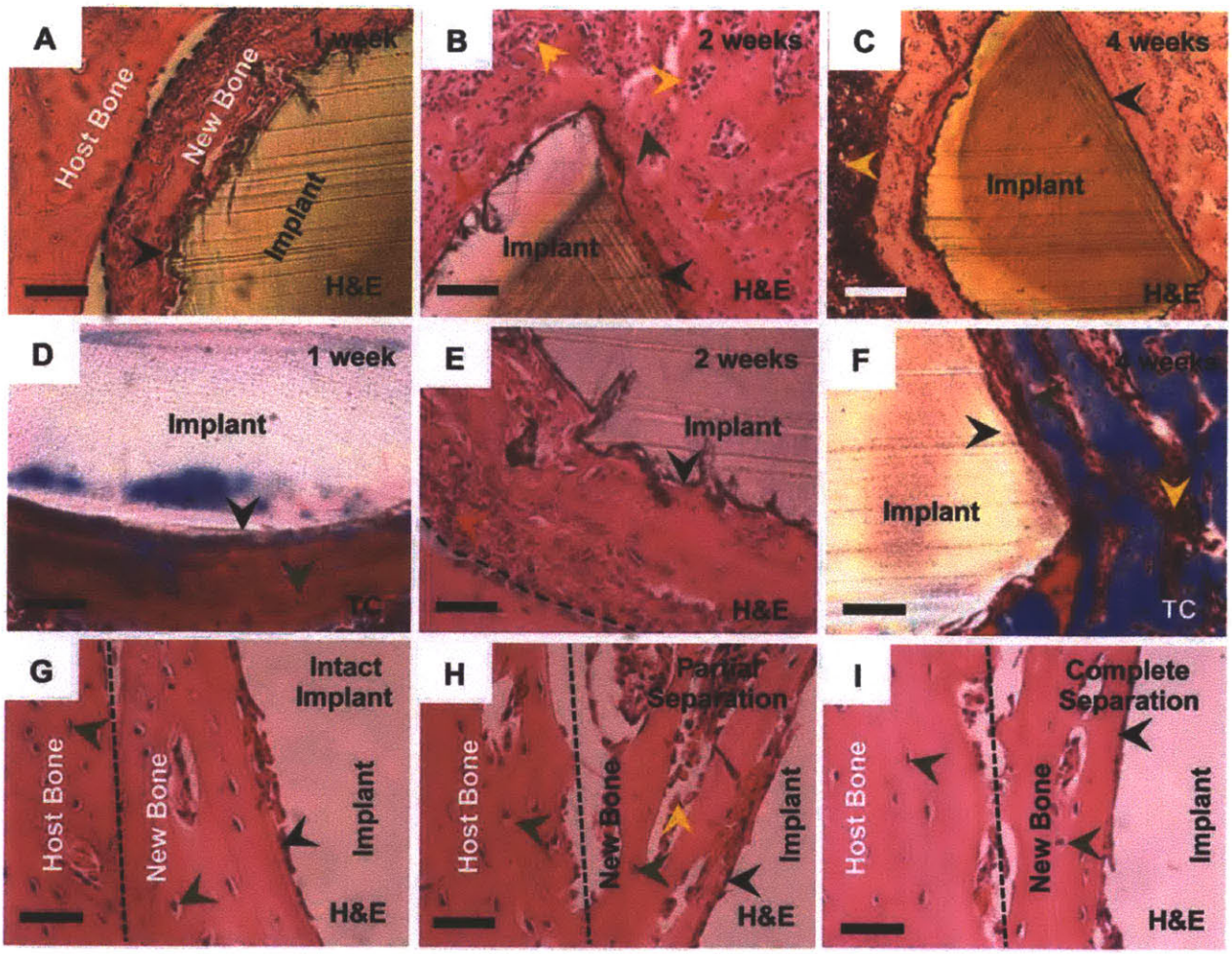

Figure 3.5. Histology of implants with various coating formulations demonstrating bone tissue morphogenesis at the implant interface. (**A** to **F**) Implants coated with X_{20} + Y_{60} at 1, 2 and 4 weeks post-implantation demonstrating the process of implant integration with the parent bone tissue. Cement lines (broken black line) are observed on some sections. (**G**) The plane of fracture in implants with the X_{20} + Y_{60} coating is indicated by a broken black line at 4 weeks which depict an intact implant, partial separation from the host bone and complete separation from the host bone. The new bone-implant interface is intact. Sections were viewed under bright field microscopy. Scale bars: (A and C) are 200 μm; (B) and (D to G) are 50 μm. Arrows: black, bone/implant interface; red, active osteoblasts; dark green, osteocytes; yellow, marrow cells. H&E: hematoxylin & eosin stain, TC: Masson's trichrome stain.

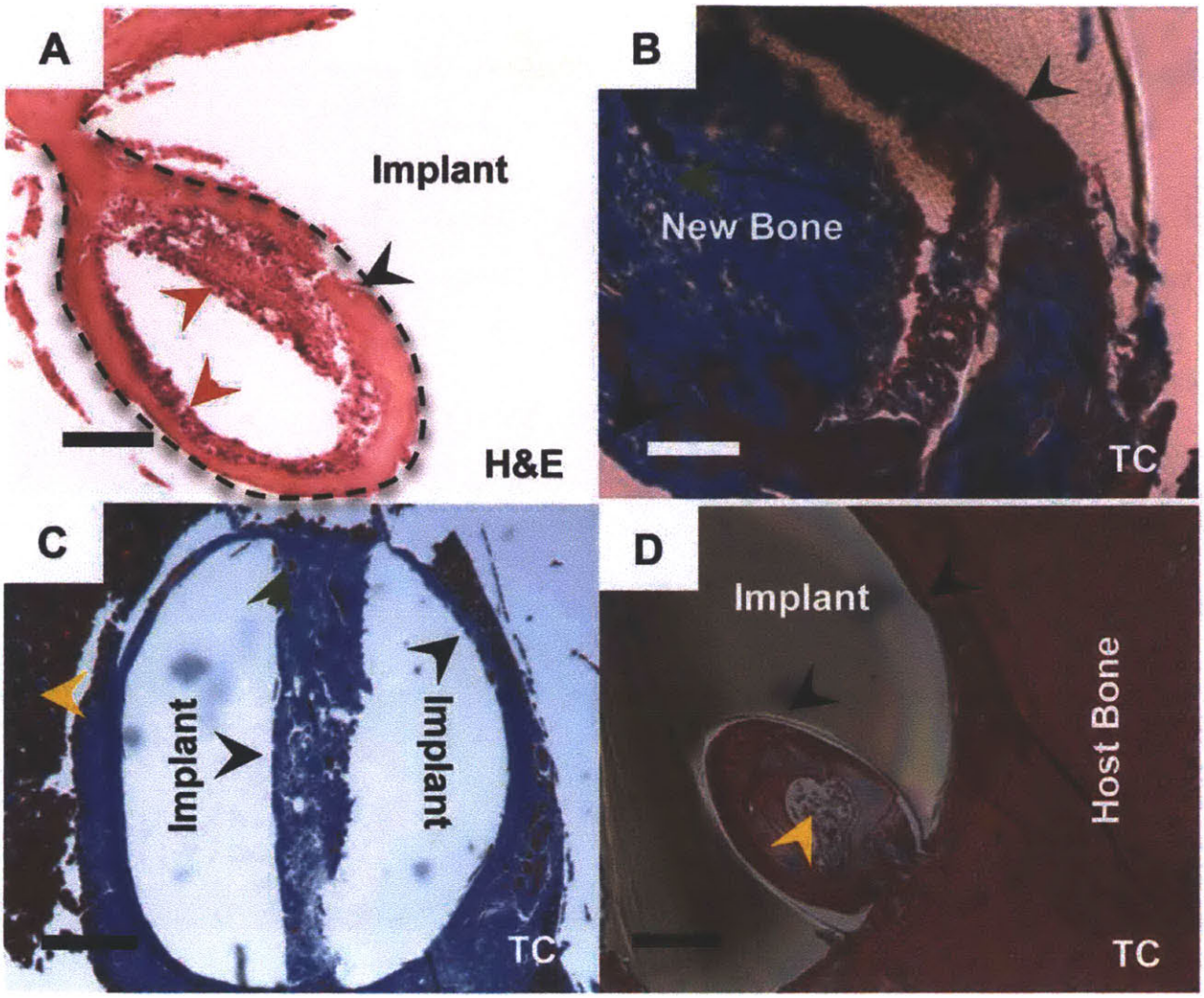

Figure 3.6. Bone deposition in the channels of drilled implants. Representative sections (*n* = 5-6 per group) of drilled implants after 4 weeks, which were coated with X_{20} + Y_{60}. (**A**) Granulation tissue (broken black line) penetrated the channel and supplied progenitor cells. (**B**) Newly deposited bone (blue) matures (red) and (**C**) gradually filled up the channel at 4 weeks. (**D**) Bone (blue and red) is present throughout the channel of a drilled implant. Sections were viewed under brightfield microscopy. Scale bars in (A, B and D) are 100μm and in (C) is 400 μm. Arrows: black, bone/implant interface; red, active osteoblasts; dark green, osteocytes; yellow, marrow cells. H&E: hematoxylin & eosin stain, TC: Masson's trichrome stain.

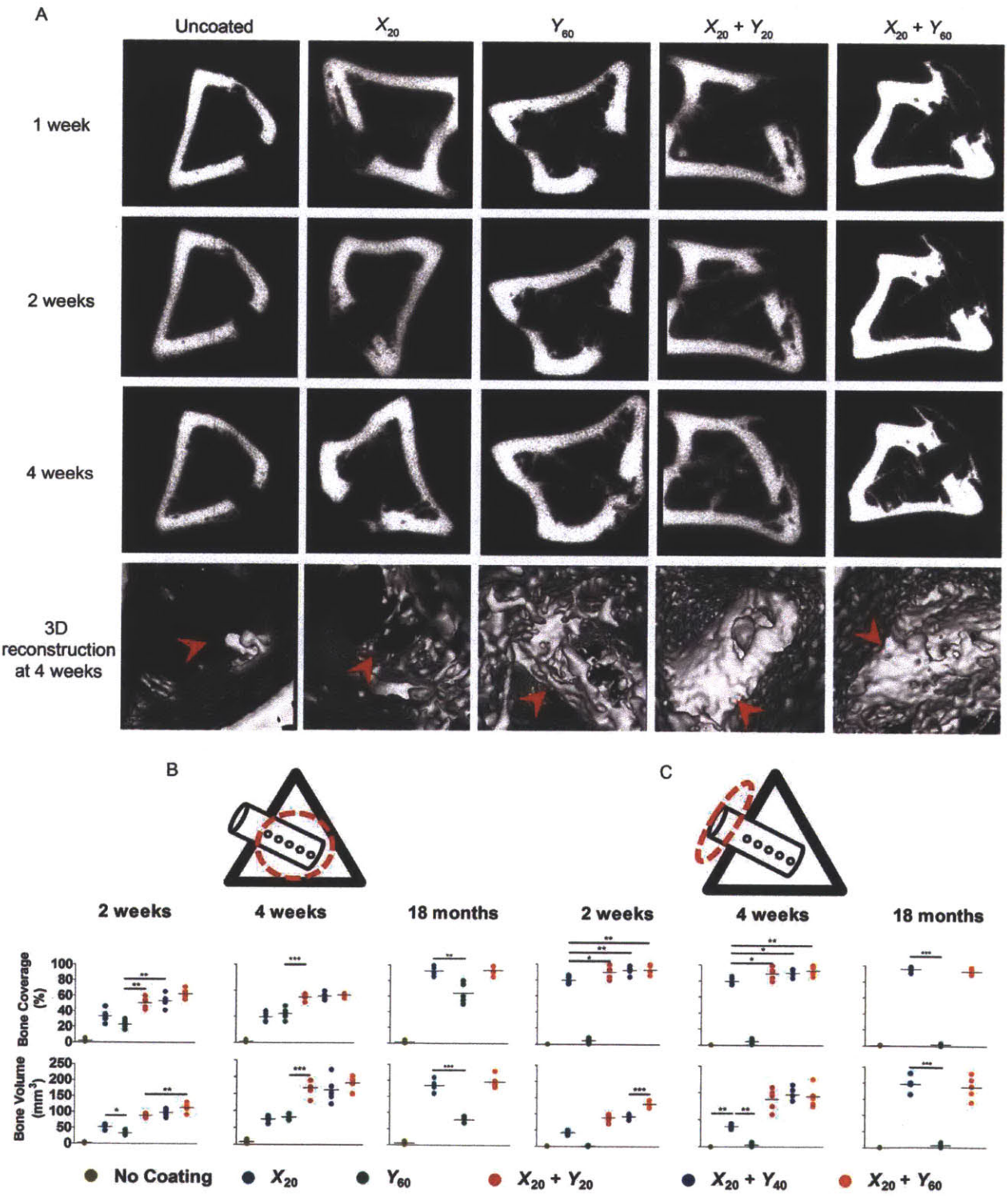

Figure 3.7. µCT imaging of bone formation on drilled PEEK implants. (**A**) Radiographs of bone formation around drilled implants with different coatings at 1, 2, and 4 weeks. Red arrows indicate location of the implant. (**B** and **C**) The images in (A) were used to quantify bone

regeneration at 2 and at 4 weeks within (B) and outside the medullary canal (C) (using regions of interest marked by dotted red circles). Each point represents individual implants. Data are means ± SEM (*n* = 5-6 per group). *p < 0.05, **p < 0.01, ANOVA with Tukey post hoc test. Data for smooth implants are provided in appendix B; fig. B11.

3.5 References

1. G. Labek, M. Thaler, W. Janda, M. Agreiter, B. Stöckl, Revision rates after total joint replacement: cumulative results from worldwide joint register datasets. *J. Bone. Joint. Surg. Br.* **93**, 293-297 (2011).

2. S. D. Ulrich, T. M. Seyler, D. Bennett, R. E. Delanois, K. J. Saleh, I. Thongtrangan, M. Kuskowski, E. Y. Cheng, P. F. Sharkey, J. Parvizi, Total hip arthroplasties: What are the reasons for revision? *Int. Orthop.* **32**, 597-604 (2008).

3. G. Lewis, Alternative acrylic bone cement formulations for cemented arthroplasties: Present status, key issues, and future prospects. *J. Biomed. Mater. Res. Part B Appl. Biomater.* **84**, 301-319 (2007).

4. R. A. Berger, J. H. Lyon, J. J. Jacobs, R. M. Barden, E. M. Berkson, M. B. Sheinkop, A. G. Rosenberg, J. O. Galante, Problems with cementless total knee arthroplasty at 11 years followup. *Clin. Orthop. Relat. Res.* **392**, 196-207 (2001).

5. L. Sun, C. C. Berndt, K. A. Gross, A. Kucuk, Material fundamentals and clinical performance of plasma-sprayed hydroxyapatite coatings: a review. *J. Biomed. Mater. Res. A* **58**, 570-592 (2001).

6. X. Zheng, M. Huang, C. Ding, Bond strength of plasma-sprayed hydroxyapatite/Ti composite coatings. *Biomaterials* **21**, 841-849 (2000).

7. L. Meirelles, A. Arvidsson, M. Andersson, P. Kjellin, T. Albrektsson, A. Wennerberg, Nano hydroxyapatite structures influence early bone formation. *J. Biomed. Mater. Res. A* **87**, 299-307 (2008).

8. D. A. Puleo, A. Nanci, Understanding and controlling the bone-implant interface. *Biomaterials* **20**, 2311-2321 (1999).

9. M. M. Martino, F. Tortelli, M. Mochizuki, S. Traub, D. Ben-David, G. A. Kuhn, R. Muller, E. Livne, S. A. Eming, J. A. Hubbell, Engineering the growth factor

microenvironment with fibronectin domains to promote wound and bone tissue healing. *Sci. Transl. Med.* **3**, 100ra89 (2011).

10. M. Nakashima, A. H. Reddi, The application of bone morphogenetic proteins to dental tissue engineering. *Nat. Biotechnol.* **21**, 1025-1032 (2003).

11. E. T. Pashuck, M. M. Stevens, Designing Regenerative Biomaterial Therapies for the Clinic. *Sci. Transl. Med.* **4**, 160sr4 (2012).

12. E. J. Carragee, E. L. Hurwitz, B. K. Weiner, A critical review of recombinant human bone morphogenetic protein-2 trials in spinal surgery: emerging safety concerns and lessons learned. *Spine J.* **11**, 471-491 (2011).

13. G. Decher, Fuzzy Nanoassemblies: Toward Layered Polymeric Multicomposites. *Science* **277**, 1232-1237 (1997).

14. T. Boudou, T. Crouzier, K. Ren, G. Blin, C. Picart, Multiple functionalities of polyelectrolyte multilayer films: new biomedical applications. *Adv. Mater.* **22**, 441-467 (2010).

15. G. Decher, J.B. Schlenoff, Multilayer Thin Films: Sequential Assembly of Nanocomposite Materials (New York: Wiley) Second Edition (2012).

16. N. J. Shah, J. Hong, M. N. Hyder, P. T. Hammond, Osteophilic multilayer coatings for accelerated bone tissue growth. *Adv. Mater.* **24**, 1445-1450 (2012).

17. H. Petite, V. Viateau, W. Bensaid, A. Meunier, C. de Pollak, M. Bourguignon, K. Oudina, L. Sedel, G. Guillemin, Tissue-engineered bone regeneration. *Nat. Biotechnol.* **18**, 959-963 (2000).

18. L. Hong, H. C. Xu, K. de Groot, Tensile strength of the interface between hydroxyapatite and bone. *J. Biomed. Mater. Res.* **26**, 7-18 (1992).

19. R. Skripitz, P. Aspenberg, Attachment of PMMA cement to bone: force measurements in rats. *Biomaterials* **20**, 351-356 (1999).

20. C. Lavernia, D. J. Lee, V. H. Hernandez, The increasing financial burden of knee revision surgery in the United States. *Clin. Orthop. Relat. Res.* **446**, 221-226 (2006).

21. A. Di Martino, M. Sittinger, M. V. Risbud, Chitosan: a versatile biopolymer for orthopaedic tissue-engineering. *Biomaterials* **26**, 5983-5990 (2005).

22. D. Ren, H. Yi, W. Wang, X. Ma, The enzymatic degradation and swelling properties of chitosan matrices with different degrees of N-acetylation. *Carbohydr. Res.* **340**, 2403-2410 (2005).

23. Z. Tang, Y. Wang, P. Podsiadlo, N. A. Kotov, Biomedical Applications of Layer-by-Layer Assembly: From Biomimetics to Tissue Engineering. *Adv. Mater.* **18**, 3203-3224 (2006).

24. P. K. Zysset, X. E. Guo, C. E. Hoffler, K. E. Moore, S. A. Goldstein, Elastic modulus and hardness of cortical and trabecular bone lamellae measured by nanoindentation in the human femur. *J. Biomech.* **32**, 1005-1012 (1999).

25. D. M. Lynn, R. Langer, Degradable poly(beta-amino esters): Synthesis, characterization, and self-assembly with plasmid DNA. *J. Am. Chem. Soc.* **122**, 10761-10768 (2000).

26. A. Shukla, K. E. Fleming, H. F. Chuang, T. M. Chau, C. R. Loose, G. N. Stephanopoulos, P. T. Hammond, Controlling the release of peptide antimicrobial agents from surfaces. *Biomaterials* **31**, 2348-2357 (2010).

27. N. J. Shah, M. L. Macdonald, Y. M. Beben, R. F. Padera, R. E. Samuel, P. T. Hammond, Tunable dual growth factor delivery from polyelectrolyte multilayer films, *Biomaterials* **32**, 6183-6193 (2011)

28. T. Crouzier, F. Sailhan, P. Becquart, R. Guillot, D. Logeart-Avramoglou, C. Picart, The performance of BMP-2 loaded TCP/HAP porous ceramics with a polyelectrolyte multilayer film coating. *Biomaterials* **32**, 7543-7554 (2011).

29. S. Facca, C. Cortez, C. Mendoza-Palomares, N. Messadeq, A. Dierich, A. P. Johnston, D. Mainard, J. C. Voegel, F. Caruso, N. Benkirane-Jessel, Active multilayered capsules for in vivo bone formation. *Proc. Natl. Acad. Sci. U.S.A.* **107**, 3406-3411 (2010).

30. H. Seeherman, J. M. Wozney, Delivery of bone morphogenetic proteins for orthopedic tissue regeneration. *Cytokine Growth Factor Rev.* **16**, 329-345 (2005).

31. X. Dong, Q. Wang, T. Wu, H. Pan, Understanding adsorption-desorption dynamics of BMP-2 on hydroxyapatite (001) surface. *Biophys. J.* **93**, 750-759 (2007)

32. A. Sachs, A. Wagner, M. Keller, O. Wagner, W. D. Wetzel, F. Layher, R. A. Venbrocks, P. Hortschansky, M. Pietraszczyk, B. Wiederanders, H. J. Hempel, J. Bossert, J. Horn, K. Schmuck, J. Mollenhauer, Osteointegration of hydroxyapatite-titanium implants coated with nonglycosylated recombinant human bone morphogenetic protein-2 (BMP-2) in aged sheep. *Bone* **37**, 699-710 (2005).

33. M. C. Peters, P. J. Polverini, D. J. Mooney, Engineering vascular networks in porous polymer matrices. *J. Biomed. Mater. Res.* **60**, 668-678 (2002).

34. J. C. Reichert, A. Cipitria, D. R. Epari, S. Saifzadeh, P. Krishnakanth, A. Berner, M. A. Woodruff, H. Schell, M. Mehta, M. A. Schuetz, G. N. Duda, D. W. Hutmacher, A Tissue Engineering Solution for Segmental Defect Regeneration in Load-Bearing Long Bones. *Sci. Transl. Med.* **4**, 141ra93 (2012).

35. U. M. Wikesjö, A. V. Xiropaidis, M. Qahash, W. H. Lim, R. G. Sorensen, M. D. Rohrer, J. M. Wozney, J. Hall, Bone formation at recombinant human bone morphogenetic protein-2-coated titanium implants in the posterior mandible (Type II bone) in dogs. *J. Clin. Periodontol.* **35**, 985-991 (2008).

36. K. C. Krogman, J. L. Lowery, N. S. Zacharia, G. C. Rutledge, P. T. Hammond, Spraying asymmetry into functional membranes layer-by-layer. *Nat. Mater.* **8**, 512 (Apr, 2009).

37. W. C. Oliver, G. M. Pharr, Measurement of hardness and elastic modulus by instrumented indentation: Advances in understanding and refinements to methodology. *J. Mater. Res.* **19**, 3-20 (2004).

38. C. A. Gregory, W. G. Gunn, A. Peister, D. J. Prockop, An Alizarin red-based assay of mineralization by adherent cells in culture: comparison with cetylpyridinium chloride extraction. *Anal. Biochem.* **329**, 77-84 (2004).

Chapter 4

Tunable dual growth factor delivery from polyelectrolyte multilayer films

4.1 Introduction

Aseptic loosening accounts for about 12% of all hip and knee prosthetic failures[1], almost entirely because of the failure of fixation[2] . In order to engineer a successful implant, it is necessary to address the bone as a highly vascularized tissue where a multistep process involving migration, proliferation, differentiation, and activation of several cell types is necessary for integrating the implant with the bone tissue[3]. Several growth factors have been implicated in this process[4], and bone morphogenetic proteins (BMP) have been shown to be some of the most potent bone tissue-forming proteins known amongst the growth factors investigated for bone tissue growth, and are the only growth factors capable of directly inducing de novo bone formation[5]. Recombinant human BMP-2 (rhBMP-2) is an osteogenic growth factor used extensively in both ectopic and orthotopic sites for bone generation; it has been demonstrated in various animal models for healing fracture sites and femur defects, such as in rats[6, 7], rabbits[8] and sheep[9], and is an approved product for use on humans in lumbar spine fusion [10] . The benefits of release of growth factors such as rhBMP-2 include rapid healing of tissue around the implant[11] and more complete bone remodeling over shorter time periods[12]. Recombinant human vascular endothelial growth factor (rhVEGF) is an angiogenic factor critical for both intramembranous and endochondral bone formation[3]. Angiogenesis is required for most tissues to develop and is a critical component of virtually all tissue-engineering strategies and the growth process and restructuring of bone tissue is greatly enhanced by increased vascularization[13] and the introduction of rhVEGF has been shown to enhance bone formation[14] through the development of the localized vascular system and increased blood flow. rhVEGF has been shown to act synergistically with rhBMP-2 to increase the growth of bone tissue[15]. Localized introduction of such growth factors has been demonstrated to greatly enhance bone tissue regeneration[16, 17]. Hence there is a therapeutic advantage to introducing growth

factors from the surface of implants during the healing process.

The delivery of growth factors in vivo presents many complex challenges[18]. Growth factors, specifically rhBMP-2 and rhVEGF have been delivered therapeutically for bone regeneration applications using a variety of methods, including bolus injection[19], biodegradable polymers and hydrogels[7, 20, 21] with mixed results[22]. In cases where beneficial effects were observed, large doses of the growth factors were required (from 12 µg up to 60 mg of growth factor per gram of carrier). This raises concerns regarding the safety, cost and effective delivery of these supraphysiological amounts of recombinant proteins. Control over the amount of growth factor delivered is critical in bone tissue healing applications, where an excess of rhBMP-2 may lead to undesirable incidences of hematoma, ectopic bone formation and osteoclast activation with transiently elevated bone resorption[23]. From a delivery perspective, traditional polymer formulation techniques also have the potential to denature the protein molecules at high temperature, by exposure to unfavorable solvents or through the development of a low pH environment[24]. In addition, these systems are not easily coated onto complex geometries of implants in a conformal manner. Direct injection of growth factor to a fracture site would lead to the immediate breakdown and resorption of the protein before it could begin to exhibit desired results as the growth factor must be sustained at a minimal dose level over prolonged time periods of several weeks to be effective[25]. The ratio and timing of rhBMP-2 and rhVEGF delivered may be critical to applications involving bone tissue integration[3]; beneficial effects have been observed when rhVEGF is present in quantities of half or less than rhBMP during the first few days or weeks[26], i.e. the consolidation phase, and may even be introduced prior to the introduction of rhBMP-2[27]. rhVEGF dosage must be tightly controlled, as excess amounts of rhVEGF from extended release can actually inhibit osteogenesis, cause severe vascular leakage and hypotension[28].

Towards addressing a lack of delivery systems where tunable control is necessary for the delivery of these potent growth factors[29], our primary goal was to develop a thin hydrolytically degradable coating that would incorporate controlled amounts of both rhVEGF and rhBMP-2, releasing them over varying periods of time with a corresponding dose dependent effect on endothelial and preosteoblast cells respectively. A suitable

delivery platform would exhibit a quick release of rhVEGF and a more sustained release of rhBMP-2. Polyelectrolyte multilayer films fabricated using the layer-by-layer (LbL) assembly[30], in which a charged substrate was alternately dipped in positively and negatively charged polymer baths to build nanolayered thin films has been explored as a means to successfully release various drugs and small molecules from surfaces as well as developing LbL coatings for tissue regeneration by our group[31-35] as well as others[36-41]. The LbL assembly method is unique in its ability to sequester desired concentrations of biologic drugs for controlled local delivery using room temperature and mild aqueous conditions that preserve fragile protein activity. Orthopedic implant surfaces are a compelling application as the polyelectrolyte multilayer approach can have direct and immediate benefit in this area due to the need for sequential and controlled delivery of several therapeutic systems. Introduction of more than one growth factor in vivo would initiate the different cellular cascade necessary for robust implant integration using a powerful LbL approach to generate blends of dual growth factors that can yield idealized release behavior.

4.2 Materials and Methods

4.2.1. Materials

Poly (β-aminoester) 2, hereafter called Poly2, was synthesized as previously described[42]. Poly(acrylic acid)(PAA, 306215, M_v = 1.25MDa), 3M concentrated sodium acetate buffer (S7899, pH 5.2) and penicillin/ streptomycin solution were purchased from Sigma Aldrich (St.Louis, MO). Recombinant human BMP-2 (rhBMP-2, 4577) and recombinant human vascular endothelial growth factor C (rhVEGF-C, 165 amino acids excluding His tags at the end, 4633) was obtained from Biovision Inc. (South San Francisco, CA). rhBMP-2 ELISA kits were obtained from Peprotech Inc. (Rocky Hill, NJ). 10x Phosphate buffer Saline (PBS) was obtained from Invitrogen (Carlsbad, CA). Chondroitin sulfate sodium salt (M_n = 60000) was obtained from VWR Scientific (Edison NJ).

4.2.2. Preparation of polyelectrolyte solutions

Poly2 dipping solutions were 2 mg/mL in 25 mM sodium acetate buffer. Dipping solutions containing PAA and chondroitin sulfate were prepared at 2 mg/mL in 100mM sodium acetate buffer and pH-adjusted to 5.0 with 1.0 M sodium hydroxide solution. rhBMP-2 and $rhVEGF_{165}$ dipping solutions were 40 µg/ml in 100 mM sodium acetate buffer. Poly2, PAA and chondroitin sulfate dipping solutions were replaced every 24 hours. rhBMP-2 and $rhVEGF_{165}$ dipping solutions were replenished every 24 hours by adding 40 µg/mL of growth factor to their respective pre-existing solutions. All solutions were prepared with water from a Milli-Q Plus unit (Bedford, MA) at 18.2 MΩ.

4.2.3. Polyelectrolyte multilayer film construction

Integra-ls® (Plainsboro, NJ) macroporous polycaprolactone/β-tricalcium phosphate (50wt% PCL/50wt% β-TCP) waffle cylinder scaffold, with diameter = 10mm and height = 2.5mm were cut in half using a razor blade and plasma etched with room air using a Harrick PDC-32G plasma cleaner on high RF power for 1 min and immediately immersed in Poly2 solution. First, rhBMP-2 nanolayered films were fabricated on this scaffold with a Carl Zeiss HMS programmable slide stainer with the following dipping protocol: 5 min in Poly2 solution, 3 washes (10, 20, 30 s), 5 min in PAA solution, 3 washes (10, 20, 30 s), 10 min in rhBMP-2 solution, 1 wash (10 s) and 5 min in PAA solution with 3 washes (10, 20, 30 s). This cycle was repeated to achieve 40, 80, 100 and 120 tetralayer films. Dipped scaffolds were allowed to dry for 48 hours at 4°C. Next, $rhVEGF_{165}$ nanolayered films were then fabricated on the scaffolds using the same dipping protocol to achieve 20, 30, 40, 50 and 80 tetralayer films with the rhBMP-2 dipping solution swapped for the rhVEGF165 dipping solution and the PAA replaced with chondroitin sulfate. Concurrently, controls with single growth factor films were also fabricated. The final product was stored at 4°C until released or implanted.

4.2.4. Release characterization

Growth factor coated film coated scaffolds were released at 37°C into 1 mL of 1x PBS in 1.7 ml centrifuge tubes (VWR Scientific, Edison, NJ). At a series of pre-determined time points, scaffolds were transferred into new centrifuge tubes containing fresh 1ml 1x

PBS. The previous centrifuge tubes along with the 1x PBS, were frozen down and stored at -20°C. Samples were analyzed using ELISA development kits according to manufacturer instructions. Release samples from consecutive time points were then combined and used in cellular assays (see below).

4.2.5. Cell culture

To test the efficacy of the growth factors released from the LbL films, a number of in vitro tests were performed to quantify and visualize the effect of growth factor on a cell line with a physiological response to the growth factor. rhBMP-2 initiates the differentiation of pre-osteoblast cell line MC3T3-E1 into bone. $rhVEGF_{165}$ induces proliferation and migration in HUVEC's). Each condition was repeat 3 times in triplicate (n = 3).

4.2.5.1 rhBMP-2 activity assays using MC3T3-E1 pre-osteoblast cell line

MC3T3-E1 Subclone 4 cells were grown in α-MEM, supplemented with 10% FBS, and 1% of antibiotic and anti mycotic solution (containing penicillin, streptomycin and amphotericin B) in a humidified incubator (37°C; 5% CO2 in air). Culture medium was replenished every 2-3 days and cells were sub cultured when near 100% confluence with the use of 0.05% trypsin-EDTA. All cells used in these studies were less than passage number 12. MC3T3-E1 cells were seeded at 10,000 cells/well and allowed to grow to confluency in 24 well plates (visualization and quantification) in 0.5 ml of growth medium. Cells were cultured under different experimental conditions: (1) growth medium, (2) differentiation medium (growth medium supplemented with 50 mg/ml L-ascorbic acid and 10 mM b-glycerol phosphate), (3) differentiation medium supplemented with PEM released solution containing rhBMP-2 and $rhVEGF_{165}$. Release samples from consecutive days were combined and the cell culture media was changed every two days until analysis for alkaline phosphatase or alizarin red as described below.

4.2.5.1.1. Alkaline phosphatase activity assay

Alkaline phosphatase (ALP) activity was determined on day 5 after the initiation of MC3T3-E1 osteogenic differentation by quantitation of the enzyme activity. Cells were rinsed 2x with PBS without Ca^{2+} and Mg^{2+} and fixed in 8% paraformaldehyde for 10 min at room temperature. 0.1% triton in PBS was added to the fixed cells and then frozen at 80oC for one freeze-thaw cycle. Cell lysates were transferred to an eppendorf tube, centrifuged at 15,000g for 3 min at 4°C, and the supernatant was collected. 50 µL of lysate was incubated with 150 µL of pNPP solution for 30 min at 37°C. The reaction was terminated with 0.1 M NaOH and ALP activity read on a plate reader at 405 nm. The ALP activity measurements were normalized to total protein determined by BCA assay.

4.2.5.1.2. Alizarin red S differentiation assays

After 14 days of exposure to different formulations of the release medium, MC3T3-E1 cells were assayed for calcium deposition using Alizarin red S (ARS). Cells were washed with PBS and fixed with 4% paraformaldehyde for 10 min. After three rinses of 5 min in distilled water, ARS stain solution (2% ARS in distilled water pH balanced to 4.1 with 10% ammonium hydroxide) was incubated with cells for 20 min at room temperature. Cells were then washed in distilled water 4 times for 5 min each. The ARS stained cultures were imaged with phase contrast microscopy. The ARS stain was quantified using a previously published protocol [43]. The ARS stained cultures were incubated in 10% acetic acid for 30 min at room temperature and then the cell layers were disrupted by the use a pipette tip. The cell suspensions were transferred to a microcentrifuge tube, vortexed for 30 s, paraffin wrapped and heated at 85°C for 10 min. After transferring to ice for 5 min, the tubes were centrifuged at 16,000g for 15 min and pH balanced with 10% ammonium hydroxide to pH 4.1 - 4.5. Triplicates with growth and differentiation medium controls were read on a 96-well plate with black sides and a clear bottom at 405 nm.

4.2.5.2 $rhVEGF_{165}$ activity assays using Human Umbilical Vein Endothelial Cells (HUVEC) cell line

Release media was pooled and diluted 1:1 with HUVEC media (without rhVEGF). The normalized $rhVEGF_{165}$ dose per milligram of scaffold was calculated, aliquoted and

topped up with HUVEC media (without VEGF) for a total volume of 300 µL per well for proliferation assays and 2.5ml per well for migration assays.

4.2.5.2.1. HUVEC proliferation assay

1000 HUVEC's were suspended in 300 µL of growth media and dispensed in each well of a 96 well plate (quantification) in 0.3 ml of growth medium. Cells were allowed to establish for 24 hours. HUVEC growth media was carefully removed using a pipettor without disturbing the cell layer. The combination of release and HUVEC media, was then added to the wells. Cells were allowed to proliferate for 48 hours and labeled with 10 µM bromodeoxyuridine (BrdU) kit for another 2 hours. Incorporation of BrdU into DNA was detected using an anti-BrdU peroxidase-conjugated antibody and a soluble peroxidase substrate (3,3'-5,5'-tetramethylbenzidine). The absorbance was measured at 450 nm with a 595 nm reference wavelength according to the protocol for BrdU Proliferation Assay, (Roche Diagnostics, Mannheim, Germany).

4.2.5.2.2. HUVEC migration assay

Confluent HUVEC monolayers in 24 well plates (Corning/Costar, Cambridge, MA) were "scratch" wounded using the tip of a universal blue pipette tip and rinsed with PBS. The HUVEC/Release media cocktail from different experimental conditions was pipetted into the plate. Cells were imaged under phase contrast microscope (Axiovert® 200 inverted microscope, Carl Zeiss, NY) immediately after adding media. HUVEC media with lacking rhVEGF was used as the control. Cells were incubated for 8 hours and the distance migrated by the cells. Cells were labeled with 1.5 µm Calcein AM Fluorescent Dye (354217, BD Biosciences, CA) for 30 min. The media and dye were aspirated and washed thrice with 1x PBS. Cells were then fixed with 8% paraformaldehyde and imaged under fluorescence (485 nm excitation 530 nm emission) at 20x magnification. The size of the scratch before and after 8 hours was measured using Axiovision® 4.5 software and the difference computed as the distance migrated by the cells.

4.2.5.3 In vivo evaluation of LbL films

All animal work was performed in accordance with protocols approved by the Committee on Animal Care at the Massachusetts Institute of Technology. A set of eight 100 tetralayer rhBMP-2 films (corresponding to a 6μg total scaffold load), eight 100 tetralayer rhBMP-2 films with an 80 tetralayer rhVEGF165 film on top (corresponding to a 6μg rhBMP-2 and 4μg rhVEGF165 total scaffold load) and eight 100 tetralayer Poly2/PAA bilayer films were built as implants. Sixteen 350-400 g male Sprague Dawley rats were given preoperative analgesics (1 mg/kg meloxicam and 0.05 mg/kg buprenex), and intraoperative anesthesia via 1-3% isofurane in oxygen. The right hind limb of each animal was shaved, cleaned with alcohol and povidone iodine solutions, and sterile drapes were placed around the surgical area. A 2 cm longitudinal incision, centered at the midshaft of the femur, was made laterally along the hind limb. A pocket made in the quadriceps muscle mass by blunt dissection anterior to the iliotibial band. LbL-coated PCL/βTCP scaffold was inserted into the intramuscular pocket, and wounds were closed progressively with three layers of sutures (muscle, subcutaneous, and dermal layers). Each hindlimb was implanted with either a control scaffold $[P2/PAA]_{100}$, a rhBMP-2 scaffold $[P2/PAA/rhBMP\text{-}2/PAA]_{100}$ or a scaffold with rhBMP-2/rhVEGF$_{165}$ combination film $[Poly2/PAA/rhBMP\text{-}2/PAA]_{100}$[Poly2/Chondroitin sulfate/rhVEGF$_{165}$/Chondroitin sulfate]$_{80}$ Postoperatively, rats were treated with buprenex and meloxicam until signs of distress dissipated. Rats were housed in separate cages with free access to food and water. At four and eight week time points, four rats from each group were sacrificed and the implants retrieved for analysis as described below.

4.2.5.3.1 Micro-computed tomography (MicroCT) analysis

Excised samples were immediately placed in 10% neutral buffered formalin and imaged with MicroCT (eXplore Locus, GE Medical Systems, London, Ontario) at a resolution of 27 μm with proprietary software included with the system (EVS Evolver, GE Medical Systems, Fairfield, CT). The scanning protocol was performed with a 2000 ms shutter speed, 1 x 1 binning, at X-ray tube parameters 80 kV and 450 mA. Four hundred images were taken at incremental angles, and rendered 3D images were reconstructed with the Reconstruction Utility and analyzed using MicroView (GE Healthcare, Fairfield,

CT). Threshold values were chosen by visual inspection and kept constant across 1 month or 2 month data sets. Three independent regions of interest (ROIs) were chosen per sample, and the bone analysis tool was used to measure bone mineral density and stereology measurements of each sample. Three dimensional representations of bone formation and two dimensional digital slices through the samples were also taken for qualitative comparison. Each sample was measured in triplicate for each set of data.

4.2.5.3.2 Histological analysis

After 24 h in 10% formalin, tissues were transferred to solutions of 70% ethanol prior to decalcification. Tissues were decalcified for 5 days in a solution of 15% EDTA and 10% sodium citrate buffer, pH 7.2 at 4°C under continuous stirring. Tissues were then serially sectioned, routinely processed, and embedded in paraffin. Microscope sections (4 μm) were stained with hematoxylin and eosin (H&E), Alcian Blue, and Masson's trichrome stains.

4.3. Results and Discussion

4.3.1 Fabricating a dual growth factor releasing layer-by-layer system

Both rhBMP-2 and $rhVEGF_{165}$ are homodimeric proteins which have a similar pI of about 8.5; the non-glycosylated forms have a molecular weight of about 30 kDa and 38.2 kDa respectively. Under conditions of acidic and physiological pH, both proteins are expected to be positively charged. Hence, for the layer-by-layer film assembly, we used a tetralayer architecture with 1) Poly2, a synthetic poly(β-aminoester); 2) a biocompatible polyanion (PAA or Chondroitin sulfate); 3) a growth factor (either rhBMP-2 of $rhVEGF_{165}$) and 4) a polyanion for charge reversal (Fig. 2.1.).

In order to successfully release growth factor under physiological conditions, we chose Poly2 which is a hydrolytically degradable member of the poly (β-aminoester) (PBAE) family, which has been extensively studied in gene therapy [44] applications and used for PEM fabrication for various delivery applications from multilayer films with appropriate architectures [45]. Under neutral to acidic pH conditions of film fabrication, Poly2 is stable and the amines present along the backbone of Poly2 are protonated, yielding the positive charge necessary for electrostatic LbL systems. We anticipated that

films constructed with PAA as the alternating polyanion would yield more highly ionically crosslinked films relative to chondroitin sulfate, as PAA exhibits a higher charge density. Such films should result in a more sustained release profile of rhBMP-2. An important phase of wound healing involves the secretion of glycosaminoglycans by fibroblast cells to form a hydrophilic matrix suitable for remodeling while healing. Chondroitin sulfate has been extensively investigated for wound dressing applications [46] due to its biocompatibility, non-immunogenicity and pliability. Thus it was the polyanion of choice for fabricating the $rhVEGF_{165}$ PEM films. Films with tetralayer repeat units were fabricated, where the tetralayers containing rhBMP-2 were adsorbed first, and $rhVEGF_{165}$ layers were adsorbed on top (Fig. 2.1.). We anticipated releasing growth factor from the surface of implants, where more $rhVEGF_{165}$ would be released initially for stimulating proliferation of blood vessels in vivo, followed by more rhBMP-2, which would initiate the differentiation cascade leading to the formation of new bone.

Hydrogel based dual growth factor releasing systems have been reported [7], where components are fabricated separately and do not offer the convenience of conformal coating. Here, LbL was used to conformally coat the complex geometries of an osteoconductive macroporous polycaprolactone/β-tricalcium phosphate (50wt% PCL/50wt% β-TCP) waffle cylinder scaffold, with diameter = 10mm and height = 2.5mm. The three dimensional, porous scaffold was used for in vitro and in vivo testing as a model implant (Fig. 2.1.). The choice of scaffold was governed by the following factors: (i) PCL is a biologically inert, biocompatible FDA approved material, (ii) βTCP is an osteoconductive material and typically both an osteoinductive agent, such as rhBMP-2, and an osteoconductive microenvironment are necessary for ectopic bone formation (iii) the total drug load scales with film surface area, allowing for a greater load per volume in a macroporous three dimensional substrate compared with a flat film [35].

4.3.2 In vitro kinetics of dual growth factor releasing films

While the precise growth factor dose required would depend on the specific orthopedic application, $[Poly2/PAA/rhBMP\text{-}2/PAA]_x[Poly2/Chondroitin\ sulfate/rhVEGF165/Chondroitin\ sulfate]_y$ films were constructed with the aim of demonstrating that this system could be tuned for specific applications involving bone

regeneration and that the released growth factors demonstrate a dose response behavior (Table 1). Release from the film was normalized to 1 milligram of scaffold weight, to provide a basis for comparison.

We tuned our system to demonstrate a control over total growth factor loading. Release of growth factors from the film occurs with a pH shift from pH 5.0 at dipping conditions to physiological pH 7.4 in 1x PBS, due to a combination of destabilization and charge imbalance in the films and from hydrolytic degradation of the Poly-2 backbone. Approximately one-third of the rhBMP-2 and two-thirds of the $rhVEGF_{165}$ was released after three days. While both growth factors begin release immediately upon immersion, the release profile for rhBMP-2 indicates that it takes a longer time to elute completely from the film than $rhVEGF_{165}$. The amount of growth factor released from single growth factor films (Fig. 2.2. A, B) and dual growth factor films (Fig. 2.2. C, D, E, F) is comparable, and in all cases, indicate that amounts of growth factor for each component can be independently tuned to yield a clear increase in loading with number of layers. This is an important capability for delivery film design that is not always readily attained with multilayer formulations; it indicates that the growth factor does not leach out of the film by diffusion into the dipping solution when a different growth factor is introduced. Electrostatic interactions between the growth factor and surrounding polymer chains in the film prevent it from diffusing out or being exchanged out during film assembly. Loading of rhBMP-2 and $rhVEGF_{165}$ scaled linearly with tetralayer number with 4.50 ± 0.14 ng (R^2 = 0.93) and 3.72 ± 0.080 ng (R^2 = 0.96) of rhBMP-2 and $rhVEGF_{165}$ respectively per tetralayer per milligram of scaffold (n = 3). In these films, total rhBMP-2 and total $rhVEGF_{165}$ incorporation ranged from 250 and 600 ng/mg scaffold weight and 80 to 200 ng/mg scaffold weight, respectively, as a function of number of layers. A broad range of protein incorporation in films has been previously reported from 2D substrates, from 5 ng/cm^2 upto 650 µg/cm^2 [34, 47]. The release profiles in Fig. 2.2 are characteristic of surface erosion behavior. The release profile in Fig. 2.2A indicates gradual linear release as the rhBMP-2 is completely eluted. We would expect the film would undergo bulk erosion if the water permeates into the LbL films faster than the rate of hydrolytic degradation of Poly2 and surface erosion if the rate of permeation is slower. The dominance of surface erosion is due to the prolonged

half-life of Poly2 conferred by the presence of a hydrophobic region near the ester bond and a consequent decrease in water attack on the bond, hence a slower degradation rate of the polymer. Our previous work has demonstrated that a related PBAE (Poly1), with a shorter alkyl chain near the ester bonds, releases a comparable cargo much faster [34]. In case of the single and dual growth factor releasing films, rhBMP-2 release is consistent across the different groups (x = 40, 80, 100, 120) at 27.4 ± 8.38% per day averaged over the first 2 days and 5.3 ± 0.34% per day until the end of release. In single growth factor rhVEGF165 films, release is consistent across the different groups (y = 20, 30, 40, 50), at 20 ± 0.07% per day averaged over the first 5 days, after which there is no detectable release. For dual growth factor films, it is interesting to note that the amount of $rhVEGF_{165}$ released drops to 15 ± 1.42% per day averaged over the first 5 days and 3.05 ± 0.96% per day until the end of release. It is likely that interdiffusion occurs with both growth factors during film assembly, leading to a mixing of BMP-2 and VEGF with in the film matrix, although a gradient of BMP-2 may still remain in the bottom layers of the film, leading to more extended release. Interdiffusion of components in polyelectrolyte multilayers has been reported for similar systems [48, 49].

4.3.3 In vitro rhBMP-2 activity assay

To study the rhBMP-2 dose dependent behavior of MC3T3-E1 cells in vitro, we exposed the cells to different formulations – growth media, differentiation media (growth media supplement with L-ascorbic acid and β-glycerolphosphate) and release media with the rhBMP-2 load normalized to 1 milligram of scaffold weight. Alkaline phosphatase (AP) serves as a standard early marker of induction of new bone differentiation from progenitor cells. In Fig. 2.3A and 2.3B, the AP signal is dose dependent to the amount of rhBMP-2 exposed to the cells ($p<0.05$). In Figure 2.3C, AP signal is the same across the different formulations, as expected as the amount of rhBMP-2 in the formulation is the same. Alizarin red (AR) stains for calcium deposits and allows for its visualization and quantification. AR staining was performed 14 days after exposure to the different formulations. In Figures 2.3D, 2.3E, 2.3F, staining of Alizarin Red confirms osteoblast differentiation to a mature bone phenotype from

rhBMP-2 exposure. Staining was quantified and observed to be dose dependent when the dose of rhBMP-2 was varied (Figures 2.3D, 2.3E) ($p<0.05$) and the intensity of the stain was the same when the rhBMP-2 dose was constant (Figure 2.3F). Interestingly, the staining was more diffuse when $rhVEGF_{165}$ and chondroitin sulfate was part of the formulation (Fig. 2.3E, 2.3F). We have observed in our previous work [35] that the presence of chondroitin sulfate, a glycosaminoglycan, allows for a more even distribution of rhBMP-2 in culture resulting in a more diffuse stain. In all cases, the formulations significantly outperformed the differentiation induced by the growth and differentiation media.

4.3.4 In vitro $rhVEGF_{165}$ activity assay

HUVEC's have been shown to respond to $rhVEGF_{165}$ concentration in a dose dependent manner at low concentrations of $rhVEGF_{165}$. Complimentary to these findings, we demonstrated that the $rhVEGF_{165}$ released from the LbL films was active and induced dose dependent proliferation and migration of HUVEC's.

Proliferation of HUVEC's was measured using BrdU, a synthetic nucleoside that is an analogue of thymidine and can be incorporated into the newly synthesized DNA of replicating cells substituting for thymidine during DNA replication. Cells were seeded at a low density to prevent wells from reaching confluency within the period of this study. Cells exposed to formulations were the $rhVEGF_{165}$ load was changed demonstrated a dose response behavior which was statistically significant (Fig. 2.4A, 2.4B) ($p < 0.05$). Dose response to linear increases in the number of tetralayers was also linear ($R^2 = 0.99$) which is consistent with observations elsewhere [50]. The degree of change in proliferation was statistically insignificant when the $rhVEGF_{165}$ load was kept constant (Fig. 2.4C) ($p>0.05$) (Fig. 2.5.).

Migration of HUVEC's was measured as the difference in the average size of the scratch made in a confluent monolayer of cells before and after incubating the cells with different formulations of release medium. Here too, a dose response behavior was observed with the scratch size decreasing linearly as a function of $rhVEGF_{165}$ load ($R^2 = 0.99$).

4.3.5 In vivo evaluation of LbL films using intramuscular bone formation model

We demonstrated the efficacy of the LbL coated implants in vivo. Consistent with our previous work [35], the osteoconductive scaffold and the osteoinductive rhBMP-2 formed bone at an intramuscular ectopic site. Adding an angiogenic factor accelerated the maturation of ectopic bone. Microcomputed tomography (microCT) images at four and nine week time points showed large bone deposits created in response to rhBMP-2 LbL films. Growth factor coated implants (Fig. 2.6) showed new plate-like bone trabeculae that progressively increased in thickness from four to nine weeks. Quantification of the bone mineral density (BMD) from microCT images demonstrated an increase of 28 ± 4.59% and 32 ± 2.73% at 4 and 9 weeks respectively ($p < 0.001$) for the scaffolds coated with rhBMP-2/rhVEGF$_{165}$ over the scaffolds coated with just rhBMP-2. In contrast, no bone was formed in scaffolds coated with LbL films lacking growth factor.

The bone formation was restricted to the periphery of the scaffold when just rhBMP-2 was used. Over the initial 4 week time period, a greater amount of bone was present deep within scaffold when both rhBMP-2 and rhVEGF$_{165}$ were released from the scaffold surface as measured by bone mineral density on the scaffold surface and the interior of the scaffold (Fig. 2.6A, B). Interior bone mineral density increased by 27 ± 7.1% in scaffolds with the combination growth factors, while the increase in BMP-2 eluting films was statistically insignificant. Trabecular thickness of the peripheral bone formed by the rhBMP-2/rhVEGF$_{165}$ combination scaffolds, was found to be 3 fold and 4.5 fold greater than the bone formed by the BMP-2 scaffold at 4 and 9 weeks respectively (Fig. 2.6C).

Histological sections of excised implants from the rat femur (Fig.2.7.) showed active bone formation and remodeling with osteocytes and cement lines where new bone is laid down by differentiating osteoblasts within scaffolds releasing either rhBMP-2 or the combination of rhVEGF$_{165}$ and rhBMP-2 (Fig. 2.7E-2.7L). Bone marrow with maturing trilineage hematopoiesis was occasionally observed (Fig. 2.7G). Bone was deposited on the interior surface of the scaffold, and was restricted to the area of the implant (Fig 2.7F, 2.7H, 2.7J, 2.7L). This is important, as it demonstrates that the system was able to control bone formation at an ectopic site. At 4 weeks, spicules of trabecular bone were

observed throughout the scaffold in combination growth factor releasing films, whereas the spicules were restricted to the periphery in single growth factor rhBMP-2 films. In both cases, mature lamellar bone was observed from 4 to 9 weeks as visualized by aligned collagen fibrils that are birefringent under polarized light. Interestingly, a large number of hematopoietic cells were observed around areas of mature lamellar bone at 9 weeks along with adipocytes, recapitulating the fatty marrow architecture and suggesting a high level of tissue maturation. Consistent with endochondral bone formation, a cartilage intermediate is visible in the bone tissue induced by growth factor PEM films (Fig. 2.7F, J) which is progressively replaced with bone which extends throughout the scaffold only when $rhVEGF_{165}$ is present. The de novo recapitulation of a more complete bone architecture precipitated by PEM mediated release of dual growth factor $rhVEGF_{165}$ and rhBMP-2 from the scaffold surface, suggests that there may be a greater initial concurrent vascularization process which mediates introduction of more cells in the interior on the scaffolds; none of the aforementioned biological processes is present in LbL scaffolds lacking BMP-2.

4.4. Conclusions

The ability to regulate the local availability of precise amounts of growth factors is a potent tool for bone tissue engineering where the differentiation of many stem cell types typically requires the action of several growth factors at distinct stages. The utility of rhBMP-2 and rhVEGF has been well documented in mediating interactions between host tissue and implant. We have presented polyelectrolyte multilayer films that are able to deliver independently tunable nanogram scale physiological amounts of active rhBMP-2 and rhVEGF over different timeframes and induce a corresponding dose response on physiologically responsive cell lines. It is important to note that the dose response behavior is restricted to micromolar scale quantities of growth factors, and we were able to demonstrate control at these levels using sustained release obtained with hydrolytic degradation. PEM films on an osteoconductive scaffold induced ectopic bone formation in the intramuscular region of a rat femur. The delivery of two growth factors - rhBMP-2 and rhVEGF - changed the microenvironment significantly compared to single growth factor rhBMP-2 such that the trabecular bone formed throughout the scaffold

and was more continuous and matured faster compared to single growth factor BMP-2 delivery. The ease of fabrication of this system makes it highly flexible; it can be applied to a wide variety of tissue engineering applications, including PEM films to treat diabetic ulcers, lumbar spine fusion and fracture healing. These results are an important step toward developing a system capable of multiple biologic drug delivery in vivo, and offering successful and long lasting joint replacement wound healing and repair. Furthermore, the general demonstration of dual controlled growth factor release from a thin film coating platform is a significant advance for numerous applications from implant coatings to tissue engineering.

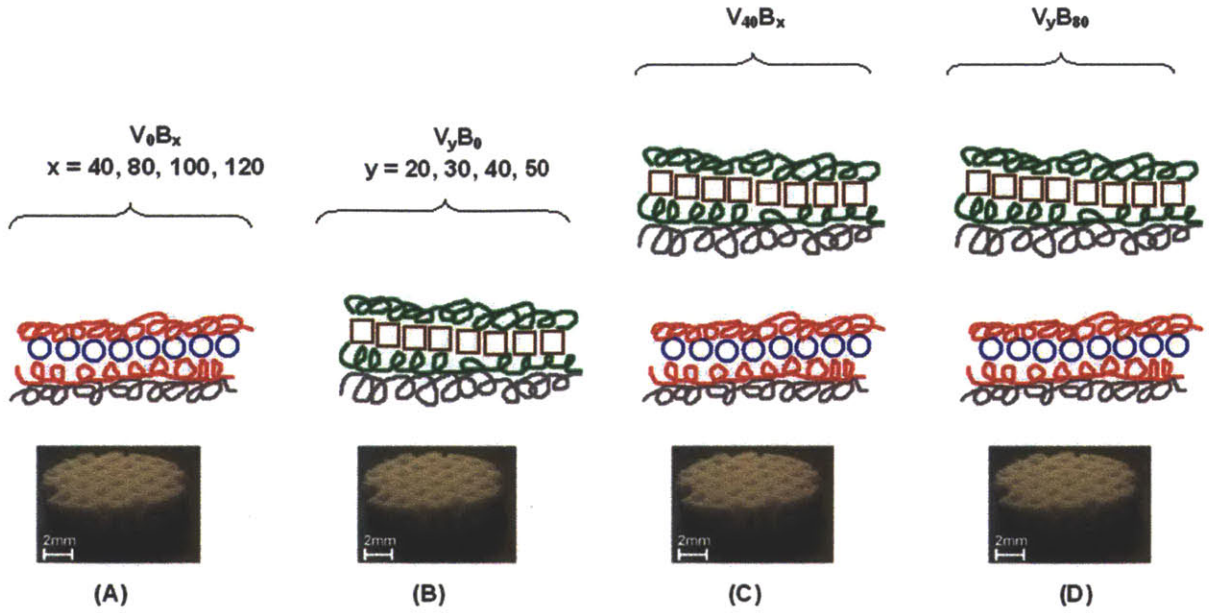

Fig. 4.1. Fabrication of polyelectrolyte multilayer films using the layer-by-layer method in a tetralayer architechture with [Poly2(+)/polyanion(-)/growth factor(+)/polyanion(-)] depicted below. Four different groups were fabricated. For single growth factor films (A) rhBMP-2 PEM films with architecture [Poly2/PAA/rhBMP-2/PAA]x, with x = 40, 80, 100, 120 and (B) rhVEGF165 PEM films with architecture [Poly2/CS/rhVEGF165/CS]y, where y = 20, 30, 40, 50. For dual growth factor films, (C) y = 40 was constant and x = 40, 80, 100, 120. (D) In another formulation, x = 80 was constant and y = 20, 30, 40, 50. The substrate was always a macroporous polycaprolactone/β-tricalcium phosphate (50wt% PCL/50wt% β-TCP) waffle cylinder scaffold, with diameter = 10mm and height = 2.5mm.

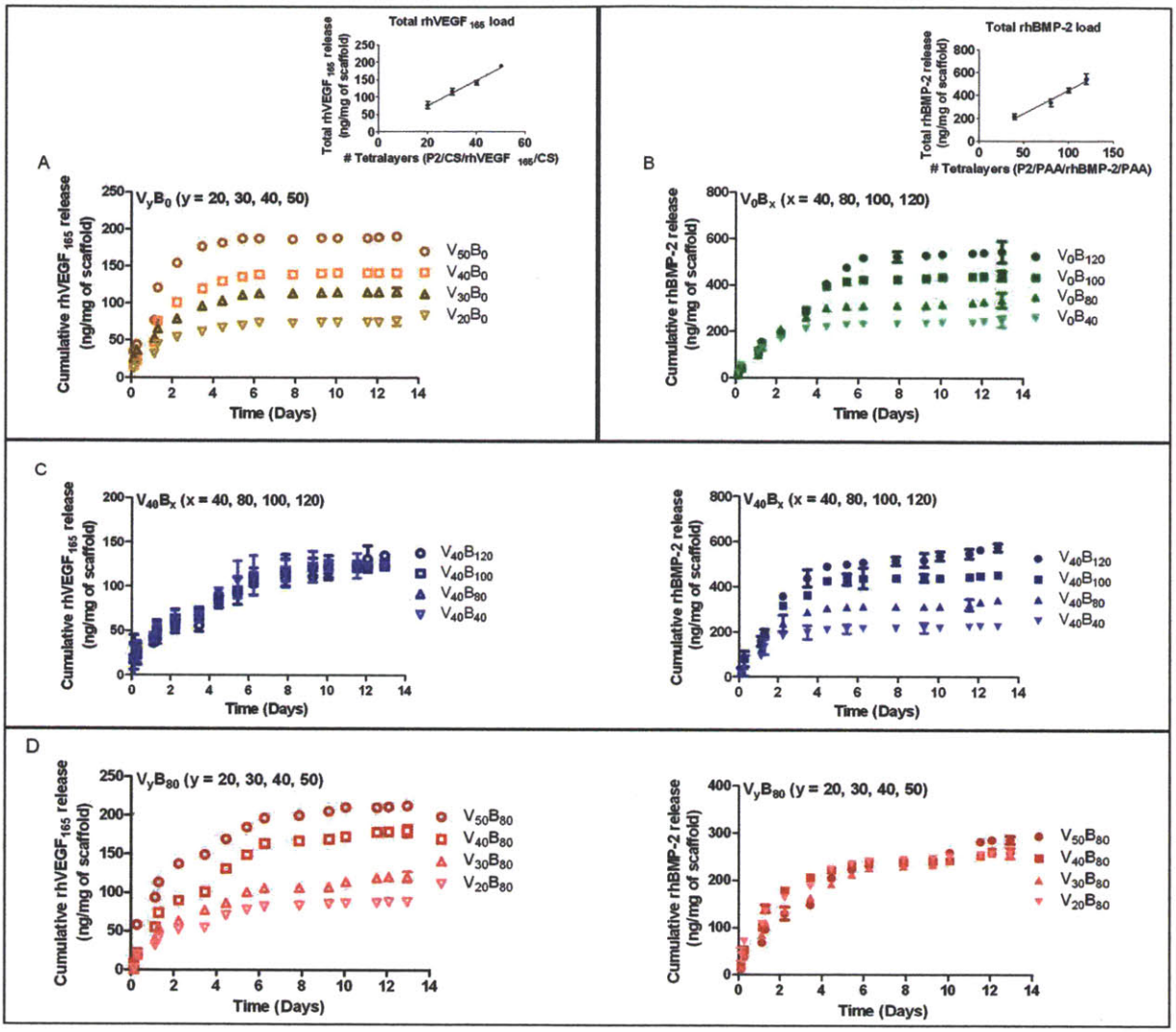

Fig. 4.2. Polyelectrolyte multilayer films were dipped in a Poly2/anion/growth factor/anion tetralayer repeat architecture on a macroporous polycaprolactone/β-tricalcium phosphate (50wt% PCL/50wt% β-TCP) waffle cylinder scaffold. Growth factor loading was controlled by varying the number of layers dipped on the scaffold. rhBMP-2 released over a period of about 2 weeks, whereas rhVEGF165 eluted completely within 8 days. 4 groups of films were fabricated and incubated in 1x PBS at pH 7.4 over 12 days to study growth factor release from the films. Growth factor release was quantified using ELISA and normalized per milligram of scaffold. Samples were in triplicate and the error bar is the standard deviation. Release from (A) Single growth factor rhVEGF$_{165}$ release and (inset) total rhVEGF$_{165}$ loading scales linearly with tetralayer number (R2 = 0.96). (B) Single growth factor rhBMP-2 release and (inset) total rhBMP-2

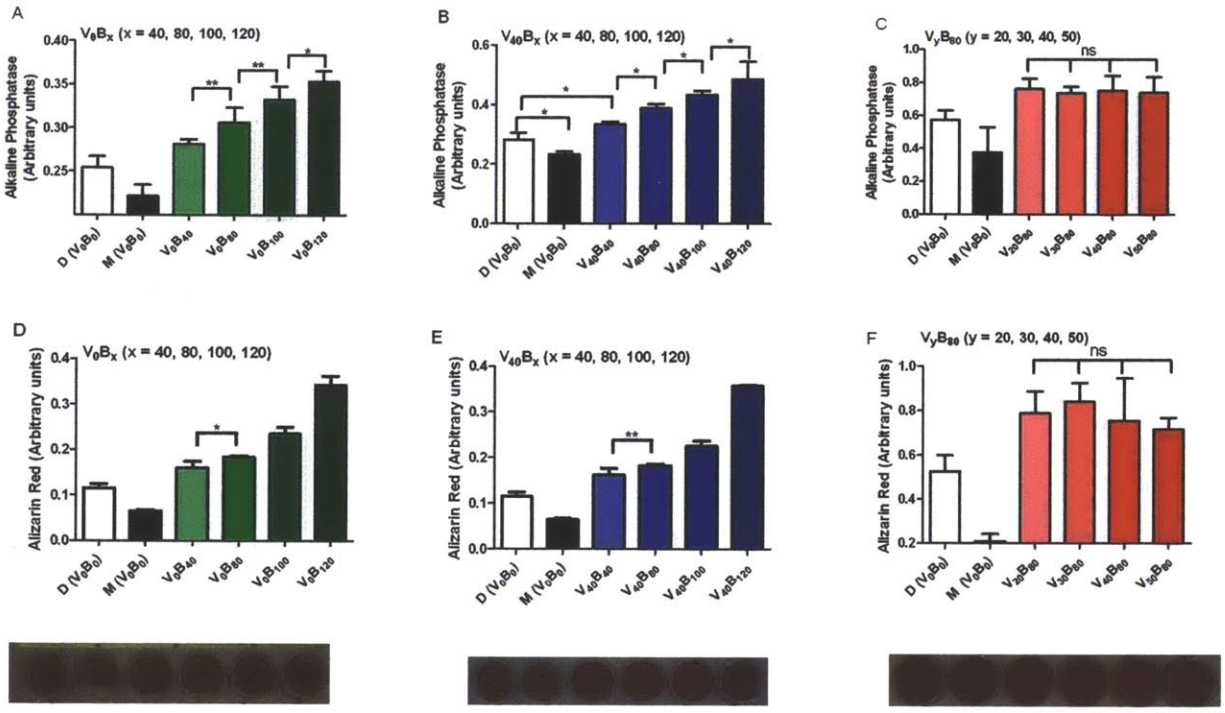

Fig. 4.3. Pre - osteoblast differentiation assay. Activity of rhBMP-2 released from the polyelectrolyte multilayer films is preserved. MC3T3-E1 cells were exposed to rhBMP-2 released from multilayer films, with the dose normalized per milligram of scaffold weight. Alkaline Phosphatase Assay demonstrates dose dependent early activation of bone differentiation cascade at Day 5. After 21 days of culture, Alizarin Red Stain confirms the presence of calcium deposits laid down during the differentiation process. Visual inspection of cultures after Alizarin red staining confirms a dose dependent presence of calcium deposits. (A, B and C) Alkaline phosphatase assay at day 3 on cells differentiated with different release formulations as depicted. (D, E and F) Alizarin red assay at day 14 on cells differentiated with different release formulation as depicted. Representative images of the alizarin red stain are below the bar graph in (D, E, F). A single factor ANOVA test allowed rejection of the null hypothesis for both assays; and a Tukey test between different groups was performed (s.d., n=9, ** $p < 0.01$; * $p < 0.05$; ns = not significant; all others $p < 0.001$).

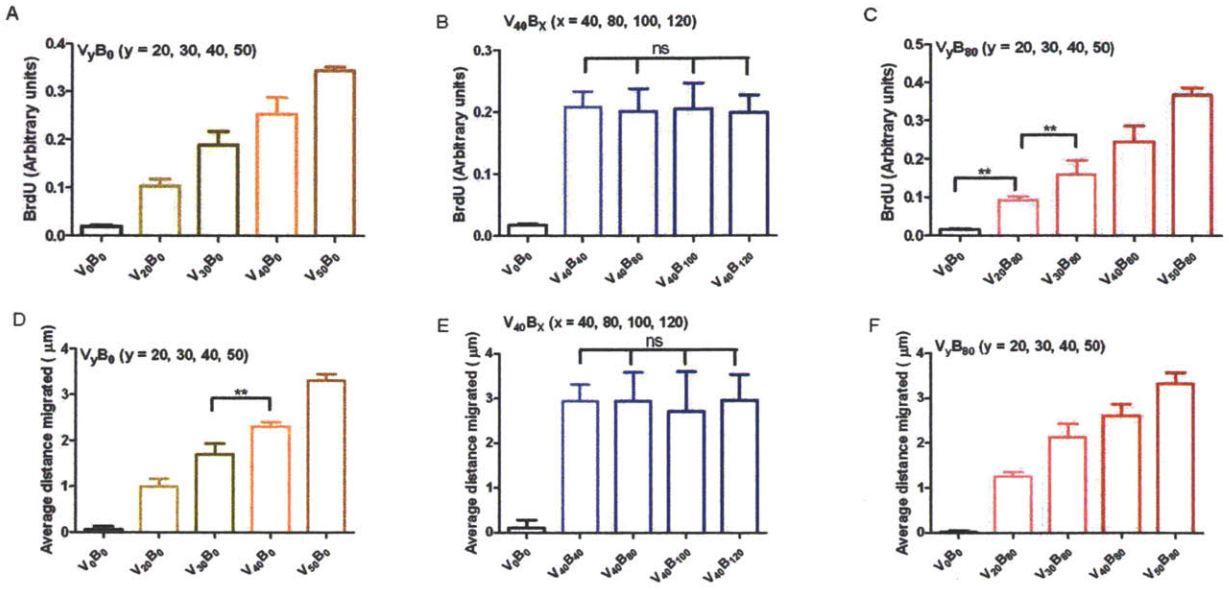

Fig. 4.4. Proliferation and Migration assays. Activity of rhVEGF165 released from the polyelectrolyte multilayer films is preserved. HUVEC cells exposed to $rhVEGF_{165}$ dose normalized per milligram of scaffold weight exhibited increased proliferation activity, as measured by BrdU. (A) 40, 80, 100 and 120 tetralayers of rhBMP-2 followed by 40 tetralayers of $rhVEGF_{165}$. (B) 40 tetralayers of rhBMP-2 followed by 20, 30, 40 and 50 tetralayers of $rhVEGF_{165}$ and (C) 20, 30, 40 and 50 tetralayers of $rhVEGF_{165}$. Closure of uniform "scratched" wound gap was monitored in HUVEC cell cultures over a period of 8 hours. Cells were fixed and imaged at 20x magnification (D) 40, 80, 100 and 120 tetralayers of rhBMP-2 followed by 40 tetralayers of $rhVEGF_{165}$. (E) 40 tetralayers of rhBMP-2 followed by 20, 30, 40 and 50 tetralayers of $rhVEGF_{165}$ and (F) 20, 30, 40 and 50 tetralayers of $rhVEGF_{165}$. A single factor ANOVA test allowed rejection of the null hypothesis for both assays; and a Tukey test between different groups was performed (s.d., n = 9, ** $p < 0.01$; * $p < 0.05$; ns = not significant; all others $p < 0.001$).

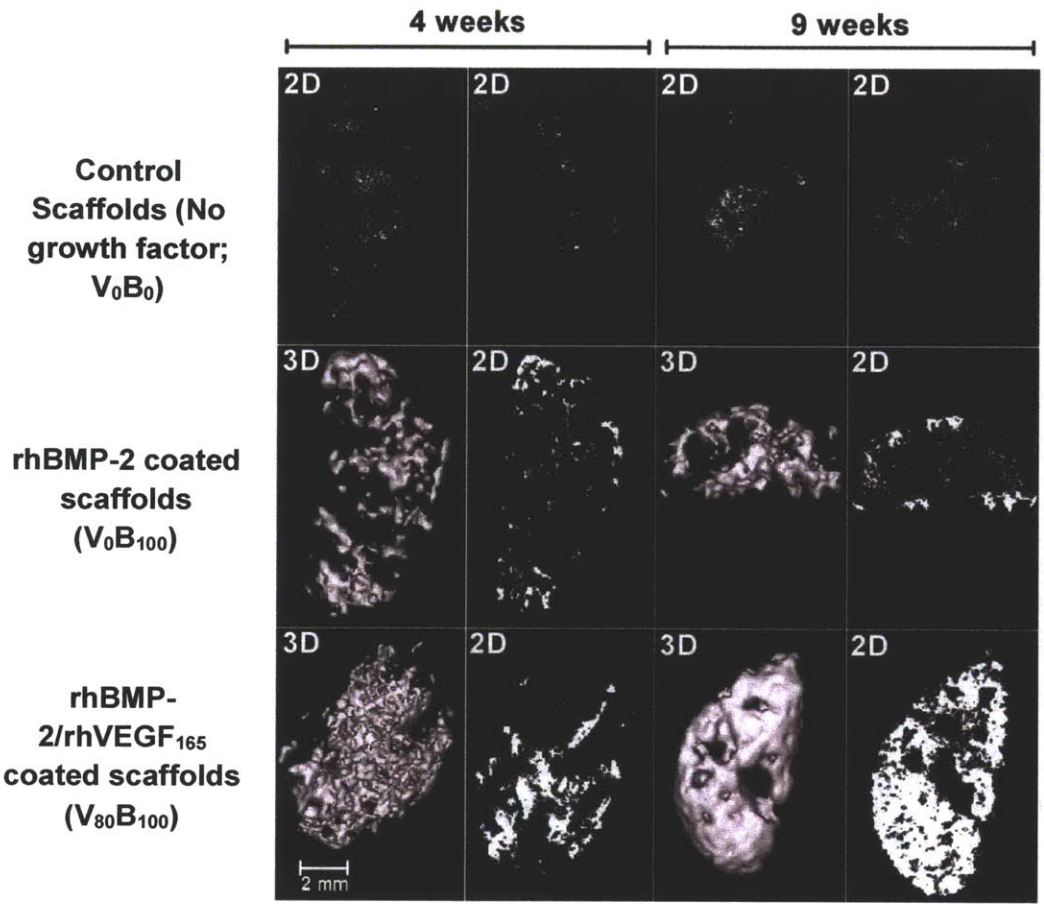

Fig. 4.5. Two dimensional microCT scans (2D) and matched three dimensional reconstructions (3D) of excised PCL-βTCP half disc scaffolds, which were implanted in the intramuscular region of rats. Implants were coated with (i) no growth factor, (ii) 6 μg of single growth factor rhBMP-2 and (iii) 6 μg of single growth factor rhBMP-2 followed by 4μg of rhVEGF$_{165}$. The amount of growth factor loaded was determined by fabricating triplicate companion copies along with the implanted scaffolds, releasing the growth factors in vitro and performing ELISA detection assays. (Top row) Control scaffolds without growth factors produce no detectable bone over the duration of the study. Low levels of backscatter is caused by the polymer. (Middle row) In single growth factor rhBMP-2 films lacking rhVEGF$_{165}$, bone formation is restricted to the periphery of the scaffold at 4 weeks and 9 weeks. (Bottom row) As a result of increased vascularity, scaffolds releasing rhVEGF$_{165}$ demonstrate a smooth, continuous profile in the ectopically formed bone which matures from 4 weeks to 9 weeks to fill the entire scaffold. In all the images, the bone formed takes the shape of the scaffold and grows inward when VEGF is present. Images are an isosurface rendering at 0.25 surface quality factor at a level threshold of 640, as defined by the proprietary Microview® software from GE Healthcare.

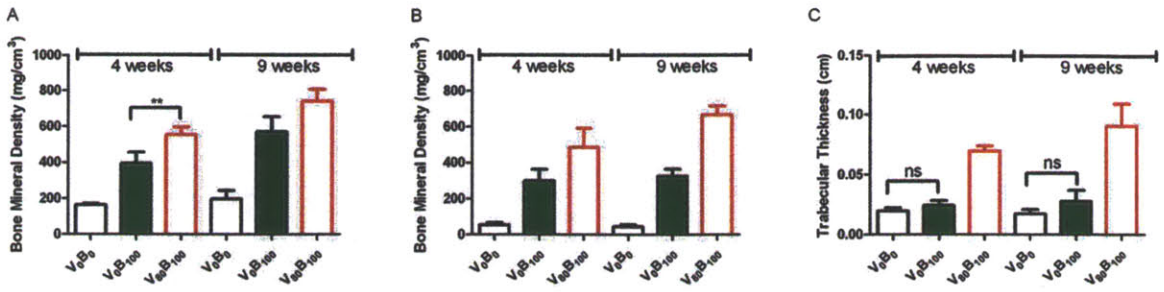

Fig. 4.6. (A) The bone mineral density (BMD) of ectopic bone formed by the rhBMP-2/rhVEGF$_{165}$ combination scaffolds is 28 ± 4.59% and 32 ± 2.73% higher than bone formed by rhBMP-2 scaffold at 4 and 9 weeks respectively at the periphery of the scaffolds. (B) In the interior, the BMD for the combination growth factor scaffolds is higher than the single rhBMP-2 scaffolds indicating that more bone is present in the interior, which matures from 4 to 9 weeks as indicated by the increase in BMD. (C) The trabecular thickness of the bone formed is an important measure of bone maturation, and the trabecular thickness of the bone formed by the combination scaffolds is about 3 times and 4.5 times that of bone formed by rhBMP-2 scaffolds at 4 and 9 weeks. (s.d., n=9, ** $p < 0.01$; ns = not significant; all others $p < 0.001$)

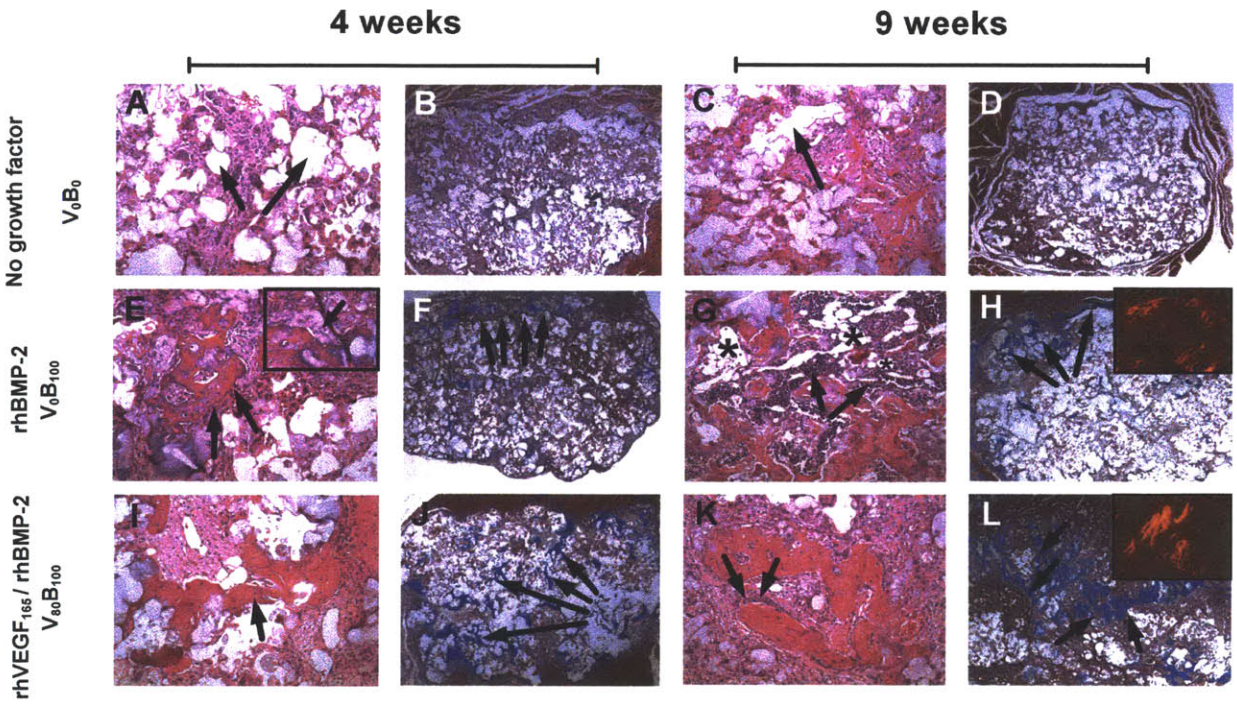

Fig. 4.7. Histology sections from rat femur intramuscular implants. (A to D) Bone is absent in control scaffolds releasing no growth factors at 4 and 9 weeks verified by (A, C) H&E staining and (B, D) lack of brilliant blue collagen staining with Masson's trichrome stain. (A, B) Arrows indicate pockets where the (PCL/βTCP) polymer scaffold is present at 4 weeks which degrades over (C, D) 9 weeks, without any bone growth in the vacant space. (E to H) Bone present in scaffolds releasing single growth factor rhBMP-2. (E) Presence of trabecular bone with (inset) osteoblasts laying down new bone which is (F) restricted to the periphery of the scaffold at 4 weeks. Of particular interest is (G) the abundant presence of hematopoietic cells surrounding the bone in spaces identified as fatty marrow space (asterisk), where (H) most of the bone formation is restricted to the periphery at 9 weeks and (inset) as bone matures, it goes from an unorganized collagen matrix structure to a lamellar structure with aligned collagen fibrils that are birefringent under polarized light. (I to L) Bone present in scaffolds releasing rhBMP-2 and rhVEGF$_{165}$. (I) Spicules of trabecular bone which is present (J) throughout the scaffold as early as 4 weeks. (K) As osteoblasts lay down new bone, spicules mature into (L) bone that fills up the empty spaces throughout the scaffold as it degrades with (inset) a greater number of birefringent aligned collagen fibrils present than fibrils formed when single growth factor rhBMP-2 is released. Bone formed is always within the scaffold. A, C, E, G, I, K are hematoxylin and eosin (H&E) stains at 10x objective magnification. B, D, F, H, J, L are Masson's trichrome stains at 2x objective magnification. Images in inset are taken at 20x objective magnification.

4.5 References

1. Ince A, Rupp J, Frommelt L, Katzer A, Gille J, Lohr JF. Is "aseptic" loosening of the prosthetic cup after total hip replacement due to nonculturable bacterial pathogens in patients with low-grade infection? Clin Infect Dis 2004;39(11):1599-1603.

2. Harris WH, Sledge CB. Total hip and total knee replacement. N Engl J Med 1990;323(11):725-731.

3. Street J, Bao M, deGuzman L, Bunting S, Peale FV, Jr., Ferrara N, et al. Vascular endothelial growth factor stimulates bone repair by promoting angiogenesis and bone turnover. Proc Natl Acad Sci U S A 2002;99(15):9656-9661.

4. Lieberman JR, Daluiski A, Einhorn TA. The role of growth factors in the repair of bone. Biology and clinical applications. J Bone Joint Surg Am 2002;84-A(6):1032-1044.

5. Wozney JM, Rosen V, Celeste AJ, Mitsock LM, Whitters MJ, Kriz RW, et al. Novel regulators of bone formation: molecular clones and activities. Science 1988;242(4885):1528-1534.

6. Patel ZS, Young S, Tabata Y, Jansen JA, Wong ME, Mikos AG. Dual delivery of an angiogenic and an osteogenic growth factor for bone regeneration in a critical size defect model. Bone 2008;43(5):931-940.

7. Kempen DH, Lu L, Heijink A, Hefferan TE, Creemers LB, Maran A, et al. Effect of local sequential VEGF and BMP-2 delivery on ectopic and orthotopic bone regeneration. Biomaterials 2009;30(14):2816-2825.

8. Sellers RS, Peluso D, Morris EA. The effect of recombinant human bone morphogenetic protein-2 (rhBMP-2) on the healing of full-thickness defects of articular cartilage. J Bone Joint Surg Am 1997;79(10):1452-1463.

9. Gerhart TN, Kirker-Head CA, Kriz MJ, Holtrop ME, Hennig GE, Hipp J, et al. Healing segmental femoral defects in sheep using recombinant human bone morphogenetic protein. Clin Orthop Relat Res 1993;(293):317-326.

10. Uludag H, Gao TJ, Porter TJ, Friess W, Wozney JM. Delivery systems for BMPs: factors contributing to protein retention at an application site. J Bone Joint Surg Am 2001;83A:S128-S135.

11. Jennissen HP. Accelerated and improved osteointegration of implants biocoated with bone morphogenetic protein 2 (BMP-2). Ann N Y Acad Sci 2002;961:139-142.

12. Maus U, Andereya S, Gravius S, Ohnsorge JA, Niedhart C, Siebert CH. BMP-2 incorporated in a tricalcium phosphate bone substitute enhances bone remodeling in sheep. J Biomater Appl 2008;22(6):559-576.

13. Peng H, Usas A, Olshanski A, Ho AM, Gearhart B, Cooper GM, et al. VEGF improves, whereas sFlt1 inhibits, BMP2-induced bone formation and bone healing through modulation of angiogenesis. J Bone Miner Res 2005;20(11):2017-2027.

14. Gerber HP, Vu TH, Ryan AM, Kowalski J, Werb Z, Ferrara N. VEGF couples hypertrophic cartilage remodeling, ossification and angiogenesis during endochondral bone formation. Nat Med 1999;5(6):623-628.

15. Samee M, Kasugai S, Kondo H, Ohya K, Shimokawa H, Kuroda S. Bone morphogenetic protein-2 (BMP-2) and vascular endothelial growth factor (VEGF) transfection to human periosteal cells enhances osteoblast differentiation and bone formation. J Pharmacol Sci 2008;108(1):18-31.

16. Murphy WL, Peters MC, Kohn DH, Mooney DJ. Sustained release of vascular endothelial growth factor from mineralized poly(lactide-co-glycolide) scaffolds for tissue engineering. Biomaterials 2000;21(24):2521-2527.

17. Luginbuehl V, Meinel L, Merkle HP, Gander B. Localized delivery of growth factors for bone repair. Eur J Pharm Biopharm 2004;58(2):197-208.

18. Richardson TP, Peters MC, Ennett AB, Mooney DJ. Polymeric system for dual growth factor delivery. Nat Biotechnol 2001;19(11):1029-1034.

19. Nielsen HM, Andreassen TT, Ledet T, Oxlund H. Local injection of TGF-beta increases the strength of tibial fractures in the rat. Acta Orthop Scand 1994;65(1):37-41.

20. Lutolf MP, Weber FE, Schmoekel HG, Schense JC, Kohler T, Muller R, et al. Repair of bone defects using synthetic mimetics of collagenous extracellular matrices. Nat Biotechnol 2003;21(5):513-518.

21. Saito N, Okada T, Horiuchi H, Ota H, Takahashi J, Murakami N, et al. Local bone formation by injection of recombinant human bone morphogenetic protein-2 contained in polymer carriers. Bone 2003;32(4):381-386.

22. Simmons CA, Alsberg E, Hsiong S, Kim WJ, Mooney DJ. Dual growth factor delivery and controlled scaffold degradation enhance in vivo bone formation by transplanted bone marrow stromal cells. Bone 2004;35(2):562-569.

23. Zara J, Siu RK, Zhang X, Shen J, Ngo R, Lee M, et al. High doses of BMP2 induce structurally abnormal bone and inflammation in vivo. Tissue Eng Part A 2011;17(9-10).

24. Fu K, Pack DW, Klibanov AM, Langer R. Visual evidence of acidic environment within degrading poly(lactic-co-glycolic acid) (PLGA) microspheres. Pharm Res 2000;17(1):100-106.

25. Jeon O, Song SJ, Yang HS, Bhang SH, Kang SW, Sung MA, et al. Long-term delivery enhances in vivo osteogenic efficacy of bone morphogenetic protein-2 compared to short-term delivery. Biochem Biophys Res Commun 2008;369(2):774-780.

26. Kokubu T, Hak DJ, Hazelwood SJ, Reddi AH. Development of an atrophic nonunion model and comparison to a closed healing fracture in rat femur. J Orthop Res 2003;21(3):503-510.

27. Eckardt H, Bundgaard KG, Christensen KS, Lind M, Hansen ES, Hvid I. Effects of locally applied vascular endothelial growth factor (VEGF) and VEGF-inhibitor to the rabbit tibia during distraction osteogenesis. J Orthop Res 2003;21(2):335-340.

28. Zisch AH, Lutolf MP, Hubbell JA. Biopolymeric delivery matrices for angiogenic growth factors. Cardiovasc Pathol 2003;12(6):295-310.

29. Zhang S, Uludag H. Nanoparticulate systems for growth factor delivery. Pharm Res 2009;26(7):1561-1580.

30. Decher G. Fuzzy nanoassemblies: Toward layered polymeric multicomposites. Science 1997;277:1232.

31. Moskowitz JS, Blaisse MR, Samuel RE, Hsu H-P, Harris MB, Martin SD, et al. The effectiveness of the controlled release of gentamicin from polyelectrolyte multilayers in the treatment of staphylococcus aureus infection in a rabbit bone model. Biomaterials 2010;31:6019-6030.

32. Kim BS, Smith RC, Poon Z, Hammond PT. MAD (multiagent delivery) Nanolayer: delivering multiple therapeutics from hierarchically assembled surface coatings. Langmuir 2009;25(24):14086-14092.

33. Shukla A, Fleming KE, Chuang HF, Chau TM, Loose CR, Stephanopoulos GN, et al. Controlling the release of peptide antimicrobial agents from surfaces. Biomaterials 2010;31(8):2348-2357.

34. Macdonald ML, Rodriguez NM, Shah NJ, Hammond PT. Characterization of tunable FGF-2 releasing polyelectrolyte multilayers. Biomacromolecules 2010;11(8):2053-2059.

35. Macdonald ML, Samuel RE, Shah NJ, Padera RF, Beben YM, Hammond PT. Tissue integration of growth factor-eluting layer-by-layer polyelectrolyte multilayer coated implants. Biomaterials 2011;32(5):1446-1453.

36. Zelikin AN. Drug releasing polymer thin films: new era of surface-mediated drug delivery. ACS Nano 2010;4(5):2494-2509.

37. Facca S, Cortez C, Mendoza-Palomares C, Messadeq N, Dierich A, Johnston APR, et al. Active multilayered capsules for in vivo bone formation. Proc Natl Acad Sci U S A 2010;107(8):3406-3411.

38. Dierich A, Le Guen E, Messaddeq N, Stoltz JF, Netter P, Schaaf P, et al. Bone formation mediated by synergy-acting growth factors embedded in a polyelectrolyte multilayer film. Adv Mat 2007 Mar;19(5):693-697.

39. Pavlukhina S, Lu Y, Patimetha A, Libera M, Sukhishvili S. Polymer multilayers with pH-triggered release of antibacterial agents. Biomacromolecules 2010;11(12):3448-3456.

40. Ai H, Jones SA, Lvov YM. Biomedical applications of electrostatic layer-by-layer nano-assembly of polymers, enzymes, and nanoparticles. Cell Biochem Biophys 2003;39(1):23-43.

41. Kotov NA, Tang ZY, Wang Y, Podsiadlo P. Biomedical applications of layer-by-layer assembly: from biomimetics to tissue engineering. Adv Mat 2006;18(24):3203-3224.

42. Lynn DM, Langer, R. Degradable poly(beta-amino esters): synthesis, characterization, and self-assembly with plasmid DNA. Journal of the American Chemical Society 2000;122:10761– 10768.

43. Gregory CA, Gunn WG, Peister A, Prockop DJ. An alizarin red-based assay of mineralization by adherent cells in culture: comparison with cetylpyridinium chloride extraction. Anal Biochem 2004;329(1):77-84.

44. Zhang J, Chua LS, Lynn DM. Multilayered Thin Films that Sustain the Release of Functional DNA under Physiological Conditions. Langmuir 2004;20(19):8015-8021.

45. Wood KC, Chuang HF, Batten RD, Lynn DM, Hammond PT. Controlling interlayer diffusion to achieve sustained, multiagent delivery from layer-by-layer thin films. Proc Natl Acad Sci U S A 2006;103(27):10207-10212.

46. Kirker KR, Luo Y, Nielson JH, Shelby J, Prestwich GD. Glycosaminoglycan hydrogel films as bio-interactive dressings for wound healing. Biomaterials 2002;23(17):3661-3671.

47. Macdonald M, Rodriguez NM, Smith R, Hammond PT. Release of a model protein from biodegradable self assembled films for surface delivery applications. J Control Release 2008;131:228-234.

48. Shukla A, Avadhany SN, Fang JC, Hammond PT. Tunable vancomycin releasing surfaces for biomedical applications. Small 2010;6(21):2392-2404.

49. Zacharia NS, Modestino M, Hammond PT. Factors influencing the interdiffusion of weak polycations in multilayers. Macromolecules 2007;40(26):9523-9528.

50. Myoken Y, Kayada Y, Okamoto T, Kan M, Sato GH, Sato JD. Vascular endothelial cell growth factor (VEGF) produced by A-431 human epidermoid carcinoma cells and identification of VEGF membrane binding sites. Proc Natl Acad Sci U S A 1991;88(13):5819-5823.

Chapter 5

Adaptive growth factor delivery from polyelectrolyte coatings promotes synergistic bone tissue repair and reconstruction

5.1 Introduction

Grafting materials have been extensively studied for their potential role in regenerating bone tissue and restoring functional properties[1, 2]. However, the primary treatment and closure of large-area bone defects continues to face major technical challenges. The gold standard for craniomaxillofacial (CMF) reconstruction, segmental bone defects and spine fusion is currently autograft transplantation, which is hampered by the limited supply of donor bone and the potential for considerable donor site morbidity associated with the tissue harvest[3, 4]. CMF reconstruction is particularly challenging due to the complexity of reconstructing the three dimensional facial geometry with fidelity while protecting the underlying delicate organ systems. Often multiple surgeries are needed that use complex permanent implant systems. These procedures can lead to permanent deformities, functional impairment and an alteration of physical appearance. There is a compelling need for an off-the-shelf device to manage many kinds of bony defects. Current challenges include the engineering of materials that can regenerate new bone tissue matrix that restores functional properties and is well-integrated with the native bone.

Bone healing and regeneration are orchestrated via the action of a number of growth factors[5, 6]. In the absence of localized morphogenetic cellular stimuli, multicellular processes necessary for bone tissue formation cannot be easily induced. We hypothesized that controlled bone formation in large defects could be induced by simultaneously delivering multiple biological growth factors at different rates, in a controlled and programmable fashion, to the site of the wound. Such an approach would promote bone matrix formation by endogenous progenitor cells by reproducing some of the natural cascade of wound healing cues in bone, and provide biological cues to induce tissue bridging across the wound.

Osteoinductive bone morphogenetic protein (BMP-2) and mitogenic platelet derived growth factor (PDGF)-BB are two of the most prominent growth factors introduced to the clinic in recent years for the treatment of defects in bone presenting as orthopedic and oral and maxillofacial problems[7, 8]. The biomaterial delivery vehicles for these regulatory molecules are essential for their effectiveness. However, bolus release of these growth factors from some injectable or implantable carriers and depots results in a rapid clearance of the protein from the target site by serum proteins. In fact, carriers containing BMP-2 in large quantities have been used in the clinic to compensate for suboptimal BMP-2 release and clearance. The inability of such carriers to modulate growth factor dose for extended time periods from the carrier has resulted in suboptimal tissue regeneration and undesired harmful side effects[9].

Moreover, CMF deformities can vary significantly between patients, requiring both precision control of bone position and shape, and guided restorative therapy that can repair and restore functional properties. These requirements are difficult to achieve with a singular material system; implants that have the appropriate mechanical properties, including metal, calcium phosphate, and degradable polyester scaffolds often do not exhibit the potential to deliver factors in a highly controlled fashion, and with appropriate loadings. Tricalcium phosphate (TCP) based scaffolds loaded with biologics have been examined, but failed to provide a highly controlled release pattern and loading amenable to clinical implementation[10]. On the other hand, hydrogel-based delivery systems can effectively present biological cues, such as growth factors at low doses[11, 12]; however, in some instances, these systems may lack tunable degradation behavior and may break down too quickly for large defect repair in higher animals. Hydrogels can work well in cases for which a physically supported cavity must be filled, but in some instances, these systems may lack either the ability to adapt structural properties for large defect repair in higher animals (as one might with a scaffold) or the independent tuning of both the loading and extended release of growth factors. In general, first-generation biomaterial delivery vehicles are unable to: a) cover large defects in such a way as to maintain a bony contour; b) provide a controlled tunable release of the growth factors; c) enable a lower dose of the growth factor to be used without reducing the osteogenic effectiveness of the device and d) often require the

addition of progenitor cells, that are expanded ex-vivo in a process with technical and regulatory challenges. Thus, there exists a strong motivation to engineer smart systems that efficiently use growth factors to mitigate safety concerns and induce localized and targeted cell-free repair.

We addressed these current design limitations through a nanolayer coating approach that can be applied to a broad range of scaffolds, from metals to degradable plastics and TCP constructs, including highly porous and geometrically complex shapes and contours that might be used for craniofacial reconstruction. In this work, the coating consisted of a micron-scale polyelectrolyte multilayer (PEM) thin film composed of layers of BMP-2 and PDGF-BB growth factors, and can be adapted to release nano- to micrograms of growth factor per unit area for extended and physiologically meaningful time periods for bone healing by endogenous progenitor cells. Our previous studies have demonstrated that we can easily apply the PEM coatings to any substrate of choice, which can be other orthopedic polymers such as polycaprolactone (PCL) and poly(ether ether ketone) (PEEK), metals such as titanium and calcium phosphates[13-16]. To demonstrate the efficacy of this approach, we chose to coat a well-studied biodegradable porous poly (lactic-co-glycolic) acid (PLGA) membrane, with well-understood physicochemical properties. This coated membrane was generated using a simple phase-inversion casting method, cut and customized to the size of the wound prior to application, allowing it to induce targeted bone repair. The polymer membrane had microstructures with interconnected pores that allowed for deposition and sequestration of active biologics within the polyelectrolyte coatings (Fig. 1a). The nanolayer coating that we designed for this system involves a hydrolytically degradable poly (β-amino ester), Poly2, and poly(acrylic acid) (PAA), that causes PDGF-BB to release quickly, along with a more sustained release of BMP-2.

The use of a highly tunable release system that is independent of the mechanical and degradation properties of the underlying substrate allowed independent investigation of impact of controlled staggered release of key growth factors. We hypothesized that time-dependent growth factor delivery from the membrane would (i) recapitulate cellular regenerative processes and substantially enhance bone formation by inducing a mitogenic and osteogenic response and, (ii) promote rapid bone repair and provide a

supporting structure to guide the regenerative process where needed. To potentially enhance bone formation by modulating bone resorption, we also explored the use of alendronate, a bisphosphonate that binds to the mineral phase of osseous tissue, and is an inhibitor of osteoclast resorption of bone. By changing the components of the system, we elucidated structure-function relationships that helped gain new insight into the formation of bone and optimal design. We demonstrated that growth factors released from the polyelectrolyte multilayers allowed direct control of the bone regenerative process to rapidly induce repair in a critical size rat calvaria defect with mechanically competent bone.

5.2 Materials and Methods

5.2.1. Materials.

Alendronate sodium trihydrate (Alfa-Aesar), PLGA (50:50) (MW ~ 38,000-54,000), PAA (Mv ~ 450,000) (Sigma) and PDGF-BB (Osteohealth) were purchased. Poly2 (Mn ~ 12,000) was synthesized using a previously reported method[34]. BMP-2 (Pfizer) was obtained through a materials transfer agreement.

5.2.2. Alendronate conjugation to membrane.

The PLGA membrane was prepared using the diffusion induced phase separation process. A homogenous 20wt% solution of PLGA in dimethylformamide (DMF) was prepared at room temperature and degassed. Using a doctor blade knife, the polymer solution was cast on a glass plate and immersed in deionized water at room temperature for 48h, thoroughly washed and dried at ambient conditions. A micrometer was used to determine the composite membrane thickness by measuring at least 10 different locations including the center. Alendronate was conjugated to PLGA using a modified version of a previously reported procedure[35] and described in Appendix C.

5.2.3. PEM deposition, characterization and release.

Multilayer coatings were deposited using the LbL method. Sodium acetate buffer (0.1M, pH 4.0) was used for preparing polyelectrolyte solutions. Polyelectrolyte solutions were prepared at 1 mg/ml (PAA, Poly2). Concentrations of PDGF-BB and BMP-2 dipping

solutions were adjusted to control the total loading in the PEMs. PLGA membranes 2 cm x 4 cm were sterilized using plasma treatment with air for 5 seconds using a Harrick PDC-32G plasma cleaner (Harrick Plasma) on high RF power and immediately immersed in Poly2 solution. Layers were deposited using a Carl Zeiss HMS-DS50 slide stainer. The substrate was immersed alternatively in Poly2 (5min), PAA (5min), either BMP-2 or PDGF-BB (5min) and PAA (5min). There were 3 wash steps of 10s, 20s and 30s in deionized water between each polyelectrolyte solution. The cycle was iterated 40 times with each growth factor. An 8mm hollow punch (Mayhew Pro) was used to produce circular test samples from the rectangular membrane.

5.2.4. In vivo critical size defect studies.

All animal work was performed in accordance with protocols approved by the Committee on Animal Care (IACUC) at MIT. The critical size defect model has been described previously[22] and described in the Appendix C.

5.2.5. μCT analysis

Anesthetized live animals were imaged with a μCT (eXplore CT120, GE Medical Systems). And the images were reconstructed and analyzed with MicroView (GE Healthcare) as described in the Appendix C.

5.2.6. Histology analysis

After euthanasia at pre-determined time points, calvaria were prepared for histology and stained with Masson's trichrome stain and imaged using brightfield microscopy as described in the Appendix C.

5.2.7. Mechanical testing of calvaria

Explanted calvaria were stored in PBS for immediate mechanical compression testing (Instron 5943). The thickness of the calvaria was measured using a set of calipers before and after applying a constant force of 10N for 60 seconds to measure stiffness. The compressive failure force, perpendicular to the regenerated calvarial bone, was the maximum load achieved before compressive fracture.

5.2.8. Statistical analysis.

Prism 5 (GraphPad) was used for all analyses. Results are presented as means ± SEM. Data were analyzed by ANOVA and comparisons were performed with a Tukey post hoc test (multiple groups). $p < 0.05$ was considered significant.

5.3. Results

5.3.1. Tunable growth factor deposition in PEM coatings

We used PEMs, which are nanostructured coatings formed by a layer-by-layer (LbL) technique of iterative adsorption of alternately charged materials, to design a tunable hydrolytically degrading system (17-20) (Fig. 5.1a). PEMs can sequester and elute multiple biologic cargos in a controlled, pre-programmed manner over several weeks; the release profiles can be easily tuned by modifying the multilayer architecture. We used Poly2, with an aliphatic backbone and a known hydrolytic degradation profile, as the cationic species in the PEM coating. The LbL coating composition consisted of Poly2, PAA, and a growth factor (PDGF or BMP-2) in a tetralayer repeat unit [Poly2/PAA/PDGF-BB/PAA] or [Poly2/PAA/BMP-2/PAA] denoted as P and B respectively. The subscript indicates the total dose of each growth factor in micrograms. To create a gradient concentration of growth factors, the BMP-2 containing layers were deposited directly on the membrane surface. Subsequently, the PDGF-BB containing layers were deposited on top of the BMP-2 containing layers.

5.3.2. Modification of support PLGA membrane

We created a porous, degradable PLGA membrane using a solvent induced ternary system PLGA-DMF-water phase inversion technique to obtain a flexible polymer membrane[21]. The resulting membrane had a hierarchical architecture and a tunable surface chemistry (Fig. 5.1b, c). The cross section of the membrane indicated pores increasing in size along the thickness of the membrane, and varied from 2μm on the top surface to 200μm on the bottom surface (Fig. 5.1c; Fig. C1). We explored the use of PLGA with end-groups conjugated with alendronate, which has a high affinity for hydroxyapatite and is used in the clinical management of osteoporosis. We activated

the PLGA terminal hydroxyl group to generate a highly efficient chloroformate leaving group, which was quantitatively substituted by the alendronate amine group (Fig. C2). The reaction placed negatively charged phosphonate end groups at the end of the hydrophobic PLGA backbone, to generate an amphiphilic molecule. We hypothesized that as the membrane degrades, the released alendronate is able to bind to hydroxyapatite, thus inhibiting bone resorption and potentially leading to rapid bone formation. Unmodified membranes and alendronate conjugated PLGA membranes are denoted as M and M_{Al} respectively. Scanning electron micrographs (SEM) of PLGA membranes coated with growth factors revealed a conformal, single coating on the membrane and the internal microstructure (Fig. 5.1e); typically the coating thickness was ~0.5 μm for single growth factor and ~1 μm for dual growth factor coatings. .

5.3.3. Bone repair in a critical size defect model

A relevant model to illustrate the clinical translational potential for treating CMF bone defects is a critical-size calvarial defect in a skeletally mature rat, corresponding to an 8mm circular wound[22]. Calvarial defects can answer questions about the biocompatibility and the biological functions of bone repair materials and morphogens before putting them into a clinical setting. The healing process in this animal model has been well characterized. It has been demonstrated that the rate of scaffold degradation is critical to bone healing[23]. We first examined the kinetics of degradation of the PLGA membrane in the wound healing environment of the defect. We held the membrane thickness constant at 120 ± 10 μm (SEM) and monitored in vivo degradation of a $P_{0.2}$ + $B_{0.2}$ coated membrane as a function of the PLA:PGA ratio in the PLGA copolymer. The objective was to select a ratio that would yield a degradation half-life of about 4 weeks to coincide with bone growth. The mass and diameter of the uncoated membranes placed in the rat cranial defect were monitored at pre-determined time intervals to determine a relationship between copolymer ratio and rate of degradation. We observed that PLA: PGA (50:50) yielded the desirable degradation profile for cranial defect healing (Fig. C3). The end-functionalization of alendronate to the PLGA (50:50) backbone did not noticeably alter the in vivo degradation kinetics.

Progenitor cell activation and bone tissue repair are highly sensitive to growth factor

dose and its local availability. To induce the desired biological response for bone tissue repair, we examined the effect of growth factor combinations released from the PEM coating. To maintain coating thickness and duration of biologic release across the different combinations, we aimed to incorporate different amounts of growth factor with the same number of layers in the coating. 40 layers of each growth factor were applied either individually or in combination in a B or P tetralayer repeat unit. Drug loading per layer was proportional to growth factor concentration and was used to control the amount of growth factor that was incorporated in the PEM coating. In dual growth factor releasing PEMs, the growth factors were arranged so that BMP-2 was incorporated in the bottom 40 layers closest to the membrane and the PDGF-BB was incorporated in the subsequent 40 layers. This resulted in a concentration gradient of growth factors within the film and allowed for differential rates of growth factor release with complete elution of PDGF-BB followed by BMP-2 in vivo (Fig. 5.2a). $P_{0.2}$ + $B_{0.2}$ coatings were applied on PLGA membranes and PDGF-BB and BMP-2 were tracked simultaneously using near-IR dyes in the same animal. PDGF-BB was detectable for about 11 days post-surgery, whereas BMP-2 was detected for 20 days. This corresponded to similar in vitro release profiles from the P and B single growth factor coatings (Fig. 5.2b). Importantly, burst release of either growth factor was not observed; rather the release was sustained over different times, as intended.

We systematically investigated the effect of growth factor formulations on inducing tissue repair (Table C1). Bone healing in this model is characterized by new bone tissue deposition and coverage of the defects. We monitored the healing process temporally using microcomputed tomography (μCT) (Fig. 5.3a). As anticipated, no bone healing was observed in an untreated defect. Spicules of bone were observed with an uncoated membrane which did not integrate with the parent bone. B and P+B layers induced a potent bone healing response and induced closure within 4 weeks post-treatment. Defects reconstructed with growth factor loaded PLGA membranes exhibited multifocal bone formation, where new bone formation initiated at the margins and gradually filled in the defect. Repair initiated by P+B layers together resulted in a smaller defect after 2 weeks compared to single factor BMP-2 induced repair (Fig. 5.3b). While increasing the total dose of BMP-2 above 0.2μg did not appear to alter the rate of bone repair, a

qualitative comparison of the two groups at 2 weeks indicated that more BMP-2 resulted in a greater level of bone remodeling activity at and around the defect site. Using the M_{AI} membrane resulted in a remarkable difference to the rate and quality of bone repair. At 2 weeks, single growth factor BMP-2 release from the M_{AI} membrane appeared to reduce the rate of bone repair, and resulted in a larger defect when compared to the unmodified membrane, likely owing to the inhibition of bone remodeling and migration of new bone into the defect. However, at the end of 4 weeks, the defect completely bridged with new bone that had a significantly higher bone volume (BV) and bone mineral density (BMD) than the single and dual growth factor groups. Taken together, these observations suggest that the alendronate binds with high affinity to newly formed bone tissue and prevents remodeling, a known physiological effect of bisphosphonates. The action of BMP-2 caused osteoblasts to continue bone deposition, thus significantly more bone tissue is present throughout the repair site. At 4 weeks, the BMD of bone formed by B layers alone was lower than that of native calvaria and bone formed by P+B layers. However, these groups had comparable BV, suggesting that BMP-2 delivery alone resulted in less mature bone.

5.3.4. Histological evaluation of regenerated bone

A histological examination revealed the underlying cellular processes involved in bone repair (Fig. 5.4a). There were no indications of adverse foreign body reactions as evidenced by the lack of foreign body giant cells, long-term inflammation or infection. Bone formation processes were completely absent in the untreated defect. Tissue formation in the uncoated membrane group was sparse, structurally immature and lacked connection with the existing bone. Loosely arranged collagen fibers were present with only partial bony ingrowth at the wound margins. Outer and inner cortical tables were variably present. In contrast, bone formed under the influence of growth factors in the treatment groups was trabecular, with evidence of remodeling and maturation with extensive bone development in a hypercellular environment that is characteristic of bone wound healing. In all growth factor treated groups, the defect was completely bridged within 4 weeks with bone that exhibited ongoing active remodeling processes for all growth factor treated groups. New bone formed as a result of B layers alone

lacked mineralization and compact bone formation. The osteoid layer had wide borders indicating that rapid tissue deposition preceded mineralization. Qualitatively, the bone formed by P+B layers had a greater number of vascular channels and a higher cell density within the bone, indicating the mitogenic role of PDGF-BB in the bone formation process. We observed that the growth factor coated PLGA polymer membrane resulted in bone repair via intramembranous ossification preceded by highly cellular granulation tissue supported by the membrane (Fig. 5.4b). We observed that as new bone filled the gap the tissue layer remodeled and reduced in thickness from 1 to 2 weeks, eventually reducing to a one-cell thick layer form after bone had completely filled the gap at about 4 weeks post-surgery. The thick tissue layer was a rich source of progenitor cells for bone repair and helped nucleate the repair machinery. Bone formation under the influence of the M_{AI} membrane bridged the gap with excess bone that lacked specific orientation and was less compact compared to bone formed under the influence of B layers alone. These observations are consistent with a lack of remodeling behavior in the presence of alendronate.

5.3.5. Comparison of bone mechanical properties

We performed compression tests to investigate the mechanical integrity of the reconstructed region and obtain a measure of the mechanical properties of the restored bone (Fig. 5.5). We measured the stiffness and compressive failure force for the regenerated bone for the different groups at the 4 week end-point and compared it to native calvaria bone that was not injured. Tissue regenerated with the uncoated PLGA membrane lacked a cohesive bone structure and thus had low stiffness and a very low resistance of 16.9 ± 3.8 (s.e.m.) MPa to compressive load. Bone formation was significant, organized and cohesive with B layers alone and thus had a higher stiffness of ~ 82 MPa, independent of BMP-2 dose. This value was ~ 27% lower than the stiffness of native calvaria bone. However, bone formation with P+B layers was comparable to that of native bone. These observations correspond well to the disparate histological observations. Bone formed with B layers alone was less mature, lacked significant mineralization, which resulted in a lower stiffness compared to native bone. On the other hand, PDGF-BB and BMP-2 co-delivery resulted in mature bone formation

with mechanical properties that closely matched those of the native calvaria. A similar structure-property relationship existed for bone formed with the M_{Al} membrane. As noted, the excess bone present was not compact and we observed that the bone was ~ 43% stiffer than the native calvarial bone. Loose tissue formed by uncoated PLGA membrane had very low resistance to compressive loads and fractured easily. Bone formed by BMP-2 alone had ~ 14% lower compressive strength than native calvaria bone and was dose independent, owing to a lack of maturation and corresponded with the observation of lower stiffness. BMP-2 and PDGF-BB acted in concert to induce bone with the same mechanical loading behavior as that of the native calvaria. M_{Al} + $B_{0.2}$ resulted in stiffer bone and the mechanical failure load was significantly lower. This is explained by the lower cohesiveness of brittle bone and the consequent non-uniform load distribution.

5.3.6. Discussion

The search for new bone regeneration strategies has emerged as a key priority fueled by the increasing medical challenges of a burgeoning aging population. In this study, we have used materials for directing bone tissue repair processes by the fine-tuned and robust tunable spatio-temporal control of biologics from a thin film coating. Recent work has demonstrated the benefit of delivering multiple growth factors for bone tissue engineering[24]. Dose tunability and delivery of these potent biologics in a manner that can be adapted for clinical application is critical to success of this strategy. In this study, we have demonstrated that the release rates of the growth factors can be tailored using the PEM coatings. Typically, growth factors are released from particle systems or scaffolds that persist in the wound and in some cases may even hinder formation of cohesive, mechanically competent bone that also recapitulates geometry[25]. The time taken to induce repair is significantly longer and the reported bone strength with these permanent systems is often lower than native bone[26]. Our studies suggest that the release of specific known growth factors, BMP-2 and PDGF-BB either individually or in combination, is critical to enhanced bone regeneration. This combination of growth factors has been reported to induce rapid and successful bone tissue regeneration[27]. This strategy of delivering multiple growth factors with tunable control is particularly

crucial in higher order animals including humans, which have a slower rate of bone repair than rodents[28]. The PEM coating can be applied even if the thickness of the supporting membrane, its mechanical stiffness, and the even material of the membrane itself were modified to tune the degradation kinetics for adoption to higher animals. In this study, through the combination of specific materials known to play a role in bone formation, we developed an understanding to control the rate, amount and quality of bone to repair a defect, and provided structure-function relationships.

Large scale production of proposed bone repair materials is a significant barrier to their clinical application and has severely limited their translational potential. Our method of making the composite polyelectrolyte coated surface is extremely scalable that can be several meters long and of controllable thickness[29]. Importantly, PEM assembly uses mild, aqueous conditions that preserve the activity of fragile biologics. We have previously demonstrated the importance of controlling the release of biologics from multilayer films by introducing the therapeutic as a layer during the PEM assembly process[30]. Lack of toxicity is critical for materials used in implantable devices, and the long-term host response to permanent implants continues to be a concern. In this work all the components were selected with biocompatibility in mind: PLGA is a biodegradable polymer with a long history of clinical use in drug delivery devices and used in bone fixation systems with no adverse immunogenic responses[31]; furthermore, the same approach with PEM coatings can be applied to other biodegradable membranes and scaffolds, as we have described previously. Previous studies have demonstrated the compatibility of the poly(β-amino ester) family in vitro and in vivo[32, 33]. PAA is a well-characterized weak polyanion with a high charge density distributed over a non-erodible backbone that has been listed as an approved excipient in the FDA's Inactive Ingredient Guide and is used in the clinic. The 10wt% PLGA-alendronate is several orders of magnitude lower than the doses that are known to cause side-effects. Consistent with these expectations, we observed no local toxicity in any of the animals treated throughout these studies. We have demonstrated in previous studies that growth factors and other biologics incorporated in multilayer coatings on devices maintains their bioactivity after release, even after room temperature storage in the dry state[14, 32]. Importantly, this strategy is cell-free and does not rely on the extraction and

ex-vivo expansion of progenitor cells for re-implantation in the body. In effect, these nanolayered coatings can be adapted on demand to induce repair in a variety of bone defect types by recruiting endogenous progenitor cells. This approach provides a new alternative to autologous bone grafts, and negates the need for transplanted stem cells in scaffolds for CMF bone repair and reconstruction. Although the true potential of any bone regeneration strategy can only be realized through large animal pre-clinical studies and ultimately human clinical trials, the data shown here suggest that bone healing using an engineered regenerative surface is a potent strategy for safe, precise and targeted tissue repair, and demonstrates the use of alternating nanolayer assembly as a platform technology with the potential to be applied universally in regenerative medicine.

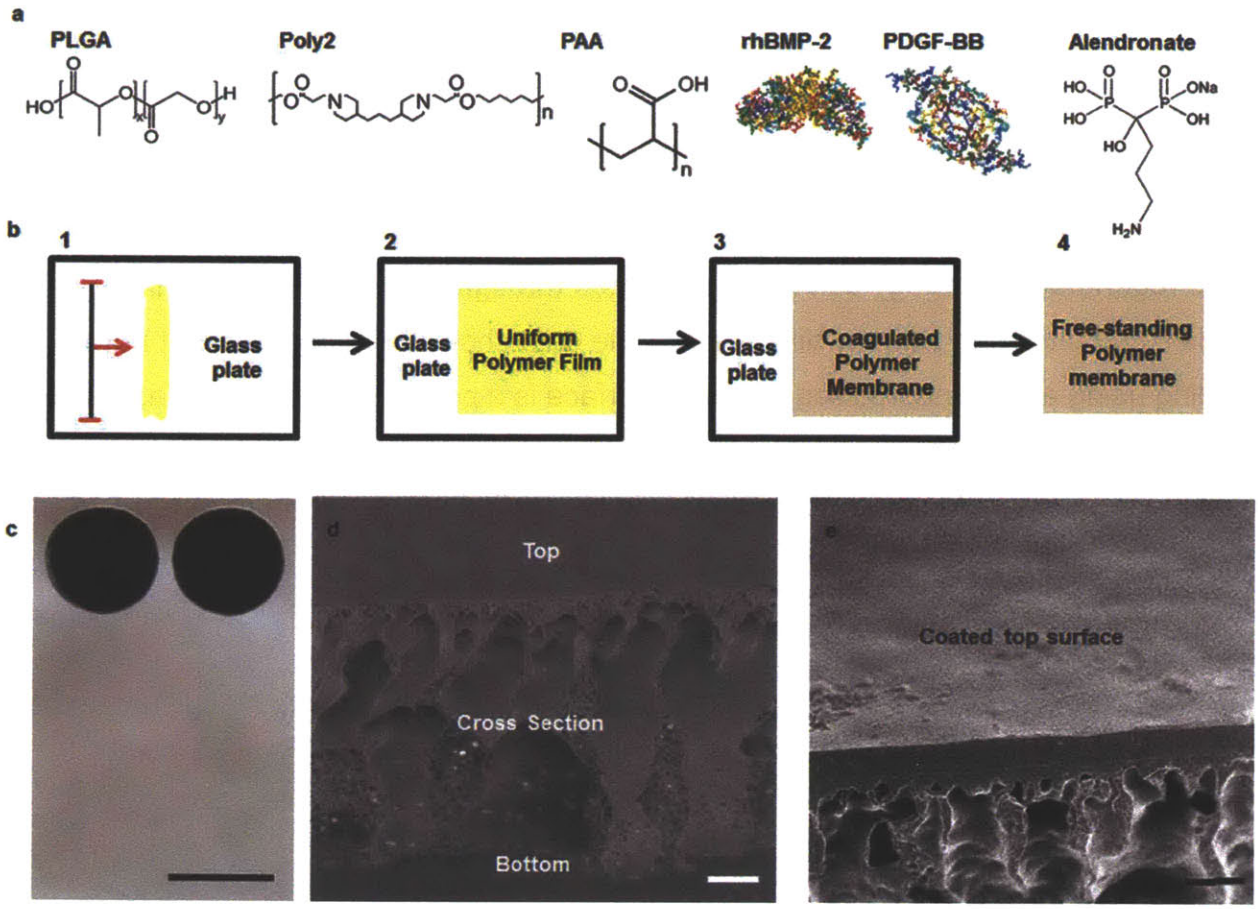

Figure 5.1. Design of the multilayer polymer "skin". (a) Molecular structures of materials in the system. Hydrophobic PLGA is used to form the membrane. Poly2, PAA, BMP-2 and PDGF-BB are part of the bioactive interface that initiates the bone wound healing cascade. The bisphosphonate molecule alendronate is conjugated to PLGA. (b) Schematic of the phase-inversion membrane formation process. (1) A PLGA-DMF solution is poured on a glass plate. (2) A doctor blade is used to spread the polymer solution uniformly on the glass plate and is (3) immersed into a deionized water bath. (4) The resulting film detaches from the glass substrate. (c) Macroscopic image of the membrane structure that results in a uniform polymer support (scale bar, 8mm). (d) Scanning electron micrographs demonstrating a highly ordered cross section (scale bar, 10μm) (e) PLGA membrane coated with $[Poly2/PAA/rhBMP\text{-}2/PAA]_{40}$ + $[Poly2/PAA/rhPDGF\text{-}BB/PAA]_{40}$ (scale bar, 2μm)

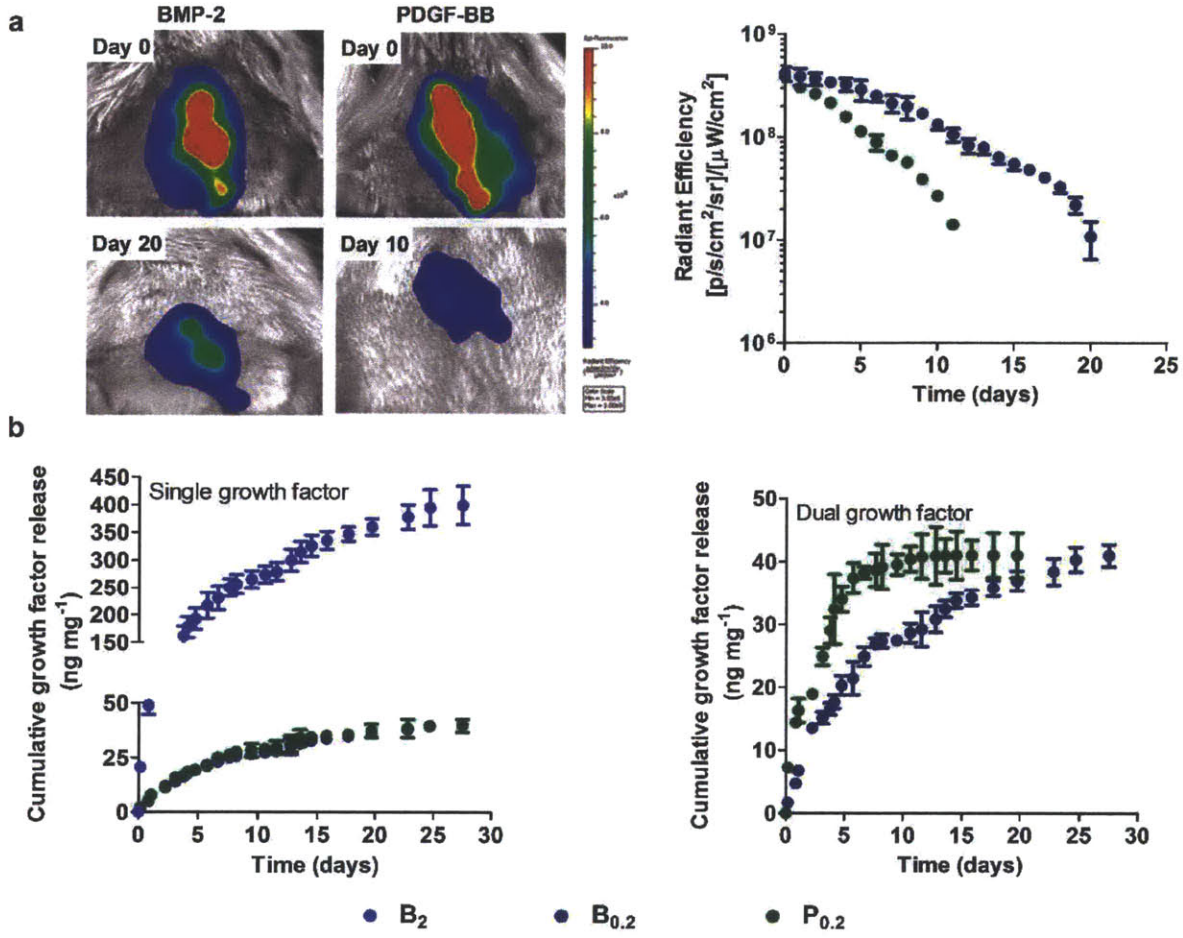

Figure 5.2. In vivo and in vitro evaluation of growth factor release. PDGF-BB and BMP-2 were loaded into the multilayers that coated the membrane and then implanted in the critical size defect of a rat calvaria (n = 4-5 per group). (a) In vivo release of PDGF-BB and BMP-2 was tracked for 11 and 20 days respectively (b) In vitro Growth factor release in single and combination films from PLGA membranes. Data represent the means±s.e.m.

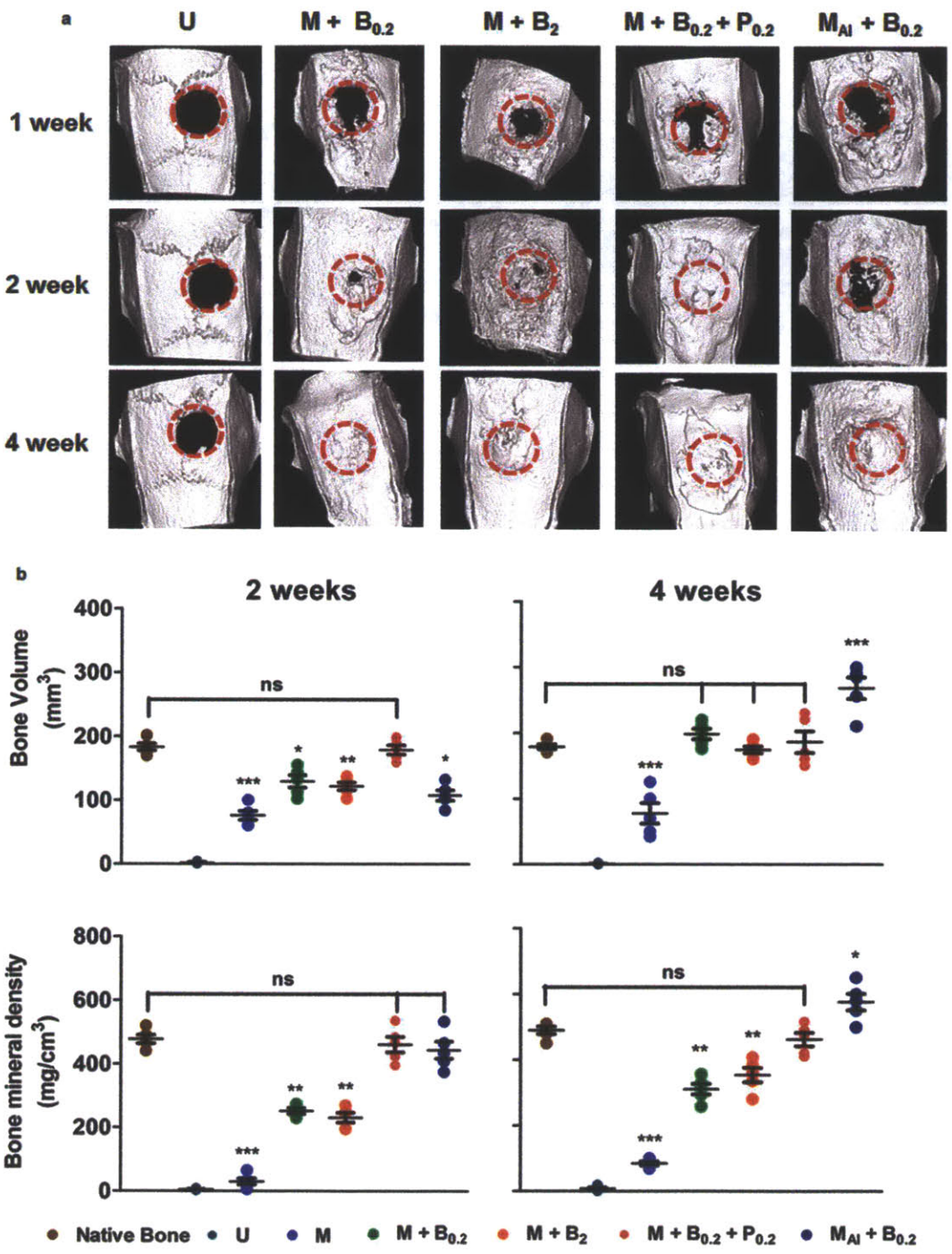

Figure 5.3. μCT imaging of bone repair in live animals. (a) Representative radiographs of bone formation around drilled implants with different coatings at 1, 2, and 4 weeks. Red broken circle indicates the location of the defect in each radiograph and has an 8mm diameter. Defect closure was achieved in all animal groups with different treatment conditions within 4 weeks. n = 5 per group. (b) The images in (a) were used to quantify bone volume and bone mineral density at 2

and 4 weeks within the regions of interest marked by dotted red circles. Each point represents individual animal. Data are means±s.e.m. (n = 5-6 per group). *$p < 0.05$, **$p < 0.01$, ***$p < 0.001$, ns = not significant, ANOVA with Tukey post hoc test. All groups are compared with the mechanical properties of the M + $B_{0.2}$ +$P_{0.2}$ group.

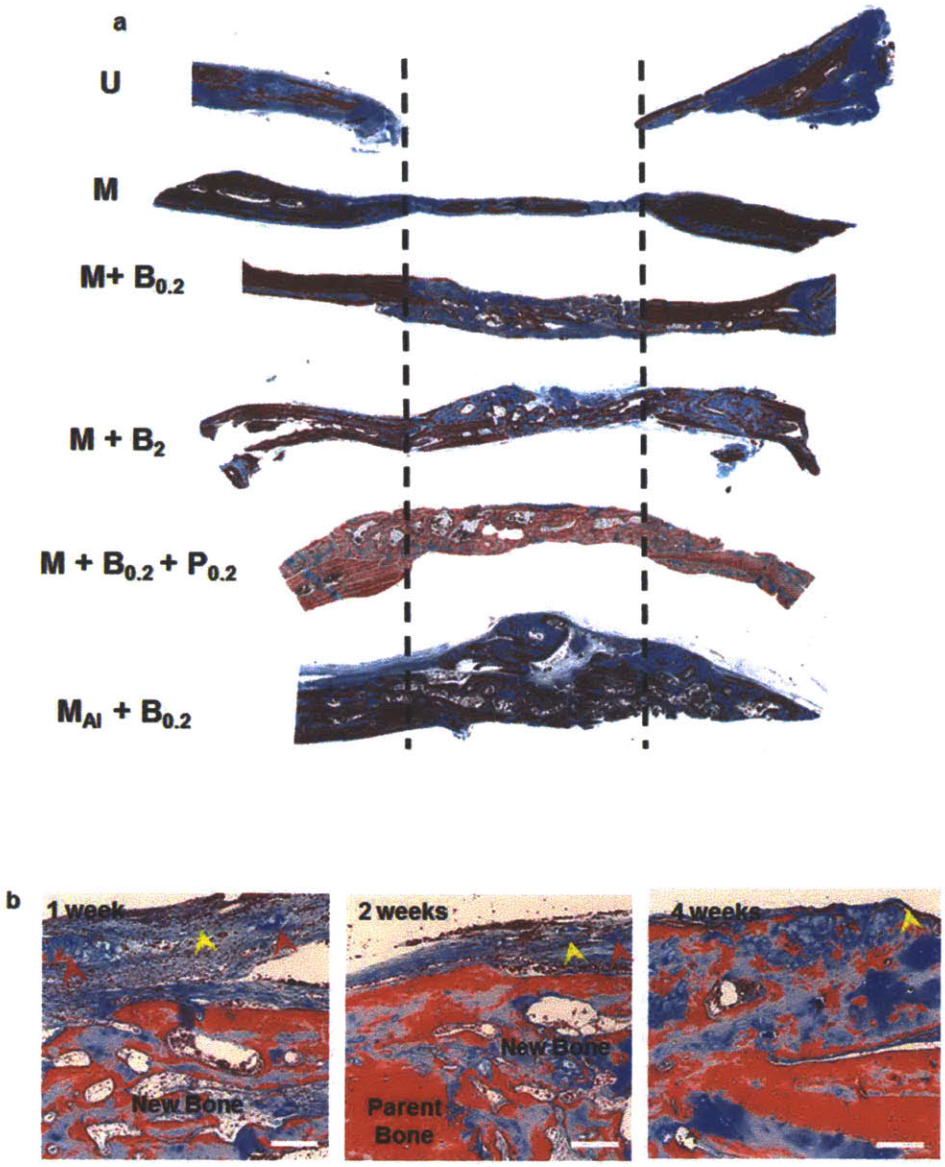

Figure 5.4. Histology of new tissue formed with various coating formulations. (a) Each image is a cross section of the calvarial defect after 4 weeks, at which time different levels of bone tissue morphogenesis was observed at the defect site. The broken lines indicate the position of the defect site and are 8mm apart. Collagen is represented by blue and osteocytes (mature bone) is represented by red. Sections were stained with Masson's trichrome stain and viewed under bright field microscopy. (b) Granulation tissue layer at 1, 2 and 4 weeks during bone repair in the M + $B_{0.2}$ + $P_{0.2}$ treatment group. The tissue gradually reduces in thickness from 1 to 4 weeks as bone repair is completed. Pieces of the PLGA membrane were observed in some section (scale bar, 30μm). Arrows: red, PLGA membrane; yellow, granulation tissue layer.

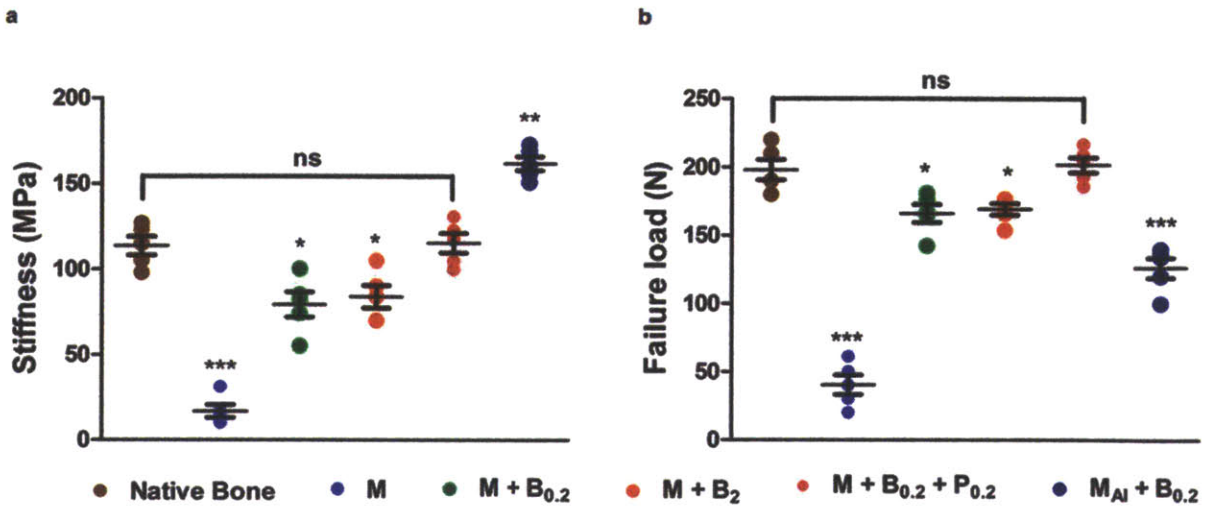

Figure 5.5. Mechanical compression testing of calvaria bone (a) Stiffness and (b) Failure load from different groups are presented at 4 weeks after implantation. Data are means±s.e.m. (n = 5 implants per group). *p < 0.05; **p < 0.01; ***p < 0.001, ns = not significant, ANOVA with a Tukey post hoc test. All groups are compared with the mechanical properties of the M + $B_{0.2}$ +$P_{0.2}$ group.

5.5 References

1. Place ES, Evans ND, & Stevens MM (2009) Complexity in biomaterials for tissue engineering. Nat Mater 8(6):457-470.

2. Woodruff MA, et al. (2012) Bone tissue engineering: from bench to bedside. Materials Today 15(10):430-435.

3. Neovius E & Engstrand T (2010) Craniofacial reconstruction with bone and biomaterials: review over the last 11 years. Journal of plastic, reconstructive & aesthetic surgery : JPRAS 63(10):1615-1623.

4. Dimitriou R, Jones E, McGonagle D, & Giannoudis PV (2011) Bone regeneration: current concepts and future directions. BMC medicine 9:66.

5. Vo TN, Kasper FK, & Mikos AG (2012) Strategies for controlled delivery of growth factors and cells for bone regeneration. Adv Drug Deliv Rev 64(12):1292-1309.

6. Hollinger JO, Hart CE, Hirsch SN, Lynch S, & Friedlaender GE (2008) Recombinant human platelet-derived growth factor: biology and clinical applications. The Journal of Bone & Joint Surgery 90(Supplement_1):48-54.

7. Triplett RG, et al. (2009) Pivotal, randomized, parallel evaluation of recombinant human bone morphogenetic protein-2/absorbable collagen sponge and autogenous bone graft for maxillary sinus floor augmentation. Journal of oral and maxillofacial surgery : official journal of the American Association of Oral and Maxillofacial Surgeons 67(9):1947-1960.

8. Nevins M, et al. (2005) Platelet-derived growth factor stimulates bone fill and rate of attachment level gain: results of a large multicenter randomized controlled trial. J Periodontol 76(12):2205-2215.

9. Carragee EJ, Hurwitz EL, & Weiner BK (2011) A critical review of recombinant human bone morphogenetic protein-2 trials in spinal surgery: emerging safety concerns and lessons learned. Spine J 11(6):471-491.

10. Hollister SJ & Murphy WL (2011) Scaffold translation: barriers between concept and clinic. Tissue Engineering Part B: Reviews 17(6):459-474.

11. Martino MM, et al. (2011) Engineering the growth factor microenvironment with fibronectin domains to promote wound and bone tissue healing. Sci Transl Med 3(100):100ra189.

12. Lin C-C & Anseth KS (2009) PEG hydrogels for the controlled release of biomolecules in regenerative medicine. Pharmaceutical research 26(3):631-643.

13. Shah NJ, et al. (2011) Tunable dual growth factor delivery from polyelectrolyte multilayer films. Biomaterials 32(26):6183-6193.

14. Shah NJ, et al. (2013) Surface-mediated bone tissue morphogenesis from tunable nanolayered implant coatings. Sci Transl Med 5(191):191ra183.

15. Facca S, et al. (2010) Active multilayered capsules for in vivo bone formation. Proc Natl Acad Sci U S A 107(8):3406-3411.

16. Crouzier T, et al. (2011) The performance of BMP-2 loaded TCP/HAP porous ceramics with a polyelectrolyte multilayer film coating. Biomaterials 32(30):7543-7554.

17. Decher G (1997) Fuzzy Nanoassemblies: Toward Layered Polymeric Multicomposites. Science 277:1232.

18. Hammond PT (2004) Form and function in multilayer assembly: New applications at the nanoscale. Advanced Materials 16(15):1271-1293.

19. Boudou T, Crouzier T, Ren K, Blin G, & Picart C (2010) Multiple functionalities of polyelectrolyte multilayer films: new biomedical applications. Adv Mater 22(4):441-467.

20. Tang Z, Wang Y, Podsiadlo P, & Kotov NA (2006) Biomedical Applications of Layer-by-Layer Assembly: From Biomimetics to Tissue Engineering. Advanced Materials 18(24):3203-3224.

21. Mikos AG, et al. (1994) Preparation and Characterization of Poly(L-Lactic Acid) Foams. Polymer 35(5):1068-1077.

22. Spicer PP, et al. (2012) Evaluation of bone regeneration using the rat critical size calvarial defect. Nature protocols 7(10):1918-1929.

23. Alsberg E, et al. (2003) Regulating bone formation via controlled scaffold degradation. J Dent Res 82(11):903-908.

24. Lee K, Silva EA, & Mooney DJ (2011) Growth factor delivery-based tissue engineering: general approaches and a review of recent developments. Journal of The Royal Society Interface 8(55):153-170.

25. Mistry AS & Mikos AG (2005) Tissue engineering strategies for bone regeneration. Regenerative Medicine II, (Springer), pp 1-22.

26. Will J, et al. (2008) Porous ceramic bone scaffolds for vascularized bone tissue regeneration. Journal of Materials Science: Materials in Medicine 19(8):2781-2790.

27. Martino MM, et al. (2014) Growth Factors Engineered for Super-Affinity to the Extracellular Matrix Enhance Tissue Healing. Science 343(6173):885-888.

28. Giannobile; WV & Nevins M (2012) Osteology Guidelines for Oral and Maxillofacial Regeneration: Preclinical Models for Translational Research (Quintessence Publishing).

29. Krogman KC, Lowery JL, Zacharia NS, Rutledge GC, & Hammond PT (2009) Spraying asymmetry into functional membranes Layer-by-Layer. Nature Materials 8:512-518.

30. Shah NJ, et al. (2013) Surface-Mediated Bone Tissue Morphogenesis from Tunable Nanolayered Implant Coatings. Science Translational Medicine 5(191).

31. Landes CA, Ballon A, & Roth C (2006) Maxillary and mandibular osteosyntheses with PLGA and P(L/DL)LA implants: A 5-year inpatient biocompatibility and degradation experience. Plastic and Reconstructive Surgery 117(7):2347-2360.

32. DeMuth PC, et al. (2013) Polymer multilayer tattooing for enhanced DNA vaccination. Nature Materials 12(4):367-376.

33. Shukla A, et al. (2010) Controlling the release of peptide antimicrobial agents from surfaces. Biomaterials 31(8):2348-2357.

34. Lynn DM & Langer R (2000) Degradable poly(beta-amino esters): Synthesis, characterization, and self-assembly with plasmid DNA. Journal of the American Chemical Society 122(44):10761-10768.

35. Wang D, Miller S, Sima M, Kopeckova P, & Kopecek J (2003) Synthesis and evaluation of water-soluble polymeric bone-targeted drug delivery systems. Bioconjugate chemistry 14(5):853-859.

Chapter 6

Osteotropic therapy via targeted Layer-by-Layer nanoparticles

6.1 Introduction

The development, maintenance, and repair of bone require cell-mediated remodeling to sustain the structural integrity of the tissue. Disturbances in the physiological processes of osteoblast-mediated bone deposition and osteoclast-mediated bone resorption are observed in many bone-related disease states, such as osteosarcoma, cancer metastasis to bone, osteoporosis, and Paget's disease of the bone.[1] Several therapies have been developed to combat these pathologies;[1,2] however, the clinical outcomes for patients with these diseases continue to be very poor. The arsenal of available agents to treat patients has not made any substantial impact in improving their survival, and new methods for therapy are critical. Engineering a robust delivery platform with bone-tissue level specificity to treat these diseases can improve therapeutic efficacy, lower systemic toxicity, and improve disease management.

Significant fundamental work in the area of bone biology has uncovered the potential of bone-specific agents, such as bisphosphonates.[2b,3] These compounds act as pharmacophores, whereby the pyrophosphate-like structure coordinates calcium ions within the hydroxyapatite mineral in bone with high affinity and specificity. Accumulation of bisphosphonates further promotes inhibition of bone resorption by inducing apoptosis in osteoclasts that are responsible for this action. As such, this class of pharmaceutics is a potent drug for promoting homeostasis between osteoclast and osteoblast activity in, for example, osteoporosis, while also promoting tissue-specific binding and localization.

Bone targeting systems[4] have been synthesized to utilize the specificity of a variety of ligands, including bisphosphonates, tetracycline and derivatives, sialic acid, and bio-inspired materials containing similar functionalities;[2b] however, systems capable of therapeutic delivery for treatment of bone-related diseases remain limited. Towards this end, the modularity of Layer-by-Layer (LbL)-functionalized nanomedicine systems[5]

presents an attractive opportunity to incorporate these bone-specific, highly water-soluble ligands on the surface of nanotechnology for targeted drug delivery. LbL assembly[6] is a highly controlled approach to iteratively deposit materials and functionalize the surface of virtually any substrate on the basis of complementary interactions, such as electrostatics. This method allows for tunable, nanoscale precision over system design, allowing for the construction of a customizable therapeutic delivery platform.[5–8] Recent work has demonstrated the potential for LbL nanoparticle systems to promote improved pharmacokinetics and biodistribution of the carrier and drug in vivo,[9] with the ability to modulate release of encapsulated therapeutics. Complementary studies investigated tumor microenvironment cue-sensitive designs (e.g., pH-responsive)[10] that harnessed tumor hypoxia to promote enhanced localization and uptake in tumors. Further, these built-to-order systems have been recently manufactured on a scalable platform,[11] demonstrating potential to mass-produce these systems with high levels of control.

In this study, we report the synthesis of tissue-targeted LbL nanoparticles, specifically manufactured to hone in on bone tissue. To achieve this, a polyelectrolyte, poly(acrylic acid) (PAA), was functionalized with a bisphosphonate, alendronate, and subsequently electrostatically assembled in a nanoparticle coating. The functionalized particles accumulated in subcutaneous 143B osteosarcoma xenografts, where they delivered their payload, doxorubicin, in a mouse model. The targeted particles significantly attenuated tumor burden and extended animal survival, in some cases even completely eliminating tumors. The results described herein establish LbL as a modular approach to develop targeted drug carriers via adsorption of ligand-functionalized, aqueous polyelectrolytes for tissue specific targeting, further developing these systems towards clinical application.

6.2 Materials and Methods

6.2.1.PAA-Alendronate Conjugation

Alendronate (Alfa-Aesar) was conjugated to poly(acrylic acid) (Sigma) through the primary amine functional group of alendronate. Half of the free carboxyl end groups of poly(acrylic acid) was targeted for coupling. A water-soluble coupling agent was used

for the water-based reaction: 4-(4,6-dimethoxy-1,3,5-triazin-2-yl)-4-methylmorpholinium chloride (DMTMM).[13] To perform the coupling chemistry, alendronate (1.0 eq.) was added to a solution of poly(acrylic acid) (0.5 eq. considering all carboxylic groups) in 100 mL water. The solution was stirred for 10 min after which DMTMM (2.0 eq.) was added to the resulting solution. The reaction was allowed to run for 12 h at room temperature. After the reaction period, the solution was dialyzed against water for 36 h for complete removal of coupling agent and unreacted alendronate. The dialyzed solution of alendronate conjugated poly(acrylic acid) was lyophilized to yield a white foam-like product in 65% yield. ^{1}H NMR (in D 2 O): 1.33–1.9 ppm [broad signal, poly(acrylic acid)], 2.10–2.40 ppm [broad signal, poly(acrylic acid)], 2.88 ppm (^{2}H, alendronate). The degree of conjugation was estimated according to the assay protocol reported previously, whereby it was quantified following the hydrolysis of the conjugate at pH 10 with 0.1 M NaOH.[14] The estimated degree of functionalization was found to be 43.2%.

6.2.2. LbL on QDs

Carboxyl-modified quantum dots (QD800, Life Technologies) were suspended in dilute solution (~10 µL stock in 1 mL DI water) and injected in excess 10 mL polyelectrolyte (5 mg mL^{-1} for PLL-Hydrochloride (4–15 K, Sigma); 1 mg mL^{-1} PAA 450K -Alendronate) while under agitation at 4°C. Each layer was incubated for ~30 min, prior to purification via ultracentrifugation (12,500 RPM, 30 min - first layer required longer spins, subsequent purifications are much more expedient) and washing with DI water, repeated twice prior to introduction to the subsequent polyelectrolyte. The final functionalized particle was re-suspended in 1X PBS after the second wash and filtered in a 0.45 µm filter for further experimentation.

6.2.3. Liposome Synthesis

Liposomes were formulated at a mass ratio of 56:39:5 (DSPC:Cholesterol:POPG, DSPC and POPG purchased from Avanti Polar Lipids, Cholesterol from Sigma). These three components were dissolved in a 2:1 mixture of chloroform:methanol. A thin film of these materials was generated by rotary evaporation at 40°C, 150 mbar for approximately 10 min. This fi lm was allowed to dessicate overnight for complete drying.

Hydration of the lipid fi lm was conducted at 65 ° C under sonication in 0.3 M citric acid buffer (pH 4) for 1 h, after which they were filtered through a 0.2- μ m PES syringe filter and allowed to cool to room temperature. The pH of the liposomal suspension was then adjusted to 6.5 by addition of 0.3 M sodium carbonate buffer to create a gradient between the exterior and interior compartments. Doxorubicin (LC Laboratories) at a feed ratio of 3 mg drug to 50 mg lipids was then added in a 0.9% sodium chloride solution to load via a pH gradient method. The fi nal drug-loaded system was subsequently purified out of the high salt buffers and any excess, unloaded drug via centrifugal filtration (100K MWCO Millipore) and transferred to DI water for subsequent functionalization via LbL. Blank liposomes were prepared in the same fashion; however, no drug was added.

6.2.4. LbL on Liposomes

Liposomes were diluted in 1 mL DI water (from a 50 mg (total lipid) batch prepared in a final suspension of 5 mL DI water, used ~200 μ L stock to 800 μ L DI water) and injected in excess polyelectrolyte under agitation at 4 ° C as previously described for QDs. Particles were incubated for ~30 min, purified via ultracentrifugation at 10,000 RPM for ~10 min, followed by aspiration of supernatant and subsequent re-suspension in DI water. Purification was repeated twice prior to introduction to the subsequent polyelectrolyte. The final functionalized liposomal system was filtered through a 0.45-μm filter and suspended in 1X PBS for further experimentation.

6.2.5. Physicochemical Characterization

Dynamic light scattering and zeta potential analysis were conducted in 1×10^{-2} M sodium chloride at 25 ° C using a Malvern ZS90 zeta-sizer. High-performance liquid chromatography (Agilent technologies, 1:1 acetonitrile to pH 5 water mobile phase) and nanodrop absorbance measurements (480 nm) were performed to quantify doxorubicin concentrations in the prepared samples. Cryo-TEM was conducted by imaging a frozen dilute sample of the liposomal suspension at 120 kV.

6.2.6. In Vitro Binding/Cytotoxicity

143B osteosarcoma cells and human mesenchymal stem cells were seeded in 96-well tissue culture plates at a density of 1×10^3 cells/well and allowed to proliferate for 48 h.

PLL-Cy5.5 labeled particles were quantified based on fluorescence, serially diluted in cell culture media and added to the cells. After 24–48 h at 37°C, cells were washed 3× with PBS. Binding was measured by quantifying the amount of residual fluorescence in the well. Cytotoxicity was measured using a standard MTT assay.

6.2.7. Fluorescence-Activated Cell-Sorting Analysis

Measurements were performed using a BD LSRFortessa (BD biosciences, San Jose, CA). PLL-Cy5.5 fluorescence was collected following excitation at 640 nm and detected at 710/50 nm (AF700 channel). Cell-association data presented as representative histogram overlays of data collected in triplicate following 143B cell incubation with blank, PLL-Cy5.5 coated, PAA-Alendronate functionalized LbL liposomes for 2 h at 37°C in 96-well plates. Final samples ran for analysis were washed 3× with optiMEM and trypsinized immediately prior to introduction to the flow cytometer. Blue is the representative treatment; red is the control sample without treatment.

6.2.8. Confocal Microscopy

Images were taken using a Nikon A1R Ultra-Fast Spectral Scanning Confocal Microscope (Nikon instruments Inc., Melville, NY). 143B cells were seeded in a CELLview glass bottom dish (Greiner Bio-One GmbH, Germany) at 1×10^5 cells per well and grown overnight. Cells were then incubated with blank, PLL-Cy5.5 coated, PAA-Alendronate functionalized LbL liposomes (or QDs) for 2 h at 37°C. At the end of this period, cells were washed, fixed via paraformaldehyde, permeabilized via Triton-1X, and stained with phalloidin-568 for 30 min, followed by addition of DAPI for an additional 10 min, after which they were washed 3X and imaged.

6.2.9. Xenograft Development/Targeting/Treatment/Monitoring, NCR Nude

Cells were mixed in a 1:1 ratio with BD Matrigel Basement Membrane Matrix to a final density of 5×10^6 cells/0.1 mL injection. 0.1 mL injections of the matrix-cell suspension were performed in each rear hind flank of NCR nude mice (Taconic). Tumors were allowed to grow until a visible tumor was established, approximately 25 mm 2 in tumor area prior to treatment (determined by caliper measurements via the longest length and width dimensions); for tumor targeting, xenografts were allowed to grow near terminal

size (1 cm in diameter) to reduce effects of EPR. Treatments were injected in 0.1 mL 1X PBS at the concentration and treatment regimen indicated in the figure legend. Imaging was performed using whole-animal fluorescence imaging (IVIS, Xenogen, Caliper) at the time points indicated pre- and post-administration at the given fluorescence filters. For targeting experimentation, functionalized, fluorescent systems were administered at a radiant efficiency of ~3 × 10^9 (700 channel)/ ~1 × 10^9 (800 channel) in a 0.1 mL injection. This was determined by imaging the vial prior to injection and diluting as necessary in 1× PBS. Tissue harvest (liver, spleen, kidneys, heart, lungs, tumors, "gutted" skeleton) was performed at the terminal point of the experiment and imaged for fluorescence recovery against an untreated control for auto-fluorescence determination. Tumor sizes for the remediation study were monitored via caliper measurements, whereby areas based on the largest visible length and width dimensions were measured. Depth proved challenging to reliably measure at early time points due to skin thickness, therefore, it was not included for a final volume determination for real-time tumor size measurements.

6.2.10 Pharmacokinetics (Circulation), Immune-Proficient BALB/c

Fluorescent systems (PLL-Cy5.5 coated LbL-targeted empty liposomes) were administered in 0.1 mL 1× PBS injections in BALB/c mice (Taconic) at a relative concentration of ~3 × 10^9 (700 channel)/ ~1 × 10^9 (800 channel) in a 0.1 mL injection, based on fluorescence in the IVIS prior to injection. Mice were imaged pre- and post-nanoparticle administration using whole-animal fluorescence imaging (IVIS, Xenogen, Caliper) at the time points indicated and at the given fluorescent filters. Retro-orbital bleeding was performed in a cohort of injected mice to determine the serum half-life of the particles, presented on the basis of fluorescence recovery in these isolated blood samples (~ 0.1 mL blood/time point done in three different mice for each time point plotted). Fluorescence recovery was determined by imaging in the IVIS immediately following isolation and dilution 1:1 in EDTA to prevent coagulation. Final data are normalized to an untreated control blood sample to remove artifacts of auto-florescence. The data were fit to a two-compartment model (two-phase decay in PRISM), from which the fast and slow half-lives characterizing the nanoparticle formulation were extracted.

6.2.11 Histology

Tumors were resected at the terminal point of experimentation and fixed in 4% paraformaldehyde (PFA) for 48 h and transferred to 70% ethanol until processed. Tissue was embedded in paraffin wax and sections were stained with routine hematoxylin and eosin (H&E) and Masson's trichrome stain.

6.2.12. Statistical Analysis : Experiments were performed in triplicates, or otherwise indicated. Data were analyzed using descriptive statistics, single-factor analysis of variance (ANOVA), and presented as mean values ± standard deviation (SD) from three to eight independent measurements. Statistical comparisons between different treatments were assessed by two-tailed t tests or one-way ANOVA assuming significance at $P < 0.05$.

6.3. Results and Discussion

LbL-targeted nanoparticle systems were generated by covalent modification of PAA (M_v ~ 450 K, **Figure 6.1**A) with alendronate (Figure 6.1B) at 40% functionalization of the total carboxylic groups on the PAA molecule (Figure 6.1C). Alendronate was coupled via its amino functional handle to PAA through an amide bond. As both of the components were water soluble, we used methyl morpholine-based water-soluble coupling agents to perform amide coupling (Figure D1, Appendix D). The immobilization of the molecule onto the PAA backbone was confi rmed by ^{31}P and ^{1}H NMR. The functionalized PAA-Alendronate polymer was subsequently used as the polyanionic layer in LbL assembly, iteratively adsorbed on a solid nanoparticle substrate in alternation with polycationic poly- L –lysine (PLL), as schematically illustrated in Figure 1D. PAA is a wellcharacterized[12] weak polyanion with a high charge density and a non-erodible backbone. It is listed as an approved excipient in the FDA's Inactive Ingredient Guide and is used in clinically approved drug formulations as a stabilizer and thickener to tune the rheological properties of the injectable or topically applied therapeutic. As such, PAA presented a suitable material for introducing tissue specificity and targeting via alendronate functionalization.

To establish these systems as osteotropic delivery systems, initial investigations employed a 25 nm quantum dot (QD) (CdSeTe core) for imaging purposes to

understand how the coating directed particle association with osteosarcoma cells (143B) in vitro and in vivo, as well as other hard tissue in vivo. These particles were fabricated as shown in Figure 1D, with linear film growth observed for three bilayers of (PLL/PAA-Alendronate) to a final z -average hydrodynamic diameter of 115 nm, with a PDI of 0.19, and zeta-potential of −39 mV (1×10^{-2} M NaCl in DI water, 25 ° C; Figure D2, Appendix D).

Incubation of LbL-targeted QD 705 nanoparticles with 143B cells showed significant binding and cell uptake after 2h at 37°C (see Figure 6.2A), where red is representative of QD_{705} nanoparticle fluorescence. Nanoparticle binding, on the basis of QD_{705} fluorescence, was further characterized and observed to be dose-dependent for a range of concentrations, over which little cytotoxicity (48 h incubation) was observed, as shown in Figure 6.2B. The number of bilayers (1, 2, and 3, whereby 1, 2, and 3 layers of the targeted PAA-Alendronate polymer are incorporated on the particle surface) was also investigated. These results are shown in Figure D3 (Appendix D). It was observed that the in vitro binding affinities and cytotoxicity profile were similar across different bilayer numbers. Previous work[9b] established the improved biological performance of QD nanoparticles with 3 or more bilayers; therefore, we focused on the three-bilayer LbL-targeted QD particles for in vivo assessment of targeting.

To evaluate this system *in vivo*, LbL-targeted QD_{800} nanoparticles were administered via the tail vein in NCR nude mice with ectopically induced 143B osteosarcoma xenografts. Particle distribution in live animals was tracked using whole-animal *in vivo* fluorescence imaging (Figure 6.3A). Immediately following administration, the particles rapidly accumulated in the bone tissue regions, particularly in the parietal region of the cranium, spinal column, and hind limb regions. At later time points, particles trafficked to the 143B xenografts, consistent with targeted interactions with the tumor matrix. Controls for uncoated, untargeted QDs and coated QDs with unconjugated PAA showed no specific affinity for hard tissue and had little to no accumulation in the xenografts, suggesting the enhanced permeation and retention effect does not account for much of this tumor localization (Appendix D; figure D4). Tumor-specific accumulation was significant and observed over the course of 8 days (Figure 6.3B). Such a long period of accumulation may be due to the strong binding affinity between

alendronate and the osteosarcoma tissue, leading to much longer residences times of the nanoparticle in the tumor. The tumors were resected after 8 days, along with necropsy of other relevant tissue, and analyzed via recovered fluorescence to investigate post-mortem particle distribution. Significant localization of particles was observed in xenografts (accounting for ~30% fluorescence recovered), relative to ~40% in the liver and smaller fractions in each of the other organs (spleen, kidneys, heart, lungs) harvested (Figure 6.3C, Appendix D; figure D5). Accumulation in the liver is a common challenge for all nanoparticle delivery platforms, though we have shown in other work that the use of hyaluronic acid can lower accumulation considerably compared to other systems. Future work will investigate its use for introducing tissue specificity via ligand functionalization.

To visualize the biodistribution of both the coating and nanoparticle in real time, the bisphosphonate-targeted polymer, PAA-Alendronate, was labeled with a near-IR, Cy5.5 dye and adsorbed onto the surface of QD_{800} to allow for two-color *in vivo* imaging of the targeted, 3 bilayer $(PLL/PAA_{Cy5.5}\text{-Alendronate})_3$ nanoparticle. We observed co-localization of the two components – the PAA-Alendronate outer layer and the quantum dot - in the xenografts (Figure 6.3D, Appendix D; figure D5) for up to 9 days, further substantiating these systems as serum-stable targeted platforms for delivery.

Next, we applied the coating, (PLL/PAA-Alendronate), to drug-loaded particle systems for targeted delivery and treatment of diseased tissue. For this purpose, the coatings were adapted to a liposomal carrier for use in drug delivery (Figure 6.4A). Initial work focused on empty, negatively-charged liposomal carriers, containing DSPC (1,2-distearoyl-*sn*-glycero-3-phosphocholine), cholesterol, and POPG (1-palmitoyl-2-oleoyl-*sn*-glycero-3-phospho-(1'-*rac*-glycerol)), functionalized with one bilayer of PLL/PAA-Al, which yielded 170 nm nanoparticles with a zeta-potential of -20 mV (Appendix D; figure D6), to validate these systems for LbL-targeted delivery. Due to size considerations for systemic delivery, fabrication was truncated after a single bilayer due to the significant increase in size associated with adsorption of a single bilayer (80-90 nm per bilayer). Differences in bilayer thickness relative to films on QDs could be due to the relative fluidity of the liposomal substrate. Consistent with results for the LbL-targeted QDs, binding of the LbL-functionalized liposomes to 143B cells was observed

to be dose-dependent and not apparently cytotoxic (Figure 6.4B). Rapid internalization after a 2 hour incubation with the 143B cells, visualized by confocal microscopy (Figure 6.4C) and confirmed via flow cytometry (Figure 6.4D), was also observed. The high levels of red, diffuse nanoparticle fluorescence (visualized by incorporation of PLL-Cy5.5 in the LbL coating), along with a marked shift in cell-associated fluorescence observed by flow cytometry, suggested this system enabled high levels of nanoparticle binding and uptake, providing a promising platform for LbL-targeted drug delivery.

Osteosarcomas are known to be responsive to conventional chemotherapeutics, such as doxorubicin, so we next explored the incorporation of doxorubicin in the liposomal carrier for subsequent LbL functionalization. We were able to incorporate doxorubicin into stable DSPC:Cholesterol:POPG liposomes with high drug-loading efficiency (97%) at 5.5 w/w% (drug/lipid). During subsequent coating with a single bilayer of (PLL/PAA-Alendronate), no drug loss was observed, and liposomal morphology remained unchanged, as illustrated in Figure 6.4A. The LbL-functionalized doxorubicin-loaded liposome was characterized by a hydrodynamic diameter of approximately 210 nm in size with a zeta-potential of -20 mV, measured in 10 mM NaCl (Appendix D; figure D6). The targeted liposomal carriers were found to be particularly potent against 143B cells, with high levels of toxicity over a wide-range of doxorubicin-loaded concentrations following incubation for 24 hours and 48 hours (Figure 6.4E), whereas the uncoated control showed about 8-fold lower levels of toxicity (Figure 6.4F).

Translating these systems *in vivo*, we first investigated the pharmacokinetics of the coated liposomal system in the absence of drug. Shown in Figure 6.5A is the circulation profile of this system on the basis of fluorescence recovery following systemic administration of the PLL-Cy5.5 labeled carriers to immune-proficient BALB/c mice. Based on a two-compartment model, the targeted carriers exhibited half-lives of 0.23 hours (fast) and 18.7 hours (slow), indicative of a stable, long-circulating system that could promote enhanced delivery of loaded therapeutics.

In tumor-bearing NCR nude mice, the same PLL-Cy5.5 labeled, targeted system was observed to accumulate in the target diseased tissue rapidly, with the ability to persist in the tumor up to the terminal point of the study - 100 hours (Figure 6.5B, Appendix D; figure D7). Biodistribution results (Figure 6.5C, Appendix D; figure D7) at the terminal

point of this investigation further corroborated these systems as stable delivery platforms that preferentially locate in osteosarcoma xenografts at high levels (~35% on the basis of fluorescence recovery, relative to ~47% in the liver, ~7% in the kidneys). Elevated amounts of recovered fluorescence in the liver suggested that hepatic clearance is the primary means of excretion; however, the large number associated with the liver, in addition to the values reported for other tissue, is not meant to be wholly quantitative, as the data is reported as percent of the total fluorescence recovered from only the tissue collected. The relative ratios of fluorescence between tissue confirmed that we were able to achieve a high level of tumor specificity relative to the other tissue, which validated this system for further investigation towards therapeutic delivery.

After observing high levels of tumor localization for the targeted empty liposomal formulation, the efficacy of the LbL-targeted doxorubicin-loaded liposomes was evaluated against 143B osteosarcoma xenograft-bearing NCR nude mice. Initial attempts at determining the optimal dosing regimen (drug concentration and number/timing of injections) employed a dose escalation study of serial 1 mg/kg, 2 mg/kg, and 3 mg/kg (based on doxorubicin loading) injections starting at day 10 post-tumor inoculation with each treatment separated by one week. As observed in Figure 6.6A, untreated osteosarcoma tumors grew beyond terminal size (diameter > 1 cm) after 19 days post-inoculation. Treated mice for both the uncoated and coated versions survived repeated dosing out to 30 days, after which comparisons in terminal tumor size were drawn. As observed visually in Figure 6.6A and quantified in Figure 6.6B, LbL-targeted doxorubicin-loaded liposome treated mice showed significantly reduced terminal tumor sizes relative to the uncoated doxorubicin-loaded liposome control (characterized by measurements on the longest x-y dimensions). This observation is consistent with enhancement of the therapeutic potency of the loaded drug due to preferential accumulation of the targeted system in the 143B xenografts.

Results from the dose escalation study indicated that a higher dose was necessary to effectively remediate the tumor. For this purpose, LbL-targeted doxorubicin-loaded liposomes were administered at a doxorubicin concentration of 5 mg/kg, along with an uncoated, drug-loaded control at the same concentration. Xenograft-bearing mice were allowed to develop tumors to an area of ~25 mm^2 [measured in the longest length and

width dimensions] after which they were treated, with repeated injections one week apart for 3 total treatments until a terminal point at day 40. We observed enhanced efficacy of the LbL-targeted doxorubicin-loaded liposome, relative to the uncoated control, as determined by caliper measurements and visual inspection of the terminal point harvested xenografts (Figure 6.6C). Varying levels of therapeutic benefit for the targeted group were observed from complete remediation (NT – no tumor observed) to tumor maintenance (tumor reduction of 30% from day 0 on average), whereas the uncoated control group mice showed significant tumor growth (several beyond the maximum allowable tumor burden of 1 cm in diameter; growth of 550% from day 0 on average). These results highlight the capabilities of the LbL-targeted nanoparticle approach for highly effective chemotherapeutic treatment in tumor-bearing mice.

Histological analysis via a Masson's trichrome stain of recovered osteosarcoma (143B) tumor tissue following treatment with each the targeted and untargeted doxorubicin-loaded liposomal formulations at 5 mg/kg is displayed in Figure 6.7. Initially, the tumor demonstrates an abundance of 143B cells (stained red) and connective tissue (stained blue) in the tumor mass (left column). Particles coated with alendronate for targeting the tumor tissue resulted in significant cell death (right column, top row). A lower level of cell death resulted in tumors with uncoated nanoparticles (right column, middle row). Virtually no change in the tumor infrastructure was observed in untreated animals (right column, bottom row). Micro-CT analysis of these tumors immediately prior to resection (Appendix D; figure D8) complements this data, clearly demonstrating the enhanced efficacy of the targeted system relative to the uncoated control. These observations suggest the potency of this approach to deliver the payload in an efficacious manner to the 143B osteosarcoma solid tumor.

6.4. Conclusions

LbL is a versatile platform to functionalize nanoparticles in ways that promote improved biological performance. Prior art has established LbL as a means to impart protein-resistive, long-circulating properties to nanoparticle systems, with a means to control biodistribution of both the carrier and drug in a complex systemic environment. This investigation further demonstrates the modularity of this approach to impart targeting capabilities to the nanoparticle to diseased tissue to achieve enhanced

treatment outcomes. We capture this potential with the synthesis of osteotropic nanoparticles via incorporation of alendronate-functionalized PAA as a means of surface modification of drug-loaded liposomes. Different nanoparticle core substrates may be used for imaging and treatment for a variety of bone diseases. While surgical resection of a primary tumor will continue to be the first-line of treatment, subsequent treatment with the osteotropic nanoparticles has the potential to decrease recurrance rates and increase successful outcomes. These functional nanoparticles are also highly promising for future investigations towards treatment of bone-localized metastases of invasive cancer cell types such as breast and lung cancer. The potential to further generalize this approach towards the built-to-order manufacture of different targeted delivery systems continues to provide much promise for LbL nanoparticles.

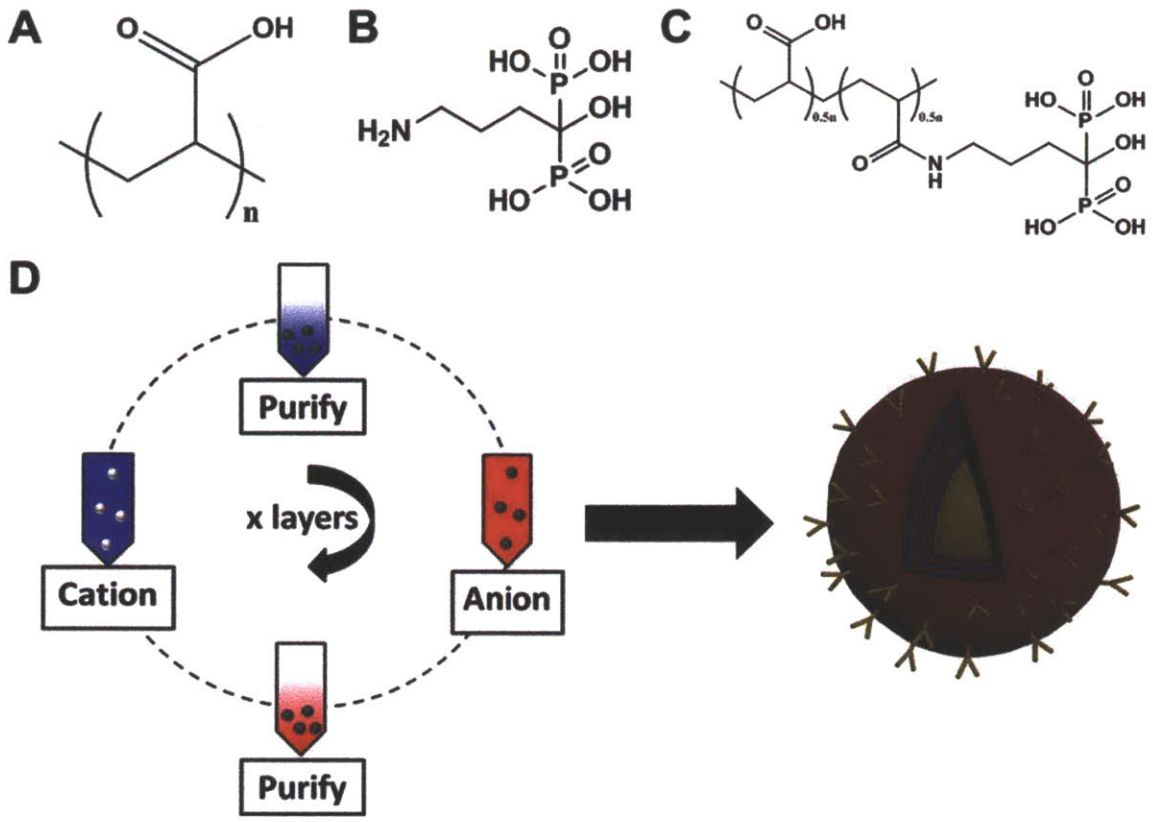

Figure 6.1. Achieving bone tissue level specificity of LbL coated nanoparticles. (A) Aqueous anionic polyelectrolyte, poly(acrylic acid) [PAA, MW 450K], functionalized with the **(B)** bisphosphonate targeting moiety, alendronate [for high specificity to hydroxyapatite in bone], to yield **(C)** the aqueous, ligand-functionalized polymer at 40% side-chain functionalization (**Figure S1**), which is used for complementary, iterative adsorption to the polycationic component (poly-L-lysine, PLL) in the film on the NP substrate, schematically illustrated in **(D)**.

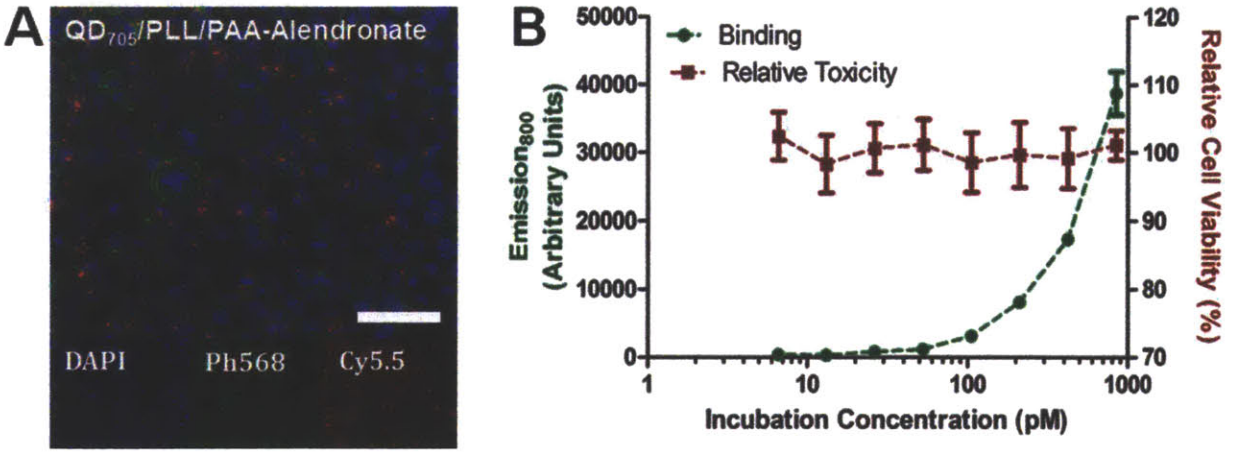

Figure 6.2. *in vitro* assessment of LbL-targeted QD NPs incubated with 143B osteosarcoma cells. (A) Confocal microscopy of 143B cells incubated with the LbL-targeted QD_{705} core NPs for 2 hours. Blue staining representative of a Hoescht nuclear stain, green representative of a phalloidin stain of the actin filamentous cell structure, and red representative of the nanoparticle fluorescence (QD_{705} fluorescence). Scale bar representative of 20μm. **(B)** Binding and relative cytotoxicity of 3 bilayer [PLL/PAA-Alendronate] LbL-targeted QD_{800} core NPs following incubation for 2 hours in 143B cells. Fluorescence emission data corresponds to that of the nanoparticle core (QD_{800}).

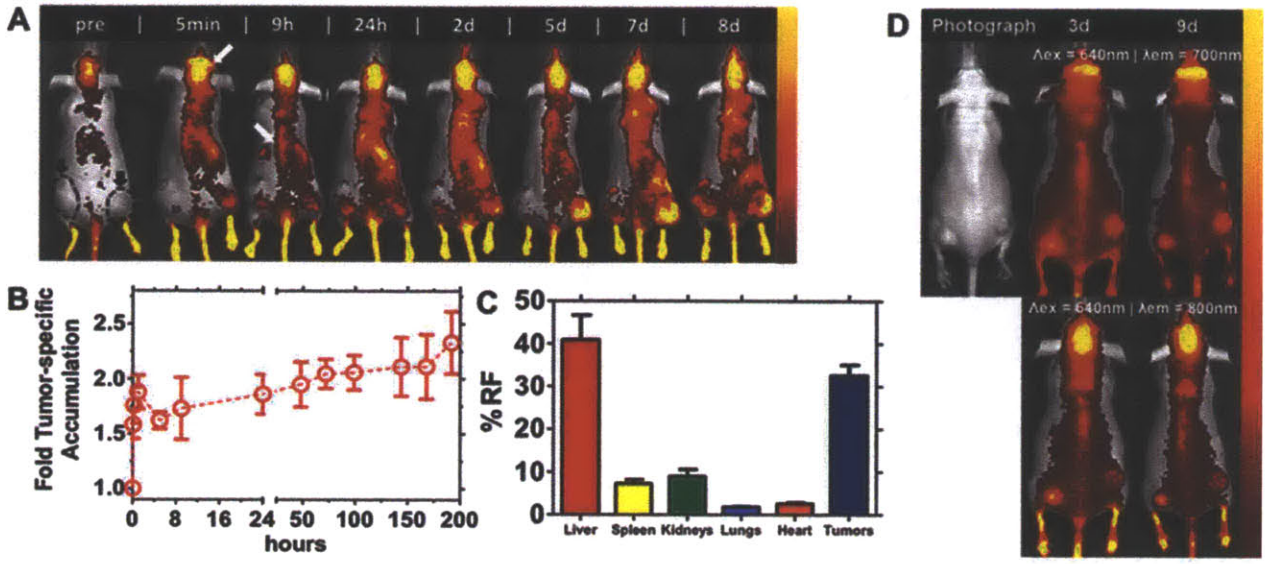

Figure 6.3. *in vivo* evaluation of LbL-targeted QD_{800} core NPs. (A) Representative live-animal imaging of LbL-targeted QD_{800} core NPs following systemic administration to 143B osteosarcoma xenograft-bearing NCR nude mice. Imaging conducted at λ_{ex} = 640 nm, λ_{em} = 800 nm for up to 8 days. Hind-flank xenografts identified in the pre-injection image; arrows at 5 minutes and 9 hours indicate binding to native bone tissue. **(B)** Quantification of fold tumor-specific accumulation normalized to tissue auto-fluorescence pre-injection for the systemically administered LbL-targeted QD_{800} core NPs, as visualized in **(A)**. n = 3 mice (6 tumors); data presented as mean +/- SEM. **(C)** Biodistribution data corresponding to endpoint of **(A)** (quantified as percent recovered fluorescence following harvest of relevant tissue after 8 days post-administration). n = 3 mice (6 tumors); data presented as mean +/- SEM. **(D)** Co-localization of QD_{800} NP core with LbL-film containing labeled PAA-Alendronate$_{700}$; top row [PAA-Alendronate$_{700}$ channel] – imaging conducted at λ_{ex} = 640 nm, λ_{em} = 700 nm, bottom row [QD_{800} channel] - imaging conducted at λ_{ex} = 640 nm, λ_{em} = 800 nm.

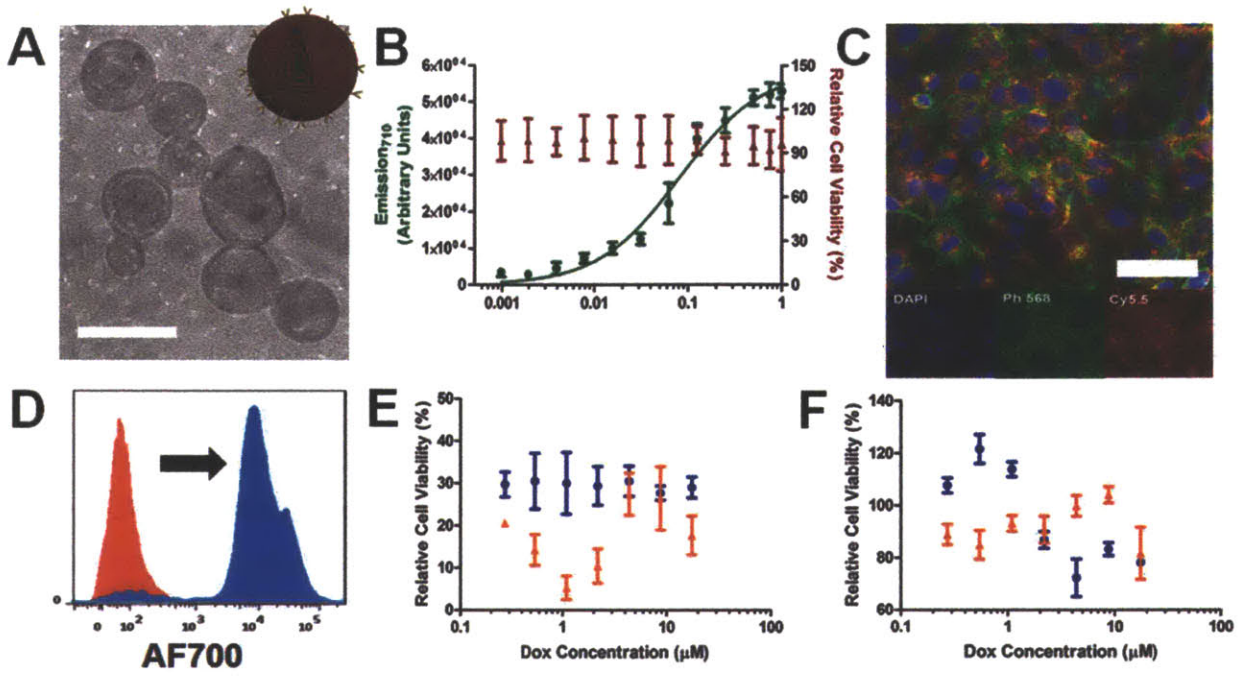

Figure 6.4. *in vitro* evaluation of LbL-targeted liposomal NPs in 143B cells. (A) Cryo-TEM of LbL-targeted doxorubicin-loaded liposomal NPs. Scale bar representative of 200 nm. **(B)** Binding (2 hour incubation) and relative cytotoxicity (48 hour incubation) of LbL-targeted empty liposomal NPs over a range of concentrations, based on fluorescence, in 143B cells (λ_{ex} = 675 nm, λ_{em} = 710 nm; tracked using PLL_{700} as cationic component in LbL film). **(C)** Confocal microscopy of 143B cells incubated with the LbL-targeted empty liposomal NPs [tracked via PLL_{700} polycationic component in LbL film] for 2 hours. Blue staining representative of a Hoescht nuclear stain, green representative of a phalloidin stain of the actin filamentous cell structure, and red representative of the nanoparticle fluorescence ($PLL_{Cy5.5}$ polymer shell fluorescence). Scale bar representative of 10 μm. **(D)** Representative cell-associated NP fluorescence following a 2 hour incubation of 143B cells with the LbL-targeted empty liposomal NPs. **(E)** *in vitro* cytotoxicity of LbL-targeted doxorubicin-loaded liposomal NPs and the corresponding **(F)** uncoated doxorubicin-loaded liposomal control following 48 hour (blue) and 72 hour (red) incubation periods over a range of doxorubicin concentrations.

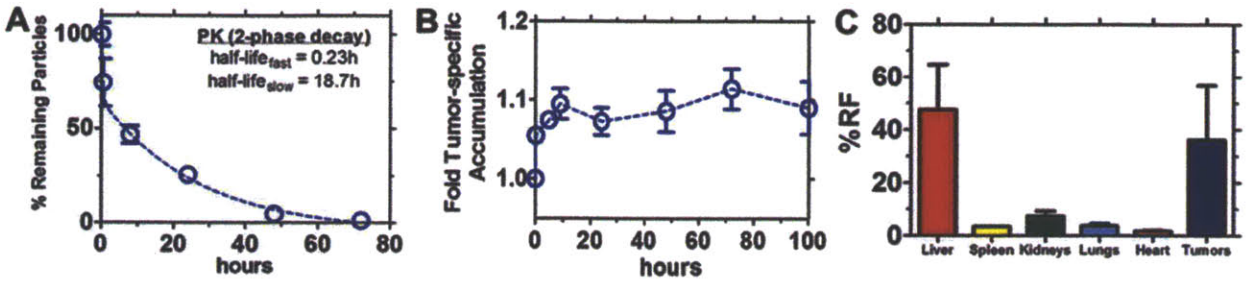

Figure 6.5. Biological evaluation of LbL-targeted empty liposomal NPs. LbL-targeted empty liposomal NPs tracked via PLL_{700} polycationic component in surface coating. Circulation data in **(A)** normalized to % remaining particles recovered, on the basis of fluorescence [λ_{ex} = 640 nm, λ_{em} = 700 nm], immediately following systemic administration to immune proficient BALB/c mice; data presented as mean +/- SEM (n = 3). Two-compartment model fit to determine half-lives displayed. Data includes background subtraction of blood auto-fluorescence. **(B)** Quantification of fold tumor-specific accumulation normalized to tissue auto-fluorescence pre-injection for the systemically administered LbL-targeted blank liposomal core NPs to 143B xenograft-bearing NCR nude mice; data presented as mean +/- SEM (n = 3). **(C)** Biodistribution data corresponding to endpoint of **(B)** (quantified as percent recovered fluorescence [λ_{ex} = 640 nm, λ_{em} = 700 nm] following harvest of relevant tissue after 100 hours post-systemic administration); data presented as mean +/- SEM (n = 3).

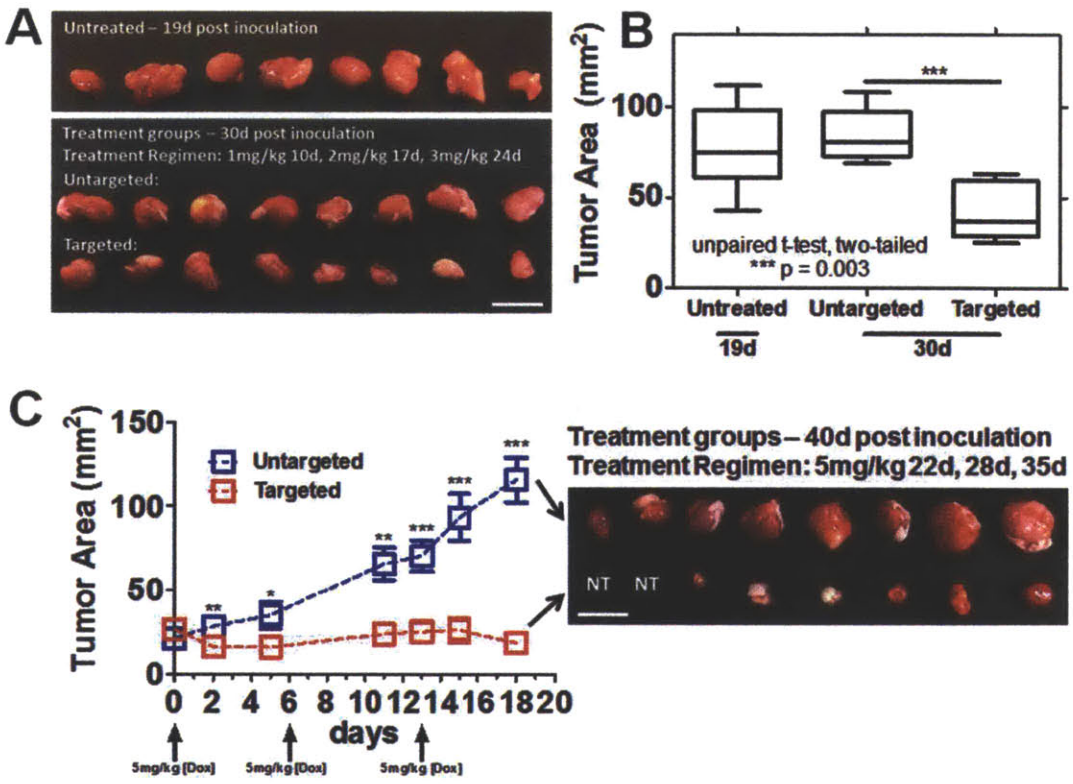

Figure 6.6. 143B xenograft tumor remediation following treatment with doxorubicin-loaded liposomal formulations. (A) *in vivo* tumor remediation of 143B xenografts in NCR nude mice for LbL-targeted doxorubicin-loaded liposomal NPs, against untreated and uncoated doxorubicin-liposomal NPs. Untreated control xenografts were sacrificed 19 days post-inoculation of xenograft due to tumor burden exceeding 1 cm. Untargeted and targeted Dox-liposomal formulations were sacked at 30 days post-inoculation following a dose-escalation study with the following treatment regimen: day 10 at 1 mg/kg, day 17 at 2 mg/kg, day 24 at 3 mg/kg. Terminal point shown with final tumor area displayed in **(B)**. Statistics are from an unpaired t-test, two-tailed to compare the untargeted and targeted formulations at each time point. Data presented as mean +/- SEM; n = 4. **(C)** Caliper measurements for *in vivo* tumor remediation with repeated dosing of 5 mg/kg for both targeted and untargeted formulations at 22 days, 28 days, and 35 days post-inoculation (displayed as day 0, day 6, and day 13 in **(C)**). Statistics are from an unpaired t-test, two-tailed to compare the untargeted and targeted formulations; *$p < 0.05$; **$p < 0.01$; ***$p < 0.001$. Data presented as mean +/- SEM; n = 4. Resection of tumors from terminal point of **(C)**, n = 4 for each group, displayed from the final caliper measurement.

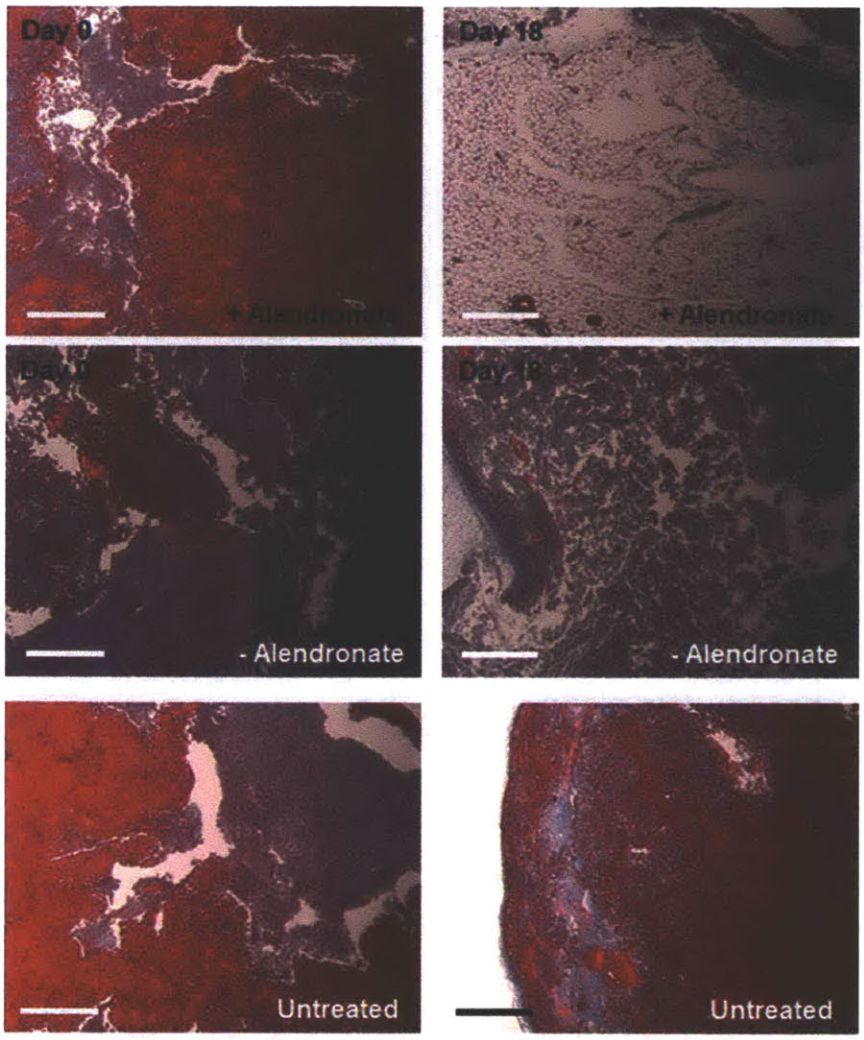

Figure 6.7. Representative histology of 143B tumors harvested at 18 days post-treatment corresponding to the terminal point in **Figure 6C**. (**left column)** tumors prior to treatment; (**right column)** tumors at the 18 day terminal point post treatment of 3 repeated injections at 5 mg/kg doxorubicin. **(top row)** tumors treated with PAA-Alendronate coated doxorubicin-loaded liposomes, **(middle row)** uncoated dox-loaded liposomes, and **(bottom row)** untreated animals. Masson's trichrome stain – red = 143B osteosarcoma cells, blue = connective tissue; scale bars representative of 100 μm.

6.5. References

1. G. Rodan, T. Martin, Science 2000, 289, 1508.

2. a) G. Mundy, Nat. Rev. Cancer 2002, 2, 584;
b) D. Wang, S. Miller, P. Kopecková, J. Kopecek, Adv. Drug Delivery Rev. 2005, 57, 1049.

3. E. Giger, B. Castagner, J.-C. Leroux, J. Controlled Release 2013, 167, 175.

4. a) V. Hengst, C. Oussoren, T. Kissel, G. Storm, Int. J. Pharm. 2007, 331, 224;
b) S.-W. Choi, J.-H. Kim, J. Controlled Release 2007, 122, 24;
c) D. Heller, Y. Levi, J. Pelet, J. Doloff, J. Wallas, G. Pratt, S. Jiang, G. Sahay, A. Schroeder, J. Schroeder, Y. Chyan, C. Zurenko, W. Querbes, M. Manzano, D. Kohane, R. Langer, D. Anderson, Adv. Mater. 2013, 25, 1449;
d) K. Ramanlal Chaudhari, A. Kumar, V. Megraj Khandelwal, M. Ukawala, A. Manjappa, A. Mishra, J. Monkkonen, R. Ramachandra Murthy, J. Controlled Release 2012, 158, 470;
e) R. C. Kiran, K. Abhinesh, K. Vinoth Kumar Megraj, K. M. Anil, M. Jukka, S. R. M. Rayasa, Adv. Funct. Mater. 2012, 22.

5. a) I. G. David, C. Frank, J. Phys. Chem. B 2001, 105;
b) G. Schneider, V. Subr, K. Ulbrich, G. Decher, Nano Lett. 2009, 9, 636;
c) P. Pattekari, Z. Zheng, X. Zhang, T. Levchenko, V. Torchilin, Y. Lvov, Phys. Chem. Chem. Phys. 2011, 13, 9014;
d) S. Yuk, K. Oh, S. Cho, S. Kim, S. Oh, J. Lee, K. Kim, I. Kwon, Mol. Pharm. 2012, 9, 230;
e) A. Sexton, P. Whitney, S.-F. Chong, A. Zelikin, A. Johnston, R. De Rose, A. Brooks, F. Caruso, S. Kent, ACS Nano 2009, 3, 3391;
f) Q. Zhao, B. Han, Z. Wang, C. Gao, C. Peng, J. Shen, Nanomedicine 2007, 3, 63;
g) T. Shutava, S. Balkundi, P. Vangala, J. Steffan, R. Bigelow, J. Cardelli, D. O'Neal, Y. Lvov, ACS Nano 2009, 3, 1877;
h) D. I. Gittins, F. Caruso, Adv. Mater. 2000, 12, 1947;

i) T. G. Shutava, P. P. Pattekari, K. A. Arapov, V. P. Torchilin, Y. M. Lvov, Soft Matter 2012, 8, 9418.

6. G. Decher, Science 1997, 277.

7. N. J. Shah, M. N. Hyder, J. S. Moskowitz, M. A. Quadir, S. W. Morton, H. J. Seeherman, R. F. Padera, M. Spector, P. T. Hammond, Sci. Transl. Med. 2013, 5, 191ra83.

8. M. N. Hyder, N. J. Shah, P. T. Hammond, Multilayer Thin Films: Sequential Assembly of Nanocomposite Materials, 2nd ed. (Eds: G. Decher, J. B. Schlenoff), Wiley-VCH, Weinheim, Germany 2012.

9. a) Z. Poon, J. Lee, S. Morton, P. Hammond, Nano Lett. 2011, 11, 2096;
b) S. Morton, Z. Poon, P. Hammond, Biomaterials 2013, 34, 5328.

10. a) Z. Poon, D. Chang, X. Zhao, P. Hammond, ACS Nano 2011, 5, 4284;
b) X.-Z. Yang, J.-Z. Du, S. Dou, C.-Q. Mao, H.-Y. Long, J. Wang, ACS Nano 2012, 6, 771.

11. S. W. Morton, K. P. Herlihy, K. E. Shopsowitz, Z. J. Deng, K. S. Chu, C. J. Bowerman, J. M. DeSimone, P. T. Hammond, Adv. Mat. 2013.

12. a) L. Bromberg, J. Controlled Release 2008, 128, 99;
b) X. Yan, R. Gemeinhart, J. Controlled Release 2005, 106, 198;
c) Y. Hu, Y. Ding, D. Ding, M. Sun, L. Zhang, X. Jiang, C. Yang, Biomacromolecules 2007, 8, 1069.

13. M. Kunishima, C. Kawachi, K. Hioki, R. Terao, S. Tani, Tetrahedron 2001, 57, 1551.

14. M. I. Walash, M. E. Metwally, M. Eid, R. N. El-Shaheny, Chem. Cent. J. 2012, 6, 25.

Chapter 7

Conclusions and Future Directions

7.1. Thesis Summary

This thesis has focused on the development of next-generation implants that can recapitulate aspects of the natural healing cascade and integrate with the existing body tissues. New approaches to treat large traumatic and congenital are explored, with a particular emphasis on recapitulating tissue form and function through the use of composite biodegradable implants, which can also be extended to design targeted therapies for delivery of potent drugs to specific tissues within the body. In each instance, layer-by-layer (LbL) assembly was used to achieve modification of the surface at different length scales – from the macroscale to the nanoscale. The primary findings of each thesis chapter are highlighted below.

In Chapter 2, an osteophilic modular coating for substrates was explored, that simultaneously presented hydroxyapatite, an inorganic component of the bone complexed with biocompatible polymers, and rhBMP-2, a bone growth factor to accelerate the regeneration of stable bone tissue. The findings highlight the characteristics of this alternative uniform coating method for hydroxyapatite, which can be performed at ambient conditions, without the need for high temperature processes. Introduction of hydroxyapatite and rhBMP-2 upregulated osteogenic markers at earlier times in MSCs which resulted in greater calcium deposition in culture. We have presented an alternative method for the fabrication of hybrid multilayer films consisting of organic and inorganic components for bone tissue healing.

In Chapter 3, the system described in Chapter 2 was explored further, along with an understanding of its mechanical properties. It was demonstrated that this coating promoted stable mechanical fixation of an implant in a surrogate rodent model. Osteoconductive hydroxyapatite (HAP) and osteoinductive bone morphogenetic protein 2 (BMP-2) contained within the nanostructured coating acted synergistically to induce osteoblastic differentiation of endogenous progenitor cells within the bone marrow,

without indications of a foreign body response. The tuned release of BMP-2, controlled by a hydrolytically degradable poly(β-amino ester), was essential for tissue regeneration and, in the presence of HAP, the modular coating encouraged the direct deposition of highly cohesive trabecular bone on the implant surface. The results of this study suggested that a synthetic materials approach can be harnessed to access the osteogenic differentation potential of endogenous precursor bone marrow stem cells and mediate specific, long-term host-tissue interactions. This approach provides a path to developing next-generation biologically integrated bone implants with superior stability, fewer incidences of failure and lower rates of patient morbidities.

In Chapter 4, the use of multiple growth factors from a scaffold surface coating for bone growth was explored. PEM films that sequestered BMP-2 and angiogenic VEGF (vascular endothelial growth factor) in different ratios were explored. No burst release of either growth factor was observed as the films degraded. The release of BMP-2 was sustained over a period of 2 weeks, while VEGF eluted from the film over the first 8 days. In vivo, the mineral density of ectopic bone formed de novo by rhBMP-2/rhVEGF165 PEM films was approximately 33% higher than when only rhBMP-2 was introduced, with a higher trabecular thickness. Bone formed throughout the scaffold when both growth factors were released, which suggests more complete remodeling due to an increased local vascular network. This study demonstrated a promising approach to delivering precise doses of multiple growth factors for a variety of implant applications where control over spatial and temporal release profile of the biologic is desired.

In Chapter 5, the use of multiple growth factors on a flexible, biodegradable implant surface was explored to repair critical size bone defects in a rat calvaria. An implantable multilayer flexible biodegradable polymer "skin" carrying active growth factors was developed. The growth factors eluted over readily adapted time scales to recapitulate the wound healing cascade and induced rapid bone repair. Through the addition of specific osteophilic materials, we interrogated and directed cellular processes to optimize design. The polymer "skin" promoted local bone formation that bridged a critical-size defect in the rat calvaria as early as 2 weeks after implantation. Mature, mechanically competent bone regenerated the native calvaria form, indicating the

potential of this approach as an off-the-shelf, cell-free option for bone tissue repair and restoration.

Lastly, in Chapter 6, a new method to target potent chemotherapeutic drugs to the bone tissue was explored, using methods developed in Chapter 5. This work investigated an approach for generating functional and targeted drug carriers specifically for treating primary osteosarcoma. This was accomplished via surface modification of drug-loaded nanoparticles with an aqueous polyelectrolyte, poly(acrylic acid) (PAA), side-chain functionalized with alendronate, a potent clinically-used bisphosphonate. Nanoparticles coated with PAA-Alendronate are observed to bind and internalize rapidly in human osteosarcoma 143B cells. Encapsulation of doxorubicin, a front-line chemotherapeutic, in an LbL-targeted liposome demonstrates potent toxicity in vitro. Active targeting of 143B xenografts in NCR nude mice with the LbL-targeted doxorubicin liposomes promotes enhanced, prolonged tumor accumulation and significantly improved efficacy.

7.2. Future Directions

While the work in this thesis helps answer several questions related to bone tissue repair and regeneration, there is potential to explore the systems further and address challenges that have been presented to the technology.

7.2.1. Sequential release of therapeutics

A unique characteristic of LbL films is the possibility of releasing multiple therapeutic factors over adaptable time scales that can help address potential post-operative complications in the case of orthopedic implants, such as pain and infection, while speeding up implant integration and tissue repair. In practice, however, it has been challenging to control the release of various factors in sequence due to interdiffusion effects, by which small molecules and proteins are able to move within the LbL film during the film assembly and release phases. The resulting 'blend' results in co-release of the therapeutic factors – which may be beneficial, as was seen in this work. However, some applications would require a more sequential release approach. Prevention of infection would require the antibiotic to first eliminate any bacteria, following which new

bone can be generated. Such a film can be constructed with the help of 'barrier' layers that can potentially block inter-diffusion of species and prevent co-release. This would require a more fundamental approach to study the mechanism of film assembly and disassembly and the use of species (such as high aspect ratio materials) that can block interdiffusion.

7.2.2. Pre-clinical studies in large animal models

The work presented here uses widely accepted rodent models for evaluating coated implant systems. Translating these new therapies to clinical application will require the use of more advanced pre-clinical models that closely mimic conditions in the human joint. This includes the use of canine, goat, rabbit or sheep models that can be performed through collaboration. For CMF repair, testing the promising formulations from this work in a rabbit model would provide significant insight into the possibility of translating the adaptive release system for use in the clinic.

7.2.3. Dental Implants coated using the LbL approach for rapid osseointegration

Threaded root-form endosseous dental implants are the solution for the replacement of natural teeth. However, the true integration of implant with bone requires a significant amount of time, which can be up to several months. Often, healing of tissue around the implant can be delayed, leading to lengthy delays before dental patients are able to fully recover function after treatment.

As a next step, it would be logical to investigate the promising growth factor films to promote osseointegration in dental implants to establish their efficacy in dental applications toward single step dental implant approaches. The outcome of this work could be an immediate and rapid post-surgical healing outcome around the dental implant by facilitating soft tissue regeneration, along with vascularization and osteogenesis enabled by the native remodeling processes.

7.2.4. Therapy with disease-modifying properties for osteoarthritis

One of the focus areas of this thesis was on implant integration to prevent premature failure for hip and knee implants. One of the reasons for joint replacement is

osteoarthritis, caused by cartilage degradation. This complex condition affects load-bearing joints and currently has no known cure. The complexity of the disease is the reason why particular targets are difficult to choose to reverse the disease. Various types of inhibitors for aggrecanases and collagenases have been tried and failed clinical trials because of the redundancy of the disease pathway. One approach to overcome this process could be to use anabolic therapy by introducing growth factors into the synovial joint space and promoting cartilage matrix formation to reverse OA and reverse progression of joint degradation. To do this, we are exploring the use of charge interactions to form 'soft' growth factors polyplexes that are positively charged and can penetrate the cartilage and anchor within the negatively charged matrix over sustained time periods to promote chondrogenesis and matrix formation. This approach could potentially be combined with a long-term analgesic and a biomarker discovery platform to attenuate pain and stratify patient population to design clinical trials and provide therapy to those who would most benefit from it.

7.2.5. Translational considerations of LbL coated biomedical products

LbL offers a unique solution to modifying existing biomedical products, including orthopedic implants and conferring new properties to them. A key translational consideration is to be mindful of how this would be viewed by the regulatory agencies, which would determine the pathway to clinical approval for these devices. It would, therefore, be of tremendous value to start building procedures in to the lab-scale LbL coating process that may help answer some of these questions. Important among these is the sterilization of the device post-coating. This could be addressed in the form of procedures such as clean-room (or biosafety cabinet) LbL fabrication for biologic drug based coatings. The shelf-life of these coatings is also important, and key to acceptance by the end-users of the product. The hydrolytically degradable poly(β-amino ester) used throughout this work, is currently not used in the clinic and would need to undergo clinical safety trials prior to its use as part of a coating. As these systems are developed further, future projects could focus on using larger pre-clinical animal models that may help move them move closer to clinical translation, with shorter developmental times.

7.3 Concluding Remarks

The work presented in this thesis has contributed to a greater understanding of engineering the interface of biomedical implants and therapeutics with specific functionalities to potentially improve clinical outcomes. The LbL drug delivery coatings are a new way to induce implants to biologically integrate with existing bone tissue, induce targeted bone repair that fills in large defects and target potent therapeutics to the bone tissue itself. Importantly, the work described here is cell-free and does not require the extraction and ex-vivo expansion of progenitor cells and re-implantation. There are significant barriers to the translational of such a therapy, very high costs and regulatory hurdles. This approach is also not off-the-shelf and typically requires multiple procedures to be performed on the patient. These coatings were developed with a vision to incorporate them in next-generation therapies and will, undoubtedly, improve the current standard of care. Translating this technology will require a multi-pronged approach, in which patents and partnerships will play critical roles. The chances of success for a biologic based approach would be significantly enhanced by having a strong, stable partnership with an established company, where the technology could be out-licensed. On the other hand, lower-risk, lower-cost approaches using analgesics, antibiotics and antimicrobial surfaces would be a good target for a start-up company to develop in-house. These pathways could be the quickest for translation into the clinic to ultimately improve the quality of healthcare, lower costs and result in a better quality of life.

Appendix A

Materials and Methods Section

Materials. Poly (β-aminoester) (Poly2) was synthesized as previously described [1]. All other materials were purchased from Sigma Aldrich (St. Louis, MO) or Invitrogen (Carlsbad, CA) unless otherwise noted.

Preparation of electrostatic films. Hydroxyapatite nanoparticle suspension (10 wt%) was diluted 5 fold in sodium acetate buffer (0.1 M), sterile filtered through a 0.45 μm cellulose acetate membrane (VWR Scientific, Edison, NJ) and added 1:1 (v/v) to chitosan solution in sodium acetate buffer (2 mg/ml). Poly(acrylic acid) and Poly2 dipping solutions were prepared in sodium acetate buffer (1 mg/ml). rhBMP-2 solution, a gift from Pfizer Inc. (Cambridge, MA), was diluted to 250 μg/ml in sodium acetate buffer from a 10mg/ml stock solution.

Polyelectrolyte multilayer film construction. Glass coverslips or silicon substrates were plasma etched with room air using a Harrick PDC-32G plasma cleaner on high RF power for 5 or 1 min respectively and immediately immersed in the Chitosan/HAP, Chitosan or Poly2 solution for 10 min. In general, the osteoconductive films were fabricated on this scaffold with a Carl Zeiss HMS programmable slide stainer with the following dipping protocol: 5 min in Chitosan (HAP) solution, 3 washes (10, 20, 30 s), 5 min in PAA solution and 3 washes (10, 20, 30 s). This cycle was repeated to achieve films with different number of bilayers. Next, the degradable multilayer was fabricated in tetralayer format atop the osteoconductive baselayers with the following dipping protocol: 5 min in Poly2 solution, 3 washes (10, 20, 30 s), 5 min in PAA solution, 3

washes (10, 20, 30 s), 5 min in rhBMP-2 solution, 1 wash (10 s) and 5 min in PAA solution with 3 washes (10, 20, 30 s). The cycle was repeated to achieve 20 tetralayers. Only parts of this procedure were followed for fabricating control groups, as described, where only either one of the multilayers were needed.

Film morphology characterization. Film thickness was measured using a Dektak 150 Profilometer. Films were scratched using a razor blade until the substrate was exposed. Film thickness was determined by the average step height of 3 scans 3000 μm long perpendicular to the scratch. The surface morphology and roughness of the films was examined using a Nanoscope IV atomic force microscope (Veeco Metrology, Santa Barbara, CA). Scanning electron microscope (SEM) images and energy dispersive X-Ray spectroscopy (EDX) line-scans were performed in a JEOL JSM 6700 scanning electron microscope. Surface zeta potential measurements where performed using a Delsa™ Nano C Zeta Potential Analyzer (Beckman Coulter, CA) with a flat surface cell unit as per the manufacturer's protocol. All measurements were performed at least in triplicate.

rhBMP-2 release characterization. Substrate coated with film were released at 37°C into 1 mL of 1x PBS in 2 ml centrifuge tubes (VWR Scientific, Edison, NJ). At a series of pre-determined time points, the coated substrate was transferred into new centrifuge tubes containing fresh 2 ml 1x PBS. Release fractions were frozen down and stored at -20°C. Samples were analyzed using rhBMP-2 ELISA development kits (Peprotech, NJ) according to manufacturer instructions. Release of rhBMP-2 was normalized to film volume (area of substrate x film thickness). All release studies were performed in triplicate.

In vitro cellular assays. Adult mesenchymal stem cells (Lonza) were cultured in α-MEM supplemented with 20% FBS and 1% penicillin-streptomycin solution. 10,000 cells were seeded on each glass cover slip coated with different combinations of the electrostatic films with appropriate controls as described in the paper. Alkaline phosphatase assay was performed on day 5. After 14 days of culture under different conditions, calcium deposits on the cover slips were assayed using alizarin red staining and quantified using a previously described protocol [2]. Media was changed and aliquots were frozen down every 48 hours and assayed for specific bone marker proteins using human bone panel assay 1B (Millipore) according to the manufacturer's protocol. All assays were performed in triplicate. For visualization and morphology at predetermined timepoints, cells were fixed in 4% paraformaldehyde for 15 minutes and permeabilized with 0.1% Triton X-100 for 10 minutes. Cells were washed 3x with PBS between each step. Alexa Fluor® 647 phalloidin was used to label actin filaments, 4′,6-Diamidino-2-phenylindole dihydrochloride (DAPI) was used to stain the nucleic acids in the cell nucleus. Osteocalcin production was visualized by staining with a primary osteocalcin antibody (OC4-30 (Abcam, Cambridge, MA)) followed by a secondary goat anti-mouse Alexa Fluor® 488 antibody.

References

[1] D. M. Lynn, R. Langer, J. Am. Chem. Soc. 2000, 122, 10761.

[2] C. A. Gregory, W. G. Gunn, A. Peister, D. J. Prockop, Anal Biochem 2004, 329, 77.

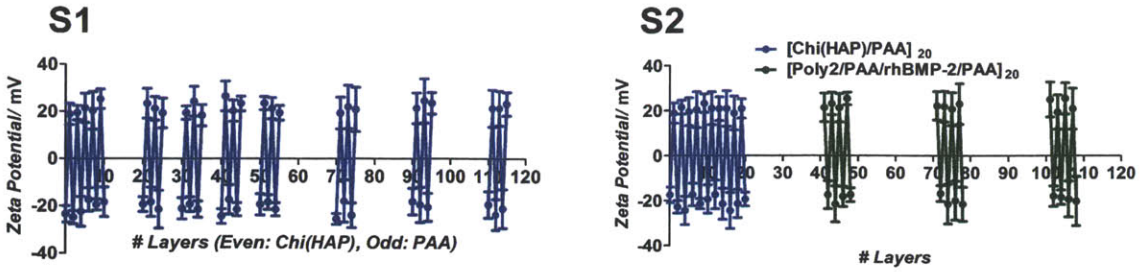

Figure A1 (Left) ξ-potential measurements during [Chi(HAP)/PAA] film assembly confirmed charge reversal at each layer through 60 bilayers (as measured periodically). (Right) Representative ξ-potential reversal during fabrication of both modules of the multilayer film - here $[Chi(HAP)/PAA]_{20}$ followed by $[Poly2/PAA/rhBMP\text{-}2/PAA]_{20}$ is used as an example.

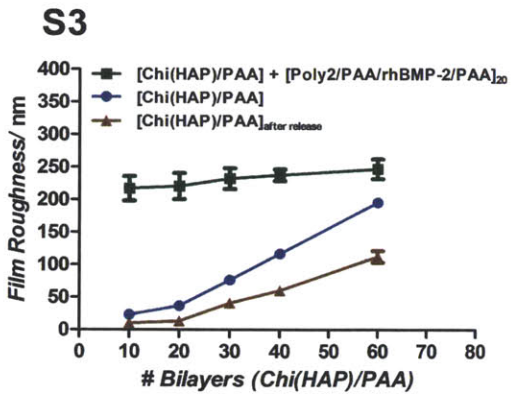

Figure A2 Surface roughness of the multiayers before and after release of growth factors.

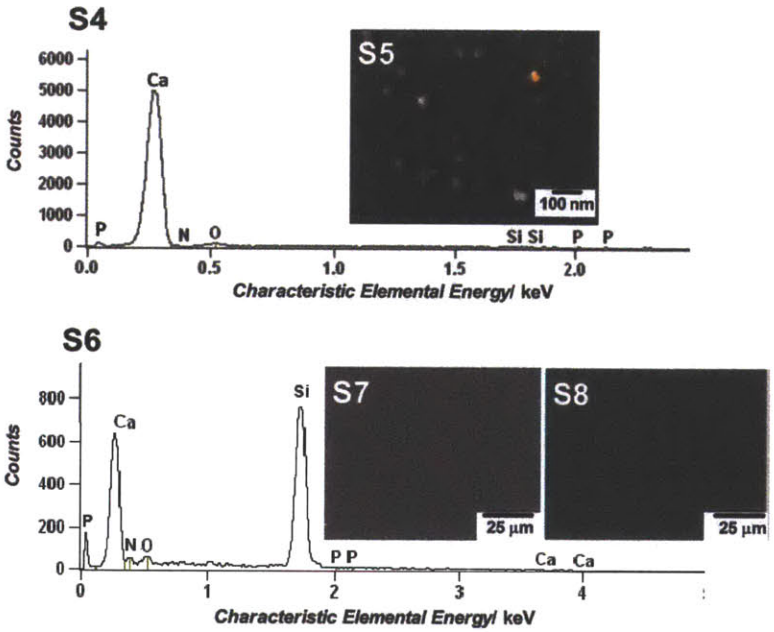

Figure A3 Elemental analysis using energy dispersive X-Ray spectroscopy (EDX) profile of an HAP particle on the film surface. Calcium, along with phosphate, nitrogen and oxygen are detected. (S5, S7, S8) EDX calcium mapping of the $[Chi(HAP)/PAA]_{20}$ multilayer film. Calcium present in HAP (S7) is detected as green spots in S8. Silicon (substrate) is also detected.

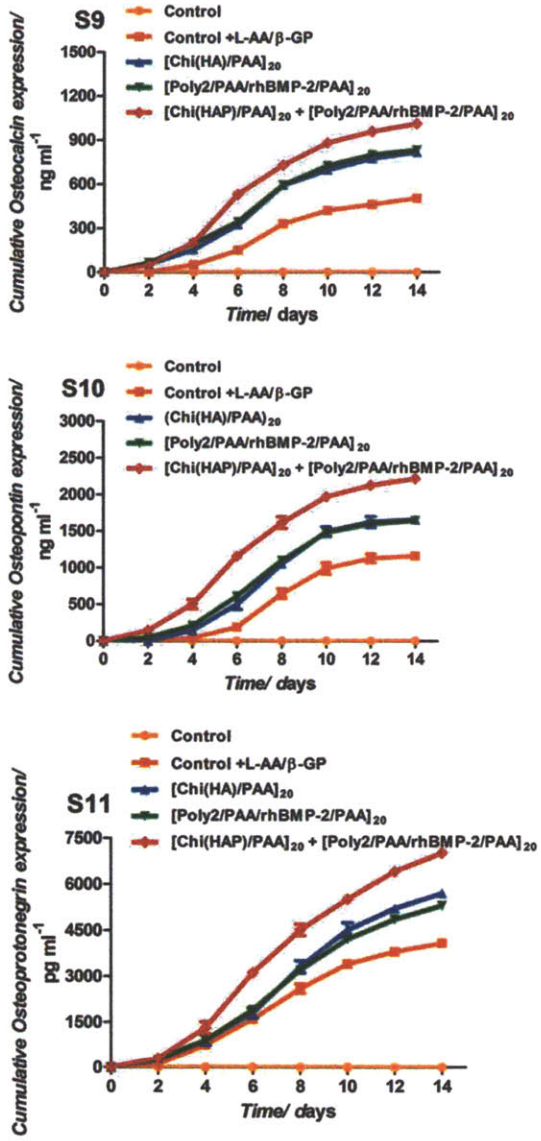

Figure A4 Cumulative expression of osteocalcin, osteopontin and osteoprotonegrin. Compared to the L-AA+ β-GP control, the highest expression levels are observed in the group containing the osteoconductive and osteoinductive layers ($p<0.001$ at each timepoint). Upregulation in the $[Chi(HAP/PAA]_{20}$ and $[Poly2/PAA/rhBMP\text{-}2/PAA]_{20}$ multilayer groups is similar and statistically not significant but is higher than the L-AA+ β-GP control ($p<0.001$ at each timepoint). The data plotted in Figures S9, S10, S11 are the same as in Figures 2.3C, 2.3E, 2.3F respectively.

Appendix B

Methods

Preparation of electrostatic films

Multilayer films were made using the layer-by-layer method (*13-15*). All solutions were prepared in 0.1M, pH 4.0 sodium acetate buffer. Hydroxyapatite (HAP) nanoparticle suspension (10 wt%) (Sigma Aldrich) was diluted five-fold in buffer, sterile filtered through a 0.45 μm cellulose acetate membrane (VWR Scientific) and added 1:1 (v/v) to chitosan (Sigma Aldrich) solution (2 mg/ml). Poly(acrylic acid) (PAA) (Mv ~ 450,000) (Sigma Aldrich) and Poly2 dipping solutions were prepared (1 mg/ml). rhBMP-2 (Pfizer), was diluted to 250 μg/ml in sodium acetate buffer from a 10 mg/ml stock solution. PEEK (McMaster-Carr) was machined into various geometries and medical grade titanium dowels (Titanium Industries). PEEK rods and titanium dowels were machined into rods with diameter 1.3 mm and height 4 mm. PEEK and titanium rods were drilled to make holes 150μm in diameter. Flat PEEK substrates were machined from PEEK sheets with dimensions 10 mm × 4 mm × 1 mm (W × L × H).

PEEK rods or sheets were plasma treated with air for 10 minutes and alternatively dipped into the prepared solutions with an intermediate washing step in water. First, the osteoconductive $[Chi(HAP)/PAA]_x$ base layers were coated followed by the osteoinductive $[Poly2/PAA/rhBMP\text{-}2/PAA]_y$ layers. PEEK rods or sheets were sterilized using plasma treatment with air for 10 minutes using a Harrick PDC-32G plasma cleaner (Harrick Plasma) on high RF power and immediately immersed in a polycation solution (either the chitosan/HAP solution or Poly2 with a Carl Zeiss HMS programmable slide stainer (Microm International GmbH, Thermo Fisher Scientific). Removable parts of the equipment were autoclaved and the slide stainer was wiped thoroughly with bleach and sprayed down with 70% ethanol at least 3 times before each dipping cycle. All solutions were sterile filtered. These steps were taken to eliminate the need for post coating sterilization.

All LbL films were fabricated at room temperature. First, osteoconductive baselayers

were fabricated on the substrate with the following dipping protocol:

1. Chi(HAP) solution (5 min)
2. 3X wash in water for 10, 20, and 30 seconds
3. PAA solution (5 min) and
4. 3X wash in water for 10, 20, and 30 seconds

This cycle was repeated for 20 bilayers (X_{20}). The osteoinductive top layers were coated immediately after, using the following protocol:

1. Poly2 solution (5 min)
2. 3X washes in different water baths (10, 20, 30 s)
3. PAA solution (5 min)
4. 3X washes in different water baths (10, 20, 30 s)
5. rhBMP-2 solution (5 min)
6. 3X washes in different water baths (10, 20, 30 s)
7. PAA solution (5 min) and
8. 3 sequential washes in different water baths (10, 20, 30 s).

This cycle was repeated to load different amounts of rhBMP-2 (Y_{20}, Y_{40}, Y_{60}). Poly2 solution was changed every 12 hours and rhBMP-2 solution was changed every 24 hours. The final product was stored at 4°C until use.

Film characterization

A. Nanoindentation

A Hysitron Triboindentor (Hysitron) with a conical tip (10 μm tip diameter) at a load of 1000 μN (ramp rate 25 μN/s) and dwell time of 3 s was used for nanoindentation. A standard fused quartz sample was used to calibrate the frame compliance, and the diamond tip-area function needed for analysis. For the purposes of this study, 100 bilayers of osteoconductive layers were coated, corresponding to a thickness of 1 μm. The indentations were performed at a depth of no more than 10% of the film thickness to avoid the effect of the underlying substrate. At least 40 (20 x 20 grid)

indentations on each sample were performed from which the statistical average of the elastic modulus and hardness data were evaluated based on the Oliver-Pharr method (*37*).

B. Film Thickness

The osteoconductive base layer $[Chi(HAP)/PAA]_x$ was coated on the flat PEEK substrate and the thickness of the dry film was measured using a Nanoscope IV atomic force microscope (AFM) (Bruker). The coating was scratched in a single line with a razor blade to expose the substrate. The AFM tip was aligned perpendicular to the scratch. The surface of the coating was scanned (100 nm × 2000 μm) and the step size indicated the thickness. The osteoinductive [Poly2/PAA/rhBMP-2/PAA]y layers were then coated on the same substrate and the final thickness of the dry film was measured using a Dektak 150 Profilometer (Veeco). After the maximum duration of rhBMP-2 release (15 days), the substrate was rinsed 3x in PBS, dried with nitrogen and the thickness was measured using the AFM.

In vitro cellular assays

PEEK rods coated with LbL films containing rhBMP-2 were incubated in cell culture growth media (α-MEM supplemented with 20% FBS, 1% penicillin-streptomycin solution), which served as a release medium and incubated at 37°C. The release medium was periodically changed and assayed for rhBMP-2 using ELISA (Peprotech). Adult human mesenchymal stem cells (Lonza) were cultured in media as described above and seeded 10,000 cells/well on PEEK sheets coated with the electrostatic films. Alizarin red (Sigma) assays were performed using the using a previously described protocol *(38)*. Alkaline phosphatase (ALP; Roche Applied Science) activity was determined on day 5 after the initiation of osteogenic differentation by quantifying the enzyme activity. Cells were rinsed 2X with PBS without Ca^{2+} and Mg^{2+} and fixed in 4% paraformaldehyde for 10 min at room temperature. 0.1% triton in PBS was added to the fixed cells and frozen at -80°C for one freeze-thaw cycle. Cell lysates were transferred to an Eppendorf tube, centrifuged at 15,000 g for 3 min at 4°C, and the supernatant was collected. 50 ml of lysate was incubated with 150 mL of pNPP solution for 30 min at

37°C. The reaction was terminated with 0.1 M NaOH and ALP activity read on a plate reader at 405 nm. The ALP activity measurements were normalized to total protein determined by BCA assay. Cells cultured in growth media and differentiation medium (growth medium supplemented with 50 mg/ml L-ascorbic acid and 10 mm β-glycerol phosphate) were used as additional controls.

Labeling and tracking rhBMP-2

rhBMP-2 was labeled with Alexa 647 (Invitrogen) following an adapted version of the manufacturers protocol. 2 mg/ml in 0.1M sodium acetate buffer (pH 4.0) was used for labeling. rhBMP-2 was observed to precipitate in the presence of bicarbonate buffer. After completion of reaction, the mixture was dialyzed for 24 hours at 4°C using a 6,000-8,000 MWCO Spectra/Por dialysis membrane (Spectrum Laboratories) to remove the free, unreacted dye and sodium bicarbonate buffer was exchanged with 0.1M sodium acetate buffer (pH 4.0) at. The solution was lyophilized and the protein was used to prepare LbL films.

IVIS Spectrum preclinical imaging system and Living Image software (Caliper) were used to acquire and quantitate the fluorescence (ex/em 650/668 nm), respectively. Images were taken immediately after surgery and at most once every 24 hours after the first 4 weeks and every 48 hours subsequently until loss of signal.

Quantifying bioactivity of labeled rhBMP-2

rhBMP-2 was labeled with Alexa Fluor 647 following the manufacturer's protocol (Invitrogen). The concentration of labeled and unlabeled growth factor were measured (using ELISA) and matched at 250 μg/ml and identical labeled and unlabeled rhBMP-2 films were constructed on PEEK rods (Y_{60}) and incubated in cell culture media (α-MEM supplemented with 20% FBS, 1% penicillin-streptomycin solution), which served as a release medium and incubated at 37°C. The release medium was changed every 24 hours and assayed for rhBMP-2 using ELISA (Peprotech) and stored at -20°C for 2 weeks. Adult mesenchymal stem cells (Lonza) were cultured in media in 6-well tissue culture plates (BD Biosciences) at 10,000 cells/well. Every 24 hours, the media was

changed and frozen aliquots were added to cell culture. A matched concentration of rhBMP-2 stock was added as an additional control. These groups were assayed using the alizarin red (n = 6 per group) (Appendix B; fig. B2).

In vivo animal studies

All animal work was performed in accordance with protocols approved by the Committee on Animal Care (IACUC) at MIT. Adult male Sprague-Dawley rats (350-400 g; Charles River) were anesthetized and both lower limbs were shaved, disinfected with povidone iodine, and draped in a sterile manner. A 5-mm skin incision was made at the proximal tibial metaphysis in the region of the tibial tuberosity and extended to the underlying fascia and periosteum. The implant site was prepared by intermittent drilling a 1.4-mm unicortical hole through the cortical and cancellous bone below the patella ligament in order to gain access to the medullary cavity of the proximal metaphysis. This was done using a customized handheld drill (Aseptico) with dental burrs (FST), and operated at a low rotary speed with saline irrigation. The implant (diameter 1.3 mm) was inserted without tapping and was flush with the external surface of the tibia entry site. The incision was closed in two layers with 5-0 polyglycolic acid sutures (Vicryl) in subcutaneous tissues and skin, respectively. This procedure was repeated in the opposite limb. Animals were allowed unrestricted activity upon recovery and provided with analgesics.

The eight groups are referred to throughout the paper and are listed here were implants that were – uncoated, coated with X_{20}, Y_{60}, $X_{20} + Y_{20}$, $X_{20} + Y_{40}$, $X_{20} + Y_{60}$, X_{20} and 60 bilayers of [Poly2/PAA], each soaked in rhBMP-2. Within each group, animals were subject to measurements of 5 parameters: ELISA of the marrow for growth factor release, tracking of fluorescently labeled in vivo growth factor release, micro-CT scans (same group of animals), FACS analysis, and tensile testing. Three animals and 5 independent implants at each time point were used for all other measures listed above for each group. In addition, at least 5 implants at each time point were used for the pull-out tests for each formulation. A total of 36 animals were used for the titanium pull-out tests with the uncoated, coated X_{20}, Y_{60} groups $X_{20} + Y_{60}$ at 1 and 4 weeks.

Protocol for implant histology

PEEK implants that were removed from the site of implantation using pull-out tests were incubated in 4% paraformaldehyde for 24 hours and dehydrated in 70% ethanol for 24 hours. These samples were embedded in glycol methacrylate (JB-4 Plus Embedding Media, Polysciences) following the manufacturer's protocol. Briefly, fresh infiltration solution was prepared by carefully weighing 1.25gm of catalyst (benzoyl peroxide, plasticized) and adding to 100 ml Solution A while stirring on a magnetic stirrer until dissolved. Infiltration was performed on a platform shaker (VWR Scientific) at room temperature by placing specimens in three 30 minute changes of infiltration solution, 10 times the volume of the specimen to allow for the removal and replacement of all alcohols or tissue fluids. Embedding media was prepared using 25ml of freshly made Infiltration Solution and 1.0ml of JB-4 Plus Solution B thoroughly. The specimen was oriented in a block holder, such that the features of interest would be part of block sections (drilled holes, implant/bone interface, etc.) and 1.5-2 ml of embedding solution was added per specimen. H&E and Masson's trichrome stains were performed on block sections.

MSC isolation and FACS analysis

After euthanasia, tibiae were explanted and a 0.8-mm burr hole extending into the medullary cavity was drilled from the knee joint. A hypodermic needle was inserted into the medullary cavity and connected to a heparinized syringe to aspirate bone marrow. The medullary cavity was flushed with 4 ml cell culture media and aspirated. Samples were digested (45 min at 37°C) with 0.25% trypsin in phosphate-buffered saline (PBS). Next, enzymes were inactivated with cell culture media, and recovered cells were washed with PBS. One-hundred microliters of sample were frozen for rhBMP-2 ELISA measurements. Recovered cells were analyzed by flow cytometry (LSR Fortessa HTS, BD Biosciences) with monoclonal anti-rat antibodies against CD29, CD44, CD45, CD90 (BioLegend), and BMPR1/2 (Santa Cruz Biotechnology).

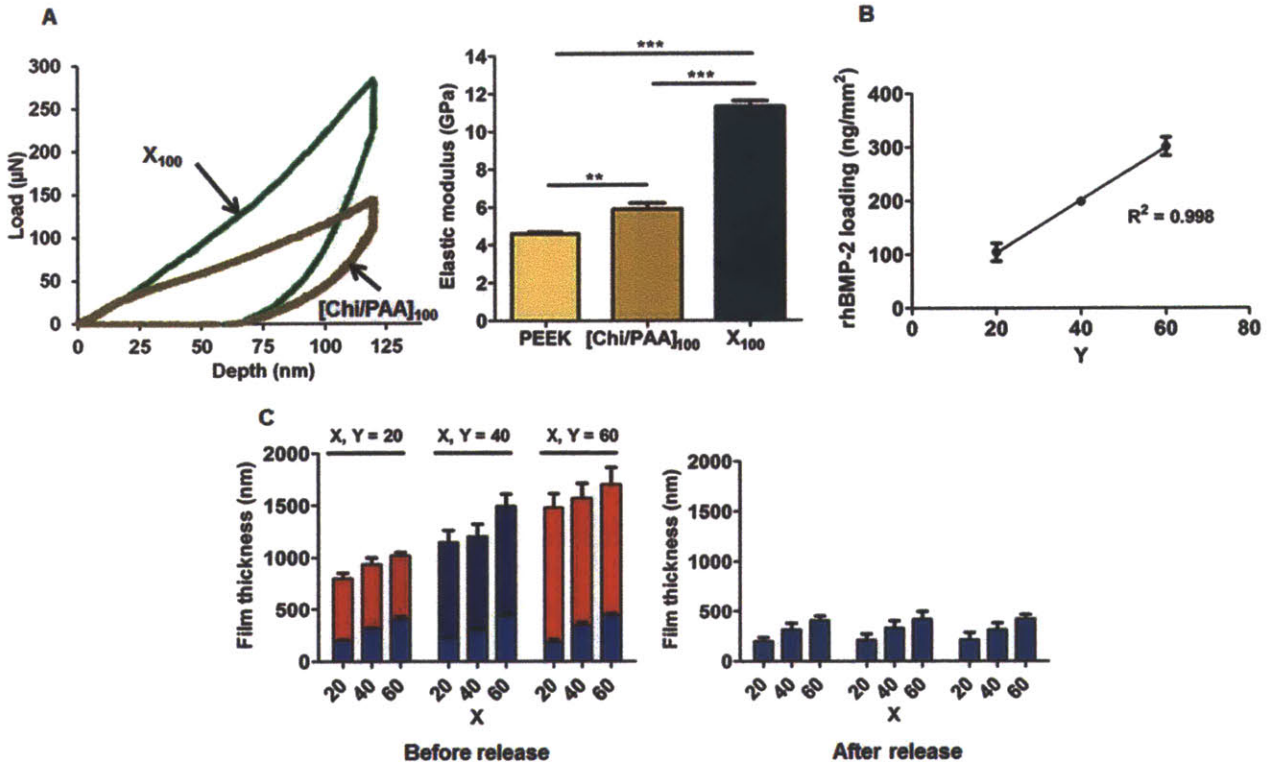

Fig. B1. Osteogenic layer-by-layer film characteristics. (**A**) Nanoindentation load vs. depth curves for osteoconductive base layers with and without HAP (n = 20). Elastic modulus was calculated using the Oliver-Pharr method (*45*). Elastic modulus of the PEEK substrate and the osteoconductive base layers with and without HAP. Data are means ± SEM (n = 20). $^{**}P < 0.01$, $^{***}P < 0.001$ versus control, ANOVA with a Tukey post hoc test. (**B**) Loading of rhBMP-2 is a function of the number of rhBMP-2 layers. Data are means ± SEM (n = 9). (**C**) Total thickness of the films is a function of the number of layers in the film. Colors: teal, X_{20}; red, Y_{20}; blue, Y_{40}; orange, Y_{60}. Thickness of the osteoconductive base layer is similar after release of rhBMP-2. Data are means ± SEM (n = 9).

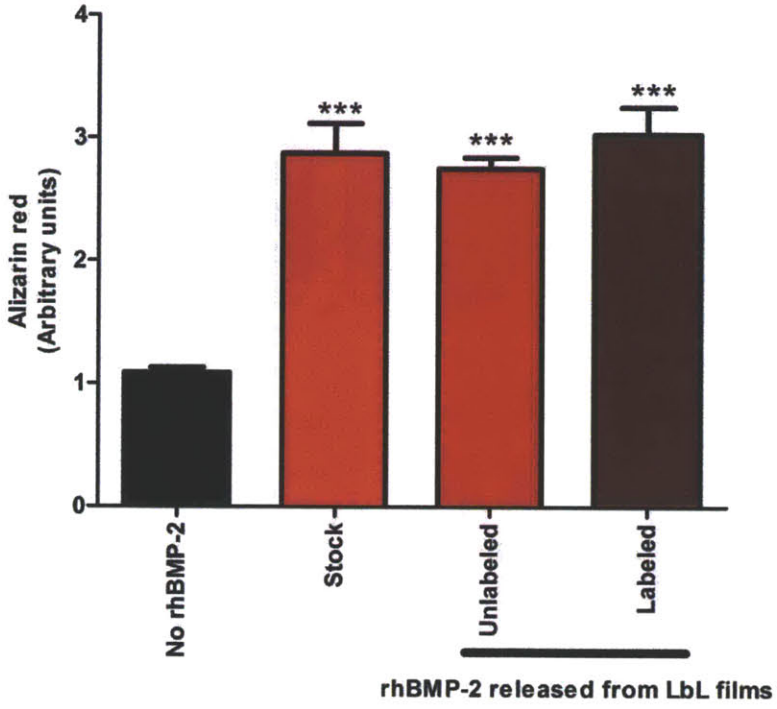

Fig. B2. In vitro bioactivity of rhBMP-2 after release. Alizarin red stain for calcium deposits by differentiating progenitor mesenchymal stem cells exposed to matched concentrations of labeled, unlabeled rhBMP-2 released from films, and matched stock rhBMP-2. Results were normalized to cultured cells not exposed to rhBMP-2 (control). Data are means ± SEM (n = 9). ***P < 0.001 versus control, ANOVA with a Tukey post hoc test.

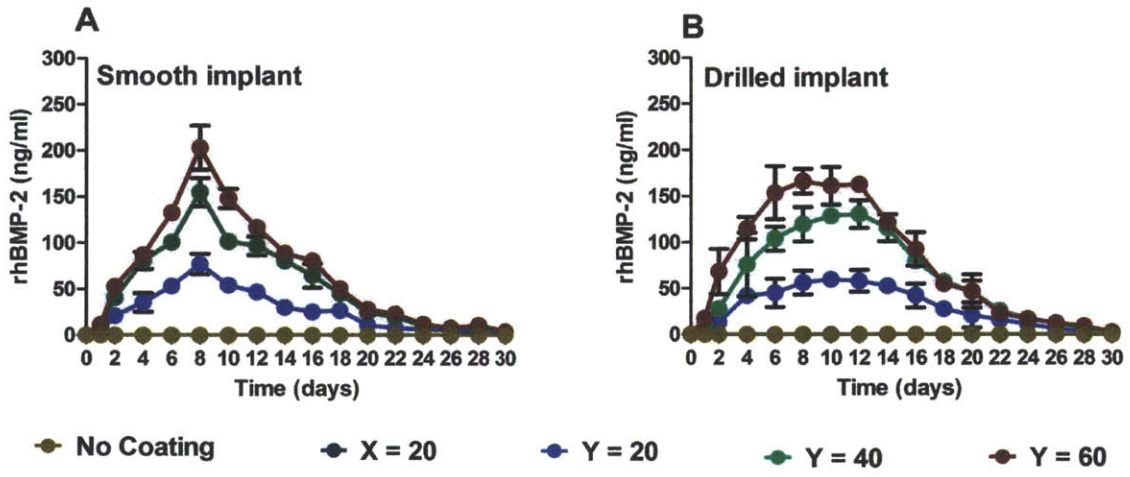

Fig. B3. In vivo detection of rhBMP-2 release from smooth and drilled implants. (**A** and **B**) Release of rhBMP-2 from Y coatings without the underlying X_{20} layers. Uncoated implants and implants with only an X_{20} coating were also assayed for rhBMP-2 detection.

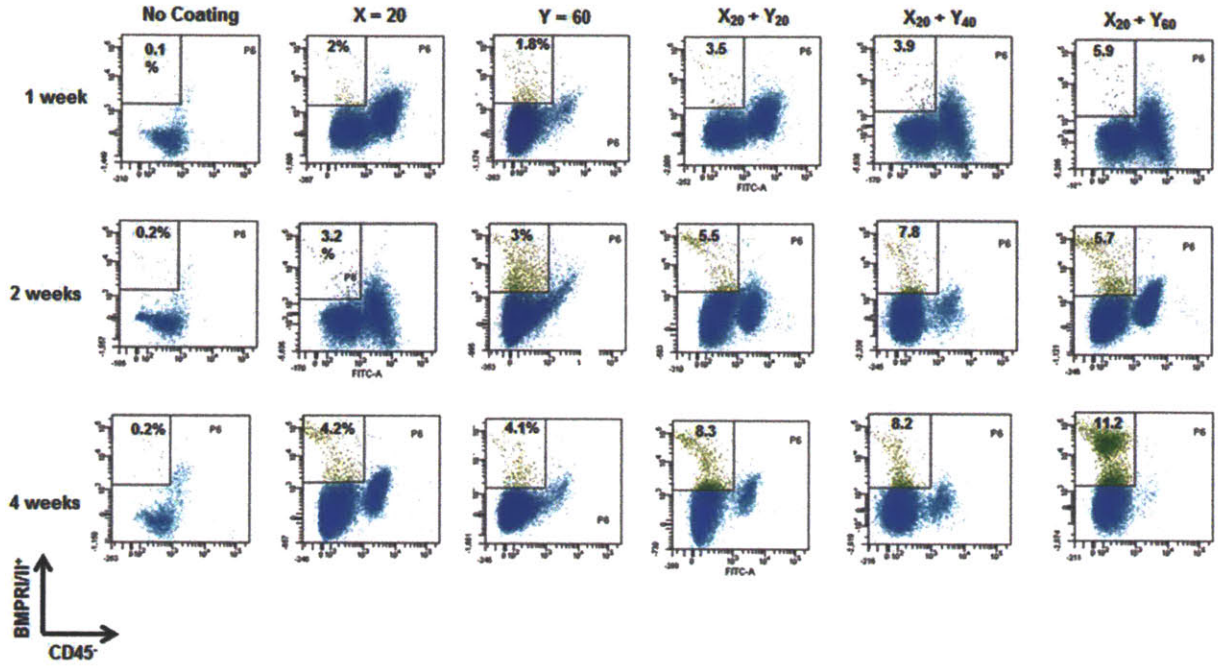

Fig. B4. Flow cytometry plots for all study groups. The upper left quadrant in each plot contains cells that are positive for osteoblast phenotype ($CD29^+CD44^+CD45^-CD90^+BMPRI/II^+$)

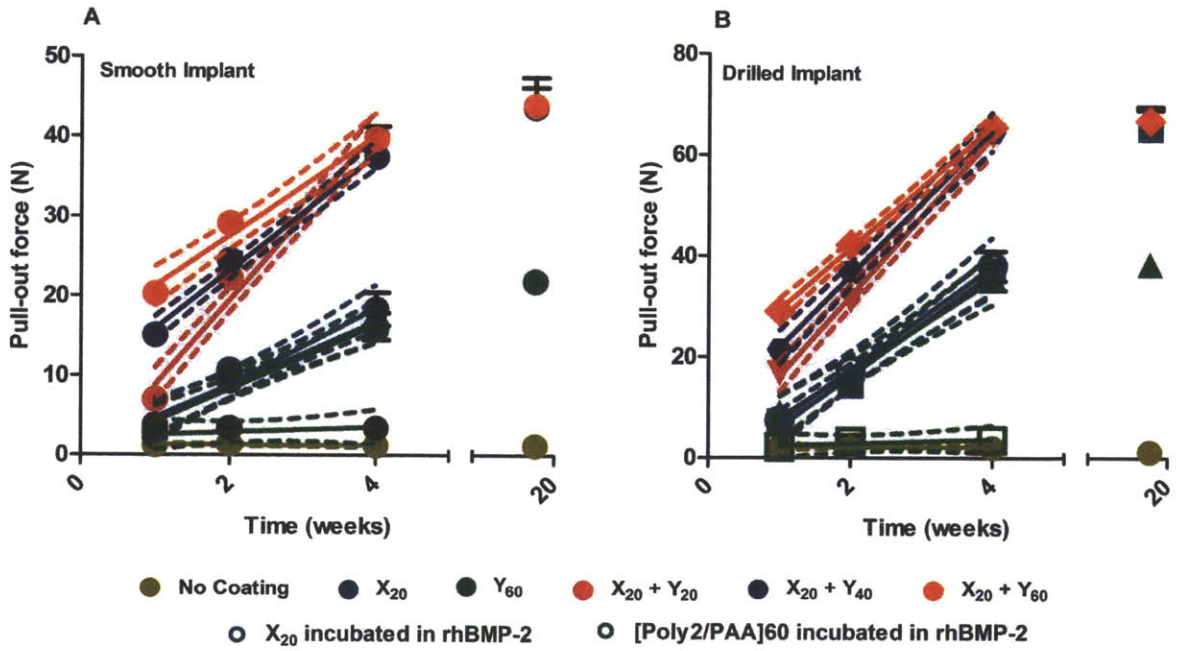

Fig. B5. Average pull-out tensile force over time. Pull-out tensile force increased linearly for all coated implants with a coating ($R^2 \geq 0.98$). A comparison in the slopes indicated that, for smooth implants, the differences in the slopes yields $P < 0.0001$ (ANCOVA). Data are means ± SEM ($n = 5$) for both smooth and drilled implants between all groups.

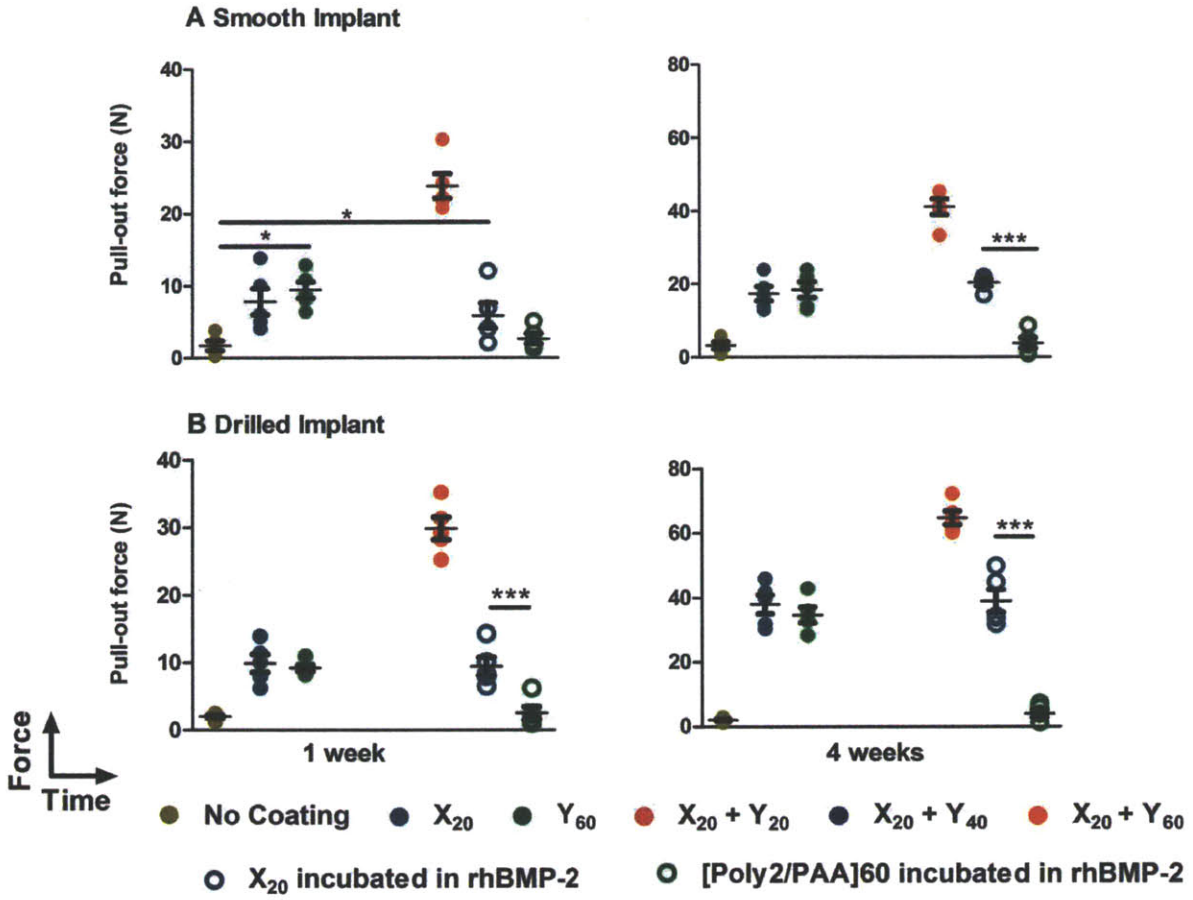

Fig. B6. Pull-out tensile force testing of medical-grade titanium implants from the tibia. Data from both smooth and drilled implants is represented for tests performed at 1 and 4 weeks post-implantation. Data are means ± SEM (n = 5 implants per group time point). *P < 0.05, *** P < 0.001, ANOVA with a Tukey post hoc test.

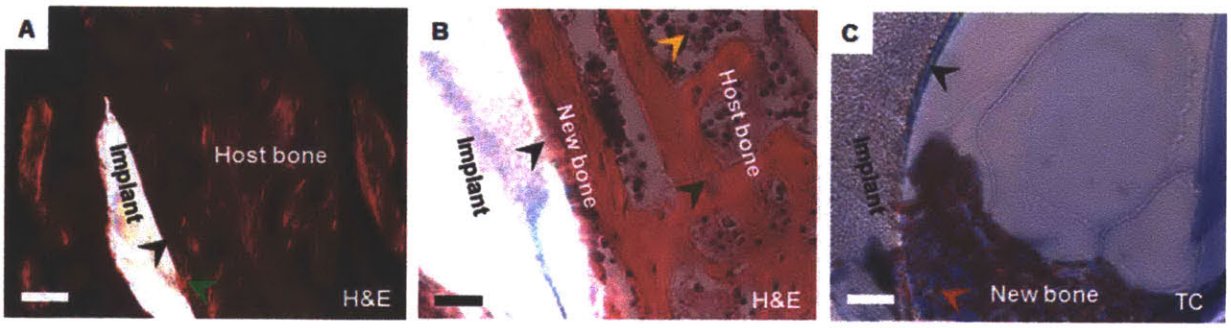

Fig. B7. Arrangement of new bone on X_{20}-coated PEEK implants at 4 weeks. There is a lack of new, mature collagen fibrils in the periprosthetic space. (**A**) Few aligned collagen fibers are present at the implant surface. (**B**) New bone connects with the existing host bone. (**C**) The new bone does remain tethered to the implant pore wall after the pull-out test. Scale bars: 50 μm in (B, C); 200 μm in (A). Arrows: red, active osteoblasts; black, bone/implant interface; lime green, new birefringent bone; dark green, osteocytes; yellow, marrow cells. H&E: hematoxylin & eosin stain, TC: Masson's trichrome stain.

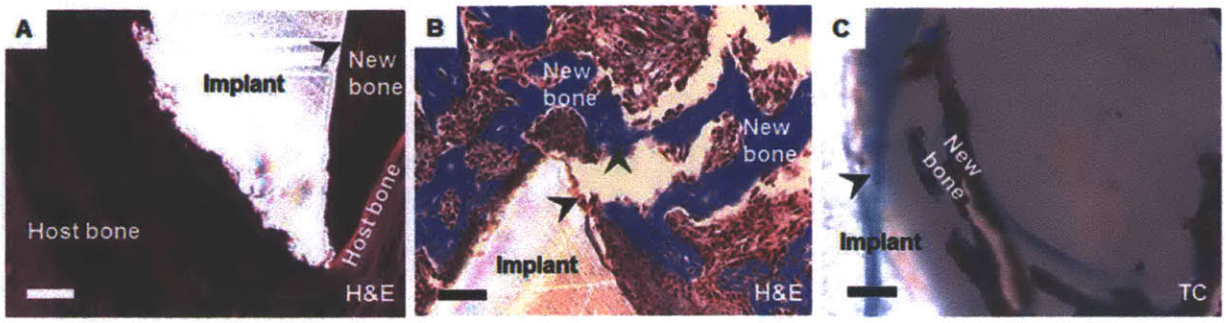

Fig. B8. Arrangement of new bone on Y_{60}-coated PEEK implants at 4 weeks. There is a lack of apposition of the new bone, which is located primarily in the periprosthetic space. (**A**) Aligned collagen is present at sites distal from the implant. (**B**) The volume of new bone is extensive but is located away from the implant surface. (**C**) Regeneration of bone tissue within the implant pores is not conformal to the hole wall with few connections to the wall surface. However, the new bone does remain tethered to the implant pore wall after the pull-out test. Scale bars: 100 μm in (A, B); 50 μm in (C). Arrows: black, bone/implant interface; green, osteocytes. H&E: hematoxylin & eosin stain, TC: Masson's trichrome stain.

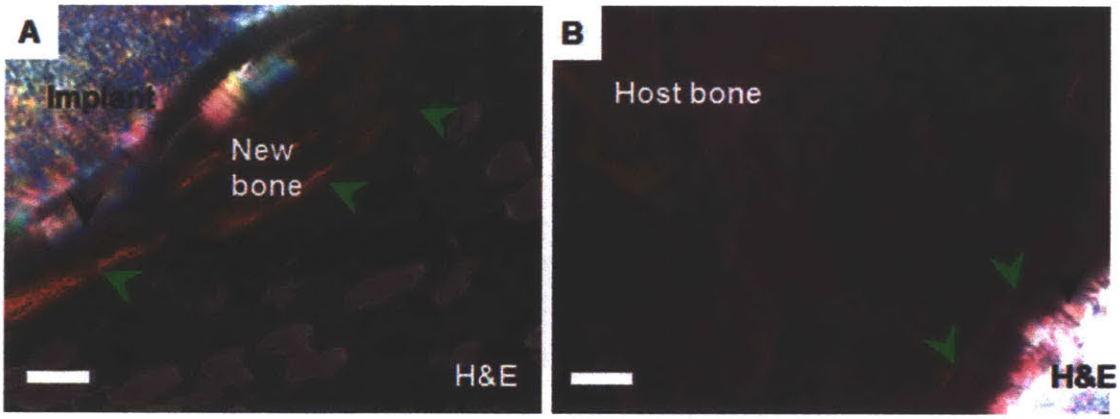

Fig. B9. Collagen formation around X_{20} + Y_{60}–coated PEEK implants at 4 weeks. (**A**) Mature, aligned collagen fibrils in the new bone were observed in the periprosthetic space and the bone was conformal to the implant shape. (**B**) Aligned collagen (in red) was also observed in the new bone extending outward from the implant surface. Arrows indicate regions near the implant where significant birefringence is observed. Scale bar: 50 μm. Arrows: black, bone/implant interface; lime green, new birefringent bone. H&E: Hematoxylin & eosin stain, TC: Masson's trichrome stain.

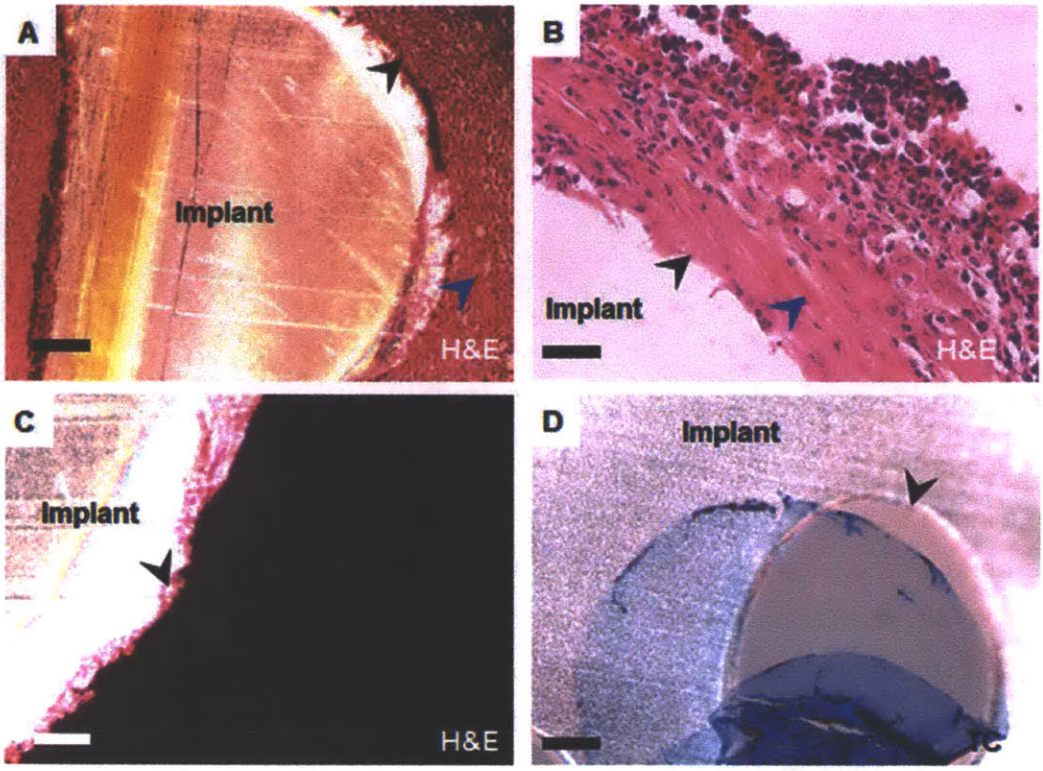

Fig. B10. Fibrotic tissue around uncoated drilled and smooth PEEK implants at 4 weeks. (**A** and **B**) There was a lack of new bone formation in the periprosthetic space or at the implant surface. Instead, there were undifferentiated precursor cells and a thin layer of fibrous tissue. (**C**) There was a lack of aligned collagen (birefringence) with osteocytes on or around the implant. (**D**) Regeneration of bone tissue within the implant pores is absent and the fibrous tissue detaches from the implant after the pull-out test, as above. Scale bars: 50 μm in (B, D, F); 200 μm in (A). Arrows: black, bone/implant interface; blue, fibrous tissue. H&E: hematoxylin & eosin stain, TC: Masson's trichrome stain.

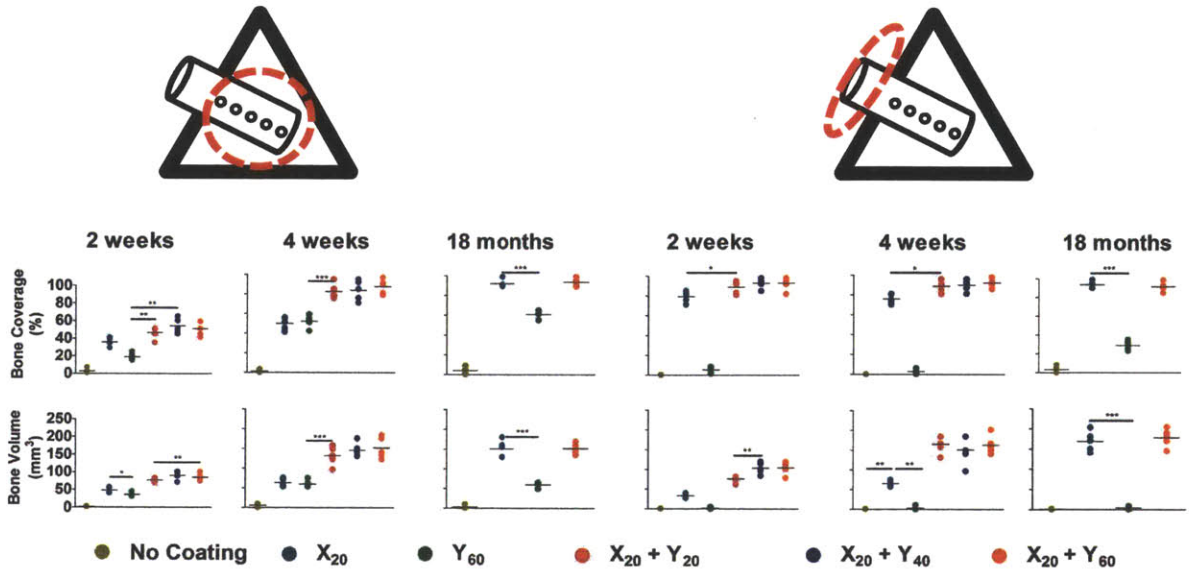

Fig. B11. Bone coverage and bone volume data for smooth implants. Quantitative measurements were obtained from μCT images of PEEK implants at 2 weeks, 4 weeks, and 18 months. Data are means ± SEM (n = 5-6 per group). *P < 0.05, **P < 0.01, ANOVA with a Tukey post hoc test.

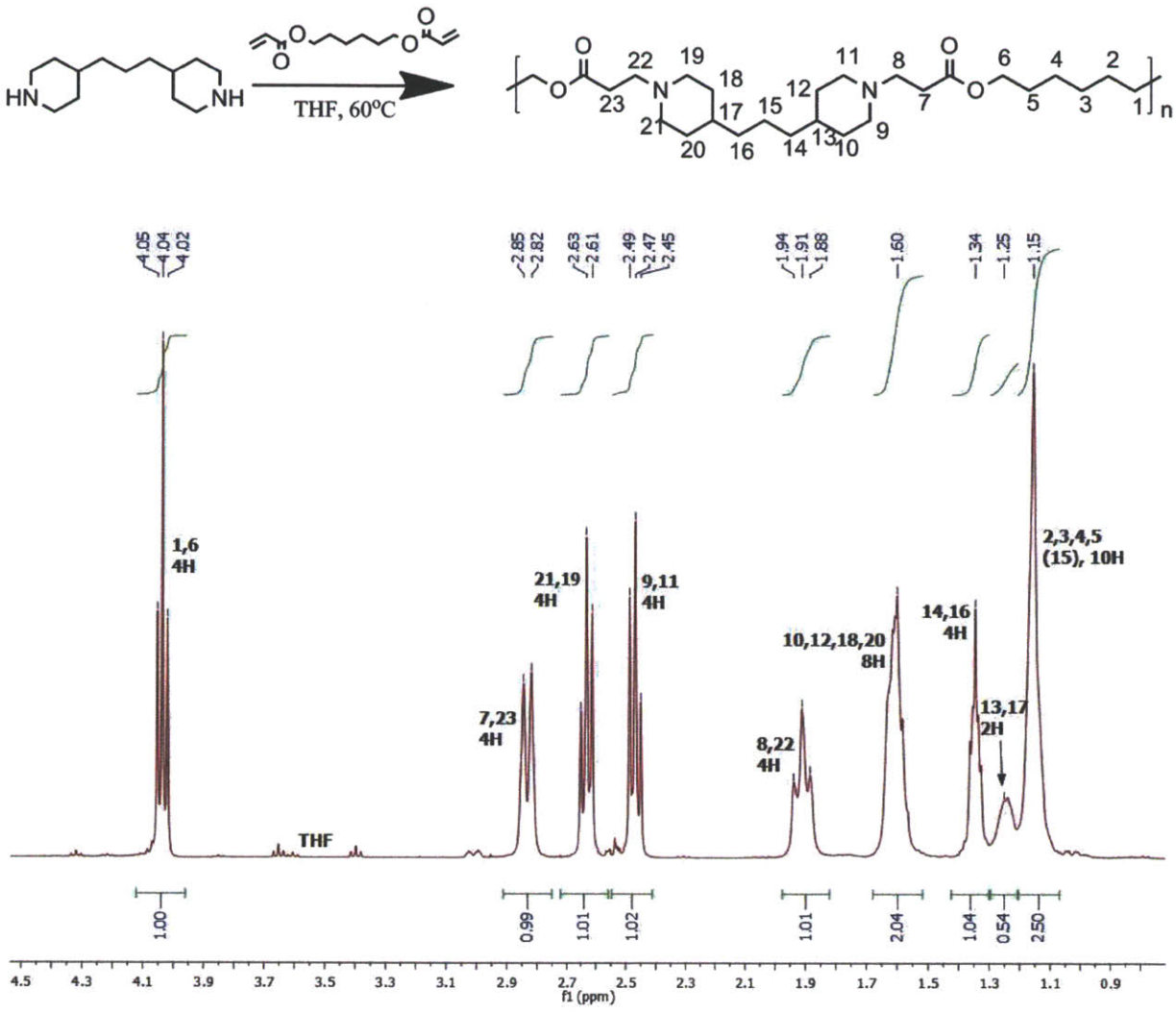

Fig. B12. Nuclear magnetic resonance (NMR) characterization of Poly2. Representative proton (^{1}H) NMR spectra of Poly-2 in $CDCl_3$. The methylene group at 4.03 ppm (t, 2H, -C$\underline{H}_2$-OCO-CH_2-) has been taken as reference for proton integration.

Table B1: Coating formulation groups in the study. In formulations 3 to 6, rhBMP-2 was incorporated as single layers within the LbL multilayers. In formulations 7 and 8, rhBMP-2 was introduced by incubating the multilayers in rhBMP-2 solution (250 µg/ml) for 24 hours.

Formulation	Group
1	Uncoated control
2	$[Chi(HAP)/PAA]_{20}$
3	$[Poly2/PAA/rhBMP\text{-}2/PAA]_{60}$
4	$[Chi(HAP)/PAA]_{20}$ + $[Poly2/PAA/BMP/PAA]_{20}$
5	$[Chi(HAP)/PAA]_{20}$ + $[Poly2/PAA/BMP/PAA]_{40}$
6	$[Chi(HAP)/PAA]_{20}$ + $[Poly2/PAA/BMP/PAA]_{60}$
7	$[Chi(HAP)/PAA]_{20}$ incubated in rhBMP-2
8	$[Poly2/PAA]_{60}$ incubated in rhBMP-2

Table B2: Total rhBMP-2 dose delivered from coatings on smooth and drilled implants. Smooth implant surface area was 17.60 mm^2, whereas drilled implants were 20.26 mm^2. Total dose was calculated based on rhBMP-2 release data in Fig. 2. Data are means ± SEM (n = 9).

Coating	rhBMP-2 dose (μg)	
	Smooth implants	Drilled implants
X_{20} + Y_{20} (or Y_{20})	1.87 ± 0.06	2.13 ± 0.11
X_{20} + Y_{40} (or Y_{40})	3.49 ± 0.15	4.03 ± 0.24
X_{20} + Y_{60} (or Y_{60})	5.32 ± 0.14	6.10 ± 0.11
X_{20} + rhBMP-2 soak	1300 ± 70	1480 ± 70
[Poly2/PAA]$_{60}$ + rhBMP-2 soak	2110 ± 20	2390 ± 63

Table B3: Interfacial tensile strength of smooth implants. Strengths were calculated from pull-out force data from in Fig. 4A. Data are means ± SEM (n = 5).

Group	Interfacial tensile strength (MPa)					
	PEEK implants				Titanium implants	
	1 week	2 weeks	4 weeks	18 months	1 week	4 weeks
Uncoated	0.07 ± 0.01	0.08 ± 0.02	0.07 ± 0.02	0.07 ± 0.05	0.10 ± 0.08	0.18 ± 0.12
X_{20}	0.20 ± 0.03	0.61 ± 0.11	0.92 ± 0.22	2.48 ± 0.32	0.45 ± 0.23	0.99 ± 0.25
Y_{60}	0.17 ± 0.01	0.57 ± 0.11	0.90 ± 0.18	1.24 ± 0.19	0.54 ± 0.14	1.05 ± 0.27
X_{20} + Y_{20}	0.40 ± 0.03	1.36 ± 0.14	2.21 ± 0.11			
X_{20} + Y_{40}	0.86 ± 0.07	1.39 ± 0.12	2.12 ± 0.10			
X_{20} + Y_{60}	1.15 ± 0.08	1.76 ± 0.19	2.25 ± 0.20	2.49 ± 0.45	1.36 ± 0.22	2.33 ± 0.28
X_{20} soaked in rhBMP-2	1.04 ± 0.26	0.53 ± 0.12	0.22 ± 0.13		0.33 ± 0.22	1.16 ± 0.12
$[Poly2/PAA]_{60}$ soaked in rhBMP-2	0.19 ± 0.19	0.19 ± 0.11	0.13 ± 0.08		0.15 ± 0.09	0.22 ± 0.18

Table B4: Interfacial tensile strength of drilled implants. Strengths were calculated from pull-out force data from Fig. 4B. Data are means ± SEM (n = 5).

Group	Interfacial tensile strength (MPa)					
	PEEK implants			Titanium implants		
	1 week	2 weeks	4 weeks	18 months	1 week	4 weeks
Uncoated	0.10 ± 0.03	0.12 ± 0.02	0.10 ± 0.03	0.10 ± 0.07	0.11 ± 0.03	0.12 ± 0.03
X_{20}	0.36 ± 0.08	0.71 ± 0.05	1.84 ± 0.21	3.22 ± 0.42	0.56 ± 0.17	2.16 ± 0.38
Y_{60}	0.44 ± 0.06	0.76 ± 0.11	1.77 ± 0.30	1.90 ± 0.15	0.52 ± 0.16	1.97 ± 0.30
X_{20} + Y_{20}	0.83 ± 0.11	1.54 ± 0.14	3.16 ± 0.16			
X_{20} + Y_{40}	1.06 ± 0.09	1.82 ± 0.13	3.19 ± 0.20			
X_{20} + Y_{60}	1.44 ± 0.06	2.08 ± 0.06	3.24 ± 0.14	3.30 ± 0.31	1.70 ± 0.21	3.68 ± 0.27
X_{20} soaked in rhBMP-2	1.88 ± 0.33	0.86 ± 0.19	0.37 ± 0.11		0.54 ± 0.17	2.21 ± 0.45
$[Poly2/PAA]_{60}$ soaked in rhBMP-2	0.18 ± 0.16	0.16 ± 0.08	0.10 ± 0.06		0.14 ± 0.12	0.22 ± 0.15

Appendix C

Methods

Alendronate conjugation to membrane.

The PLGA membrane was prepared using the diffusion induced phase separation process. A homogenous 20wt% solution of PLGA in dimethylformamide (DMF) was prepared at room temperature and degassed. Using a doctor blade knife, the polymer solution was cast on a glass plate and immersed in deionized water at room temperature. The resulting membrane was rinsed continuously with deionized (DI) water for 2h, immersed in DI water for an additional 48h and dried at ambient conditions. A micrometer was used to determine the composite membrane thickness by measuring at least 10 different locations including the center. Alendronate was conjugated to PLGA using a modified version of a previously reported procedure (1) and described in Appendix C. As a representative synthetic procedure, 1g of PLGA was dissolved in 15mL of dichloromethane, and added to 15 mg of p-nitrophenyl chloroformate and 10μL of pyridine to activate the terminal hydroxyl group of the polymer, corresponding to ~10wt% functionalization. The reaction was carried out for 4h in an ice bath under inert atmosphere. The resulting solution was further diluted by the addition of 10 mL of dichloromethane, and subsequently extracted with 0.1% HCl and brine. After separation, the organic phase was dried over magnesium sulfate, filtered and evaporated to yield activated PLGA polymer. Activated PLGA was dissolved in 5 mL of DMF, and treated with 10mg of alendronate and 5μL of triethylamine (mixed prior to addition) for 24h at room temperature under inert atmosphere. After 24h, the reaction mixture was precipitated in cold ether, washed with water, filtered and vacuum dried. Additional dialysis was carried out for 48h to remove free alendronate through 6K MWCO membrane. ^{31}P-NMR was carried out on the dialyzed product to confirm conjugation.

Characterization and *in vitro* studies.

Films were characterized using a a JEOL 6700 Field Emission Scanning Electron Microscope. For *in vitro* release experiments, coated membranes were incubated in 1ml cell culture media (α-MEM supplemented with 20% FBS, 1% penicillin-streptomycin solution) at 37 °C. The release medium was changed at pre-determined time points and assayed for BMP-2 and PDGF-BB using ELISA (Peprotech).

***In vivo* critical size defect studies.**

All animal work was performed in accordance with protocols approved by the Committee on Animal Care (IACUC) at MIT. Animals were cared for in an AAALAC certified MIT animal facility meeting federal, state, local, and NIH guidelines for animal care. The critical size defect model has been described previously (2). Skeletally mature adult male Sprague-Dawley rats (350-400 g; Charles River) were used in the study. Soft tissue dissection after a scalp incision was used to expose the calvarium. The periosteium was scraped off to expose the underlying bone. A trephine drill (Salvin Dental Specialties) was used to create a circular critical size defect (8.0mm diameter) with intermittent irrigation of the site with phosphate buffer saline. The calvarium was excised and discarded while maintaining the dura and a PLGA membrane (8.0mm diameter) was placed on the defect site and immobilized with sutures to the surrounding soft tissue. The wound and incision were closed and animals were provided with analgesics until recovery.

In vivo tracking of PDGF-BB and BMP-2

PDGF-BB and BMP-2 were labeled with Alexa 750 and 647 respectively (Invitrogen) following an adapted version of the manufacturer's protocol. 2 mg/ml in 0.1M sodium acetate buffer (pH 4.0) was used for labeling. After completion of reaction, the mixture was dialyzed for 24 hours at 4°C using a 6,000-8,000 MWCO Spectra/Por dialysis membrane (Spectrum Laboratories) to remove the free, unreacted dye and sodium bicarbonate buffer was exchanged with 0.1M sodium acetate buffer (pH 4.0) at. The solution was lyophilized and the protein was used to prepare LbL films. IVIS Spectrum preclinical imaging system and Living Image software (Caliper) were used to acquire and quantitate the fluorescence in the same animal (ex/em 749/775 nm and 650/668 nm for PDGF-BB and BMP-2 respectively). Images were taken immediately after surgery and once every 24 hours until loss of signal.

µCT analysis and histology evaluation.

Anesthetized live animals were imaged with a µCT (eXplore CT120, GE Medical Systems). Scanning protocol: Shutter speed (325 s), 2×2 binning, 70 kV, 50 mA, 220 images, 0.877° increments, gain: 100 and offset: 20. Images were reconstructed and analyzed with MicroView (GE Healthcare). Defect margins were established to delineate a standard region of interest (ROI) per animal. A threshold value (constant for all groups) was selected and the bone mineral density (BMD) and bone volume (BV) were measured using the Bone Analysis tool.

Histology analysis

After euthanasia at pre-determined time points, calvaria were excised and fixed in 4% paraformaldehyde (PFA) for 48 hours and transferred to a 70% ethanol solution. Calvaria were partially decalcified for about 4 hours using a rapid decalcifying formic acid/hydrochloric acid mixture (Decalcifying Solution, VWR). The defect area was cut in cross-section with a razor blade and embedded in paraffin wax. Sections (5 µm) of the cross section were stained with Masson's trichrome stain and imaged using brightfield microscopy.

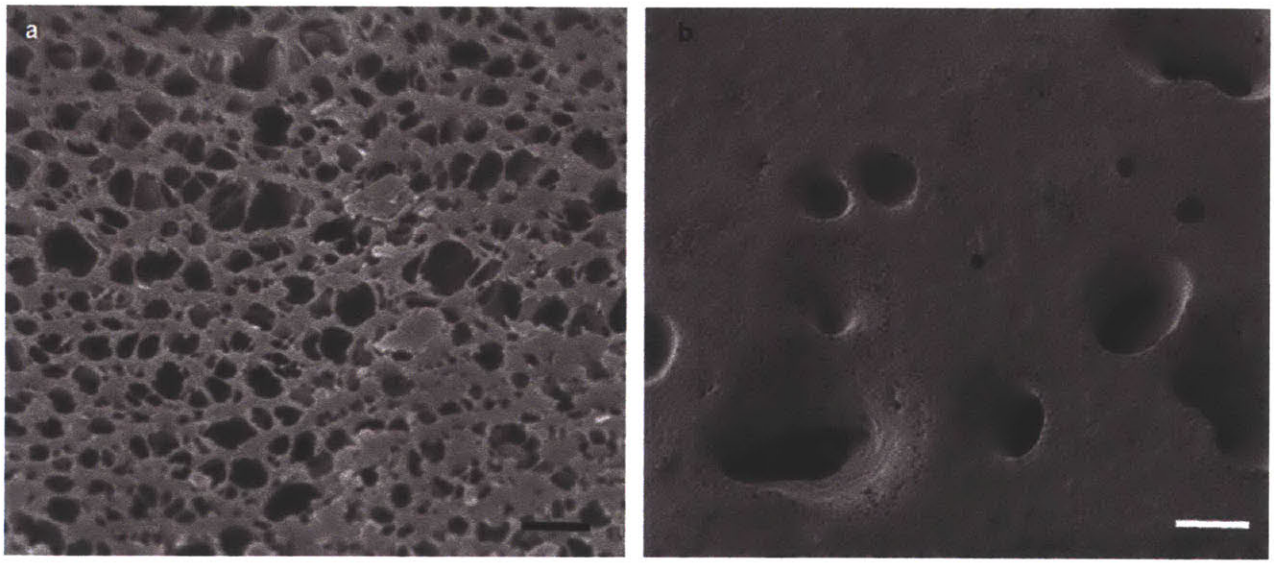

Figure C1. Scanning electron micrographs of the membrane surface. (a) Top surface (scale bar, 1µm) and (b) bottom surface (scale bar, 100µm).

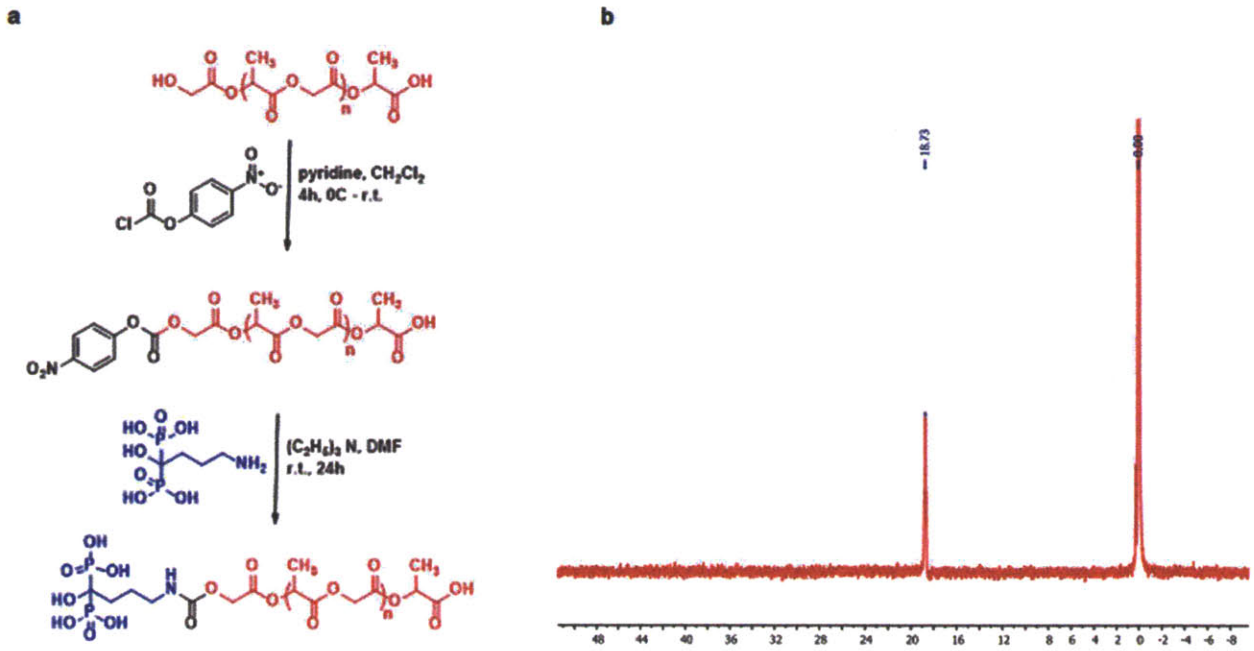

Figure C2. Conjugation of PLGA with alendronate and product characterization. (a) Conjugation scheme of PLGA with alendronate and (b) ^{31}P-NMR on the conjugated PLGA-alendronate product which shows the P signal at 18.7 ppm relative to phosphoric acid standard corresponding to alendronate phosphonate moiety.

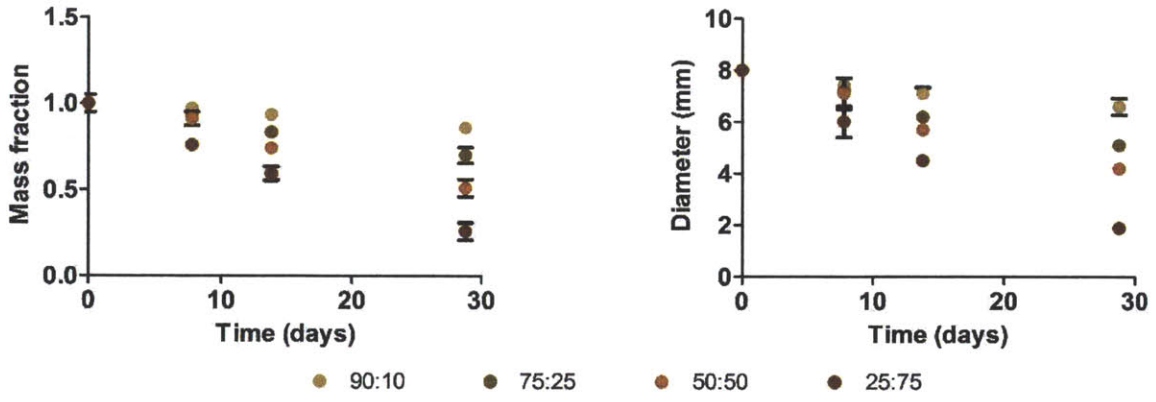

Figure C3. Membrane degradation and growth factor release. Degradation profiles of $P_{0.2}$ + $B_{0.2}$ coated PLGA membrane in a rat calvaria as a function of the PLA:PGA ratio. Degradation was measured by dry mass difference and change in diameter. Data represent the means±s.e.m., n = 3-4 per group per time point

	Experimental Group	Description
1	Untreated (U)	Untreated defect
2	PLGA (50:50) membrane only (M)	Defect treated with an uncoated membrane
3	PLGA Membrane + BMP-2 (0.2μg) ($M + B_{0.2}$)	Membrane coated with low dose BMP
5	PLGA Membrane + BMP-2 (2 μg) ($M + B_2$)	Membrane coated with high dose BMP
4	PLGA Membrane + BMP-2 (0.2μg) + PDGF-BB (0.2μg) ($M + B_{0.2} + P_{0.2}$)	Membrane coated with low dose BMP and low dose PDGF
6	PLGA-Alendronate Membrane + BMP-2 (0.2μg) ($M_{Al} + B_{0.2}$)	PLGA-Alendronate membrane coated with low dose BMP

Table C1: Experimental groups used in this study

References

1. Wang D, Miller S, Sima M, Kopeckova P, & Kopecek J (2003) Synthesis and evaluation of water-soluble polymeric bone-targeted drug delivery systems. Bioconjugate chemistry 14(5):853-859.

2. Spicer PP, et al. (2012) Evaluation of bone regeneration using the rat critical size calvarial defect. Nature protocols 7(10):1918-1929.

Appendix D

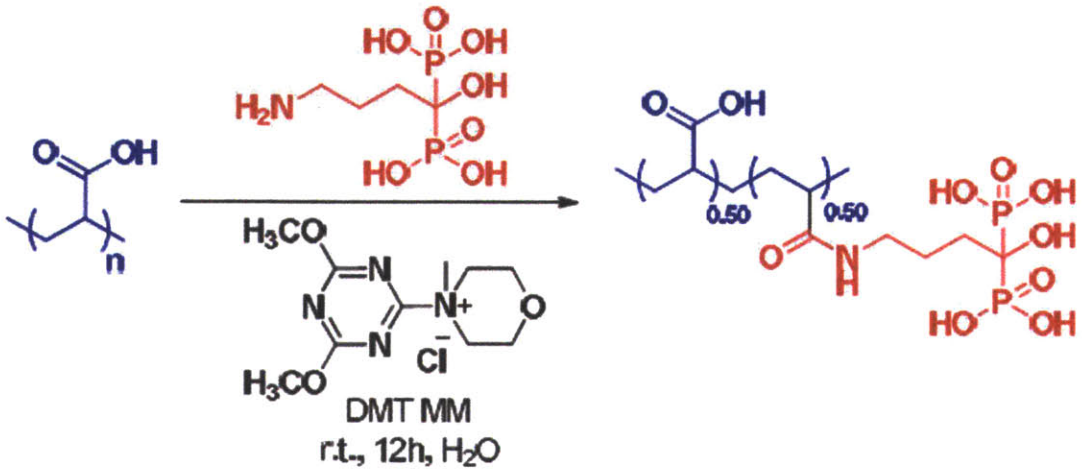

Figure D1. Synthesis of PAA-Alendronate. Approximately 40% functionalization achieved.

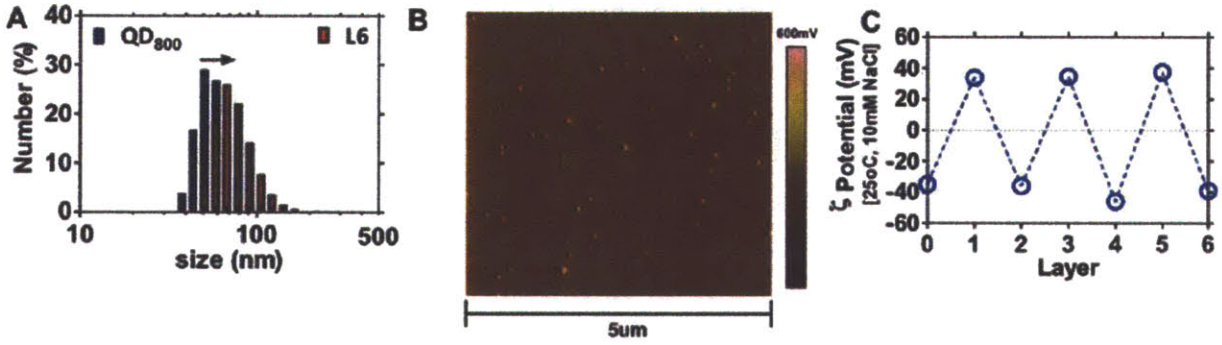

Figure D2. LbL QD characterization. (A) Dynamic light scattering histogram overlay of pre- and post-LbL functionalized QD800 NP core. **(B)** Atomic Force Micrograph of QD800/(PLL/PAA-Al)3 NPs. **(C)** ζ-potential data following each LbL deposition step.

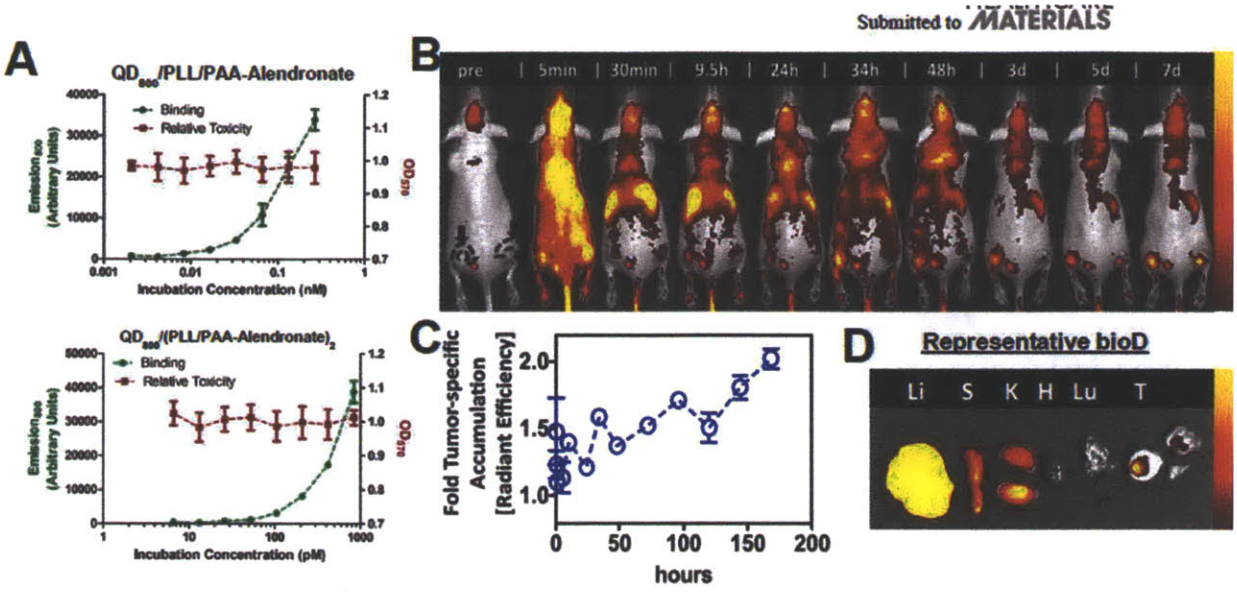

Figure D3. Variation on number of layers on targeted LbL NP stability. (A) *in vitro* binding of 1- and 2-bilayer targeted LbL NPs [QD800/(PLL/PAA-Al)x]. **(B)** *in vivo* fluorescence imaging (640nm, 800nm) following systemic administration of 4L targeted LbL NPs. **(C)** quantification (n = 3 mice, 2 hind flank tumors/mice) of tumor-specific accumulation above pre-injection autofluorescence. **(D)** representative biodistribution data at terminal point from imaging (7d) following systemic administration of 2-bilayer LbLtargeted QD800 NPs. Li = liver; S = Spleen; K = Kidneys; H = Heart; Lu = lungs; T = Tumors.

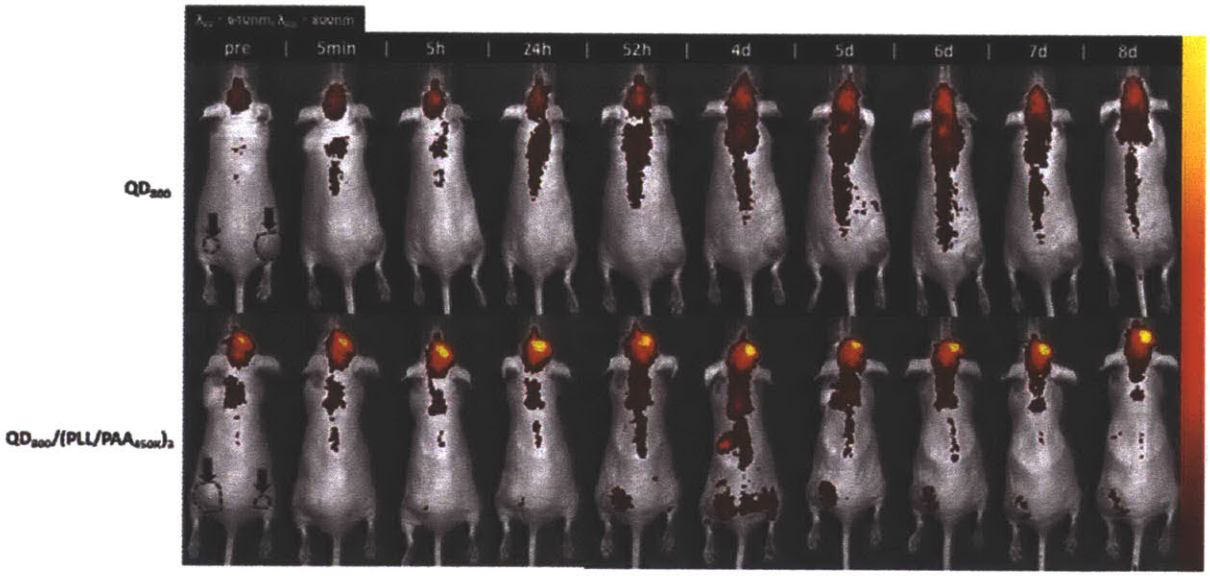

Figure D4. Controls. (top) uncoated carboxylate-modified QD800 NPs. (bottom) untargeted, 3-bilayer (PLL/PAA) LbLfunctionalized NPs.

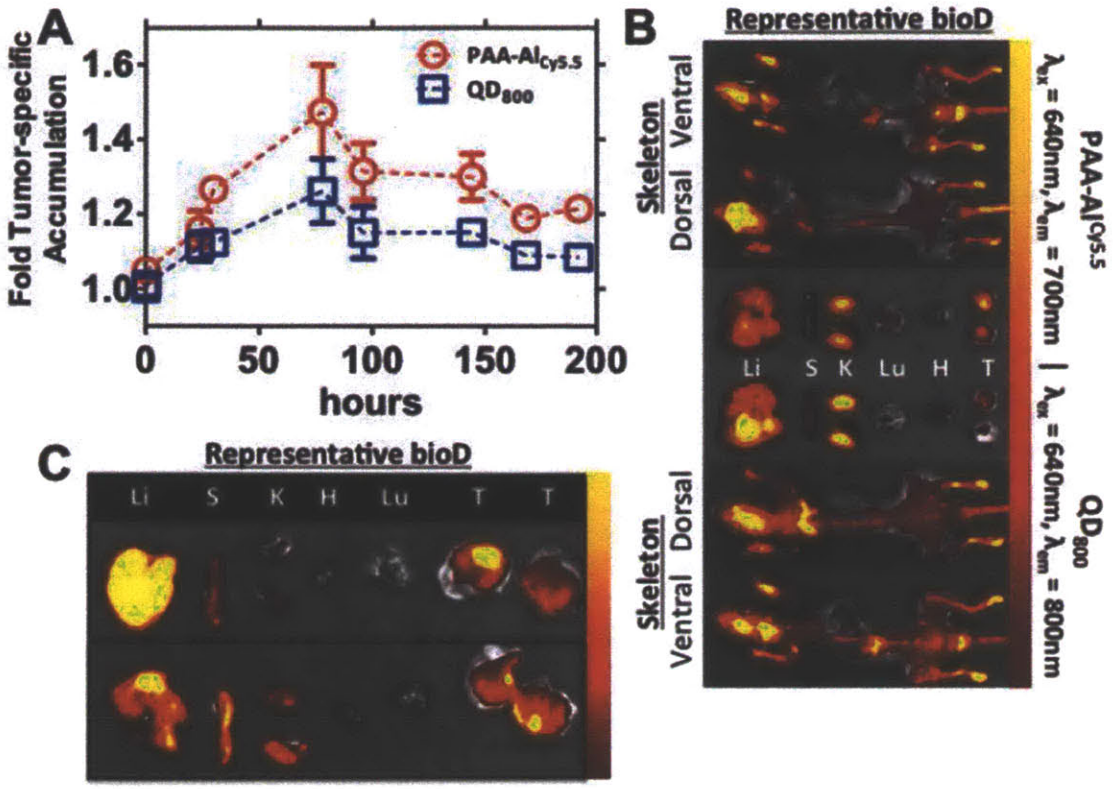

Figure D5. Supplemental data to Figures 6.3 and 6.4. **(A)** Fold tumor specific accumulation as a function of time of the Cy5.5-labeled PAA-Al terminal layer polymer on the QD800 surface. **(B)** Corresponding representative biodistribution (n = 3) of the mice at the terminal point (7d). Tissue harvest (liver, spleen, kidneys, heart, lungs, tumors, and gutted skeleton [ventral and dorsal]) displayed for same animal at terminal point for both channels [PAA-AlCy5.5; QD800]. **(C)** Representative biodistribution data corresponding to quantification in **Figure 6.4D** at terminal point. Li = liver; S = Spleen; K = Kidneys; H = Heart; Lu = lungs; T = Tumors.

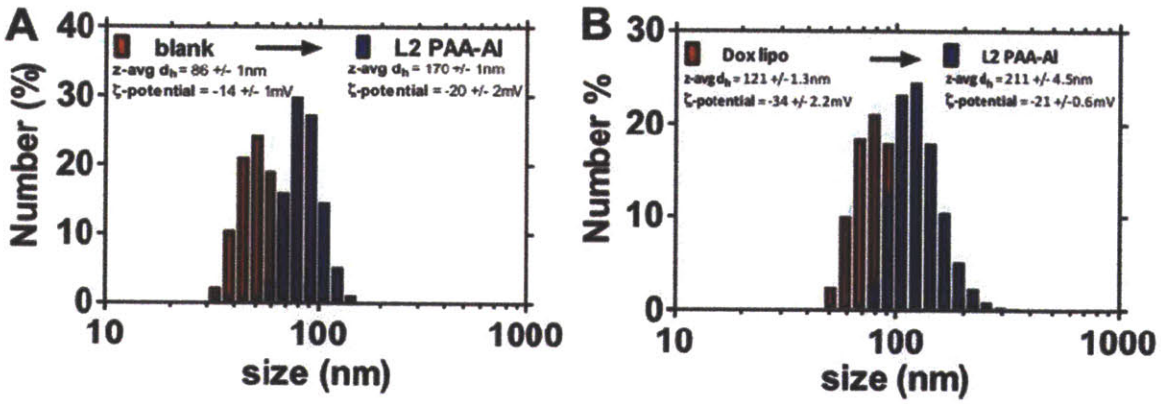

Figure D6. Dynamic light scattering overlays of formulated liposomes and corresponding functionalization via LbL for both **(A)** empty liposome core (for PK data in BALB/c) and **(B)** doxorubicin-loaded liposomes in efficacy studies.

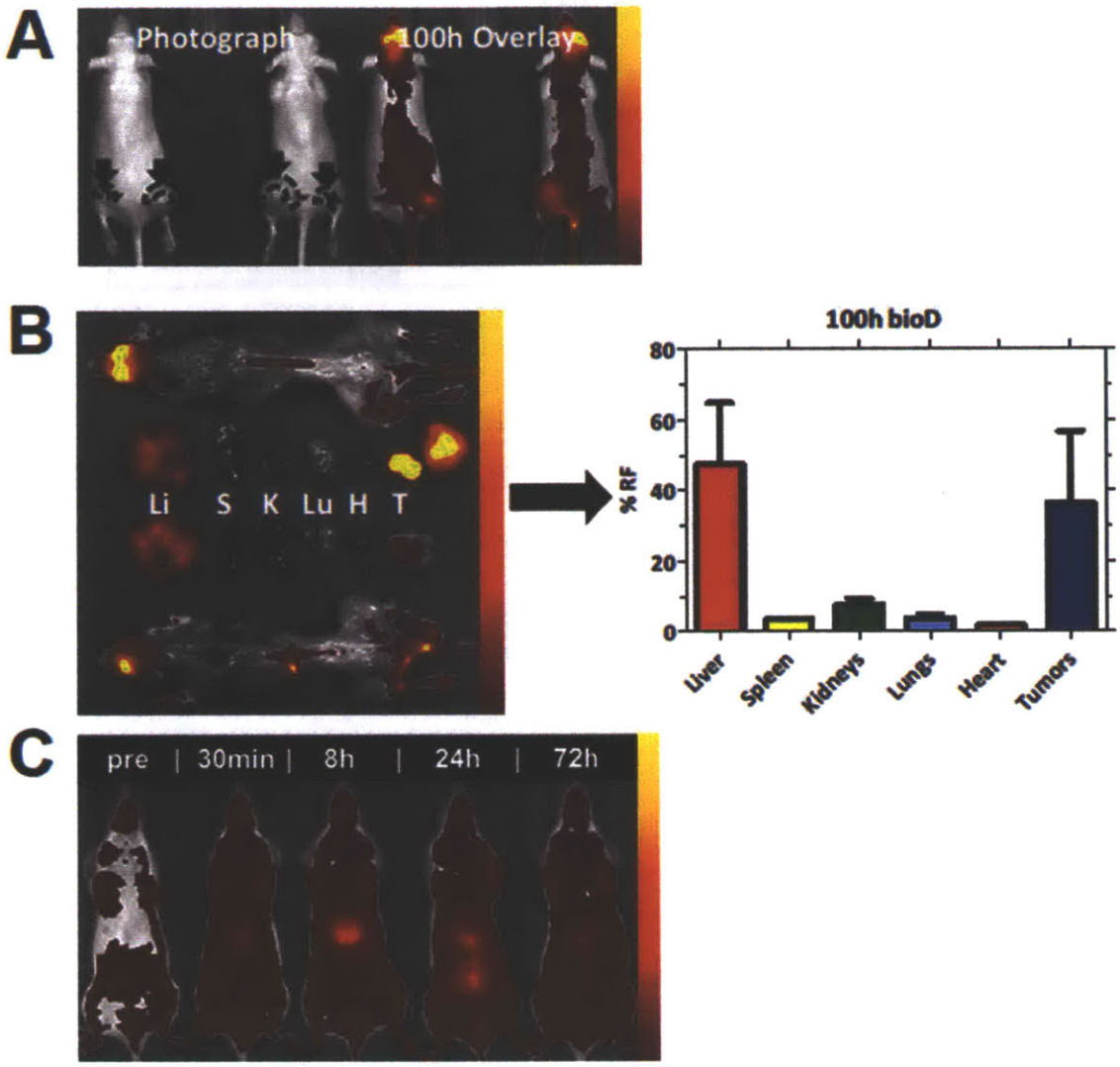

Figure D7. (A) *in vivo* imaging of NCR nude mice at 100h following systemic administration of LbL-targeted empty liposomal NPs. **(B)** Corresponding biodistribution data of harvested tissue and skeleton (dorsal), along with quantification presented as percent recovered fluorescence for tissue (sans skeleton). **(C)** Representative biodistribution (ventral *in vivo* fluorescence imaging) following systemic administration of LbL targeted NPs (empty lipo/PLLCy5.5/PAA-Al) in BALB/c mice for PK studies (presented in **Figure 6.5**). Li = liver; S = Spleen; K = Kidneys; H = Heart; Lu = lungs; T = Tumors.

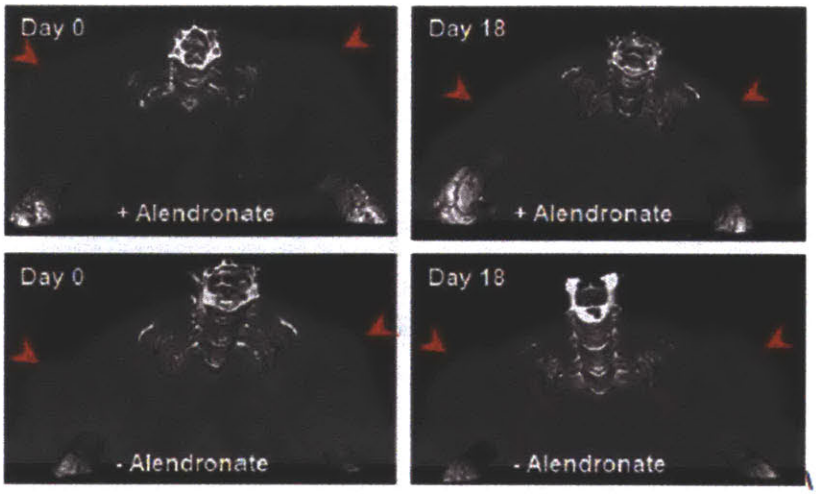

Figure D8. Initial and final representative μCT images of tumor burden (red arrows) in live animals treated with LbL-targeted doxorubicin-loaded liposomes.